

DISS. ETH NO. 26848

***Microfluidic Formation of Artificial Cell  
Membranes and Compartments for Permeation  
Studies and Cascade Reactions***

A thesis submitted to attain the degree of  
DOCTOR OF SCIENCES of ETH ZURICH  
(Dr. sc. ETH Zurich)

presented by

SIMON BACHLER

MSc in Pharmaceutical Sciences, University of Basel

BSc in Life Science Technologies, FHNW

Konstrukteur EFZ

born on 11<sup>th</sup> January 1989

citizen of Stäfa (ZH)

accepted on the recommendation of

Prof. Dr. Petra S. Dittrich (Examiner, ETH Zurich)

Prof. Dr. Stefanie D. Krämer (Co-Examiner, ETH Zurich)

Prof. Dr. Martin Kuentz (Co-Examiner, FHNW)

2020



**Dissertation**

**Microfluidic Formation of Artificial Cell  
Membranes and Compartments for Permeation  
Studies and Cascade Reactions**

**Simon Bachler**

# Abstract

Lipid membranes serve as dynamic boundaries between the extracellular environment and the cytosol, allowing cells to compartmentalize their biochemical functions. These lipid borders are effective barriers that maintain the composition and internal compartments of cells. Lipid membranes are selectively permeable to small molecules, enabling specific transport processes that control the selective passage of substances. In the field of bottom-up synthetic biology, lipid membranes are the scaffold to create minimal cells and to mimic reactions and processes at or across their membrane. Vesicles and droplet interface bilayers are generally used to study cells as simplified models, where microfluidic platforms can improve the creation and investigation of artificial cell membranes and their compartments. Using microfluidics, it is possible to control the experimental conditions more precisely than in bulk assays, and to generate artificial membranes that are very close to the thickness and composition of cellular lipid membranes. The integration of artificial cells in microfluidic systems is still challenging and existing methods have some shortcomings.

The focus of this work was first to improve current platforms for the hydrodynamic trapping of vesicles created by swelling or electroformation. We used microfluidic devices to study the interaction of both peptides and toxins with lipid membranes, observing their permeation, membranolytic effects, and pore formation. These artificial cells, however, were largely polydisperse and the encapsulation of substances remained challenging. We therefore developed a method based on microfluidic droplet arrays to address this issue, where droplets were precisely placed with a spotting device in close proximity on the surface of a plate with micro-fabricated cavities. Droplets were coated with a phospholipid monolayer and droplet interface bilayers formed when two or more droplets were brought into contact. These artificial cells were monodisperse, allowing straightforward encapsulation of substances, and enabling the tailoring of the membrane composition. We initially analyzed the artificial cell membranes and compartments through an integrated fluorescence microscope. Subsequently, we developed a protocol to separate and extract the droplets, and to interface our platform with label-free matrix-assisted laser desorption/ionization and liquid chromatography mass spectrometry analysis. Translocation of molecules across membranes was tailored by the addition of the pore-forming toxin alpha-hemolysin to selected droplets. Our method delivered the automated formation of one- and two-dimensional multi-compartmental droplet networks. We demonstrated the effectiveness of our approach by connecting droplets containing different compounds and enzyme solutions, and performing both translocation experiments and multistep enzymatic cascade reactions across the droplet network. Moreover, we investigated the permeation of molecules across the lipid membranes, an important component in drug

development to predict the absorption of substances. Example model permeants were added to donor droplets, and the permeation across symmetric and asymmetric lipid bilayer membranes to acceptor droplets was monitored. With this approach, we were able to identify the permeability coefficients.

Our platform has the potential to become a tool for the screening of drug membrane permeability in the future. The embedding of membrane proteins and the fusion of cell-derived vesicles with the membrane are feasible research directions. Finally, the platform may prove useful for other studies such as the three-dimensional assembling towards artificial cell colonies and creating complex artificial systems for bottom-up synthetic biology.

# Zusammenfassung

Lipidmembranen dienen Zellen als dynamische Barriere zwischen der extrazellulären Umgebung und dem Zytosol welches ihnen ermöglicht, ihre biochemischen Funktionen in Kompartimente zu unterteilen und diese aufrechtzuerhalten. Zellmembrane sind selektiv permeabel für kleine Moleküle und erlauben den Austausch von Substanzen durch spezifische Transportprozesse. Im Feld der synthetischen Biologie werden mithilfe von Lipiddoppelschichten vereinfachte Zellen und Kompartimente erzeugt, wodurch zellspezifische Reaktionen und Prozesse simplifiziert nachgestellt werden können. Dabei werden zum Beispiel Vesikel und spezifische Wasser-in-Öl Emulsionen zur Herstellung von Zellmodellen verwendet. Zur Untersuchung und Erzeugung von künstlichen Zellmembranen und -kompartimenten können mikrofluidische Systeme eingesetzt werden. Dies ermöglicht eine bessere Kontrolle von experimentellen Bedingungen im Vergleich zu konventionellen Versuchsaufbauten. Zudem können Modellzellmembranen generiert werden, welche ähnliche Dicken und Zusammensetzungen aufweisen, wie Lipiddoppelschichten von realen Zellen. Die Eingliederung von künstlichen Zellen in mikrofluidische Systeme ist auch zur heutigen Zeit eine Herausforderung und bestehende Methoden besitzen noch Schwachstellen, welche optimiert werden müssen.

Der Fokus dieser Doktorarbeit war zunächst, bestehende Methoden der Herstellung von Vesikeln und deren hydrodynamische Immobilisierung mittels mikrofluidischer Plattformen zu verbessern. Anhand derer wurde die Interaktion von Peptiden und Toxinen mit der Lipiddoppelschicht von Vesikeln untersucht. Dabei konnte deren Einfluss an verschiedenen Effekten, wie die Zerstörung der Membran, auftretende Permeation oder die Ausbildung von Poren beobachtet werden. Allerdings waren die künstlichen Zellen polydispers und die Einschliessung von Substanzen war eine Herausforderung. Aus diesem Grund haben wir eine mikrofluidische Methode entwickelt, welche auf Wasser-in-Öl Emulsionen basiert. Wassertropfen im Nanoliter-Bereich konnten unter Öl, spezifisch und genau, auf einer mit Kavitäten mikrostrukturierten Platte platziert werden, was eine Immobilisierung der Wassertropfen ermöglichte. Dem Öl wurden Phospholipide hinzugegeben, welche sich zu einer Lipidmonoschicht um die Wassertropfen anlagerten. Durch ein automatisiertes sehr nahes platzieren von zwei oder mehr Wassertropfen entstand ein Kontakt durch den sich aus der Lipidmonoschicht eine Lipiddoppelschicht bildete. Diese Modellzellen waren monodispers und erlaubten eine direkte Einkapselung von Substanzen, sowie eine einfache Anpassung der Membranzusammensetzung. Zunächst wurden die künstlichen Zellmembranen und -kompartimente durch ein integriertes Fluoreszenzmikroskop analysiert. Anschliessend wurde ein Protokoll entwickelt um die einzelnen Kompartimente zu separieren und zu

extrahieren. Die entnommenen Kompartimente konnten danach mit Label-freien Matrix-unterstützten Laser-Desorption/Ionisation und Flüssigchromatographie mit Massenspektrometrie-Kopplung analysiert werden. Ein Transfer von Molekülen über die Membranen wurde durch die Ausbildung von Poren mithilfe des Toxins alpha-Hämolyisin, auf unsere Bedürfnisse zugeschnitten und gesteuert. Mit der entwickelten mikrofluidischen Methode war es möglich, automatisiert, ein- und zweidimensionale Netzwerke mit multiplen Kompartimenten zu formieren. In dem wir verschiedene Kompartimente, welche unterschiedliche Substanzen und Enzyme beinhalten, zu einem Verbund anordneten, konnte die Leistungsfähigkeit der Plattform demonstriert werden. Wir beobachteten zum einen den Transfer von Substanzen durch die Poren, und zum anderen war es möglich eine mehrstufige Kaskadenreaktion durchzuführen. Weiterführend untersuchten wir die Permeation von Molekülen über die Lipiddoppelschicht. Dies ist ein wichtiger Faktor in der Erforschung und Entwicklung neuartiger Arzneistoffe, und ermöglicht die intestinale Absorption von Substanzen abzuschätzen. Wir verwendeten Fluorophore als Beispielarzneimittel und untersuchten die Permeation von einem Kompartiment in das andere, durch symmetrische und asymmetrische Lipidmembranen. Dadurch war es möglich die Permeabilitätskoeffizienten zu ermitteln.

Unsere Plattform könnte in der Zukunft ein etabliertes Hilfsmittel werden, um die Permeabilität von Wirkstoffen im grösseren Massstab zu testen. Andere mögliche zukünftige Forschungsrichtungen wären Membranproteine einzubauen und die künstlichen Membranen mit Vesikeln (welche aus Zellenmembranen gewonnen wurden) zu fusionieren. Weiterführend, wäre die Plattform auch einsetzbar für die Formierung von dreidimensionalen künstlichen Zellnetzwerken und die Generierung von komplexen Systemen im Bereich der synthetischen Biologie.

# List of Content

<b>CHAPTER 1 INTRODUCTION.....</b>	<b>1</b>
1.1 Cell Membranes and Compartments .....	2
1.2 Permeation and Transport Processes across Membranes .....	5
1.3 Microfluidic Devices for the Creation and Investigation of Cell-Mimicking Compartments and Permeation Analysis .....	13
1.4 Scope and Structure of this Doctoral Thesis .....	27
1.5 References .....	29
<b>CHAPTER 2 INTERACTION OF PEPTIDES AND TOXINS WITH LIPID MEMBRANES STUDIED ON A MICROFLUIDIC DEVICE .....</b>	<b>38</b>
2.1 Abstract .....	40
2.2 Introduction .....	41
2.3 Experimental Section .....	43
2.4 Results and Discussion .....	47
2.5 Conclusion .....	56
2.6 Acknowledgements .....	57
2.7 References .....	57
<b>CHAPTER 3 TAILORED TRANSLOCATION AND REACTION CASCADES IN NANOLITER DROPLET NETWORKS.....</b>	<b>60</b>
3.1 Abstract .....	61
3.2 Introduction .....	62
3.3 Methods .....	64
3.4 Results .....	70



3.5	Discussion.....	77
3.6	Acknowledgements.....	79
3.7	References.....	79
3.8	Supplementary Information.....	83
	<b>CHAPTER 4 PERMEATION STUDIES ACROSS SYMMETRIC AND ASYMMETRIC MEMBRANES IN MICRODROPLET ARRAYS .....</b>	<b>89</b>
4.1	Abstract.....	90
4.2	Introduction.....	91
4.3	Experimental Section.....	93
4.4	Results and Discussion.....	98
4.5	Conclusion.....	105
4.6	Acknowledgements.....	106
4.7	References.....	106
4.8	Supplementary Information.....	109
	<b>CHAPTER 5 CONCLUSION AND OUTLOOK .....</b>	<b>116</b>
5.1	General Conclusion.....	117
5.2	Outlook.....	119
5.3	References.....	122
	<b>ACKNOWLEDGEMENTS .....</b>	<b>123</b>
	<b>ABBREVIATIONS.....</b>	<b>124</b>
	<b>CURRICULUM VITAE.....</b>	<b>127</b>



## Chapter 1

# Introduction

## 1.1 Cell Membranes and Compartments

The fundamental unit of living organisms is the cell [1]. All living organisms are composed of one or more cells from the smallest and least complex to the largest and most complex [2]. In multicellular organisms, the precise location of cells and the location of intracellular organelles within cells are essential for normal development and function [2]. Life-sustaining biochemical reactions take place in cells [3]. Cells are displayed by many different shapes and architectures [3, 4]. Hooke first discovered the cell in plants in 1665 [1]. Up to today, it is still matters of speculation how the first cell came into existence and how life originated [5]. In the origin of life, formation of lipid borders played a crucial role [6, 7]. These lipid borders maintain as plasma membranes the internal composition of the cell [5]. Figure 1-1 shows a generalized cell and its different components and compartments [8].

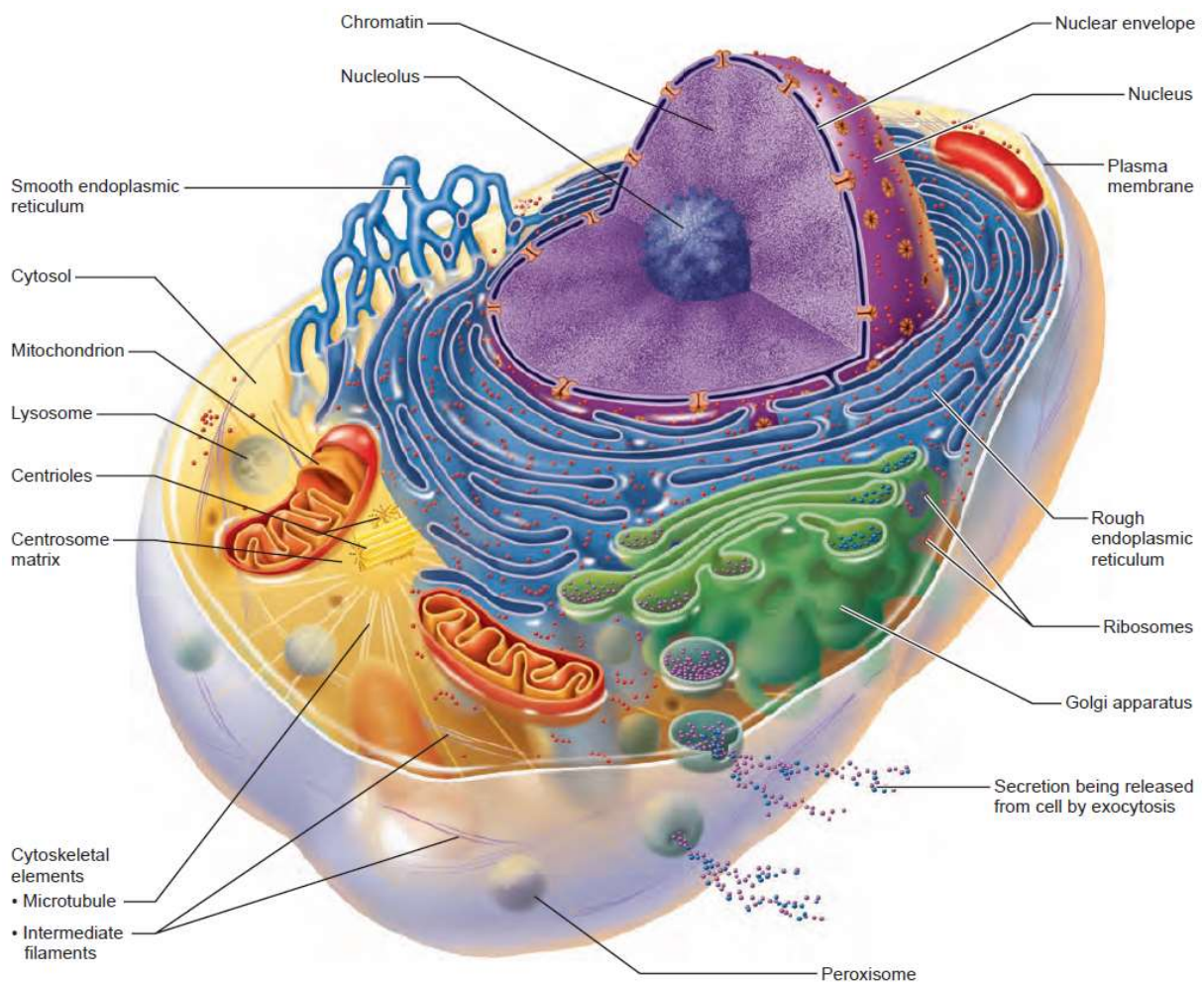


Figure 1-1: Structure of the generalized cell with different components and compartments (not all organelles are drawn to the same scale). This illustration features a model cell common to many human cells, but no cell is exactly like this one. Source: Marieb, Elaine N., *Essentials of Human Anatomy & Physiology*, (10<sup>th</sup> ed.), ©2012 [8]. Reprinted by permission of Pearson Education, Inc., New York.

Cells compartmentalize their biochemical functions in a variety of ways for example by creating physical barriers, which separate a compartment by membranes and/or proteins [9]. A cell can perform its specific functions more efficiently with compartments [10]. Eukaryotic cells have evolved an interactive intracellular system, which is called endomembrane system [8, 11]. Different molecules are moved with membrane-enclosed transport carriers among membrane-bound compartments [11]. A cell contains organelles as compartments like the mitochondria, endoplasmic reticulum, peroxisomes, Golgi apparatus, and lysosomes [8]. Most of these organelles are surrounded by a membrane and this barrier enables these organelles to maintain an internal environment different from the surrounding cytosol [8]. This compartmentalization is crucial for the function of a cell [8] and the separation of functions results in evolvable and robust systems [9, 12, 13]. Biochemical activities would be chaotic without the membranes since many enzymes would be randomly mixed [8]. The lipid composition allows the endomembrane system to recognize compartments and that organelles can interact with each other [8].

Figure 1-2 illustrates the structure of the plasma membrane as interface of the cell with its environment [3]. The plasma membrane separates the two of the body's major fluid compartments, (i) the extracellular fluid outside and (ii) intracellular fluid within cells [8]. This membrane consists of a double layer of lipids (bilayer) with polar head groups facing to the interior and exterior aqueous environments, carbohydrate and phosphate components, and a large number of proteins embedded in the membrane [2, 4]. The lipid bilayer is formed with amphiphilic lipid molecules [14]. Phospholipids contain a non-polar hydrophobic tail and a polar hydrophilic head as visualized in Figure 1-2 [14]. Most polar head groups of phospholipids consist of glycerol conjugated to a nitrogenous compound (e.g., choline, serine, or ethanolamine) via a phosphate bridge [14]. The nitrogenous group is positively charged and the phosphate group is negatively charged [14]. The non-polar tail of phospholipids is formed by two long-chain fatty acids [14]. Both fatty acids are covalently linked to the glycerol component of the hydrophilic head [14]. The hydrophobic tail of lipids in a bilayer meet in the middle of the membrane and form the non-polar region [4]. Due to the amphipathic nature and shape of phospholipids, they form spherical micelles (with the tails inward) and/or bilayers (bimolecular sheets with the hydrophobic tails sandwiched between the polar head groups) spontaneously in aqueous solutions [15]. The lipid composition varies in different cell types and is often asymmetric [14, 15]. Many lipid bilayers also contain cholesterol especially in eukaryotic plasma membranes [14, 15].

As illustrated in Figure 1-2 different proteins are incorporated within the lipid bilayer [8, 14]. Transmembrane proteins span the entire thickness of the membrane to be exposed to the interior and exterior of the cell [14]. Other proteins are embedded within the outer or inner lipid leaflet [14]. In contrast to peripheral proteins, which are not embedded in the lipid membrane,

## Chapter 1

but rather loosely attached to e.g. integral proteins [8]. Peripheral proteins support the membrane [8]. Transmembrane proteins control the internal ion concentrations, establish a transmembrane electrical potential, and provide the cell with nutrients [3]. Some plasma membrane proteins mediate specific interactions of cells with their immediate environment [3]. The activity of the cell is influenced by transmembrane receptors, which convert the binding of extracellular signaling molecules (e.g., growth factors and hormones) into electrical or chemical signals [3].

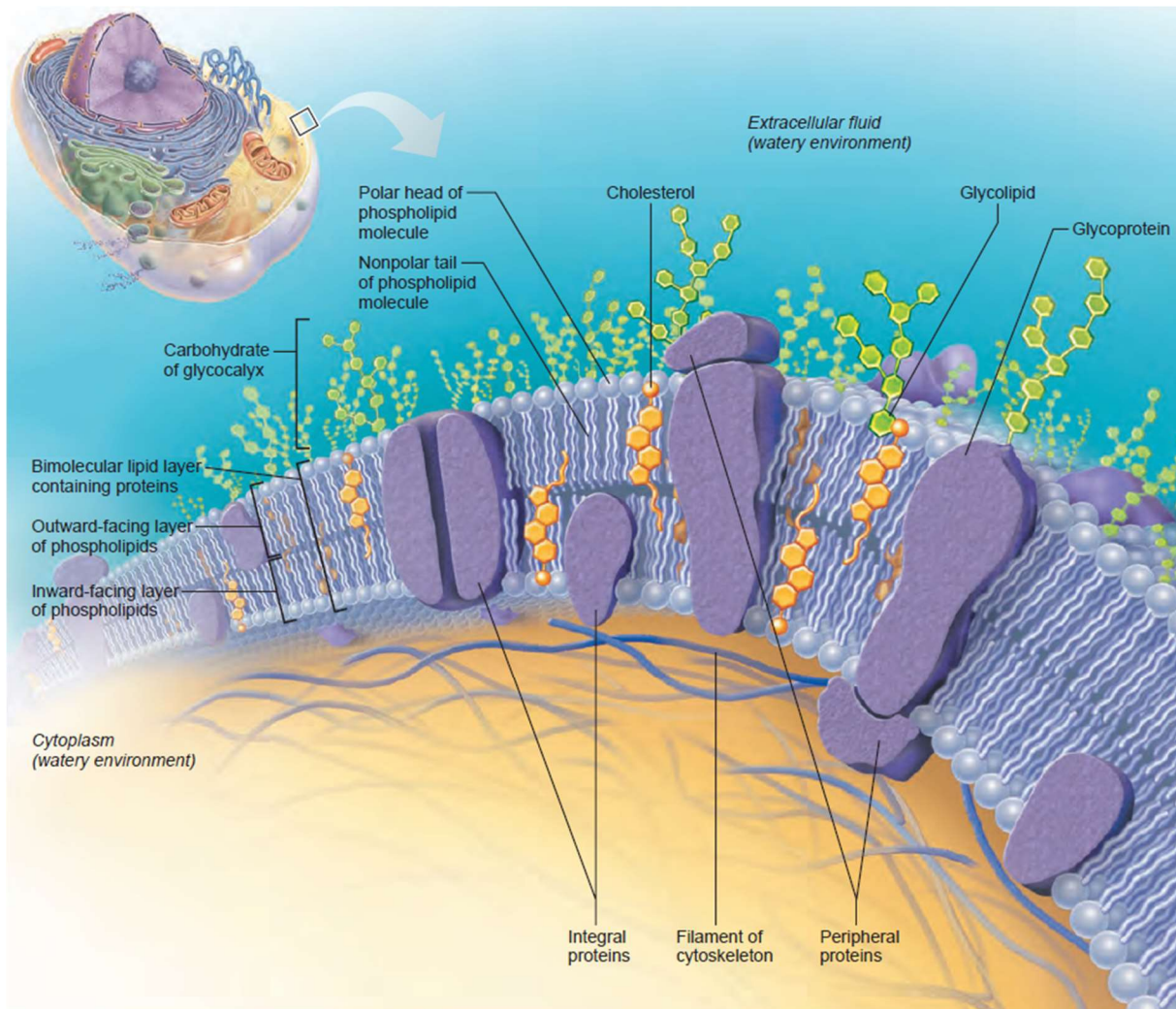


Figure 1-2: Structure of the cell membrane according to the fluid mosaic model. The phospholipid bilayer forms the basic structure of the membrane. The associated proteins are involved in membrane functions such as membrane transport, cell-to-cell recognition, and catalysis. Source: Marieb, Elaine N., *Essentials of Human Anatomy & Physiology*, (10<sup>th</sup> ed.), ©2012 [8]. Reprinted by permission of Pearson Education, Inc., New York.

## 1.2 Permeation and Transport Processes across Membranes

The membrane of a cell is selectively permeable to small molecules [5]. As discussed, the phospholipid bilayer membrane forms a barrier that prevents the free exchange of biological molecules between the external environment and the cytoplasm of the cell [5]. The selective passage of small molecules across the phospholipid bilayer is mediated by permeation and specific transport proteins [5]. Figure 1-3 describes different transport processes across cell membranes [16].

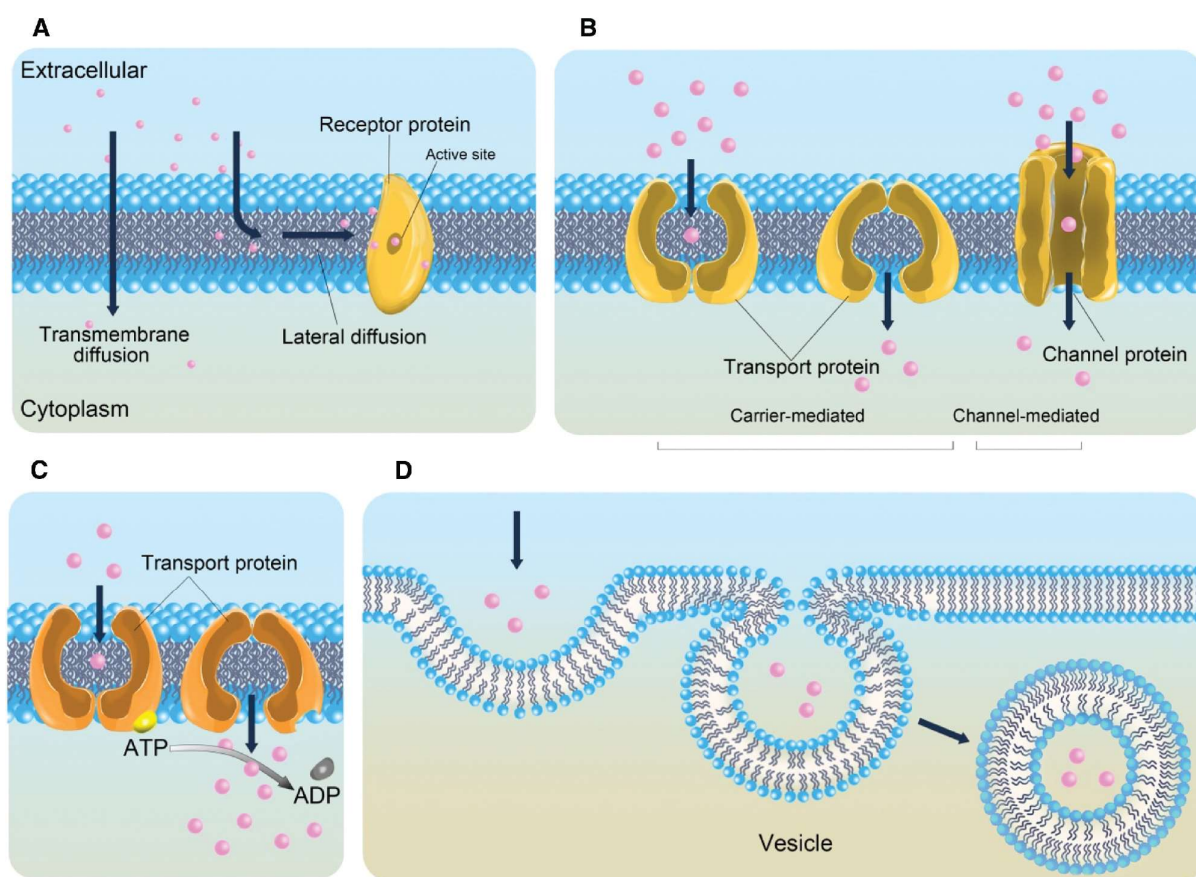


Figure 1-3: Illustration of transport processes across cell membranes by the movement of molecules (pink dots). (A) Passive permeation moves down the concentration gradient and occurs spontaneously. Some substances can either permeate across the membrane or laterally diffuse in the membrane to reach a target embedded in the lipid bilayer. (B) Facilitated diffusion mediated either by channel or carrier proteins. (C) Active transport with input of energy against the concentration gradient. Adenosine triphosphate (ATP) is converted to adenosine diphosphate (ADP). (D) Endocytosis process by formation of a lipid vesicle. Reprinted from Li et al. [16] with permission from De Gruyter / Creative Commons.

Compounds that can translocate across cell membranes are of great importance in medicines, pharmaceutical sciences, and biology [17]. Molecules, which cross cell membranes, are useful for biological research application including but not limited to indicators of ion concentrations, enzyme substrates, fluorescent dyes, and various protein inhibitors [17]. In pharmaceutical sciences and medicines, many drugs need to be absorbed in the gut and/or are acting on

intracellular targets, for example reverse transcriptase inhibitors used for the treatment of the human immunodeficiency virus or statins that inhibit cholesterol production [17].

### 1.2.1 Passive Permeation

Molecules diffuse down their concentration gradients across a lipid bilayer visualized on the left-hand side in Figure 1-3A [15, 16]. The rate at which compounds permeate varies enormously [15]. Small non-polar molecules, e.g.,  $\text{CO}_2$  and  $\text{O}_2$ , diffuse fast across lipid bilayers [15]. Small uncharged polar molecules, e.g., urea and water, diffuse much slower across a lipid bilayer compared to small non-polar molecules [15]. For water, the diffusion process across a semipermeable membrane is often referred to as osmosis [8]. On the other hand, lipid bilayers are almost impermeable to ions (and other charged molecules), e.g.,  $\text{Na}^+$  or  $\text{K}^+$  [15]. The high degree of hydration and the charge of these molecules prevents them from entering the hydrocarbon chains of the lipid bilayer [15].

There are two main models to describe the kinetics for the permeation of drug-like molecules across lipid bilayer membranes [18-20]. The first one is the diffusion model according to *Fick's* first law (visualized on the left-hand side in Figure 1-3A) [16, 18]. The second one is a flip-flop model in which an amphiphilic compound (i) partitions into one lipid layer, (ii) then performs flip-flop (translocation) to the other lipid layer, and (iii) partitions out of the lipid layer on the opposite side of the membrane [18, 21]. Figure 1-4 shows the flip-flop model with an example compound [18].

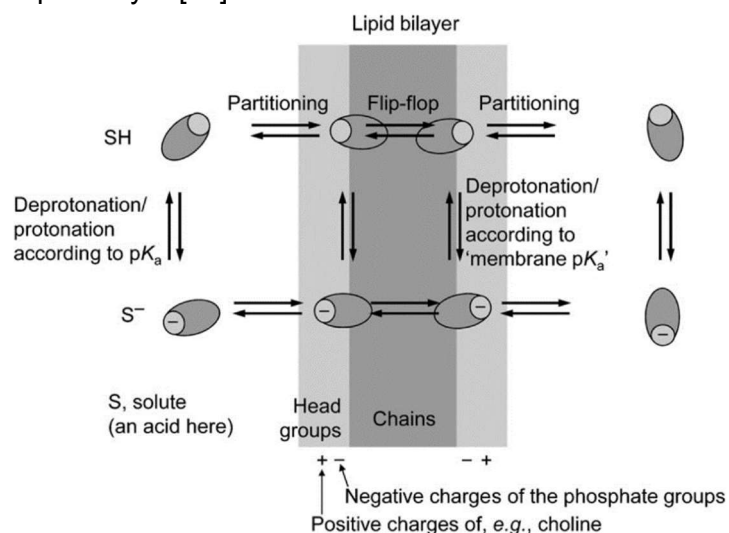


Figure 1-4: Model of lipid bilayer permeation and partitioning with an amphiphilic compound (monoprotic acid). The lipid bilayer is visualized as head groups (light grey) and chains (dark grey). The hydrophilic moiety (light grey) of the compound prefers the polar head groups in the lipid membrane. Whereas, the hydrophobic part (dark grey) of the compound assembles within the lipid chains. The compound partitions between the two lipid leaflets and the aqueous phases (white). The protonation state of the molecule can change. Reprinted from Krämer et al. [18] with permission from Wiley.

### 1.2.2 Passive and Active Transport by Proteins

Cell membranes can allow the passage of different (polar) molecules, which do not or only very slowly cross synthetic lipid bilayers, e.g., ions, amino acids, nucleotides, sugars, and many cell metabolites [15]. Special carrier and channel proteins are transferring such



substances across the cell membrane [15]. Many carrier and channel proteins show saturation and can be inhibited by certain compounds [8].

Figure 1-3B illustrates the passive transport process called facilitated diffusion, which requires no energy input [8, 16]. The transported molecules either move through water-filled protein channels or bind to protein carriers [8]. Molecules moving through these proteins follow the concentration gradient [8]. Channel proteins usually transport water or ions across aqueous channels from one side of the membrane to the other [8]. Channels are selective based on the pore size and charges of amino acids present in the channel [8]. Some channels are gated and controlled, others are always open [8]. Also association and binding sites can be present in channels [8]. Carrier proteins bind specific substances of a certain class of molecules [8, 15]. For example, they transport amino acids and sugars since these classes of molecules are too large for passage across channels [8]. The carrier proteins undergo conformational changes to allow a molecule to be transported through the membrane [15].

Figure 1-3C shows how substances are moved against a concentration gradient with active transport processes [8, 16]. Here, the transport protein is coupled to a source of metabolic energy [15]. In primary active transport, the energy comes from the hydrolysis of adenosine triphosphate (ATP) to adenosine diphosphate (ADP) [8]. The transport of two (or more) substances is coupled in secondary active transport [22]. One molecule moves down its concentration gradient and the other molecule moves against its concentration gradient [22]. For example, sodium is moved by an ATP-powered pump across the cell membrane against its concentration gradient and the energy is stored in the ion gradient [8]. When then sodium moves down its chemical gradient it provides energy for the uphill movement of another substance against its chemical gradient [22].

### 1.2.3 Drug Absorption

Pharmaceutical patient treatments are primarily administered by oral drug delivery [23]. In this area, absorption, solubility, and bioavailability are important topics. The gut mainly absorbs nutrients, carbohydrates, amino acids, vitamins, fat, and minerals [23]. This absorption processes require a selectively permeable barrier [24]. The intestinal mucosa consists of an epithelial cell barrier that separates the gut lumen from the body [25]. The epithelial cells establish a barrier between the internal milieu and sometimes hostile external environments [24]. When a drug is administered, it must be present in the bloodstream to reach its intended target inside of the body for most applications [26]. In this regard, pharmacokinetics describes the time course of a drug within the body and includes the processes of absorption, distribution, metabolism, and excretion (ADME) [27]. The term bioavailability describes the fraction of drug reaching the systemic circulation [26]. Any factors that impede the active drug from reaching

the systemic circulation influence the bioavailability [26]. These factors include permeation across physiologic barriers, the effect of transporters, and metabolism of the drug before it reaches the systemic circulation [26]. Figure 1-5 shows the drug absorption and metabolism process [28]. During drug uptake, metabolism can for example take place in the gut wall and the liver (first-pass effect) [28].

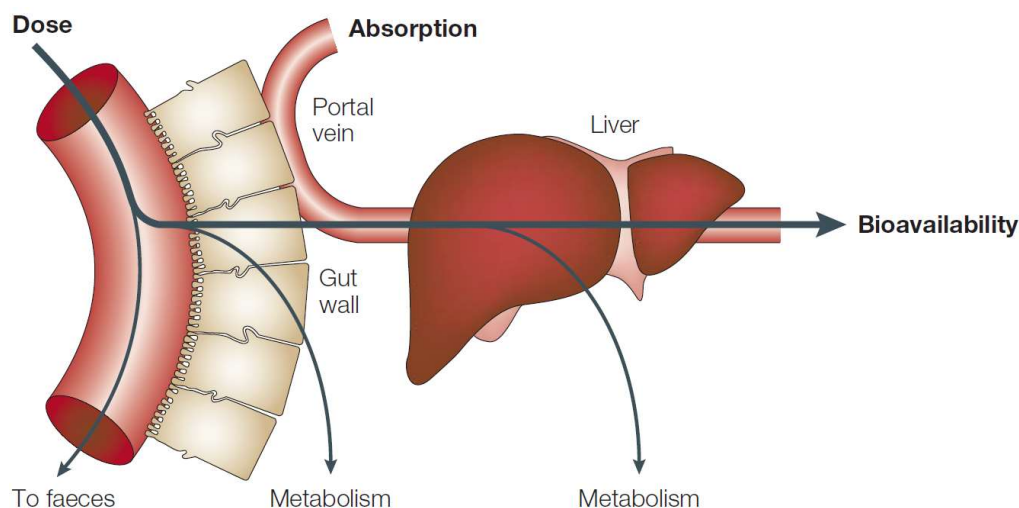


Figure 1-5: Drug absorption and metabolism. Reprinted from Waterbeemd et al. [28] with permission from Nature Publishing Group.

In drug discovery and development, it is important to classify compounds. In this regard, the biopharmaceutical classification system (BCS) was developed [29-31]. The BCS correlates the bioavailability and the drug product dissolution (Figure 1-6) [29]. Here, the optimal case would be to reach for high solubility (insures that drug solubility will not limit dissolution), fast dissolution (insures that the gastric emptying process is the rate-limiting step for absorption of highly soluble and highly permeable drugs), and high permeability (insures that drug is completely absorbed during the limited transit time through the small intestine) [32, 33]. Later, the biopharmaceutical drug disposition classification system (BDDCS) [34] (to predict drug disposition and potential drug-drug interactions in the intestine and the liver [33]) and the developability classification system (DCS) [35, 36] (to address issues in product development [35]) were introduced.

A drug will in most cases only be absorbed when it is in solution [29]. It is possible to increase the solubility / dissolution of a poorly soluble drug with different drug formulation approaches [30, 37] for example with lipid-based formulations [38]. On the other hand, it is difficult to increase the permeability or decrease the first-pass metabolism for a selected compound [39]. Therefore, it is also important to understand how molecules translocate across membranes and how metabolic mechanisms work. In this doctoral thesis, we focus on the processes at and across the membranes and compartments. Besides drug absorption, there are also

intracellular targets, where a drug needs to reach the interior of a cell by translocating across the membrane [17, 40].

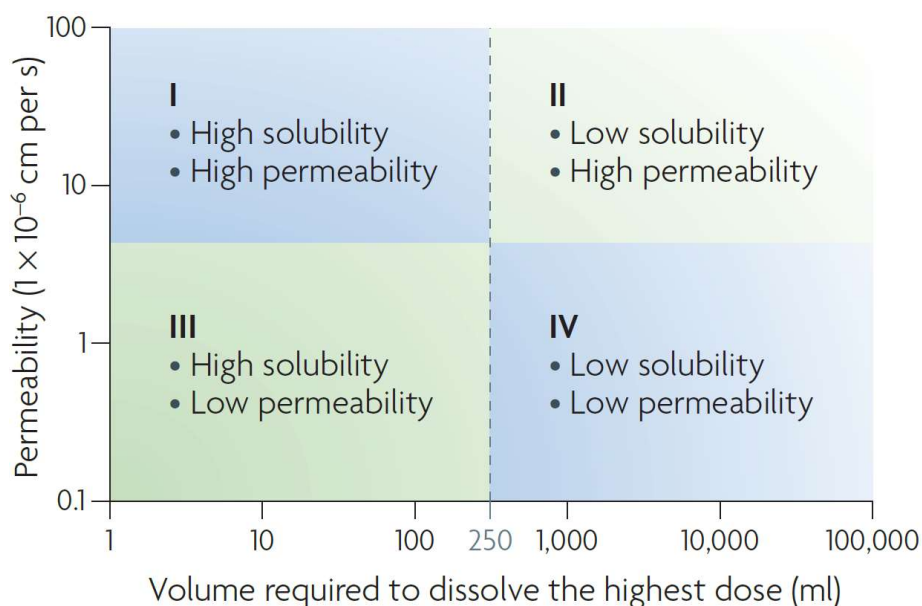


Figure 1-6: Biopharmaceutical classification system (BCS) characterization of drugs based on permeability and solubility measures. Reprinted from Rautio et al. [31] with permission from Nature Publishing Group.

#### 1.2.4 Common Permeation Predicting Methods

Membrane permeability predicting methods and assays play an important role in drug screening [41-43]. Lipinski formulated “the rule of 5” to estimate solubility and permeability in discovery and development settings [44]. Poor permeation or absorption of a drug is more likely when there are more than 5 H-bond donors, 10 H-bond acceptors, the calculated Log P is greater than 5, and the molecular weight is greater than 500 Dalton [44]. Later variants were introduced, which for example stated that for a compound the number of rotatable bonds should be  $\leq 10$  and the polar surface area (PSA) should be  $\leq 140 \text{ \AA}^2$  [45]. These rules-of-thumb are important when developing a new drug. However, almost every molecule behaves differently and to select the best candidates for advancement in drug discovery and development, it is also important to assess the permeability in assays [46]. Figure 1-7 illustrates different possibilities to probe for the potential if a drug passes across biological membrane [42]. The octanol/water partition coefficient, parallel artificial membrane permeability assay (PAMPA), and cellular monolayers are discussed in the following sub chapters.

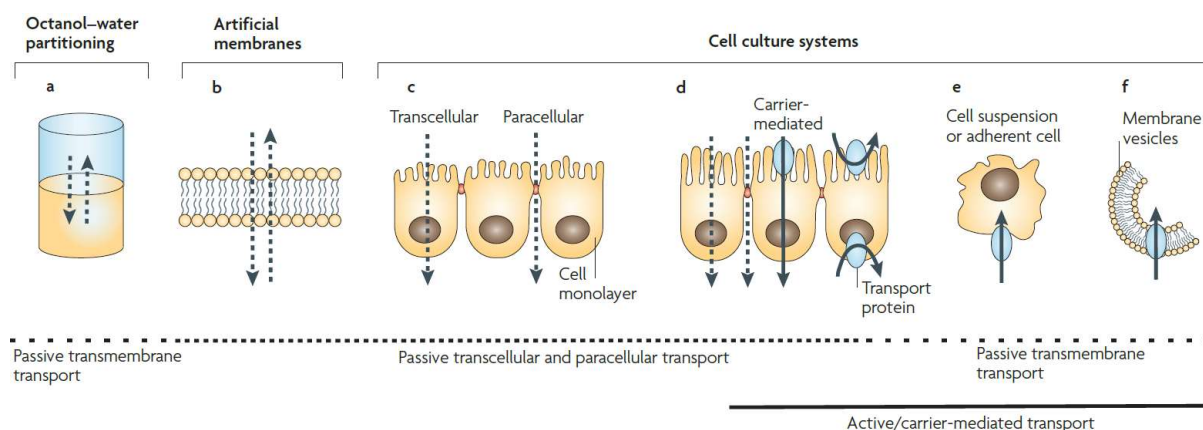


Figure 1-7: Multiple techniques assess the potential of a drug to pass biological membranes by different processes. a) Octanol-water partitioning system. Dotted lines indicate passive and solid lines indicate carrier-mediated transport routes. b) Artificial membranes. c) A monolayer-forming cell line with passive paracellular and passive transcellular pathways with negligible carrier-mediated transport. d) A monolayer-forming cell line with carrier-mediated and passive drug transport routes. e) An adherent or suspension cell line that overexpresses either an uptake or an efflux transport protein. f) The inverted membrane vesicles from a cell line expressing an efflux transport protein allow efflux protein-mediated accumulation of a substrate in the vesicles. Reprinted from Sugano et al. [42] with permission from Nature Publishing Group.

#### 1.2.4.1 Octanol/Water Partition Coefficient

Partition coefficients between two immiscible liquids are used to determine the lipophilicity of a compound [47-49]. Most commonly used is the octanol-water partitioning coefficient [46]. Partition coefficients describe the partition equilibrium of a solute between an immiscible organic solvent and water [48, 49]. Figure 1-7a shows the principle of the octanol-water partitioning system [42]. Organic solvent-water partitioning systems are often used to model the distribution of drugs into the cell membrane, rather than the drug permeation across phospholipid bilayer membranes [42]. A drug should have an optimal lipophilicity to permeate across a membrane [48]. The drug will be trapped in the membrane when it is too lipophilic [48]. The partition coefficient  $\text{Log } P$  describes the lipophilicity of a drug, which is valid only for a single electrical species [48]. The apparent distribution coefficient as  $\text{Log } D$  is often used for ionizable drugs at pH 7.4 [48]. The  $\text{Log } D$  is valid for a pH-dependent mixture of all electrical species present at the defined pH [48].

#### 1.2.4.2 Parallel Artificial Membrane Permeability Assay (PAMPA)

PAMPA is a commonly used cell-free *in vitro* permeability testing technique. PAMPA was developed by Kansy et al. to assess the passive cell membrane permeability of drug compounds [41, 50-52]. In this method, two-layered multi-well plates are used to measure permeation through barriers formed between the top and bottom wells [41, 50-52].

Figure 1-8 illustrates PAMPA well plates [53]. PAMPA is suitable for predicting purely passive permeation. This is not possible in cell-based assays, where carrier-mediated active and passive transport coexist [41, 42, 50-52]. In PAMPA, the barriers formed between the donor

and acceptor wells consist of porous filters soaked in a mixture of lipid and hydrocarbon oil or pure hydrocarbon oil [41, 51, 52]. In phospholipid-free PAMPA, often hexadecane is used as oil [51, 54]. When using lipids in PAMPA, phospholipids closely resembling the mixture found in reconstituted brush border lipids were used [51, 55, 56]. The lipid composition consisted for example of a 3% w/v lipid solution (consisting of cholesterol, phosphatidylcholine, phosphatidylethanolamine, phosphatidylserines, and phosphatidylinositols) in 1,7-octadiene [51, 56, 57]. The typical thickness of the barrier in PAMPA is ~10-100  $\mu\text{m}$  [41, 51, 52]. However, biological lipid bilayer membranes are approximately 5 nm thick. Diffusion through the barrier is measured by concentration changes in the acceptor and donor wells and leads to typical assay times between 2-18 hours [41, 52]. Incorporation of membrane proteins is not possible with PAMPA.

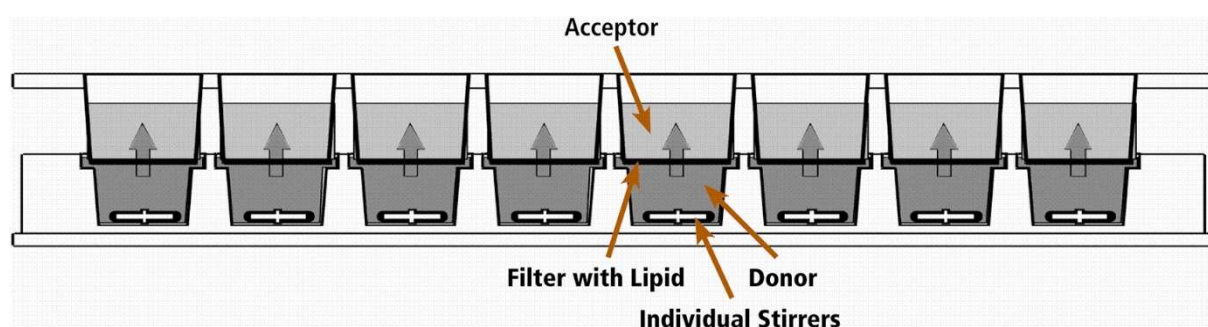


Figure 1-8: Schematic illustration of the parallel artificial membrane permeability assay (PAMPA), which is typically applied in a 96-well plate. ©2018 Pion Inc. Reprinted from website of Pion Inc. with permission from Pion Inc. 2020 and from Berben et al. [53] with permission from Elsevier / Creative Commons.

### 1.2.4.3 Cellular Monolayers

Cellular monolayers are used for *in vitro* cell-based assays, and are common alternatives to PAMPA [41, 42]. Some endothelial and epithelial cell lines differentiate into cell monolayers that form barriers resembling the physiological barriers of the blood-brain barrier endothelium or the intestinal epithelium [42]. A paracellular transport route between the cells is provided by some of these monolayer-forming cells lines with negligible carrier-mediated transport [42]. For example, very small hydrophilic drugs can diffuse across paracellular routes in leaky barriers [42]. A cellular monolayer that expresses a carrier protein can be used to investigate carrier-mediated and passive transport processes [42]. Several transport proteins can be simultaneously expressed in Caco-2 [58-61] and Madin-Darby canine kidney (MDCK) [62, 63] cellular monolayers [42]. Figure 1-9 shows a sketch of a monolayer grown on a permeable filter [64]. Other methods are the Ussing chamber [65, 66] or everted gut sacs [67].

Monolayer permeation prediction assays are very well established in pharmaceutical research and are used for screening of drug candidates. However, monolayer-forming cell lines take time until they are grown and have a fixed composition of the membrane and their usage in a systematic drug screening with varying membrane related factors are limited.

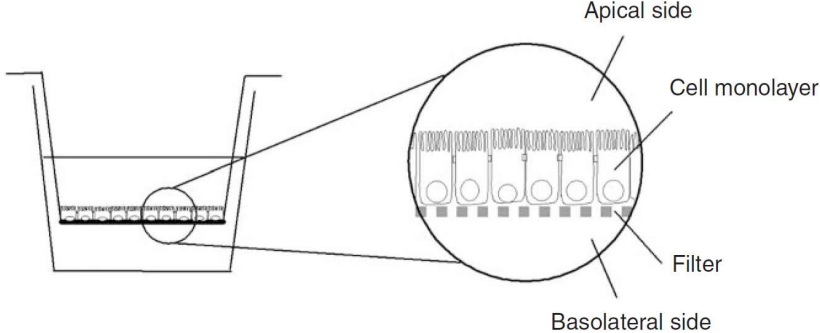


Figure 1-9: Sketch of a Caco-2 monolayer grown on a permeable filter support. Reprinted from Hubatsch et al. [64] with permission from Nature Publishing Group.

### 1.3 Microfluidic Devices for the Creation and Investigation of Cell-Mimicking Compartments and Permeation Analysis

Microfluidic platforms are microchannel systems and enable the combination of several laboratory functions onto a single device. They are commonly also referred to as lab-on-chip (LOC) or miniaturized total analysis systems ( $\mu$ TAS) [68]. A significant advantage of these microfluidic platforms compared to traditional laboratory methods lies in the small volumes and small size of the devices [69]. Microfluidic systems for integrated analysis and chemical processing were introduced in the late eighties and are still being further developed. In general terms, microfluidics is a field concerned with handling small amounts of fluids (nano- to attoliters) in an assembly of structures in the micrometer scale [70]. Typical microfluidic systems operate in the laminar flow regime, so that no turbulence is observed and surface forces dominate volume forces. Hence, the mixing of two merging parallel fluid streams occurs only by diffusion. Microfluidics enables different functional units (for separation, reaction, and detection) to be incorporated into a single channel network and, therefore, facilitates the analysis and serial processing of samples. Subfields in microfluidics include droplet-based microfluidics, continuous-flow microfluidics, digital microfluidics, DNA chips (microarrays), and single-cell analysis. The miniaturization and integration of several steps into one device is one of the important aims of LOC [71].

In droplet-based microfluidics, nano- to picoliter sized droplets can be generated in a microfluidic device using two immiscible fluids [72]. It is possible to form the droplets in a T-junction or in a flow-focusing device [73]. Another possibility is the step emulsification for the generation of a monodispersed emulsion [74]. An oil phase and an aqueous phase are often used in combination with a surfactant for stabilization [75]. Furthermore, it is possible to generate up to thousands of monodisperse, ultra-small, and finite droplets per second [73]. Each of these small quantities of liquid can serve as individual microreactors [72]. As alternatives to chip based systems, droplets can be deposited on a microarray plate [76]. These plates carry hydrophilic spots, which act as recipients for individual microdroplets [77]. Afterwards, it is possible to perform matrix-assisted laser desorption/ionization mass spectrometry (MALDI-MS) experiments with these plates.

Microfluidic methods offer unique control over processes and enable applications from bioanalytics to biomimetics as well as permeation studies relevant for pharmaceutical approaches. Moreover, the laminar flow properties of microfluidic channel networks, and the creation of biocompatible environments, offer prospects for the future development of automated and high-throughput synthetic biology-based platforms [78]. In the following

subchapters, microfluidic devices for the generation and investigation of artificial cell membranes and compartments are reviewed.

### 1.3.1 Microfluidic Devices for Studies with Vesicles

Microfluidic systems have been used to generate, capture and/or analyze liposomes referred to as vesicles [79-84]. Vesicles are self-assembled lipid structures and are the most commonly used lipid bilayer model systems since they have an aqueous core surrounded by a phospholipid bilayer [16, 85]. Figure 1-10 illustrates different classes of vesicles.

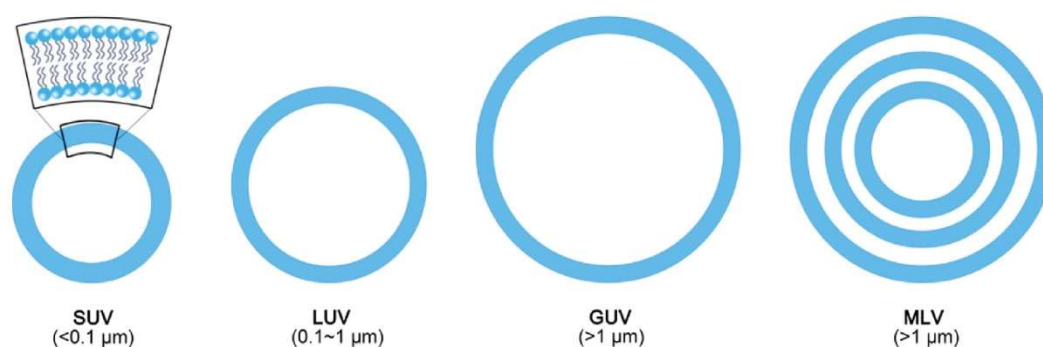


Figure 1-10: Schematic representation of lipid based vesicles (not to scale). Vesicles are classified according to their size and lamellarity (from left to right): SUV (small unilamellar vesicle) with a size below 100 nm, LUV (large unilamellar vesicle) with a size between 100-1000 nm, GUV (giant unilamellar vesicle) with a larger size than 1000 nm, and MLV (multi-lamellar vesicle) [85]. Reprinted from Li et al. [16] with permission from De Gruyter / Creative Commons.

Vesicles formed by synthetic and extracted lipids are used to create artificial cells in the field of synthetic biology [86-90]. The membrane of vesicles and other artificial cells with a lipid bilayer are very close to the thickness and composition of cellular lipid membranes. In a bottom-up approach, vesicles mimic the compartmentalization of cells towards multifunctional eukaryotic synthetic cells, which constructions strive to reconstitute cellular phenomena *in vitro* (Figure 1-11) [91, 92]. One of the key challenges in the creation of artificial cells is the formation of a cell-like architecture, where different biochemical compounds are retained in smaller organelles within the cell and each organelle has a specific biological function. Significant achievements were presented recently in artificial cell models, reporting the realization of a vesicle bioreactor [88], multi-step reactions [89, 90, 93], genetic circuits [94, 95], controlled



division [96], communication across membranes [97], and others [7, 98-104]. Multi-step and cascade reactions in individual compartments are of particular interest since most biological pathways include several steps [89, 105-108].

To investigate these processes, microfluidic systems have been used to immobilize and analyze vesicles [79], e.g. large unilamellar vesicles (LUVs) [80] or giant unilamellar vesicles (GUVs) [81]. A vesicle trap was surrounded by a circular valve to form a small chamber of a few hundred picoliters [81]. This two-layered analytical microfluidic device allows hydrodynamic trapping, treatment, and analysis (Figure 1-12c) of up to 60 individual GUVs or cells [81, 109]. The trapped objects

can be exposed to chemical treatments like drugs, penetrating peptides, lysis buffers, antibodies, or staining dyes with precisely controlled durations while being constantly monitored with microscopic or spectroscopic methods. Other methods for immobilizing GUVs in microfluidic channels are shown in Figure 1-12a/b/d/e [109-113].

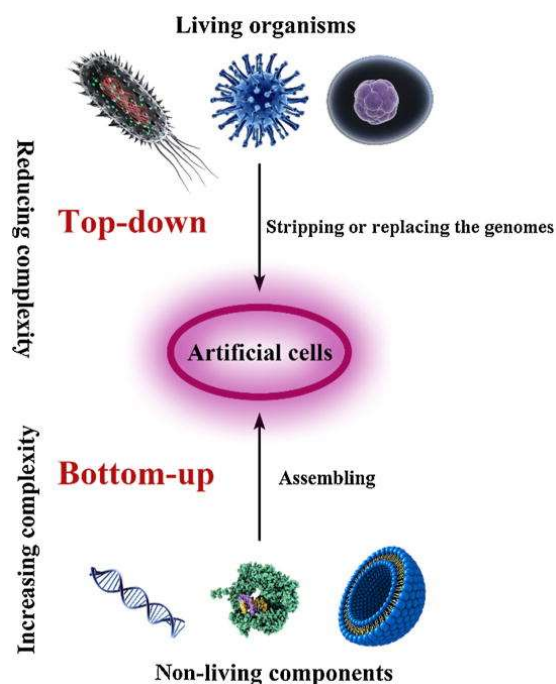


Figure 1-11: Top-down and bottom-up approaches for the construction and design of artificial cells. Reprinted from Xu et al. [91] with permission from Elsevier / Creative Commons.

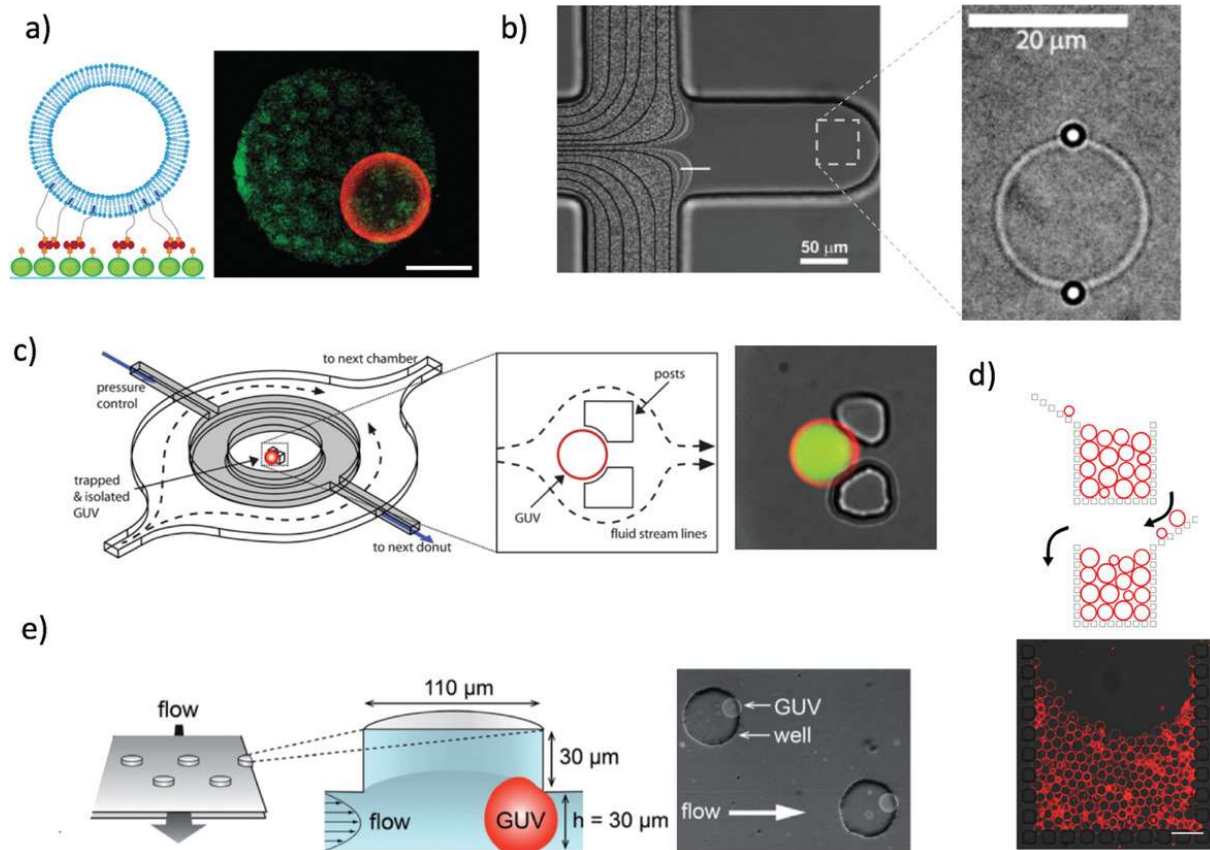


Figure 1-12: Different strategies for immobilizing giant unilamellar vesicles (GUVs) in microfluidic channels. Figure assembly reprinted and adapted from Robinson et al. [109] with permission from Wiley. a) Surface modifications: A water-soluble molecule (cholesterol-PEG-biotin) is used as a linker, which can bind via avidin to biotinylated bovine serum albumin (previously absorbed on a glass surface) (scale bar: 10  $\mu\text{m}$ ). Reprinted and adapted from Kuhn et al. [110] with permission from Oxford University Press. b) Dead-end channels to trap GUVs. Reprinted and adapted from Vrhovec et al. [111] with permission from Royal Society of Chemistry. c) Polydimethylsiloxane chip for hydrodynamic trapping of GUVs. Reprinted and adapted from Robinson et al. [81] with permission from AIP Publishing. d) High-capacity traps for multiple GUVs (scale bar: 50  $\mu\text{m}$ ). Reprinted and adapted from Yandrapalli et al. [112] with permission from Royal Society of Chemistry / Creative Commons. e) Ceiling wells to trap GUVs. Reprinted and adapted from Yamada et al. [113] with permission from Royal Society of Chemistry.

Moreover, microfluidic chips were used for permeation studies with vesicles [79, 80]. Figure 1-13 shows a microfluidic vesicle screening platform to monitor the lipid membrane permeability of tetracyclines [79]. Vesicles were immobilized onto the glass surface in a stripe pattern by an avidin-biotin bond. Microchannels allowed continuous delivery of buffer and tetracycline. The fluid flow resembled the drug transport via blood in the human body. The formation of a fluorescent drug-europium complex, which indicated permeation, inside the vesicles was monitored.

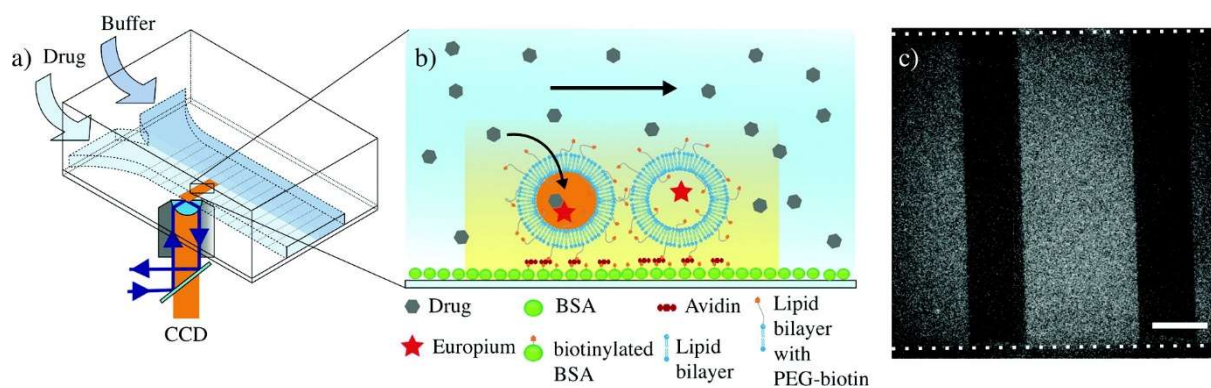


Figure 1-13: Microfluidic vesicle screening platform for tetracyclines. a) Sketch of the experimental setup. Tetracyclines and buffer were supplied through a microchannel to vesicles immobilized on the bottom glass slide in a microfluidic chip (mounted on a total internal reflection fluorescence (TIRF) microscope). b) Visualization of the detection assay. Vesicles containing  $\text{Eu}^{3+}$  were immobilized via an avidin linker to biotinylated bovine serum albumin (patterned onto the surface by microcontact printing). A fluorescent europium-tetracycline complex was formed when permeation of tetracycline across the lipid membrane occurred. c) The vesicles were stained with Dil to illustrate the stripe pattern. The channel walls are indicated by the dotted lines (scale bar: 50  $\mu\text{m}$ ). Reprinted from Kuhn et al. [79] with permission from American Chemical Society.

A vesicle-based fluorescence assay was developed, which is capable to determine permeation kinetics of basic drug-like solutes across lipid bilayers (Figure 1-14) [80]. Vesicles were captured on the chip surface [114]. The permeation of a weak base along a concentration gradient was analyzed. This resulted in a net proton release and the resulting pH changes were monitored with pH-sensitive fluorophores.

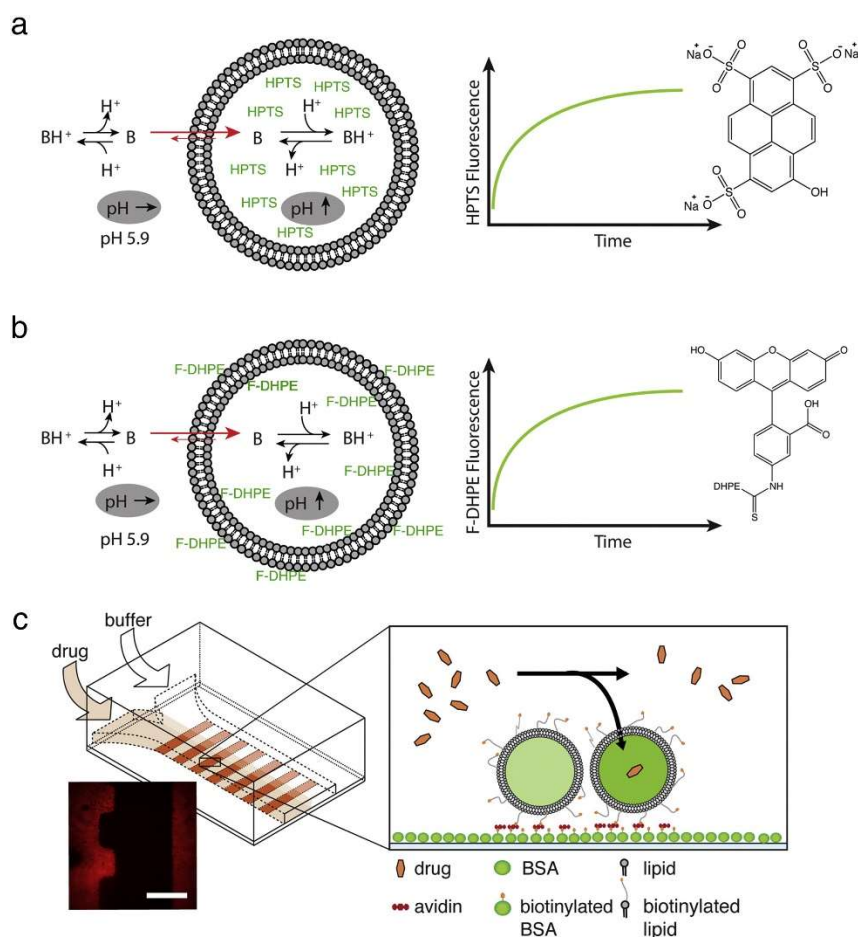


Figure 1-14: Permeation assay with vesicles. *a,b*) The outer compartment was buffered with MES/NaCl at pH 5.9, whereas the inner compartment (vesicle lumen) was unbuffered. A weak base ( $B/BH^+$ ) was added and permeation resulted in a net proton ( $H^+$ ) release at the outer membrane surface and a net proton capture at the inner surface to reach an equilibrium. A pH-sensitive fluorophore changed its fluorescence due to the pH change (indicated by “pH  $\uparrow$ ”) dye in the vesicle lumen (a) or at the surface of the inner membrane (b). The proton at the outer membrane surface was neutralized by the buffer system (indicated by “pH  $\rightarrow$ ”). *c*) A microfluidic chip was thereafter used for this assay. Buffer and drug solution are flowing over HPTS-containing vesicles captured by biotin/avidin on the chip surface. The glass surface of the chip was modified (small insets) by microcontact printing in a patterned fashion [114] (scale bar: 50  $\mu m$ ). This enables the measurement of unspecific (dark area, no vesicles) and specific (red area, immobilized vesicles) fluorescent increases in the same image series. Reprinted and adapted from Eyer et al. [80] with permission from Elsevier.

Vesicles were generated with help of microfluidic devices [84, 115-118]. Especially interesting are multicompartments vesicles, which were first produced one-by-one though manual pipetting of droplet [83, 90] and later with a microfluidic device using double emulsions as templates [82]. Figure 1-15 illustrates the formation of uniform single bilayer vesicles with or without inner compartments formed by surfactant-assisted microfluidics. Further, vesicles in vesicles (vesosomes) were generated with a microfluidic method [103].

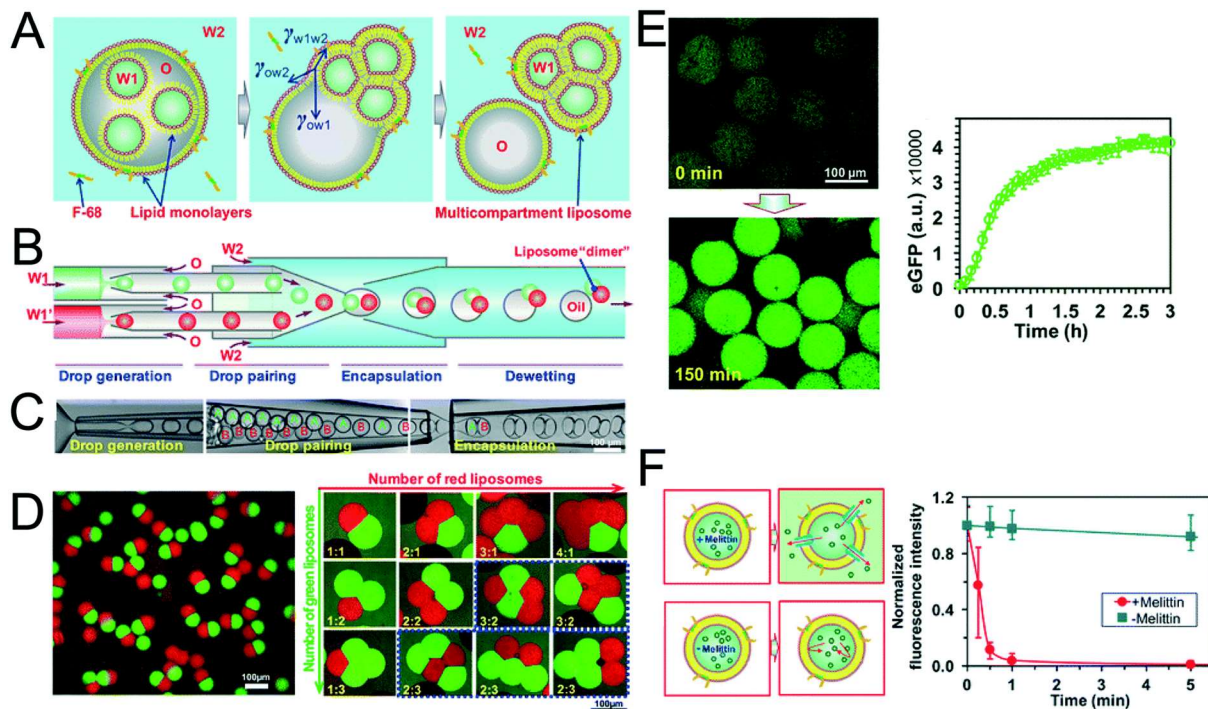


Figure 1-15: Multicompartment vesicles. A) Schematics showing surfactant-assisted assembly of multicompartment vesicles. B,C) Cartoon and snapshots of capillary microfluidic device used to generate two-compartment vesicles. D) Confocal images of vesicles with two compartments (left) and vesicles with up to five compartment (right) with controlled configurations structures. E) In vitro transcription and translation of enhanced green fluorescent protein in vesicles and corresponding expression kinetics. F) Melittin was introduced in the vesicle bilayer (left) and the corresponding kinetics of time-dependent release of calcein fluorescence is shown (right). Reprinted from Trantidou et al. [83] and Deng et al. [82] with permission from Royal Society of Chemistry / Creative Commons and American Chemical Society, respectively.

Multivesicular droplets generated with a microfluidic platform were used as a cell model system to study compartmentalized biochemical reactions (Figure 1-16) [89]. The multivesicular droplets can be trapped in an array and analyzed. A two-step enzymatic reaction was performed. This approach mimics cellular organelles with optimized reaction parameters (e.g. ions and pH) in the individual compartment.

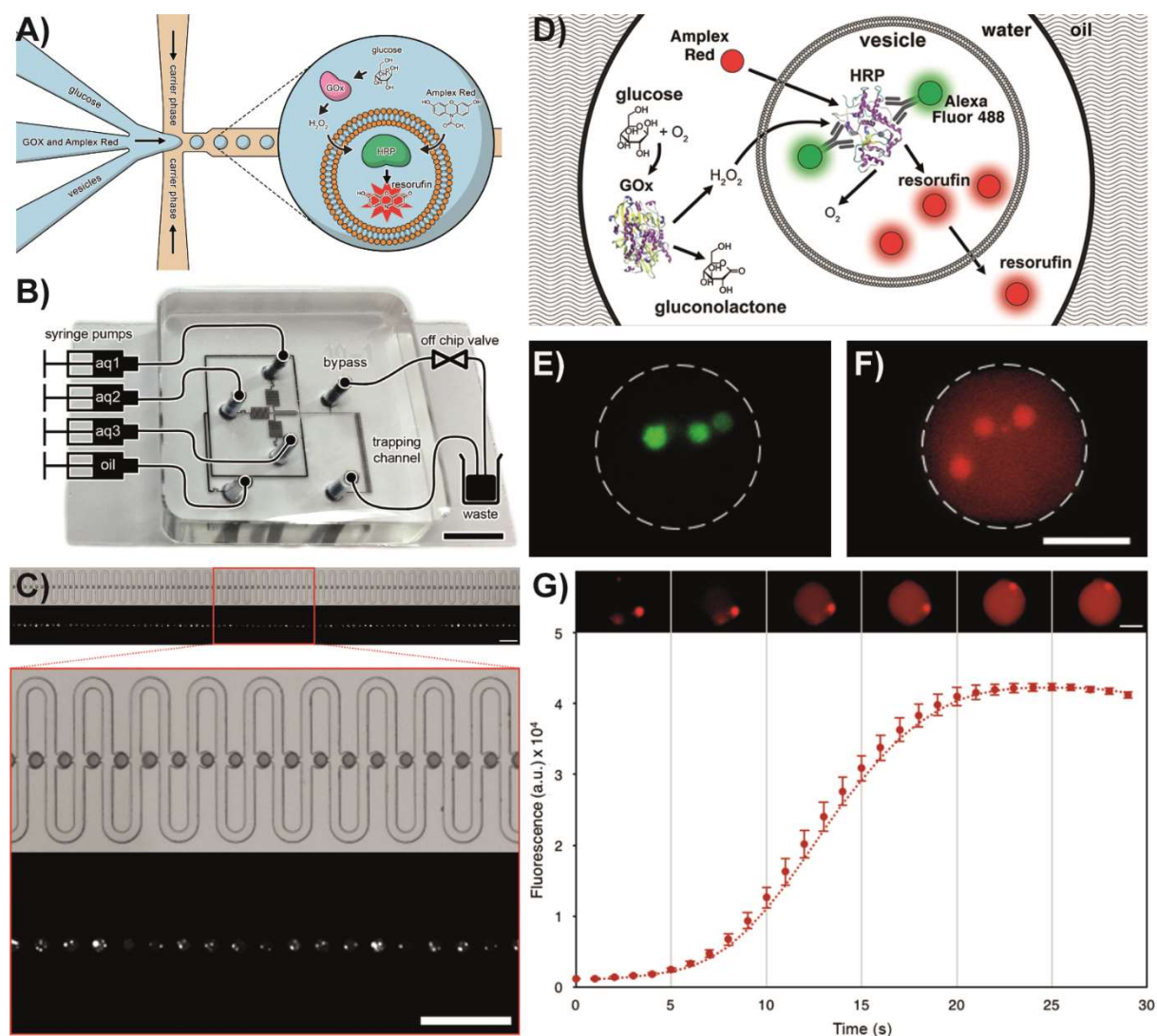


Figure 1-16: Multivesicular droplets. A) Scheme of the platform. B) Illustration of the microfluidic chip setup (scale bar: 5 mm). The setup used four syringe pumps that supply the carrier phases (oil) and aqueous (aq 1-3) to the chip. The droplets were generated on-chip immobilized in a trapping array. A bypass valve can be opened to stop the flow of droplets through the trapping array. C) Top view of the 89-trap array. First row: Trapped droplets in the array. Second row: Fluorescence image of the same array. The vesicles were filled with calcein (scale bar: 250  $\mu\text{m}$ ). D) Sketch of an enzymatic cascade assay performed in multivesicular droplets. Glucose oxidase (GOx) converts glucose to hydrogen peroxide and gluconolactone. Hydrogen peroxide and Amplex Red permeate across the lipid bilayer into the vesicle. The labelled horseradish peroxidase (HRP) react with the two substrates to form resorufin and oxygen. Resorufin is then diffusing from the vesicle to the droplet lumen (sketch not to scale). E) Alexa Fluor 488 labelled HRP encapsulated in three vesicles inside multivesicular droplets. F) Image of the same multivesicular droplets. Resorufin was generated in the enzyme cascade assay and it was observed in the droplet interior and lumen of the vesicles (scale bar: 25  $\mu\text{m}$ ). G) Plot and image sequence of the pixel intensity of the entire multivesicular droplets. Reprinted and adapted from Nuti et al. [89] with permission from Royal Society of Chemistry.

### 1.3.2 Droplet Interface Bilayers (DIBs)

Phospholipid-stabilized water-in-oil droplets have been used to create artificial lipid bilayer membranes; these are referred to as droplet interface bilayers (DIBs) [41, 119-127]. A bilayer is formed between two aqueous droplets when phospholipids are present in hydrocarbon oil [41, 128]. Lipids self-assemble at the surface of one droplet to form a lipid monolayer at the water-oil interface [41, 128]. Contact between this aqueous droplet and another unites the lipid monolayers, creating a DIB membrane of roughly 5 nm thickness [128]. DIBs consist of a phospholipid bilayer in contrast to polymersomes, which are lacking the biological relevance of lipids and for membrane proteins. Figure 1-17 illustrates the principle of a DIB. The monolayers can be created with two different techniques: (i) lipid-out approach: phospholipids are placed in the oil phase as inverse micelles and (ii) lipid-in approach: phospholipids in the form of vesicles are placed in the water phase [129].

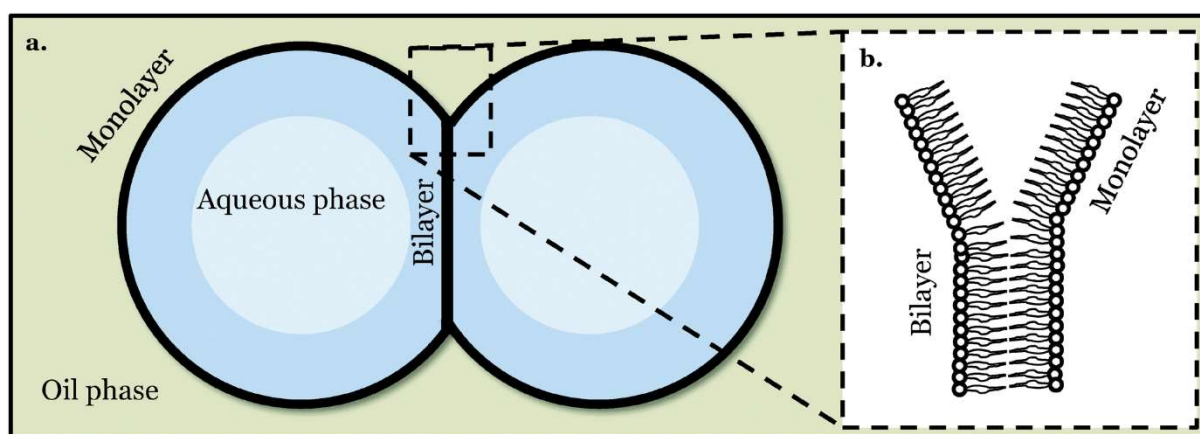


Figure 1-17: Aqueous droplets are deposited into an oil reservoir together with phospholipids. The phospholipids assemble to a lipid monolayer on the surface of the droplets. When the droplets are brought into contact (a), the lipid monolayers adhere together and form a lipid bilayer (b). Reprinted and adapted from Freeman et al. [130] with permission from Royal Society of Chemistry.

DIBs have also been formed in microfluidic channels through electrical manipulation [131, 132] and by pushing the droplets together [41, 128, 133]. Microfluidic devices are capable of high-throughput formation of 1D arrays of DIBs [41, 121] and complex long-range 2D and 3D DIB networks [134] between nanoliter-sized aqueous droplets [41]. Droplet microfluidics enables the formation of monodisperse droplets with precise volumes in the order of cell volumes, i.e., several nanoliters, as well as efficient encapsulation of smaller vesicles and compounds. Droplets can be created, guided to specific locations, and immobilized [41, 78, 125, 135]. Many studies with closed systems used polydimethylsiloxane (PDMS) [78, 120-122, 125, 127, 136]. However, molecules can diffuse into the PDMS [137, 138], resulting in the loss of water and fast shrinkage of droplets and other instabilities [89, 139, 140], and swelling of PDMS occurs due to the uptake of solvents like hexadecane [78, 135, 140, 141].

Translocation or permeation across DIB membranes are investigated with different approaches [41, 78, 142-145]. Pore forming peptides or toxins like alamethicin [120, 125, 146, 147], alpha-hemolysin ( $\alpha$ -HL) [78, 135, 148-155], anthrax toxin [156], or equinatoxin II [157] incorporated into the membrane are used to connect individual artificial cells. Furthermore, translocation can occur across channels or transport proteins inserted in DIBs [158, 159]. In setups with electrodes, charged molecules migrate also by electrostatic attraction [160]. Even single-stranded DNA molecules were electrically driven through a single  $\alpha$ -HL pore, which is called voltage-driven molecule translocation [161].

Hydrodynamic trapping of droplets was integrated in a microfluidic device to form DIBs [127]. Figure 1-18 shows as example a microfluidic hydrodynamic trapping platform for *in situ* electrical characterization [125]. Two T-junction generated droplets coated with lipids of alternating compositions in the microfluidic device. The droplet stream is routed to multiple hydrodynamic traps to capture the droplets. Every trap is designed to hold two droplets. The two narrow exit channels in each trap served to direct the alternating droplets into vacant traps without permitting the droplets to escape after capture. With this platform it was possible to assemble DIBs from monolayers with different compositions and the formation of asymmetric bilayers that were stable for at least 18 h. The intramembrane potential was evaluated by conducting parallel capacitance-based measurements.

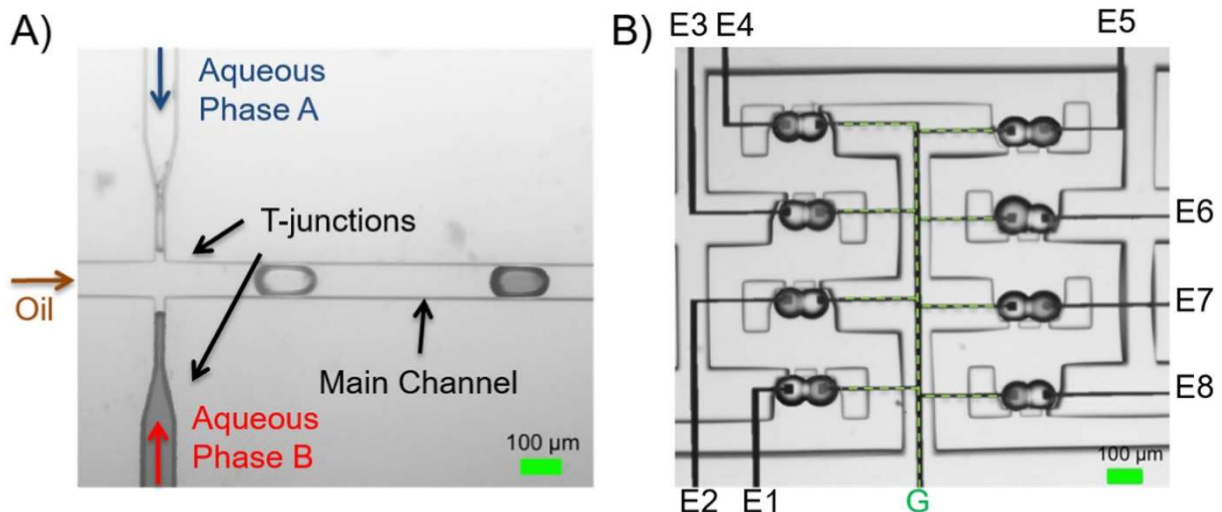
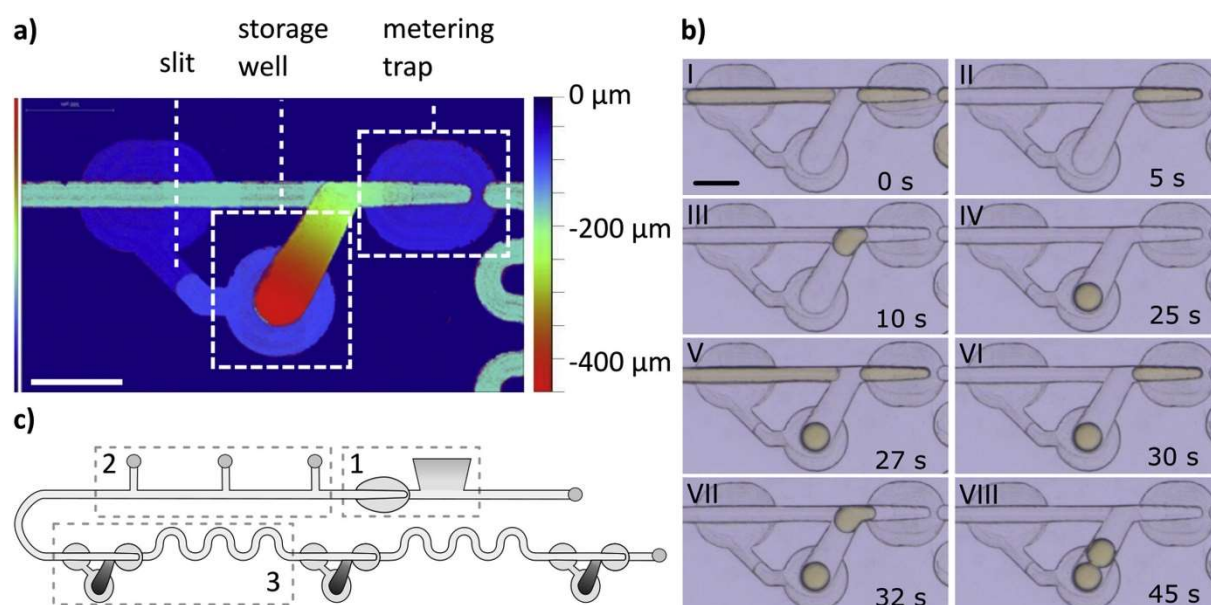


Figure 1-18: Chip design for the generation of droplet interface bilayers (DIBs). A) Two T-junction generated droplets of alternating aqueous composition. B) Droplets were routed and trapped in a microfluidic pathway and formed asymmetric DIBs. In each droplet trap, square electrode pads were deposited on the glass surface. The electrodes in black (E1-E8) were connected to an independent channel of a patch clamp amplifier headstage and the central electrodes (green dashed line overlays) were connected and used as a common ground connection (G). Reprinted from Taylor et al. [125] with permission from Elsevier.

Another microfluidic method to trap two droplets next to each other is visualized in Figure 1-19 [135]. The device contains metering and storing modules. These are hydrodynamic traps that enable the capture of lipid-coated droplets. The platform allows to split, merge, and removal of



aqueous phases. The droplets are trapped and positioned next to each other to form DIBs. Moreover, a set of special modules provide the possibility for dilutions of the sample content. Translocation of different molecules across the DIB membrane were monitored on this device. In addition, other methods investigated the translocation of different compounds across DIB membranes [41, 78, 142-145].



*Figure 1-19: Microfluidic device for sequential generation of droplet interface bilayers (DIBs). a) Visualization of the microfluidic trap architecture with different channel heights. The trap consisted of different parts: (i) metering of ~9 nL droplets, (ii) deepening and widening storage well, and (iii) slit for equalizing the flow of oil. b) Formation of a DIB in one metering and storing module: an aqueous solution was metered into portions (I) and after the flow of oil was stopped (II) the droplet was dragged to the bottom of the trap (III-IV). Following this, metering of a second type of aqueous solution was performed (V-VI), and the droplet was guided to the storage well (VII) to contact the already positioned droplet to form a DIB (VIII). (Scale bars: a) and b) 500  $\mu\text{m}$ .) c) Sketch of the microfluidic device: 1) metering module, which allows a serial dilution, 2) inlets for aqueous solutions, 3) metering and storing module with serpentine channel for mixing of droplets content (this feature was important when the droplets were diluted). Reprinted from Czekalska et al. [135] with permission from Elsevier.*

Cells communicate with each other in a controlled manner in living tissues and DIBs can be used to mimic communication experiments in artificial cellular networks [41, 78, 122, 128, 148-151, 153-155, 162, 163]. For example, communication between the artificial cells was started by the activation of light [164]. Moreover, chemical signals can be propagated across the DIB network by transplanting enzymatic reaction cascades for inter-droplet communication [122].

Figure 1-20 illustrates the formation of a DIB network in a microfluidic chip [78]. The platform uses a design that allows the controlled positioning and storage of droplets (stabilized with lipids). DIB networks were generated in a shift register. Translocation of different molecules across DIBs were studied and quantified.

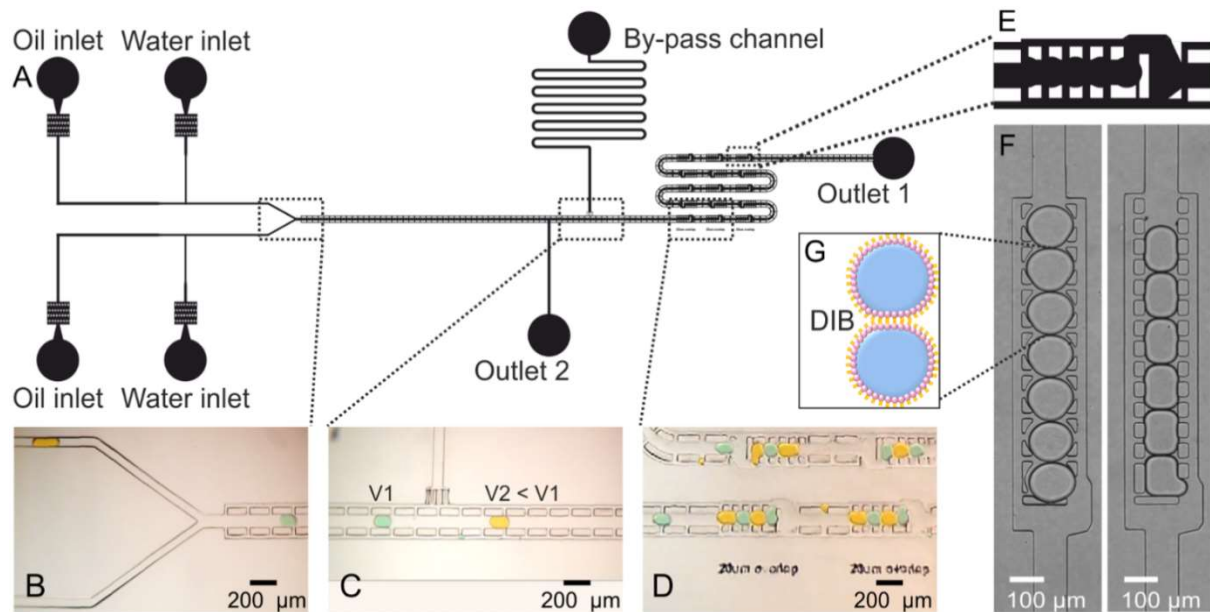


Figure 1-20: Microfluidic platform for the generation of droplet interface bilayer (DIB) networks. A) Sketch of the device. T-Junctions were used to produce droplets with different content. B) Droplet alternation was enabled by a Y-Junction. C) Main channel with a by-pass to reduce droplet velocity and divert the oil phase. D) Multiple traps to hold droplets in the absence of flow. E) Scheme of a shift register, which allowed droplets to be trapped within the pillars. F) Droplet network arrangement in two different shift registers. Left-hand side: The pillar structure allowed droplets to remain locked when the oil flow was stopped. Right-hand side: Droplets showed backflow or moved outside of the pillars when the tubing at the inlets were detached. G) Sketch of a DIB. Reprinted from Schlicht et al. [78] with permission from Nature Publishing Group.

Artificial cell networks called multisomes are an attempt to recapture the aforementioned optimized cellular organization [165]. Multisomes consist of aqueous droplets in a 3D assembly with defined compositions encapsulated within small drops of oil in water and were first generated with pipetting, later improved by microfluidic methods [103, 136].

Large 3D DIB networks were formed using a 3D droplet printer (Figure 1-21) [148, 163]. The precise placement of droplets in defined patterns and geometries is required to achieve functional 3D aqueous droplet networks. A glass capillary was used to fabricate a printer nozzle with an external diameter of  $\sim 100 \mu\text{m}$ . The nozzle was attached to a poly(methyl methacrylate) chamber with a piezoelectric transducer. The droplets were printed in a container, which was filled with a mixture of hexadecane and silicone oil AR 20. Two nozzles were used simultaneously, which allowed the patterning of two droplet types. Other approaches to generate 3D DIB networks used a snap off technique [166] or microfluidic chambers [134].

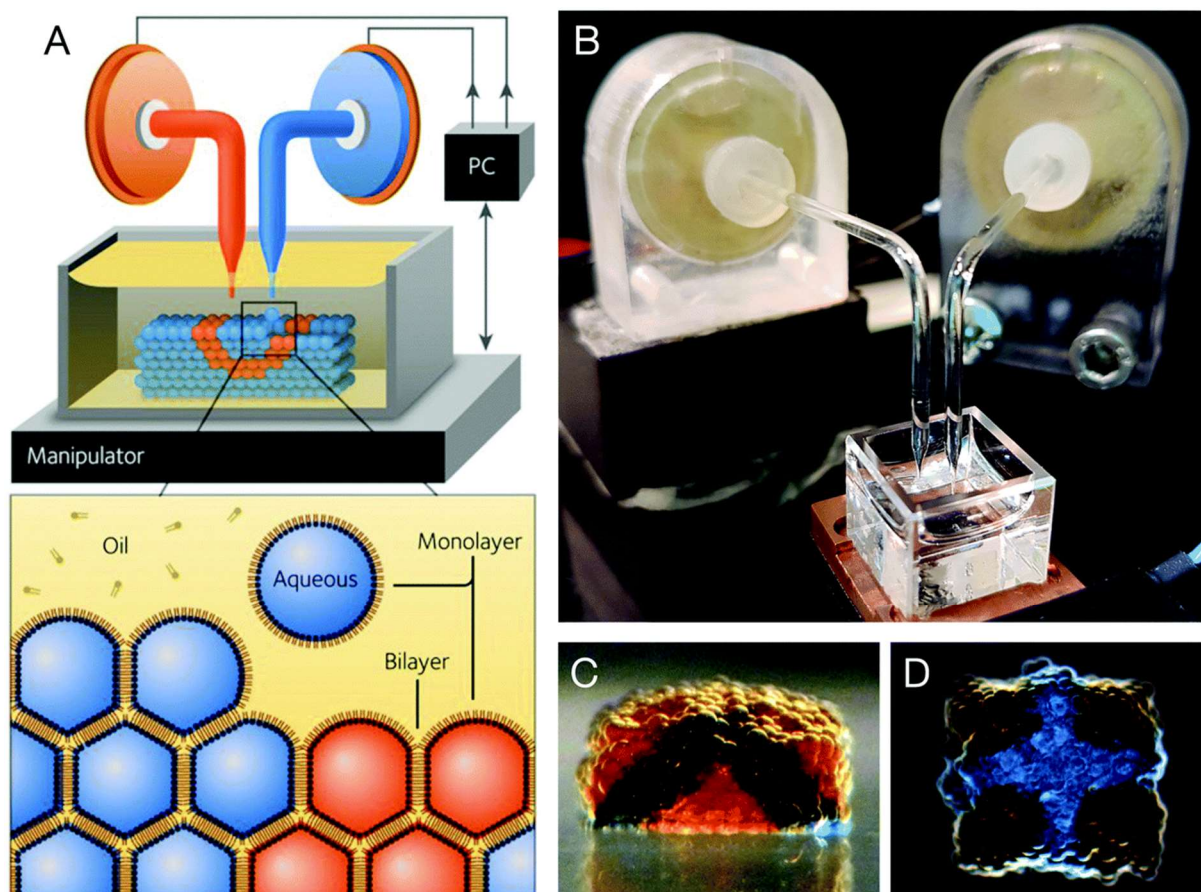


Figure 1-21: A tissue-like material printed as 3D aqueous droplet network [148]. A) Two printing nozzles printed droplets with different content into a 3D-patterned droplet network. A micromanipulator and piezo transducer (PC) were used to move the recipient oil chamber. B) Photograph of the 3D droplet printer. C,D) Droplet networks printed with different droplet types. Reprinted from Booth et al. [163] with permission from Royal Society of Chemistry.

Figure 1-22 shows parallelized assays in hydrogel and droplet interface bilayers [163]. For example, calcium translocation across alpha-hemolysin pores was investigated in multiple droplet hydrogel bilayers (Figure 1-22A) [167]. Several similar measurements were carried out in parallel after depositing a large droplet coated with a lipid monolayer on top of an array of smaller lipid-coated droplets (Figure 1-22B) [168]. Related approaches have been used at the single pore level [169] and with alternative bilayer arrays [170]. In addition, droplet hydrogel bilayers were used to monitor calcium flux through alpha-hemolysin pores under an applied potential in an array of thousands of hydrogel pillars (Figure 1-22C) [171].

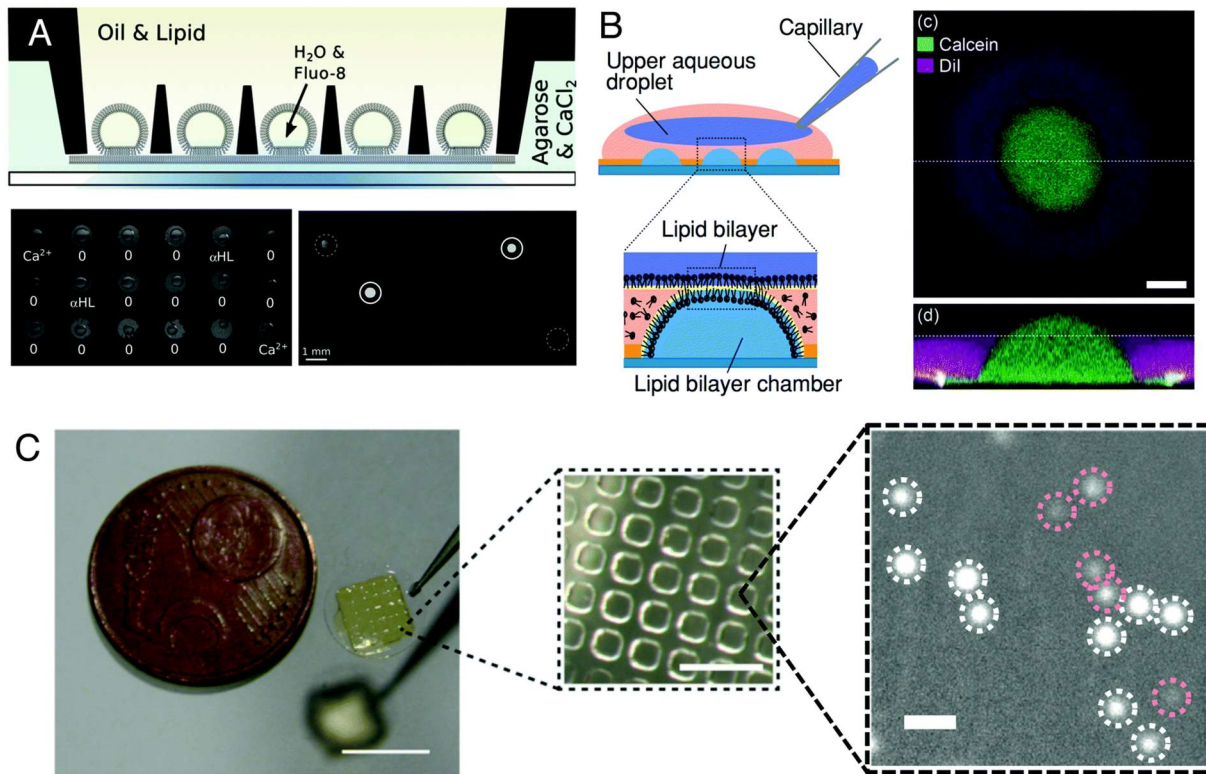


Figure 1-22: Example for parallelized assays in hydrogel and droplet interface bilayers. Figure assembly reprinted from Booth et al. [163] with permission from Royal Society of Chemistry. A) Fifteen droplet hydrogel bilayers were generated by placing a poly(methyl methacrylate) array (black) on top of a hydrogel surface (blue) and adding droplets to the individual wells. Calcium diffusion across alpha-hemolysin pores was measured with the dye fluo-8 (scale bar: 1 mm). Reprinted and adapted from Castell et al. [167] with permission from Wiley. B) A droplet was placed on top of an array of 36 droplets. All droplets were coated with a lipid monolayer. This allowed the detection of calcium translocation through alpha-hemolysin pores across all droplet interface bilayers on the same time (scale bar: 10  $\mu$ m). Reprinted and adapted from Tonooka et al. [168] with permission from Wiley. C) A hydrogel surface was brought into contact with an array of thousands of hydrogel pillars. Calcium flux under a transmembrane potential through alpha-hemolysin pores was imaged by total internal reflection microscopy (scale bars from left to right: 8 mm, 140  $\mu$ m, and 10  $\mu$ m). Reprinted and adapted from Huang et al. [171] with permission from Nature Publishing Group.

In artificial cell network assays, a label-free detection of the droplet content is important in addition to fluorescent detection. For example DIBs were generated within a conventional UV spectrometer cell [172]. Thereafter, the permeation of drug molecules across the bilayer was recorded by UV absorbance over time. Exploitation of other general methods like mass spectrometry to detect translocated materials would be advantageous [163].

## 1.4 Scope and Structure of this Doctoral Thesis

The goal of this doctoral thesis is the development of a microfluidic platform to generate artificial cell membranes and compartments for permeation studies. Microfluidics offers the possibility to miniaturize approaches and is beneficial for research studies with artificial cells. For the development of the microfluidic platform, it is crucial to understand the key parameters for tailoring membranes. First, the focus was on improvements of a platform for trapping off-chip created vesicles. However, due to limitations e.g. encapsulation of compounds and choice of lipids, an alternative method was envisioned. This method is based on droplet arrays, placed on a surface in close proximity to from a DIB between adjacent droplets. The platform should include an automated and precise positioning of droplets with a spotting device on plate. An accurate design of the plate is critical for the whole system. Of particular interest is the realization of a higher throughput than pipetting of droplets. Further, the nanoliter DIB platform was evaluated with fluorescence spectroscopy. Moreover, it is important to interface the platform with label-free end-point analysis. A protocol was developed to manipulate individual artificial cells for membrane separation and extraction of a single compartment to enable the analysis of the microdroplet content with mass spectrometry. The following thesis describes these developments and applications and is structured in the subsequent parts:

**Chapter 2** describes the combination of a microfluidic device and fluorescence correlation spectroscopy to study peptide translocation across model membranes. A previously introduced microfluidic PDMS chip for trapping giant vesicles [81] was further developed with an improved design to study processes at and across the membrane. In addition, we discuss the interaction of toxins and peptides with lipid membranes investigated on the same microfluidic chip. Unfortunately, there were some shortcomings with this platform: Asymmetric membranes and several connecting compartment with vesicles are difficult to generate. Furthermore, the size of the vesicles are not consistent. Therefore, we wanted to address these topics with a microfluidic droplet-based approach and improved the handling and investigation of different membrane compositions and artificial cell compartments.

**Chapter 3** shows tailored translocation and reaction cascades in DIB networks using a microfluidic approach. The compartments were selectively connected with the pore-forming toxin alpha-hemolysin. The aim was to develop a microfluidic solution that combines a droplet microfluidic system with a high degree of control over droplet position and composition of the artificial cell membrane into a single device. The system should facilitate, by its design, precise positioning of droplets on a plate, offering new solutions for developing DIB assays. Our method is capable of automated formation of 1D and 2D droplet networks, which we demonstrated by connecting droplets containing different enzyme and compound solutions to

## Chapter 1

perform translocation experiments and a multistep enzymatic cascade reaction across the droplet network. Mainly fluorescence microscopy and MALDI-MS were used.

We extended the use of the microfluidic platform in **Chapter 4** where microfluidic formation of artificial cell membranes for permeation studies is presented. Here we conducted again experiments with fluorescence microscopy for characterization of the platform and liquid chromatography mass spectrometry (LC-MS) as label-free method. The permeability coefficients across cell membranes of different model permeants (e.g. fluorophores) was determined. Moreover, we generated symmetric and asymmetric DIB membranes and evaluated the effect of membrane symmetry regarding the permeability of compounds.

The doctoral thesis is concluded in **Chapter 5** and future perspectives are discussed, such as the use for other lipid bilayer studies or combination with cell-derived vesicles.

## 1.5 References

1. Regev, A., S.A. Teichmann, E.S. Lander, I. Amit, C. Benoist, E. Birney, B. Bodenmiller, P. Campbell, P. Carninci, M. Clatworthy, et al., *The Human Cell Atlas*. eLife, 2017. **6**: p. e27041.
2. Ha, C.-E. and N. Bhagavan, *Essentials of medical biochemistry: with clinical cases (2nd ed.)*. 2015: Academic Press.
3. Pollard, T.D., W.C. Earnshaw, J. Lippincott-Schwartz, and G. Johnson, *Cell Biology (3rd ed.)*. 2017: Elsevier.
4. Litwack, G., *Human biochemistry*. 2017: Academic Press.
5. Cooper, G.M. and R.E. Hausman, *The cell: A molecular approach*. 2004: Sinauer Associates.
6. Szostak, J.W., D.P. Bartel, and P.L. Luisi, *Synthesizing life*. Nature, 2001. **409**: p. 387-390.
7. Walde, P., *Building artificial cells and protocell models: experimental approaches with lipid vesicles*. Bioessays, 2010. **32**(4): p. 296-303.
8. Marieb, E., *Essentials of Human Anatomy and Physiology (10th ed.)*. 2012, Benjamin Cummings and Pearson Education.
9. Diekmann, Y. and José B. Pereira-Leal, *Evolution of intracellular compartmentalization*. Biochemical Journal, 2012. **449**(2): p. 319-331.
10. Dragani, R., *What is Cell Compartmentalization and Why Does it Occur?* Available from: [sciencing.com/cell-compartmentalization-occur-7472001.html](http://sciencing.com/cell-compartmentalization-occur-7472001.html), Acces Date 22th April 2020.
11. Lippincott-Schwartz, J. and R.D. Phair, *Lipids and Cholesterol as Regulators of Traffic in the Endomembrane System*. Annual Review of Biophysics, 2010. **39**(1): p. 559-578.
12. Kitano, H., *Biological robustness*. Nature Reviews Genetics, 2004. **5**(11): p. 826-837.
13. Masel, J. and M.V. Trotter, *Robustness and evolvability*. Trends Genet, 2010. **26**(9): p. 406-14.
14. Young, B., P. Woodford, and G. O'Dowd, *Wheater's Functional Histology: A Text and Colour Atlas*. 2013: Elsevier.
15. Alberts, B., A. Johnson, P. Walter, J. Lewis, and M. Raff, *Molecular biology of the cell (4th ed.)*. 2002.
16. Li, H., T. Zhao, and Z. Sun, *Analytical techniques and methods for study of drug-lipid membrane interactions*. 2017. **37**(1): p. 20170012.
17. Yang, N.J. and M.J. Hinner, *Getting across the cell membrane: an overview for small molecules, peptides, and proteins*. Methods in molecular biology (Clifton, N.J.), 2015. **1266**: p. 29-53.
18. Krämer, S.D., D. Lombardi, A. Primorac, A.V. Thomae, and H. Wunderli-Allenspach, *Lipid-Bilayer Permeation of Drug-Like Compounds*. Chemistry & Biodiversity, 2009. **6**(11): p. 1900-1916.
19. Bemporad, D., C. Luttmann, and J.W. Essex, *Behaviour of small solutes and large drugs in a lipid bilayer from computer simulations*. Biochimica et Biophysica Acta (BBA) - Biomembranes, 2005. **1718**(1): p. 1-21.
20. Hermann, K.F., C.S. Neuhaus, V. Micallef, B. Wagner, M. Hatibovic, H.E. Aschmann, F. Paech, R. Alvarez-Sanchez, S.D. Krämer, and S. Belli, *Kinetics of lipid bilayer permeation of a series of ionisable drugs and their correlation with human transporter-independent intestinal permeability*. European Journal of Pharmaceutical Sciences, 2017. **104**: p. 150-161.
21. Thomae, A.V., T. Koch, C. Panse, H. Wunderli-Allenspach, and S.D. Krämer, *Comparing the Lipid Membrane Affinity and Permeation of Drug-like Acids: The Intriguing Effects of Cholesterol and Charged Lipids*. Pharmaceutical Research, 2007. **24**(8): p. 1457-1472.
22. Costanzo, L., *Physiology cases and problems*. 2012: Lippincott Williams & Wilkins.
23. Wilson, C.G., *The Organization of the Gut and the Oral Absorption of Drugs: Anatomical, Biological and Physiological Considerations in Oral Formulation*

- Development*, in *Controlled Release in Oral Drug Delivery*, C.G. Wilson and P.J. Crowley, Editors. 2011, Springer US: Boston, MA. p. 27-48.
24. Turner, J.R., *Intestinal mucosal barrier function in health and disease*. Nature Reviews Immunology, 2009. **9**(11): p. 799-809.
  25. Asakura, H. and T. Kitahora, *Chapter 3 - Antioxidants in Inflammatory Bowel Disease, Ulcerative Colitis, and Crohn Disease*, in *Bioactive Food as Dietary Interventions for Liver and Gastrointestinal Disease*, R.R. Watson and V.R. Preedy, Editors. 2013, Academic Press: San Diego. p. 37-53.
  26. Bardal, S.K., J.E. Waechter, and D.S. Martin, *Applied Pharmacology*. 2011, Elsevier. p. 17-34.
  27. Mannhold, R., H. Kubinyi, and G. Folkers, *Pharmacokinetics and metabolism in drug design*. Vol. 51. 2012: John Wiley & Sons.
  28. van de Waterbeemd, H. and E. Gifford, *ADMET in silico modelling: towards prediction paradise?* Nature Reviews Drug Discovery, 2003. **2**(3): p. 192-204.
  29. Amidon, G.L., H. Lennernas, V.P. Shah, and J.R. Crison, *A theoretical basis for a biopharmaceutic drug classification: the correlation of in vitro drug product dissolution and in vivo bioavailability*. Pharm Res, 1995. **12**(3): p. 413-20.
  30. Cook, J., W. Addicks, and Y.H. Wu, *Application of the Biopharmaceutical Classification System in Clinical Drug Development—An Industrial View*. The AAPS Journal, 2008. **10**(2): p. 306-310.
  31. Rautio, J., H. Kumpulainen, T. Heimbach, R. Oliyai, D. Oh, T. Järvinen, and J. Savolainen, *Prodrugs: design and clinical applications*. Nature Reviews Drug Discovery, 2008. **7**(3): p. 255-270.
  32. Chen, M.-L., G.L. Amidon, L.Z. Benet, H. Lennernas, and L.X. Yu, *The BCS, BDDCS, and Regulatory Guidances*. Pharmaceutical Research, 2011. **28**(7): p. 1774-1778.
  33. Benet, L.Z., *The role of BCS (biopharmaceutics classification system) and BDDCS (biopharmaceutics drug disposition classification system) in drug development*. Journal of pharmaceutical sciences, 2013. **102**(1): p. 34-42.
  34. Wu, C.-Y. and L.Z. Benet, *Predicting Drug Disposition via Application of BCS: Transport/Absorption/Elimination Interplay and Development of a Biopharmaceutics Drug Disposition Classification System*. Pharmaceutical Research, 2005. **22**(1): p. 11-23.
  35. Butler, J.M. and J.B. Dressman, *The Developability Classification System: Application of Biopharmaceutics Concepts to Formulation Development*. Journal of Pharmaceutical Sciences, 2010. **99**(12): p. 4940-4954.
  36. Rosenberger, J., J. Butler, and J. Dressman, *A Refined Developability Classification System*. Journal of Pharmaceutical Sciences, 2018. **107**(8): p. 2020-2032.
  37. Kuentz, M., R. Holm, and D.P. Elder, *Methodology of oral formulation selection in the pharmaceutical industry*. European Journal of Pharmaceutical Sciences, 2016. **87**: p. 136-163.
  38. Kuentz, M., *Lipid-based formulations for oral delivery of lipophilic drugs*. Drug Discovery Today: Technologies, 2012. **9**(2): p. e97-e104.
  39. Jones, C.R., O.J.D. Hatley, A.-L. Ungell, C. Hilgendorf, S.A. Peters, and A. Rostami-Hodjegan, *Gut Wall Metabolism. Application of Pre-Clinical Models for the Prediction of Human Drug Absorption and First-Pass Elimination*. The AAPS journal, 2016. **18**(3): p. 589-604.
  40. Mateus, A., A. Treyer, C. Wegler, M. Karlgren, P. Matsson, and P. Artursson, *Intracellular drug bioavailability: a new predictor of system dependent drug disposition*. Scientific reports, 2017. **7**: p. 43047-43047.
  41. Nisisako, T., S.A. Portonovo, and J.J. Schmidt, *Microfluidic passive permeability assay using nanoliter droplet interface lipid bilayers*. Analyst, 2013. **138**(22): p. 6793-6800.
  42. Sugano, K., M. Kansy, P. Artursson, A. Avdeef, S. Bendels, L. Di, G.F. Ecker, B. Faller, H. Fischer, and G. Gerebtzoff, *Coexistence of passive and carrier-mediated processes in drug transport*. Nature reviews Drug discovery, 2010. **9**(8): p. 597-614.
  43. Ghose, A.K., V.N. Viswanadhan, and J.J. Wendoloski, *A Knowledge-Based Approach in Designing Combinatorial or Medicinal Chemistry Libraries for Drug Discovery. 1. A*



- Qualitative and Quantitative Characterization of Known Drug Databases*. Journal of Combinatorial Chemistry, 1999. **1**(1): p. 55-68.
44. Lipinski, C.A., F. Lombardo, B.W. Dominy, and P.J. Feeney, *Experimental and computational approaches to estimate solubility and permeability in drug discovery and development settings*. Advanced Drug Delivery Reviews, 2001. **46**(1): p. 3-26.
  45. Veber, D.F., S.R. Johnson, H.-Y. Cheng, B.R. Smith, K.W. Ward, and K.D. Kopple, *Molecular Properties That Influence the Oral Bioavailability of Drug Candidates*. Journal of Medicinal Chemistry, 2002. **45**(12): p. 2615-2623.
  46. Kerns, E.H. and L. Di, *Pharmaceutical profiling in drug discovery*. Drug Discovery Today, 2003. **8**(7): p. 316-323.
  47. Leo, A., C. Hansch, and D. Elkins, *Partition coefficients and their uses*. Chemical Reviews, 1971. **71**(6): p. 525-616.
  48. Liu, X., B. Testa, and A. Fahr, *Lipophilicity and Its Relationship with Passive Drug Permeation*. Pharmaceutical Research, 2011. **28**(5): p. 962-977.
  49. Tehrani, E.A., F. Fournier, and S. Desobry, *Simple method to calculate octanol–water partition coefficient of organic compounds*. Journal of Food Engineering, 2004. **64**(3): p. 315-320.
  50. Kansy, M., F. Senner, and K. Gubernator, *Physicochemical high throughput screening: parallel artificial membrane permeation assay in the description of passive absorption processes*. Journal of medicinal chemistry, 1998. **41**(7): p. 1007-1010.
  51. Avdeef, A., *Absorption and drug development: solubility, permeability, and charge state*. 2012: John Wiley & Sons.
  52. Faller, B., *Artificial membrane assays to assess permeability*. Current drug metabolism, 2008. **9**(9): p. 886-892.
  53. Berben, P., A. Bauer-Brandl, M. Brandl, B. Faller, G.E. Flaten, A.-C. Jacobsen, J. Brouwers, and P. Augustijns, *Drug permeability profiling using cell-free permeation tools: Overview and applications*. European Journal of Pharmaceutical Sciences, 2018. **119**: p. 219-233.
  54. Wohnsland, F. and B. Faller, *High-Throughput Permeability pH Profile and High-Throughput Alkane/Water log P with Artificial Membranes*. Journal of Medicinal Chemistry, 2001. **44**(6): p. 923-930.
  55. Alcorn, C.J., R.J. Simpson, D.E. Leahy, and T.J. Peters, *Partition and distribution coefficients of solutes and drugs in brush border membrane vesicles*. Biochemical Pharmacology, 1993. **45**(9): p. 1775-1782.
  56. Sugano, K., H. Hamada, M. Machida, H. Ushio, K. Saitoh, and K. Terada, *Optimized conditions of bio-mimetic artificial membrane permeation assay*. International Journal of Pharmaceutics, 2001. **228**(1): p. 181-188.
  57. Sugano, K., Y. Nabuchi, M. Machida, and Y. Aso, *Prediction of human intestinal permeability using artificial membrane permeability*. International Journal of Pharmaceutics, 2003. **257**(1): p. 245-251.
  58. Takanaga, H., I. Tamai, and A. Tsuji, *pH-Dependent and Carrier-mediated Transport of Salicylic Acid Across Caco-2 Cells*. Journal of Pharmacy and Pharmacology, 1994. **46**(7): p. 567-570.
  59. Neuhoff, S., A.-L. Ungell, I. Zamora, and P. Artursson, *pH-Dependent passive and active transport of acidic drugs across Caco-2 cell monolayers*. European Journal of Pharmaceutical Sciences, 2005. **25**(2): p. 211-220.
  60. Pade, V. and S. Stavchansky, *Estimation of the Relative Contribution of the Transcellular and Paracellular Pathway to the Transport of Passively Absorbed Drugs in the Caco-2 Cell Culture Model*. Pharmaceutical Research, 1997. **14**(9): p. 1210-1215.
  61. Bermejo, M., A. Avdeef, A. Ruiz, R. Nalda, J.A. Ruell, O. Tsinman, I. González, C. Fernández, G. Sánchez, T.M. Garrigues, and V. Merino, *PAMPA—a drug absorption in vitro model: 7. Comparing rat in situ, Caco-2, and PAMPA permeability of fluoroquinolones*. European Journal of Pharmaceutical Sciences, 2004. **21**(4): p. 429-441.

62. Sasaki, M., H. Suzuki, K. Ito, T. Abe, and Y. Sugiyama, *Transcellular Transport of Organic Anions Across a Double-transfected Madin-Darby Canine Kidney II Cell Monolayer Expressing Both Human Organic Anion-transporting Polypeptide (OATP2/SLC21A6) and Multidrug Resistance-associated Protein 2 (MRP2/ABCC2)*. *Journal of Biological Chemistry*, 2002. **277**(8): p. 6497-6503.
63. Kopplow, K., K. Letschert, J. König, B. Walter, and D. Keppler, *Human Hepatobiliary Transport of Organic Anions Analyzed by Quadruple-Transfected Cells*. *Molecular Pharmacology*, 2005. **68**(4): p. 1031-1038.
64. Hubatsch, I., E.G.E. Ragnarsson, and P. Artursson, *Determination of drug permeability and prediction of drug absorption in Caco-2 monolayers*. *Nature Protocols*, 2007. **2**(9): p. 2111-2119.
65. Li, H., D.N. Sheppard, and M.J. Hug, *Transepithelial electrical measurements with the Ussing chamber*. *Journal of Cystic Fibrosis*, 2004. **3**: p. 123-126.
66. Ussing, H.H. and K. Zerahn, *Active Transport of Sodium as the Source of Electric Current in the Short-circuited Isolated Frog Skin*. *Acta Physiologica Scandinavica*, 1951. **23**(2-3): p. 110-127.
67. Alam, M.A., F.I. Al-Jenoobi, and A.M. Al-mohizea, *Everted gut sac model as a tool in pharmaceutical research: limitations and applications*. *Journal of Pharmacy and Pharmacology*, 2012. **64**(3): p. 326-336.
68. Manz, A., N. Graber, and H.M. Widmers, *Miniaturized total chemical analysis systems: A novel concept for chemical sensing*. *Sensors and Actuators B: Chemical*, 1990. **1**(1-6): p. 244-248.
69. Figeys, D. and D. Pinto, *Lab-on-a-chip: a revolution in biological and medical sciences*. *Analytical Chemistry*, 2000. **72**(9): p. 330 A-335 A.
70. Whitesides, G.M., *The origins and the future of microfluidics*. *Nature*, 2006. **442**(7101): p. 368-373.
71. Dittrich, P.S. and A. Manz, *Lab-on-a-chip: microfluidics in drug discovery*. *Nature Reviews Drug Discovery*, 2006. **5**(3): p. 210-218.
72. Teh, S.-Y., R. Lin, L.-H. Hung, and A.P. Lee, *Droplet microfluidics*. *Lab on a Chip*, 2008. **8**(2): p. 198-220.
73. Seemann, R., M. Brinkmann, T. Pfohl, and S. Herminghaus, *Droplet based microfluidics*. *Reports on progress in physics*, 2012. **75**(1): p. 016601.
74. Kawakatsu, T., Y. Kikuchi, and M. Nakajima, *Regular-sized cell creation in microchannel emulsification by visual microprocessing method*. *Journal of the American Oil Chemists' Society*, 1997. **74**(3): p. 317-321.
75. Thorsen, T., R.W. Roberts, F.H. Arnold, and S.R. Quake, *Dynamic Pattern Formation in a Vesicle-Generating Microfluidic Device*. *Physical Review Letters*, 2001. **86**(18): p. 4163-4166.
76. Küster, S.K., S.R. Fagerer, P.E. Verboket, K. Eyer, K. Jefimovs, R. Zenobi, and P.S. Dittrich, *Interfacing Droplet Microfluidics with Matrix-Assisted Laser Desorption/Ionization Mass Spectrometry: Label-Free Content Analysis of Single Droplets*. *Analytical Chemistry*, 2013. **85**(3): p. 1285-1289.
77. Steinhoff, R.F., D.J. Karst, F. Steinebach, M.R.G. Kopp, G.W. Schmidt, A. Stettler, J. Krismer, M. Soos, M. Pabst, A. Hierlemann, et al., *Microarray-based MALDI-TOF mass spectrometry enables monitoring of monoclonal antibody production in batch and perfusion cell cultures*. *Methods*, 2016. **104**: p. 33-40.
78. Schlicht, B. and M. Zagnoni, *Droplet-interface-bilayer assays in microfluidic passive networks*. *Scientific Reports*, 2015. **5**: p. 9951-9951.
79. Kuhn, P., K. Eyer, S. Allner, D. Lombardi, and P.S. Dittrich, *A microfluidic vesicle screening platform: Monitoring the lipid membrane permeability of tetracyclines*. *Analytical chemistry*, 2011. **83**(23): p. 8877-8885.
80. Eyer, K., F. Paech, F. Schuler, P. Kuhn, R. Kissner, S. Belli, P.S. Dittrich, and S.D. Krämer, *A liposomal fluorescence assay to study permeation kinetics of drug-like weak bases across the lipid bilayer*. *Journal of Controlled Release*, 2014. **173**(1): p. 102-109.

81. Robinson, T., P. Kuhn, K. Eyer, and P. Dittrich, *Microfluidic trapping of giant unilamellar vesicles to study transport through a membrane pore*. *Biomicrofluidics*, 2013. **7**(4): p. 044105.
82. Deng, N.-N., M. Yelleswarapu, and W.T.S. Huck, *Monodisperse Uni- and Multicompartment Liposomes*. *Journal of the American Chemical Society*, 2016. **138**(24): p. 7584-7591.
83. Trantidou, T., M.S. Friddin, A. Salehi-Reyhani, O. Ces, and Y. Elani, *Droplet microfluidics for the construction of compartmentalised model membranes*. *Lab on a Chip*, 2018. **18**(17): p. 2488-2509.
84. Deshpande, S., Y. Caspi, A.E.C. Meijering, and C. Dekker, *Octanol-assisted liposome assembly on chip*. *Nature Communications*, 2016. **7**: p. 10447.
85. Milcovich, G., S. Lettieri, F.E. Antunes, B. Medronho, A.C. Fonseca, J.F.J. Coelho, P. Marizza, F. Perrone, R. Farra, B. Dapas, et al., *Recent advances in smart biotechnology: Hydrogels and nanocarriers for tailored bioactive molecules depot*. *Advances in Colloid and Interface Science*, 2017. **249**: p. 163-180.
86. Luisi, P.L. and P. Stano, *Minimal cell mimicry*. *Nature Chemistry*, 2011. **3**(10): p. 755-756.
87. Buddingh', B.C. and J.C.M. van Hest, *Artificial Cells: Synthetic Compartments with Life-like Functionality and Adaptivity*. *Accounts of Chemical Research*, 2017. **50**(4): p. 769-777.
88. Noireaux, V. and A. Libchaber, *A vesicle bioreactor as a step toward an artificial cell assembly*. *Proceedings of the National Academy of Sciences of the United States of America*, 2004. **101**(51): p. 17669-17674.
89. Nuti, N., P.E. Verboket, and P.S. Dittrich, *Multivesicular droplets: a cell model system to study compartmentalised biochemical reactions*. *Lab on a Chip*, 2017. **17**(18): p. 3112-3119.
90. Elani, Y., R.V. Law, and O. Ces, *Vesicle-based artificial cells as chemical microreactors with spatially segregated reaction pathways*. *Nature Communications*, 2014. **5**: p. 5305.
91. Xu, C., S. Hu, and X. Chen, *Artificial cells: from basic science to applications*. *Materials today*, 2016. **19**(9): p. 516-532.
92. Göpfrich, K., I. Platzman, and J.P. Spatz, *Mastering Complexity: Towards Bottom-up Construction of Multifunctional Eukaryotic Synthetic Cells*. *Trends in Biotechnology*, 2018. **36**(9): p. 938-951.
93. Walde, P. and S. Ichikawa, *Enzymes inside lipid vesicles: preparation, reactivity and applications*. *Biomolecular Engineering*, 2001. **18**(4): p. 143-177.
94. Adamala, K.P., D.A. Martin-Alarcon, K.R. Guthrie-Honea, and E.S. Boyden, *Engineering genetic circuit interactions within and between synthetic minimal cells*. *Nature Chemistry*, 2016. **9**: p. 431-439.
95. Peng, R., L. Xu, H. Wang, Y. Lyu, D. Wang, C. Bi, C. Cui, C. Fan, Q. Liu, X. Zhang, and W. Tan, *DNA-based artificial molecular signaling system that mimics basic elements of reception and response*. *Nature Communications*, 2020. **11**(1): p. 978.
96. Steinkühler, J., R.L. Knorr, Z. Zhao, T. Bhatia, S.M. Bartelt, S. Wegner, R. Dimova, and R. Lipowsky, *Controlled division of cell-sized vesicles by low densities of membrane-bound proteins*. *Nature Communications*, 2020. **11**(1): p. 905.
97. Gardner, P.M., K. Winzer, and B.G. Davis, *Sugar synthesis in a protocellular model leads to a cell signalling response in bacteria*. *Nature Chemistry*, 2009. **1**: p. 377-383.
98. Luisi, P.L., F. Ferri, and P. Stano, *Approaches to semi-synthetic minimal cells: a review*. *Naturwissenschaften*, 2006. **93**(1): p. 1-13.
99. Kurihara, K., M. Tamura, K.-i. Shohda, T. Toyota, K. Suzuki, and T. Sugawara, *Self-reproduction of supramolecular giant vesicles combined with the amplification of encapsulated DNA*. *Nature Chemistry*, 2011. **3**: p. 775.
100. Zhang, Z., Z. Li, W. Yu, K. Li, Z. Xie, and Z. Shi, *Propulsion of liposomes using bacterial motors*. *Nanotechnology*, 2013. **24**(18): p. 185103.
101. Osaki, T. and S. Takeuchi, *Artificial Cell Membrane Systems for Biosensing Applications*. *Analytical Chemistry*, 2017. **89**(1): p. 216-231.

102. Weiss, M., J.P. Frohnmayer, L.T. Benk, B. Haller, J.-W. Janiesch, T. Heitkamp, M. Börsch, R.B. Lira, R. Dimova, R. Lipowsky, et al., *Sequential bottom-up assembly of mechanically stabilized synthetic cells by microfluidics*. *Nature Materials*, 2017. **17**: p. 89.
103. Deng, N.-N., M. Yelleswarapu, L. Zheng, and W.T.S. Huck, *Microfluidic Assembly of Monodisperse Vesosomes as Artificial Cell Models*. *Journal of the American Chemical Society*, 2017. **139**(2): p. 587-590.
104. Matosevic, S. and B.M. Paegel, *Layer-by-layer cell membrane assembly*. *Nature Chemistry*, 2013. **5**: p. 958.
105. Peters, R.J., M. Marguet, S. Marais, M.W. Fraaije, J.C. van Hest, and S. Lecommandoux, *Cascade reactions in multicomartmentalized polymersomes*. *Angewandte Chemie International Edition*, 2014. **53**(1): p. 146-50.
106. Nightingale, A.M., T.W. Phillips, J.H. Bannock, and J.C. de Mello, *Controlled multistep synthesis in a three-phase droplet reactor*. *Nature Communications*, 2014. **5**: p. 3777.
107. Bolinger, P.Y., D. Stamou, and H. Vogel, *An integrated self-assembled nanofluidic system for controlled biological chemistries*. *Angewandte Chemie International Edition*, 2008. **47**(30): p. 5544-9.
108. Rabe, K.S., J. Müller, M. Skoupi, and C.M. Niemeyer, *Cascades in Compartments: En Route to Machine-Assisted Biotechnology*. *Angewandte Chemie International Edition*, 2017. **56**(44): p. 13574-13589.
109. Robinson, T., *Microfluidic Handling and Analysis of Giant Vesicles for Use as Artificial Cells: A Review*. *Advanced Biosystems*, 2019. **3**(6): p. 1800318.
110. Kuhn, P., K. Eyer, T. Robinson, F.I. Schmidt, J. Mercer, and P.S. Dittrich, *A facile protocol for the immobilisation of vesicles, virus particles, bacteria, and yeast cells*. *Integrative Biology*, 2012. **4**(12): p. 1550-1555.
111. Vrhovec, S., M. Mally, B. Kavčič, and J. Derganc, *A microfluidic diffusion chamber for reversible environmental changes around flaccid lipid vesicles*. *Lab on a Chip*, 2011. **11**(24): p. 4200-4206.
112. Yandrapalli, N. and T. Robinson, *Ultra-high capacity microfluidic trapping of giant vesicles for high-throughput membrane studies*. *Lab Chip*, 2019. **19**(4): p. 626-633.
113. Yamada, A., S. Lee, P. Bassereau, and C.N. Baroud, *Trapping and release of giant unilamellar vesicles in microfluidic wells*. *Soft Matter*, 2014. **10**(32): p. 5878-85.
114. Shimanouchi, T., P. Walde, J. Gardiner, Y.R. Mahajan, D. Seebach, A. Thomae, S.D. Krämer, M. Voser, and R. Kuboi, *Permeation of a  $\beta$ -heptapeptide derivative across phospholipid bilayers*. *Biochimica et Biophysica Acta (BBA) - Biomembranes*, 2007. **1768**(11): p. 2726-2736.
115. Stachowiak, J.C., D.L. Richmond, T.H. Li, A.P. Liu, S.H. Parekh, and D.A. Fletcher, *Unilamellar vesicle formation and encapsulation by microfluidic jetting*. *Proceedings of the National Academy of Sciences of the United States of America*, 2008. **105**(12): p. 4697.
116. van Swaay, D. and A. DeMello, *Microfluidic methods for forming liposomes*. *Lab on a Chip*, 2013. **13**(5): p. 752-767.
117. Richmond, D.L., E.M. Schmid, S. Martens, J.C. Stachowiak, N. Liska, and D.A. Fletcher, *Forming giant vesicles with controlled membrane composition, asymmetry, and contents*. *Proceedings of the National Academy of Sciences of the United States of America*, 2011. **108**(23): p. 9431.
118. Kamiya, K., R. Kawano, T. Osaki, K. Akiyoshi, and S. Takeuchi, *Cell-sized asymmetric lipid vesicles facilitate the investigation of asymmetric membranes*. *Nature Chemistry*, 2016. **8**: p. 881.
119. Baxani, D.K., A.J. Morgan, W.D. Jamieson, C.J. Allender, D.A. Barrow, and O.K. Castell, *Bilayer Networks within a Hydrogel Shell: A Robust Chassis for Artificial Cells and a Platform for Membrane Studies*. *Angewandte Chemie International Edition*, 2016. **55**(46): p. 14240-14245.
120. Sarles, S.A. and D.J. Leo, *Regulated Attachment Method for Reconstituting Lipid Bilayers of Prescribed Size within Flexible Substrates*. *Analytical Chemistry*, 2010. **82**(3): p. 959-966.

121. Zagnoni, M. and J.M. Cooper, *A microdroplet-based shift register*. Lab on a Chip, 2010. **10**(22): p. 3069-3073.
122. Carreras, P., Y. Elani, R.V. Law, N.J. Brooks, J.M. Seddon, and O. Ces, *A microfluidic platform for size-dependent generation of droplet interface bilayer networks on rails*. Biomicrofluidics, 2015. **9**(6): p. 064121.
123. Leptihn, S., O.K. Castell, B. Cronin, E.-H. Lee, L.C.M. Gross, D.P. Marshall, J.R. Thompson, M. Holden, and M.I. Wallace, *Constructing droplet interface bilayers from the contact of aqueous droplets in oil*. Nature Protocols, 2013. **8**: p. 1048-1057.
124. Funakoshi, K., H. Suzuki, and S. Takeuchi, *Lipid bilayer formation by contacting monolayers in a microfluidic device for membrane protein analysis*. Analytical Chemistry, 2006. **78**(24): p. 8169-8174.
125. Taylor, G., M.-A. Nguyen, S. Koner, E. Freeman, C.P. Collier, and S.A. Sarles, *Electrophysiological interrogation of asymmetric droplet interface bilayers reveals surface-bound alamethicin induces lipid flip-flop*. Biochimica et Biophysica Acta (BBA) - Biomembranes, 2019. **1861**(1): p. 335-343.
126. Stanley, C.E., K.S. Elvira, X.Z. Niu, A.D. Gee, O. Ces, J.B. Edel, and A.J. deMello, *A microfluidic approach for high-throughput droplet interface bilayer (DIB) formation*. Chemical Communications, 2010. **46**(10): p. 1620-1622.
127. Nguyen, M.-A., B. Srijanto, C.P. Collier, S.T. Retterer, and S.A. Sarles, *Hydrodynamic trapping for rapid assembly and in situ electrical characterization of droplet interface bilayer arrays*. Lab on a Chip, 2016. **16**(18): p. 3576-3588.
128. Bayley, H., B. Cronin, A. Heron, M.A. Holden, W.L. Hwang, R. Syeda, J. Thompson, and M. Wallace, *Droplet interface bilayers*. Molecular BioSystems, 2008. **4**(12): p. 1191-1208.
129. Venkatesan, G.A., J. Lee, A.B. Farimani, M. Heiranian, C.P. Collier, N.R. Aluru, and S.A. Sarles, *Adsorption Kinetics Dictate Monolayer Self-Assembly for Both Lipid-In and Lipid-Out Approaches to Droplet Interface Bilayer Formation*. Langmuir, 2015. **31**(47): p. 12883-12893.
130. Freeman, E., J. Najem, S. Sukharev, M. Philen, and D. Leo, *The mechano-electrical response of droplet interface bilayer membranes*. Soft Matter, 2016. **12**(12): p. 3021-3031.
131. Poulos, J.L., W.C. Nelson, T.-J. Jeon, and J.J. Schmidt, *Electrowetting on dielectric-based microfluidics for integrated lipid bilayer formation and measurement*. Applied Physics Letters, 2009. **95**(1): p. 013706.
132. Aghdaei, S., M.E. Sandison, M. Zagnoni, N.G. Green, and H. Morgan, *Formation of artificial lipid bilayers using droplet dielectrophoresis*. Lab on a Chip, 2008. **8**(10): p. 1617-1620.
133. Czekalska, M.A., T.S. Kaminski, S. Jakiela, K. Tanuj Sapra, H. Bayley, and P. Garstecki, *A droplet microfluidic system for sequential generation of lipid bilayers and transmembrane electrical recordings*. Lab on a Chip, 2015. **15**(2): p. 541-548.
134. Elani, Y., X. Niu, and O. Ces, *Novel technologies for the formation of 2-D and 3-D droplet interface bilayer networks*. Lab on a Chip, 2012. **12**(18): p. 3514-3520.
135. Czekalska, M.A., T.S. Kaminski, K. Makuch, and P. Garstecki, *Passive and parallel microfluidic formation of droplet interface bilayers (DIBs) for measurement of leakage of small molecules through artificial phospholipid membranes*. Sensors and Actuators B: Chemical, 2019. **286**: p. 258-265.
136. Elani, Y., X.C.I. Solvas, J.B. Edel, R.V. Law, and O. Ces, *Microfluidic generation of encapsulated droplet interface bilayer networks (multisomes) and their use as cell-like reactors*. Chemical Communications, 2016. **52**(35): p. 5961-5964.
137. Toepke, M.W. and D.J. Beebe, *PDMS absorption of small molecules and consequences in microfluidic applications*. Lab on a Chip, 2006. **6**(12): p. 1484-1486.
138. Lenz, M., B. Sebastian, and P.S. Dittrich, *Formation of Single Micro- and Nanowires with Extreme Aspect Ratios in Microfluidic Channels*. Small, 2019. **15**(33): p. 1901547.
139. Shim, J.U., G. Cristobal, D.R. Link, T. Thorsen, Y. Jia, K. Piattelli, and S. Fraden, *Control and measurement of the phase behavior of aqueous solutions using microfluidics*. J Am Chem Soc, 2007. **129**(28): p. 8825-35.

140. Dangla, R., F. Gallaire, and C.N. Baroud, *Microchannel deformations due to solvent-induced PDMS swelling*. Lab on a Chip, 2010. **10**(21): p. 2972-2978.
141. Malmstadt, N., M.A. Nash, R.F. Purnell, and J.J. Schmidt, *Automated Formation of Lipid-Bilayer Membranes in a Microfluidic Device*. Nano Letters, 2006. **6**(9): p. 1961-1965.
142. Dixit, S.S., A. Pincus, B. Guo, and G.W. Faris, *Droplet shape analysis and permeability studies in droplet lipid bilayers*. Langmuir, 2012. **28**(19): p. 7442-7451.
143. Lopez, M., J. Denver, S.E. Evangelista, A. Armetta, G. Di Domizio, and S. Lee, *Effects of Acyl Chain Unsaturation on Activation Energy of Water Permeability across Droplet Bilayers of Homologous Monoglycerides: Role of Cholesterol*. Langmuir, 2018. **34**(5): p. 2147-2157.
144. Huang, J., M. Lein, C. Gunderson, and M.A. Holden, *Direct Quantitation of Peptide-Mediated Protein Transport across a Droplet-Interface Bilayer*. Journal of the American Chemical Society, 2011. **133**(40): p. 15818-15821.
145. Lee, Y. and S.Q. Choi, *Quantitative analysis for lipophilic drug transport through a model lipid membrane with membrane retention*. European Journal of Pharmaceutical Sciences, 2019. **134**: p. 176-184.
146. Harriss, L.M., B. Cronin, J.R. Thompson, and M.I. Wallace, *Imaging Multiple Conductance States in an Alamethicin Pore*. Journal of the American Chemical Society, 2011. **133**(37): p. 14507-14509.
147. Mruetusatorn, P., G. Polizos, P.G. Datskos, G. Taylor, S.A. Sarles, J.B. Boreyko, D.G. Hayes, and C.P. Collier, *Control of Membrane Permeability in Air-Stable Droplet Interface Bilayers*. Langmuir, 2015. **31**(14): p. 4224-4231.
148. Villar, G., A.D. Graham, and H. Bayley, *A Tissue-Like Printed Material*. Science, 2013. **340**(6128): p. 48-52.
149. Czekalska, M.A., T.S. Kaminski, M. Horka, S. Jakiela, and P. Garstecki, *An Automated Microfluidic System for the Generation of Droplet Interface Bilayer Networks*. Micromachines, 2017. **8**(3): p. 93.
150. Holden, M.A., D. Needham, and H. Bayley, *Functional Bionetworks from Nanoliter Water Droplets*. Journal of the American Chemical Society, 2007. **129**(27): p. 8650-8655.
151. Wauer, T., H. Gerlach, S. Mantri, J. Hill, H. Bayley, and K.T. Sapra, *Construction and Manipulation of Functional Three-Dimensional Droplet Networks*. ACS Nano, 2014. **8**(1): p. 771-779.
152. Elfaramawy, M.A., S. Fujii, A. Uyeda, T. Osaki, S. Takeuchi, Y. Kato, H. Watanabe, and T. Matsuura, *Quantitative analysis of cell-free synthesized membrane proteins at the stabilized droplet interface bilayer*. Chemical Communications, 2018. **54**(86): p. 12226-12229.
153. Hwang, W.L., M.A. Holden, S. White, and H. Bayley, *Electrical Behavior of Droplet Interface Bilayer Networks: Experimental Analysis and Modeling*. Journal of the American Chemical Society, 2007. **129**(38): p. 11854-11864.
154. Dupin, A. and F.C. Simmel, *Signalling and differentiation in emulsion-based multi-compartmentalized in vitro gene circuits*. Nature Chemistry, 2019. **11**(1): p. 32-39.
155. Maglia, G., A.J. Heron, W.L. Hwang, M.A. Holden, E. Mikhailova, Q. Li, S. Cheley, and H. Bayley, *Droplet networks with incorporated protein diodes show collective properties*. Nature Nanotechnology, 2009. **4**: p. 437-440.
156. Fischer, A., M.A. Holden, B.L. Pentelute, and R.J. Collier, *Ultrasensitive detection of protein translocated through toxin pores in droplet-interface bilayers*. Proceedings of the National Academy of Sciences of the United States of America, 2011. **108**(40): p. 16577-16581.
157. Rojko, N., B. Cronin, J.S.H. Daniai, M.A.B. Baker, G. Anderluh, and M.I. Wallace, *Imaging the Lipid-Phase-Dependent Pore Formation of Equinatoxin II in Droplet Interface Bilayers*. Biophysical Journal, 2014. **106**(8): p. 1630-1637.
158. Findlay, H.E., N.J. Harris, and P.J. Booth, *In vitro synthesis of a Major Facilitator Transporter for specific active transport across Droplet Interface Bilayers*. Scientific Reports, 2016. **6**: p. 39349.

159. Iwamoto, M. and S. Oiki, *Membrane Perfusion of Hydrophobic Substances Around Channels Embedded in the Contact Bubble Bilayer*. Scientific reports, 2017. **7**(1): p. 6857-6857.
160. Shinwari, M.W., D. Zhitomirsky, I.A. Deen, P.R. Selvaganapathy, M.J. Deen, and D. Landheer, *Microfabricated reference electrodes and their biosensing applications*. Sensors, 2010. **10**(3): p. 1679-1715.
161. Meller, A., L. Nivon, and D. Branton, *Voltage-driven DNA translocations through a nanopore*. Physical Review Letters, 2001. **86**(15): p. 3435.
162. Challita, E.J., J.S. Najem, R. Monroe, D.J. Leo, and E.C. Freeman, *Encapsulating Networks of Droplet Interface Bilayers in a Thermoreversible Organogel*. Scientific Reports, 2018. **8**(1): p. 6494.
163. Booth, M.J., V. Restrepo Schild, F.G. Downs, and H. Bayley, *Functional aqueous droplet networks*. Molecular BioSystems, 2017. **13**(9): p. 1658-1691.
164. Booth, M.J., V.R. Schild, A.D. Graham, S.N. Olof, and H. Bayley, *Light-activated communication in synthetic tissues*. Science Advances, 2016. **2**(4): p. e1600056.
165. Villar, G., A.J. Heron, and H. Bayley, *Formation of droplet networks that function in aqueous environments*. Nature Nanotechnology, 2011. **6**: p. 803-808.
166. Elio, J.C., S.N. Joseph, C.F. Eric, and J.L. Donald. *A 3D printing method for droplet-based biomolecular materials*. in *Proc.SPIE*. 2017.
167. Castell, O.K., J. Berridge, and M.I. Wallace, *Quantification of Membrane Protein Inhibition by Optical Ion Flux in a Droplet Interface Bilayer Array*. Angewandte Chemie International Edition, 2012. **51**(13): p. 3134-3138.
168. Tonooka, T., K. Sato, T. Osaki, R. Kawano, and S. Takeuchi, *Lipid Bilayers on a Picoliter Microdroplet Array for Rapid Fluorescence Detection of Membrane Transport*. Small, 2014. **10**(16): p. 3275-3282.
169. Urban, M., A. Kleefen, N. Mukherjee, P. Seelheim, B. Windschiegl, M. Vor der Brüggen, A. Koçer, and R. Tampé, *Highly Parallel Transport Recordings on a Membrane-on-Nanopore Chip at Single Molecule Resolution*. Nano Letters, 2014. **14**(3): p. 1674-1680.
170. Kleefen, A., D. Pedone, C. Grunwald, R. Wei, M. Firnkes, G. Abstreiter, U. Rant, and R. Tampé, *Multiplexed Parallel Single Transport Recordings on Nanopore Arrays*. Nano Letters, 2010. **10**(12): p. 5080-5087.
171. Huang, S., M. Romero-Ruiz, O.K. Castell, H. Bayley, and M.I. Wallace, *High-throughput optical sensing of nucleic acids in a nanopore array*. Nature nanotechnology, 2015. **10**(11): p. 986-991.
172. Lee, Y., H.R. Lee, K. Kim, and S.Q. Choi, *Static and Dynamic Permeability Assay for Hydrophilic Small Molecules Using a Planar Droplet Interface Bilayer*. Analytical Chemistry, 2018. **90**(3): p. 1660-1667.

## Chapter 2

# Interaction of Peptides and Toxins with Lipid Membranes Studied on a Microfluidic Device

**Parts of this chapter were originally published in the following papers:**

Bachler, S., P. Drücker, A.T. Müller, C. Del Don, E.B. Babiychuk, G. Schneider, A. Draeger, and P.S. Dittrich. *Interaction of Toxins and Peptides with Lipid Membranes Studied on a Microfluidic Device*. *Biophysical Journal*, 2018. **114**(3): p. 262a.

Reprinted and adapted with permission from Elsevier.

Bachler, S., C.-C. Lin, and P.S. Dittrich. *Combination of a microfluidic device and fluorescence correlation spectroscopy to study peptide translocation across model membranes*. *Proceedings of the 21st International Conference on Miniaturized Systems for Chemistry and Life Sciences, MicroTAS, 2017*: p. 967-968.

Reprinted and adapted with permission from Chemical and Biological Microsystems Society (CBMS).

Drücker, P., S. Bachler, H. Wolfmeier, R. Schoenauer, R. Köffel, V.S. Babiychuk, P.S. Dittrich, A. Draeger, and E.B. Babiychuk, *Pneumolysin-damaged cells benefit from non-homogeneous toxin binding to cholesterol-rich membrane domains*. *Biochimica et Biophysica Acta (BBA) - Molecular and Cell Biology of Lipids*, 2018. **1863**(8): p. 795-805.

Partly reprinted and adapted with permission from Elsevier.



Drücker, P., I. Iacovache, S. Bachler, B. Zuber, E.B. Babiychuk, P.S. Dittrich, and A. Draeger. *Membrane deformation and layer-by-layer peeling of giant vesicles induced by the pore-forming toxin pneumolysin*. *Biomaterials Science*, 2019. **7**(9): p. 3693-3705.

Partly reprinted and adapted with permission from Royal Society of Chemistry / Creative Commons.

Pillong, M., J.A. Hiss, P. Schneider, Y.-C. Lin, G. Posselt, B. Pfeiffer, M. Blatter, A.T. Müller, S. Bachler, C.S. Neuhaus, P.S. Dittrich, K.-H. Altmann, S. Wessler, and G. Schneider. *Rational Design of Membrane-Pore-Forming Peptides*. *Small*, 2017. **13**(40): p. 1701316.

Partly reprinted and adapted with permission from Wiley.

Müller, A.T., G. Posselt, G. Gabernet, C. Neuhaus, **S. Bachler**, M. Blatter, B. Pfeiffer, J.A. Hiss, P.S. Dittrich, K.-H. Altmann, S. Wessler, G. Schneider. *Morphing of Amphipathic Helices to Explore the Activity and Selectivity of Membranolytic Antimicrobial Peptides*. *Biochemistry*, 2020. **59**(39): p. 3772-3781.

Partly reprinted and adapted with permission from ACS.

Gautschi, D., C.S. Neuhaus, I. Kritikos, S. Bachler, E. Darwish, P.S. Dittrich, and G. Schneider. *Activity and Selectivity Screening of Anticancer Peptides on Cancer Cells and Liposomes*. Manuscript in preparation, 2020.

Partly reprinted and adapted with permission from Gisbert Schneider.

### **Author contributions:**

For these publications, all above mentioned authors performed experiments, analysed/discussed results, and/or wrote/commented the paper. Especially relevant for this chapter are the following contributions: S.B. improved and fabricated the microfluidic devices. S.B., P.D., A.T.M., C.S.N., D.G., C.-C.L., G.G., C.D.D., E.B.B., A.D., G.S., J.A.H., and P.S.D. performed and/or analyzed the experiments with vesicles.

## 2.1 Abstract

We developed a microfluidic device that enables trapping, treatment, and analysis of more than hundred individual giant lipid vesicles to study the interaction of molecules with lipid membranes [1]. The vesicles were immobilized in hydrodynamic traps where they could be isolated from the flow through the actuation of integrated doughnut-shaped valves that are positioned around each trap. Fast exchanges of chemical and biological solutions were performed by opening the valves.

We employed this device to monitor interactions of toxins and peptides with lipid membranes. We observed various effects such as permeation by means of fluorescence microscopy and fluorescence correlation spectroscopy, membranolysis, or pore formation. (1) Permeation studies were carried out with the HIV-1 trans-acting activator of transcription domain and the nona-arginine peptide. We found that the composition of the membrane had an influence on its permeability for the tested peptides. (2) Rupture of vesicles was observed with different antimicrobial and anticancer peptides. (3) Exposure of the toxin pneumolysin to membranes with high cholesterol concentration within the lipid bilayer showed a fast homogenous binding of the toxin to the membrane and pore formation within seconds. Furthermore, membrane deformation and layer-by-layer peeling of vesicles induced by the toxin were observed.

Our microfluidic trap array constitutes a valuable platform for peptide or toxin testing and can be used to visualize interactions of molecules with artificial cell membranes.

## 2.2 Introduction

Peptides and proteins interact with lipid membranes in various ways, e.g. they can (1) permeate across (artificial) cell membranes, (2) induce membranolysis, or (3) partition into it and form pores [1, 2]. This chapter illustrates the usage of a microfluidic system for a more systematic understanding of the interaction between peptides and toxins with lipid membranes.

The microfluidic device that allows for trapping, treatment, and analysis of giant lipid vesicles (GVs) and cells was developed from a previously published design [3]. The device can be used to treat GV with penetrating peptides, drugs, lysis buffers, toxins, or staining dyes for a precisely controlled duration while optical transparency allows for constant monitoring with microscopic or spectroscopic methods. Here, we demonstrate the versatility of our microfluidic method by showcasing different applications where we exposed the GV to peptides and toxins.

(1) It is well known that small organic molecules and peptides can permeate across lipid membranes, and various computational and experimental methods are frequently employed to predict the permeation rate. However, the mechanism of the permeation process and the influence of the membrane properties are still discussed controversially [4, 5]. Certain proteins have been shown to traverse the cell membrane by a process called protein transduction and to reach the nucleus while retaining their biological activity [6]. Short “protein-transduction domains” also known as cell-penetrating peptides (CPPs) are responsible for the cellular uptake of these proteins. CPPs are small peptides in the range of 3-18 amino acids. Due to their ability to cross membrane barriers, they cannot only be used as active compounds themselves, but also as carriers for other drug molecules. Good examples are HIV-1 trans-acting activator of transcription (TAT) domain and the nona-arginine (Arg<sub>9</sub>) that belong to the family of cationic CPP. Peptides are highly relevant as candidates for new drug molecules and drug carriers. The properties such as hydrophobicity or charge of the peptides can be tailored by altering the amino acid sequence. In consequence, the peptide can interact in various ways with cell membranes. We present a method to study interactions of fluorescently labeled peptides and membranes aiming at a more detailed understanding of the permeation process. We use GV of various membrane compositions as model membrane and follow the permeation of molecules across the membrane bilayer to the inside of the vesicle. For on-demand solution exchange with a high temporal resolution, we immobilize the GV on the previously mentioned microfluidic platform with integrated vesicle traps. We use the short polypeptides HIV-TAT and Arg<sub>9</sub> that possess the ability to cross natural cells as well as artificial membranes [7]. Herein we study the permeability in dependence of the lipid composition of the vesicle membrane. Permeation of the fluorescently labeled peptides into GV is characterized

with fluorescence correlation spectroscopy (FCS), which provides information on the intra- and extra-vesicular concentrations.

(2) The world-wide increase of resistant bacteria is a problem for our modern society and the discovery of novel antibiotics is an urgent need [8]. Computational methods facilitate the rational design of peptides and proteins with preferred properties [8-13]. Therefore, computational approaches are used in peptide research for the discovery of antimicrobial peptides (AMPs) [8, 9, 14-17]. After multiple AMPs showed cytotoxic activities against cancer cells, also anticancer peptides (ACPs) have emerged [18-21]. We hence exposed GVs in the microfluidic device to several peptides with membranolytic effects and imaged the rupture of vesicles to investigate potency and selectivity of these computationally designed AMPs and ACPs.

(3) *Streptococcus pneumoniae* is a potent human pathogen causing the disease pneumonia [22-24]. These bacteria produce the toxin pneumolysin (PLY), which is a cholesterol-dependent cytolysin [22, 25-27]. PLY is crucial for incapacitation of the immune system and breaching the host's epithelial barrier [22, 25-27]. We investigated the interaction of PLY with lipid membranes to further understand the mechanism of action for this toxin.

## 2.3 Experimental Section

### 2.3.1 Immobilization of Vesicles

GVs were used as a model system for cellular membranes and were immobilized on a microfluidic chip [2]. GVVs were prepared by swelling of dried lipid films on poly(vinylalcohol) (PVA, Merck KGaA, Darmstadt, Germany) or agarose (Ultra-low Gelling Temperature, molecular biology grade, Sigma-Aldrich). For the permeation studies, we prepared giant unilamellar vesicles (GUVs) on indium tin oxide (ITO) coated glass slides (15-25 Ohm/square, Sigma-Aldrich) with a custom electroformation device [28]. The lipid solution was then added on top of the ITO plate, PVA, or agarose film and distributed by gentle slewing. All lipids were purchased from Avanti Polar Lipids Inc. (Alabaster, AL, USA). We used as membrane labels 1,1'-dioctadecyl-3,3,3',3'-tetramethylindodicarbocyanine perchlorate (DiD, Fluorochem Ltd, Hadfield, UK), 1,1'-dioctadecyl-3,3,3',3'-tetramethylindodicarbocyanine perchlorate (DiI, Thermo Fisher Scientific), or Bodipy-PC (Thermo Fisher Scientific). Calcein (Acros Organics) or fluorescein isothiocyanate-dextran (FITC-dextran, Sigma-Aldrich) were used to visualize when the peptide solution came into contact with the vesicle or to investigate pore formation.

The chip design was adapted from previous studies performed in our lab, where a vesicle trap was surrounded by a circular valve to form a small chamber of a few hundred picoliters [3, 29]. The microfluidic chips composed of PDMS (polydimethylsiloxane, Sylgard 184) (Dow Corning, Midland, MI, USA) yielding flexible, gas permeable, and transparent devices. In brief, the bottom (fluid) layer accommodates 64 microchambers with vesicle traps in the center to capture single GVVs. Since the occupation of traps by GVVs is usually far below 100% in these trap designs [29], we adapted the design and implemented multiple traps in each chamber to increase the probability of GVVs loading. We used chambers containing three or seven traps in the improved design, which lead to a total of 192 or 448 traps per chip. Chambers can be closed by actuation of a valve moving down the top (pressure) layer, which enables the complete spatial isolation of the trapped GVVs. The chip master form was fabricated in a cleanroom environment using SU-8 2015 (Microchem, Newton, MA, USA) and processed to 20  $\mu\text{m}$  height by spin-coating, baking steps, exposure to UV light source through a foil mask, development, and silanization. From this master structure, microfluidic chips composed of PDMS were replicated with multilayer soft lithography and bonded to a glass slide using a plasma cleaner (PDC-32 G, Harrick, NY, USA). To prepare chips for the experiment, H<sub>2</sub>O was pipetted into the inlet reservoirs and forced into the chip by centrifugation at 2000 rpm for 5 min. A filtered 4% (w/v) bovine serum albumin (BSA) solution (Sigma-Aldrich) in phosphate buffered saline (PBS, Gibco Life Technologies, Paisley, UK) was then flushed into the microfluidic channels with a conventional Nanojet syringe pump (10  $\mu\text{l}/\text{min}$  for ~10 min, followed by ~10 min incubation) to coat the internal surfaces and prevent from unspecific GV rupture or

peptide binding. Subsequently, GVs were injected into to chip at a flowrate of  $\sim 1\text{-}10\ \mu\text{l}/\text{min}$  for 30 min before  $\sim 2$  bar of pressure were applied to the donut-shaped valves in the upper layer to isolate the trapped vesicles from the surrounding medium. Afterwards, the surrounding microchannels were flushed with peptide/toxin solution with  $\sim 10\ \mu\text{l}/\text{min}$  for 5 min. The flow was then reduced to  $\sim 0.5\ \mu\text{l}/\text{min}$  and the vesicle-containing compartments were opened. Upon contact to the peptides or toxins of interest, we saw translocation, rupturing, or pore-formation and monitored the effects with microscopic imaging or FCS. Figure 2-1 shows the PDMS chip with three hydrodynamic traps per chamber.

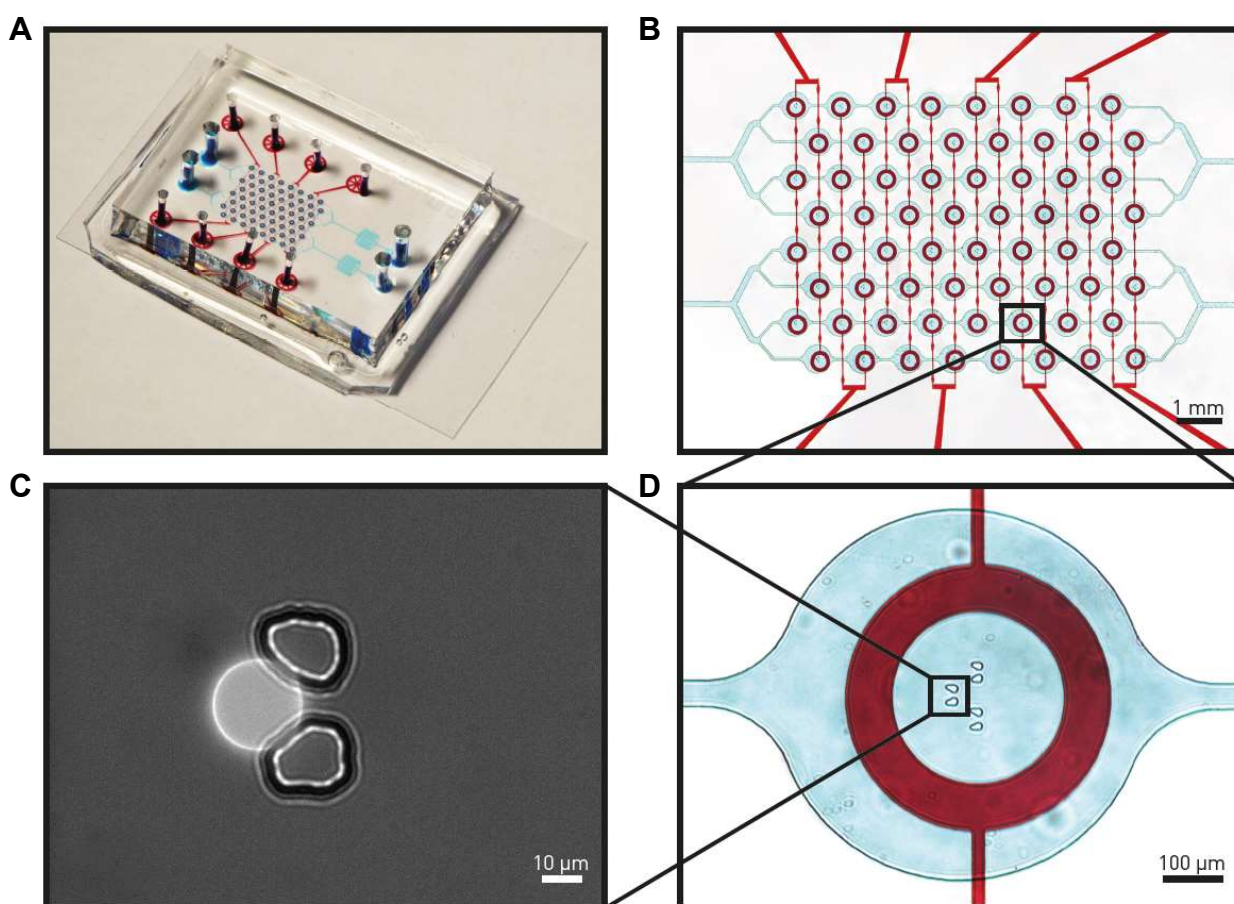


Figure 2-1: A) Photograph of the microfluidic device. For visualization, the bottom fluid channels are filled with blue food dye and the top control layer is filled with red ink. B) Micrograph of the chamber array with 64 microchambers. C) Fluorescent image of a trapped giant unilamellar vesicle (GUV). The membrane of the GUV was labeled with the fluorescent dye DiD. D) Micrograph of one microchamber defined by a circular valve (red) containing three hydrodynamic traps. Reprinted and adapted from Drücker et al. [22] with permission from Elsevier and Bachler et al. [2] with permission from Chemical and Biological Microsystems Society (CBMS).

### 2.3.2 Fluorescence Correlation Spectroscopy (FCS)

FCS is a technique that enables the sensitive detection of single fluorescent molecules [2]. The number of molecules in the detection volume and the diffusion coefficient of the fluorescent species can be determined as well. By positioning a laser spot for excitation outside and inside the vesicle, respectively, one can record the autocorrelation functions and count rates in order

to reveal the percentage of translocation at concentrations down to the low nanomolar range. Figure 2-2 shows the schematics of the detection setup to measure translocation into GUVs.

Our microscope setup is based on confocal detection and the fluctuations result from the free diffusion or transport of the probes in and out of the detection volume. When the circular valve is closed, the vesicles are isolated and not subjected to any flow or disturbances, which makes FCS measurements feasible. Opening the valves allows for fast fluid exchange and delivery of fluorescently tagged molecules.

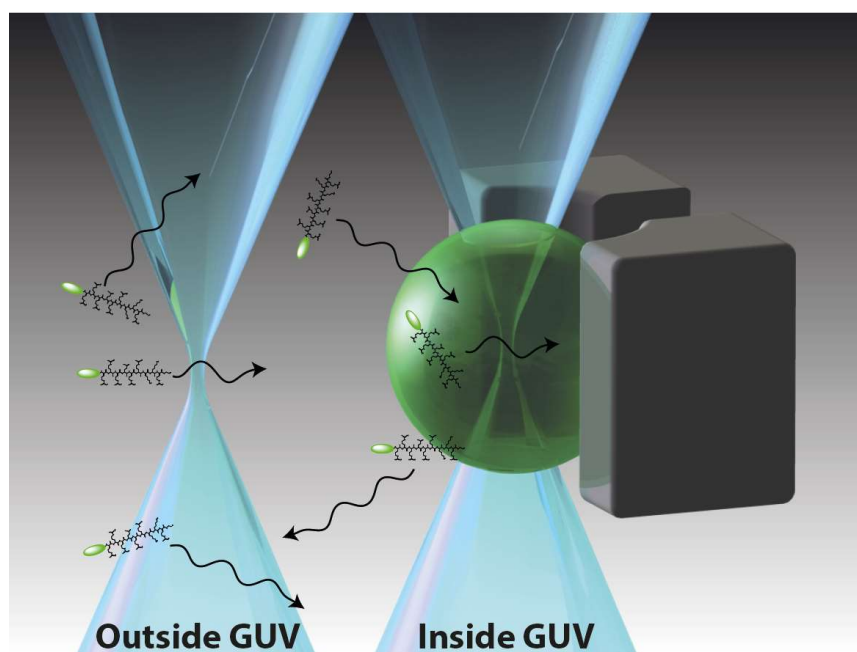


Figure 2-2: Schematics of the detection setup. The laser focus is positioned inside and subsequently outside of the trapped giant unilamellar vesicle (GUV) to detect the fluorescent molecules. Reprinted and adapted from Bachler et al. [2] with permission from Chemical and Biological Microsystems Society (CBMS).

The decay time of the autocorrelation curves correlates with the diffusion coefficient and the inverse of the correlation amplitude corresponds to the concentration of the measured molecules. Figure 2-3 illustrates autocorrelation curves with and without permeation into GUVs. The autocorrelation function of the intensity trace reveals the average number of fluorescent molecules ( $N$ ) in the detection volume by the inverse of the correlation amplitude and the average diffusion time. The values can be compared inside and outside of the vesicle to gain a better understanding of the ongoing processes. We tested peptides with fluorescein (FL) labelled to HIV-TAT (RRRQRRKKRG) and Arg<sub>9</sub> (PSL Peptide Specialty Laboratories, Heidelberg, Germany).

## Chapter 2

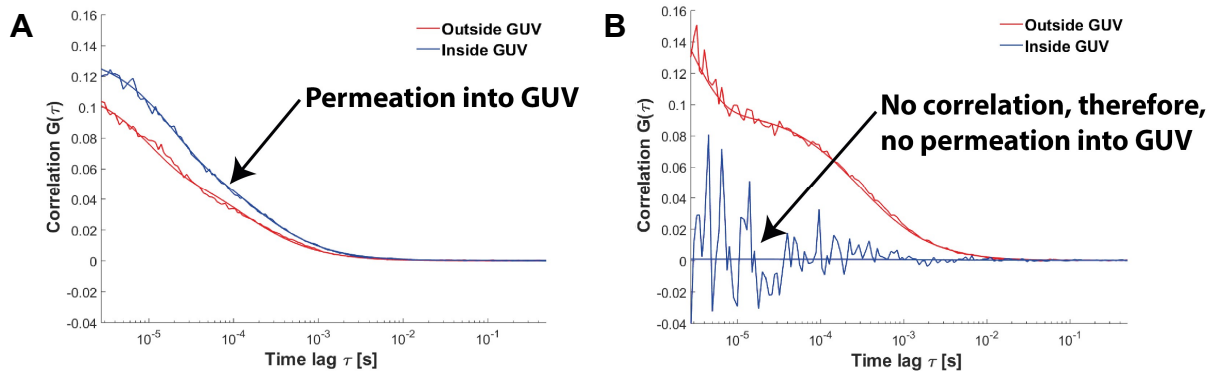


Figure 2-3: A) Representative autocorrelation curves of a fluorescently labeled peptide outside (red) and inside (blue) of a giant unilamellar vesicle (GUV). B) Auto-correlation curves outside and inside of a GUV when the peptide is not permeating across the membrane. Reprinted and adapted from Bachler et al. [2] with permission from Chemical and Biological Microsystems Society (CBMS).



## 2.4 Results and Discussion

### 2.4.1 Permeation Studies with Cell-Penetrating Peptides

We investigated the influence of different membrane compositions for the translocation of FL-HIV-TAT and FL-Arg<sub>9</sub> [2]. The measurements were carried out 10 min ( $\pm$  2 min) after opening the valves. Figure 2-4 summarizes the results for the two tested peptides at different membrane compositions, which indicate translocation of the peptides into GUVs containing anionic lipids or lipids inducing negative curvature, whereas no translocation was observed in GUVs consisting entirely of neutral lipids. With a similar method it was also possible to investigate tunable membrane potentials reconstituted in GVs [30].

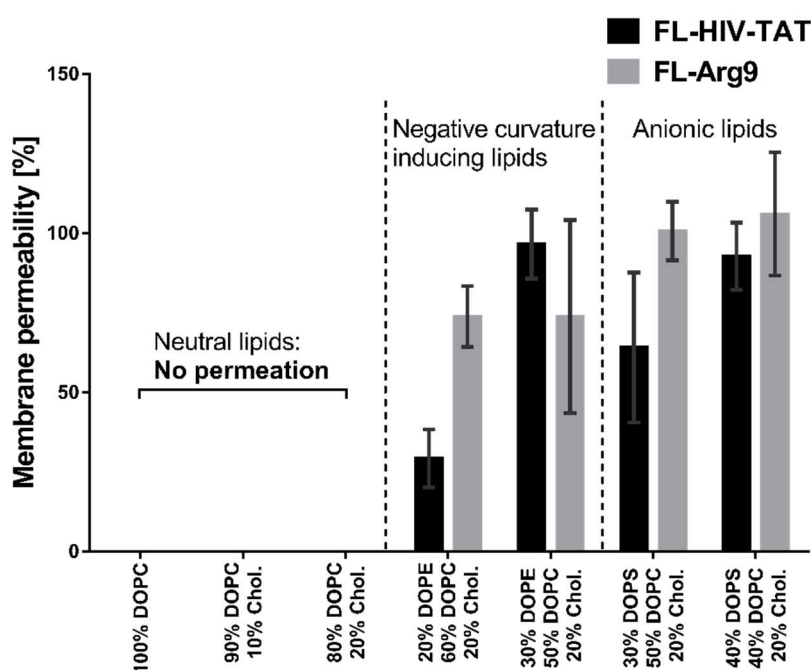


Figure 2-4: Permeability tests of 150 nM FL-HIV-TAT (black) and 150 nM FL-Arg<sub>9</sub> (grey) for different membrane compositions. The measurements were carried out 10 min ( $\pm$  2 min) after opening the valves. The count rates inside and outside of the GUVs were measured and evaluated. Reprinted and adapted from Bachler et al. [2] with permission from Chemical and Biological Microsystems Society (CBMS).

### 2.4.2 Membranolytic Peptides

Rupture of vesicles was frequently observed after long incubation times (more than 1 h) for FL-HIV-TAT and FL-Arg<sub>9</sub> peptides (Figure 2-5) [2].

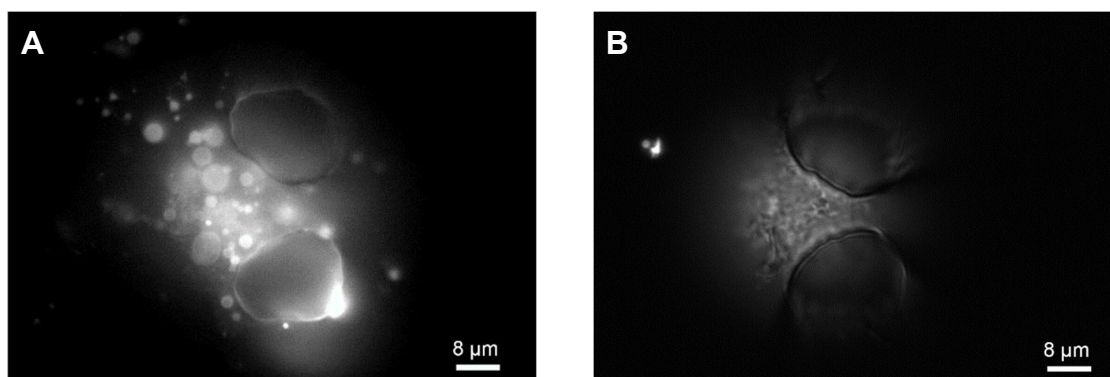


Figure 2-5: A) Ruptured vesicle which was continuously incubated for 1 hour with 150 nM FL-HIV-TAT (lipid composition: 40% DOPC, 20% Cholesterol, and 40% DOPS). B) Ruptured vesicle which was continuously incubated for 1 hour with 150 nM FL-Arg<sub>9</sub> (lipid composition: 50% DOPC, 20% Cholesterol, and 30% DOPS). The membrane of the giant vesicle was labeled with the fluorescent dye DiD. Reprinted and adapted from Bachler et al. [2] with permission from Chemical and Biological Microsystems Society (CBMS).

AMPs interaction with bacterial lipid membranes [9, 31, 32] can be mimicked with GVs. An alternative to the current target-specific antibiotic drugs could be represented by AMPs [9, 31]. AMPs from natural sources have shown promising results as potential antibiotics with a direct mode of action on the membranes of prokaryotic cells and also on some cancer cells [9, 16, 33]. The direct interaction of AMPs with membrane structures makes them less prone to development of bacterial resistance and potentially active against resistant strains as well [9, 34]. For a rational *in silico* peptide design, novel structure-based peptide representations were developed [9]. A descriptor encoded the helical amphiphilicity based on the spatial distribution of hydrophobic patterns and was employed to computationally generate potential AMPs [9]. In a virtual screening, a novel synthetic peptide (Lavracin, WDPYFAGVKKLTKAILAVRA) with potent antimicrobial activity was identified [9]. To further investigate the behavior of this peptide, we studied its activity on individual GVs with diameter between ~10-20 μm on our microfluidic chip [9]. We observed rupture of vesicles after pore formation for Lavracin using fluorescent microscopy. Binding of Lavracin to a vesicle membrane that mimics a bacterial cell led to the growth of membrane pores after the accumulation of peptide on the multilamellar GV surfaces and rupture of the GV within minutes [9]. Figure 2-6 and Figure 2-7 show how vesicles rupture when brought into contact with Lavracin. On top, we saw an influx of calcein after pore formation.

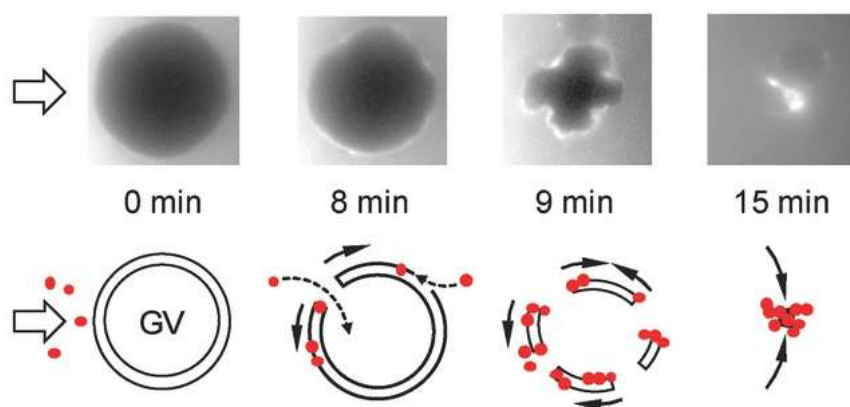


Figure 2-6: Snapshots of a video sequence demonstrating the rupture of a giant vesicle (GV) with a diameter of  $\sim 15 \mu\text{m}$  consisting of a 67% POPE and 33% POPG membrane by  $100 \mu\text{M}$  Lavracin in a microfluidic chamber. The membrane of the GV was labeled with the fluorescent dye DiD. The flow direction of the solution containing Lavracin and  $50 \mu\text{M}$  calcein as a fluorescent dye (red dots) is from left to right (open arrow). Reprinted and adapted from Pillong et al. [9] with permission from Wiley.

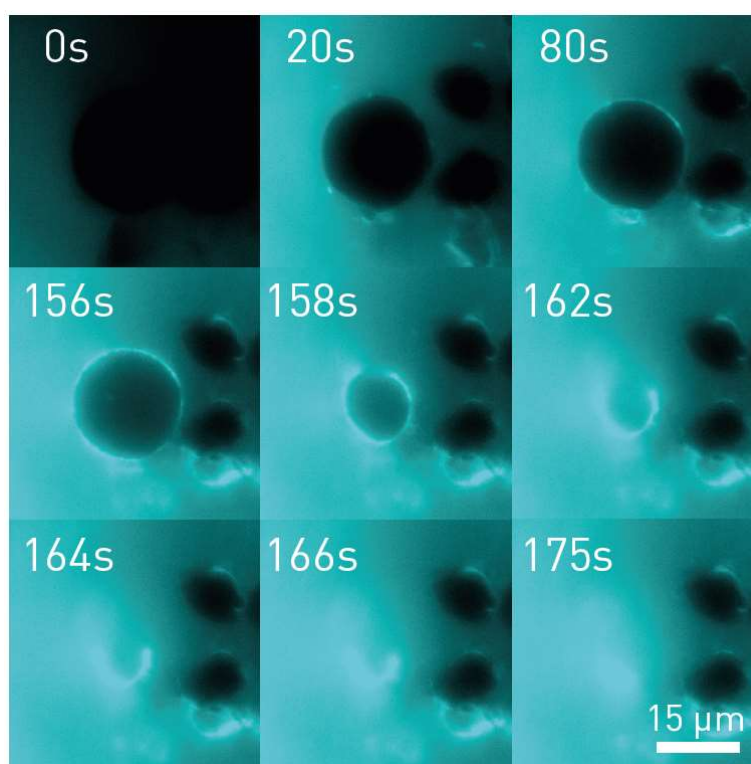


Figure 2-7: Snapshots of a video sequence demonstrating the rupture of a giant vesicle (GV) consisting of a 67% POPE and 33% POPG membrane by  $100 \mu\text{M}$  Lavracin in a microfluidic chamber. The membrane of the GV was labeled with the fluorescent dye DiD. The flow direction of the solution containing Lavracin and  $50 \mu\text{M}$  calcein as a fluorescent dye is from left to right. Reprinted and adapted from Pillong et al. [9] with permission from Wiley.

Another AMP called Peptide 6 (GLFDIVKKVLKLLK) was designed with machine intelligence and investigated in a microfluidic chamber [8]. With this peptide, formation of barrel-stave pores should not be possible (since the alpha-helices of the sequence is too short to span lipid bilayers) [8]. Figure 2-8 shows the GV rupturing process incubated with Peptide 6.

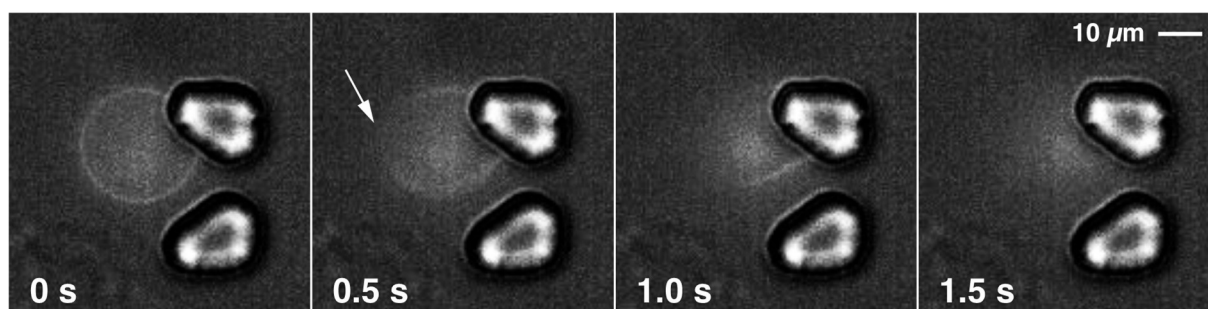


Figure 2-8: Snapshots of a video sequence of a giant vesicle (GV) with a diameter of 20  $\mu\text{m}$  and a membrane composition of 100% POPC [8]. The membrane of the GV was labeled with the fluorescent dye DiD. The microfluidic chip chamber was flushed with 50  $\mu\text{M}$  peptide 6. Reprinted and adapted from Müller et al. [8] with permission from ACS ([pubs.acs.org/doi/10.1021/acs.biochem.0c00565](https://pubs.acs.org/doi/10.1021/acs.biochem.0c00565)).

For the development of anticancer drugs, it is important to achieve a high selectivity with respect to the target cell [18]. ACPs are selectively acting on cancer but not on healthy cells. It is hypothesized that this is due to the differences in the membrane compositions of these cells [18, 35, 36]. Different models exist for the explanation of the membranolytic mechanisms, including the barrel-stave, toroidal, carpet and detergent-like models [16, 18]. For example, some ACPs create transmembrane pores or channels [16, 18]. Based on these models, it is possible to distinguish between active and inactive ACPs with a machine learning classifier to design active anticancer peptides [18, 37].

A computer based approach was used to screen for the selectivity of ACP [18]. One particularly interesting peptide was found with the name P8 (HIKKIRTWYRKAWHVLGKV) and compared with the non-selective peptide P18 (KIFKKFKTIKKVWRIFGRF) [18]. Again, the rupture of GV was investigated in a microfluidic chamber [18]. The selective peptide P8 ruptured the cancer mimicking GVs after  $\sim 56.1$  s (average) and the non-cancer mimicking GVs stayed intact for the observed time (Table 2-1) [18]. On the other hand, the non-selective P18 ruptured both cancer and non-cancer GVs in less than 2 min [18]. Control GVs that were not exposed to these peptide showed no rupturing for the observed time [18]. Examples GVs exposed to these two peptides are shown in Figure 2-9.

Table 2-1: Rupture time of giant vesicles (GVs) exposed to the selective peptide P8 and the non-selective peptide P18. The membrane composition of cancer mimicking GVs was 24% POPS, 14% cholesterol, and 62% POPC; and for non-cancer mimicking GVs 14% cholesterol and 86% POPC. The concentration of the peptides was 100  $\mu\text{M}$  together with 50  $\mu\text{M}$  FITC-dextran. The average rupture time and standard deviation (SD) is listed for the amount of analyzed GVs (N). Reprinted from Gautschi et al. [18] (manuscript in preparation).

GV composition (mol%)			Peptide	Average rupture time	SD	N
POPS	Chol.	POPC				
24	14	62	P8	56.1 s	43.5 s	5
24	14	62	P18	10.9 s	14.9 s	7
24	14	62	-	No rupture observed within 70+ min	-	11
0	14	86	-	No rupture observed within 70+ min	-	11
0	14	86	P8	No rupture observed within 70+ min	-	14
0	14	86	P18	91.3 s	25.9 s	6

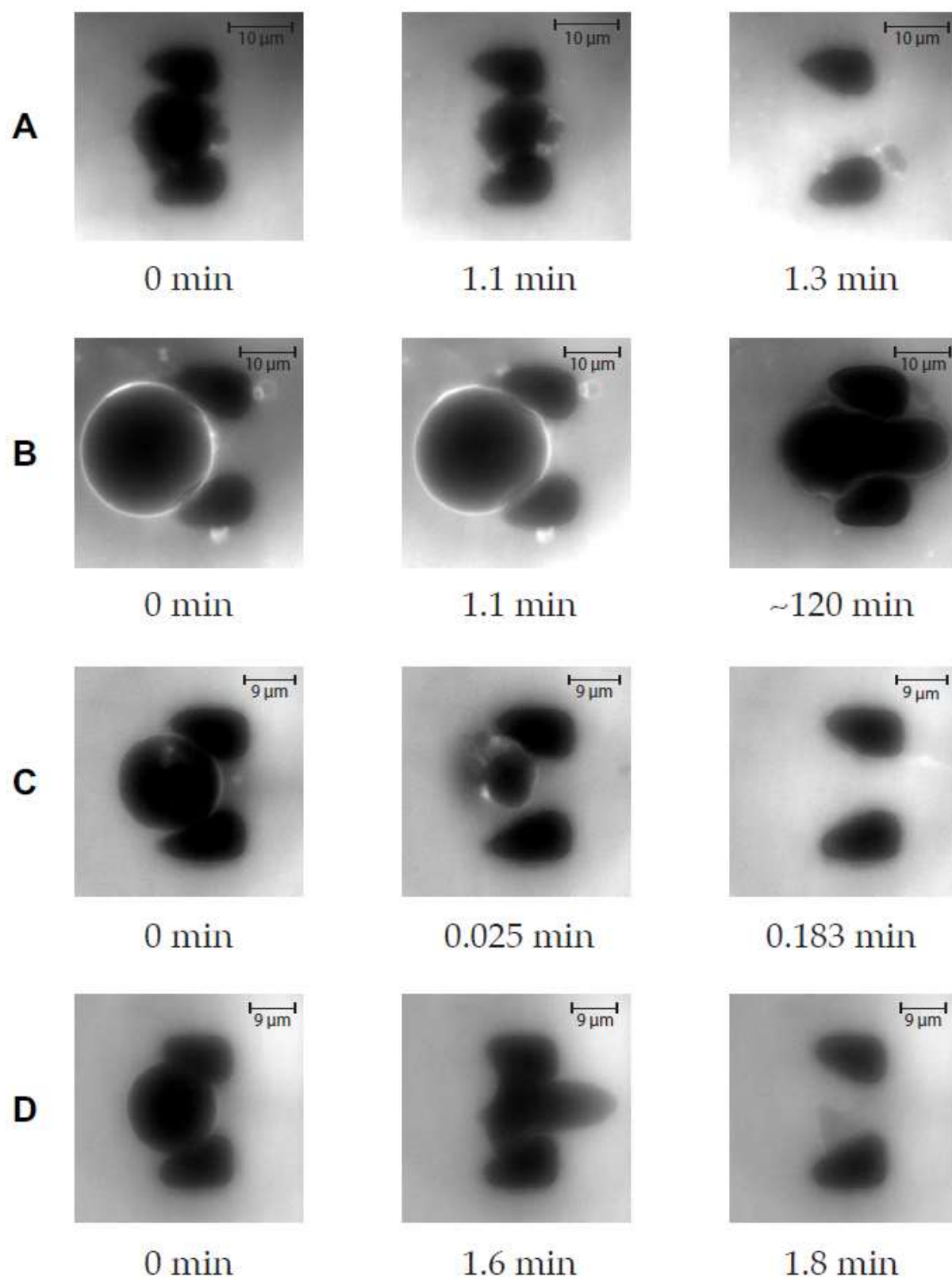


Figure 2-9: Snapshots of video sequences demonstrating the rupture of giant vesicles (GVs) by the peptides P8 and P18. The flow direction of the peptide containing 50  $\mu\text{M}$  FITC-dextran solution was from left to right. The concentration of the peptides was 100  $\mu\text{M}$ . Cancer mimicking GV are shown in A and C (24% POPS, 14% cholesterol, and 62% POPC) and non-cancer mimicking GV in B and D (14% cholesterol and 86% POPC). Selective P8 was added in A and B and non-selective P18 to C and D. Dil was used as membrane stain. Reprinted from Gautschi et al. [18] (manuscript in preparation).

### 2.4.3 Pneumolysin

Cholesterol-dependent cytolysins (like pneumolysin) are secreted as soluble monomers and bind to membranes with a high (local) cholesterol concentrations within [22, 38, 39]. When they oligomerize, inactive pre-pores are formed that eventually undergo a transition to active membrane-perforating pores [22, 38, 40]. We analyzed the binding and pore formation of pneumolysin in GVs trapped in a microfluidic device with confocal microscopy [22]. GVs featuring a high cholesterol concentration within the lipid bilayer showed fast binding and homogenous distribution of PLY in the membrane, pore formation within seconds, and thereafter an influx of FITC-dextran into the vesicle (Figure 2-10) [22, 41]. The homogenous pneumolysin distribution on the membrane was observed during the initial pneumolysin binding phase and persisted after the formation of active pneumolysin pores and perforation of the GV's membrane [22].

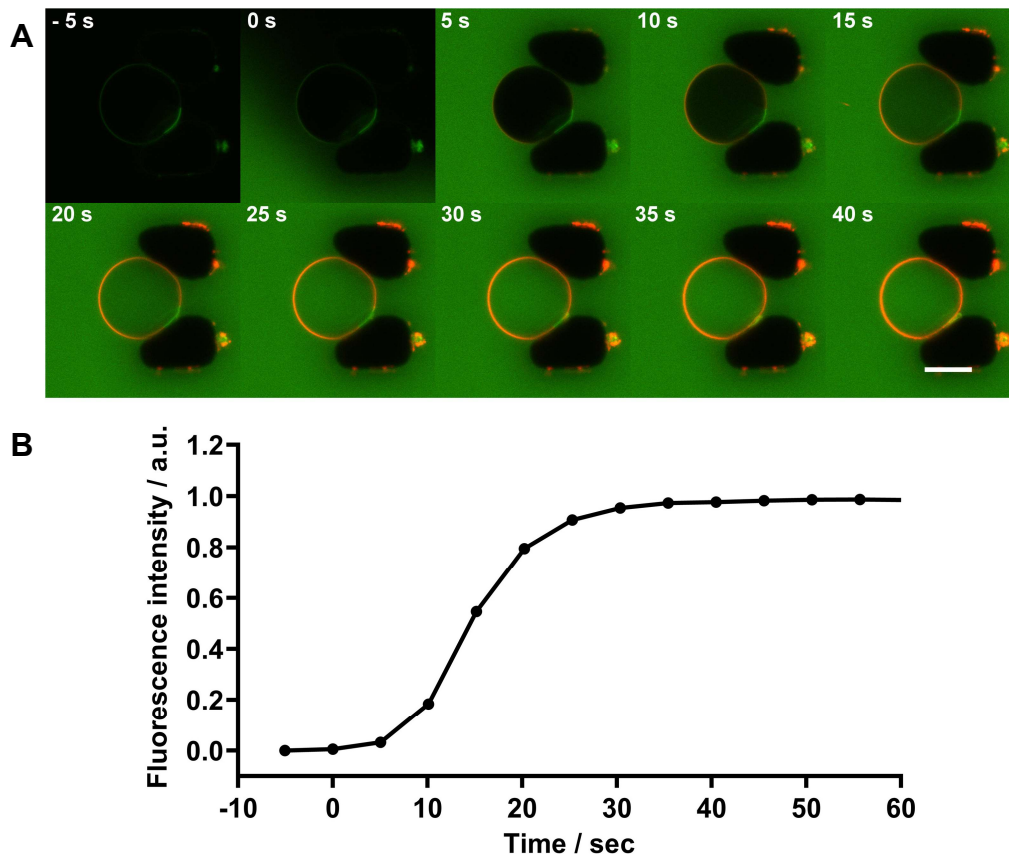


Figure 2-10: Homogeneous binding of pneumolysin (PLY) to a giant vesicle (GV). A) A GV composed of DOPC/cholesterol (50:50) and containing 0.05 mol/% Bodipy-PC was incubated with buffer containing 0.5% (w/v) FITC-dextran and mCherry-PLY (320 nM) in a hydrodynamic trap. Scale bar: 10  $\mu\text{m}$ . B) Changes in FITC-dextran fluorescence intensity in the GV's lumen (normalized to background FITC-dextran intensity),  $N = 4$ . Reprinted and adapted from Drücker et al. [22] with permission from Elsevier.

Furthermore, we found toxin-membrane aggregation that induces membrane wrinkling and membrane surface enlargements during the investigation of the interaction between pneumolysin and the membrane of individual multilamellar giant vesicles in the microfluidic device [42]. An unexpected layer-by-layer peeling resulted from these effects, which revealed the number of lamellae of the GV (Figure 2-11) [42]. It was possible to discriminate between different multilamellar membranes and predict the number of lamellae by employing transmission wide field microscopy (without being restricted by photo bleaching during prolonged observation as commonly seen in fluorescent mode) [42, 43].

Figure 2-12 shows membrane enlargement by binding and perforation of pneumolysin [42]. Some GV occasionally deform and collapse during the interaction of pneumolysin pores with membranes, showing that pneumolysin disintegrated the membrane structure [42]. Formation of many pores and toxin-membrane aggregation probably induced this effect [42]. Sometimes, we observed an increase in size of the GV (Figure 2-12A) [42]. To confirm this observation, we conducted experiments with large unilamellar vesicles (LUVs) and dynamic light scattering (DLS) [42, 44, 45]. We found also an increase of LUV size after incubating the vesicles with pneumolysin (Figure 2-12B/C) [42]. These observations suggest that pneumolysin increases the size of vesicles predominantly by membrane insertion and pore formation and possibly also through aggregation via pores [42].

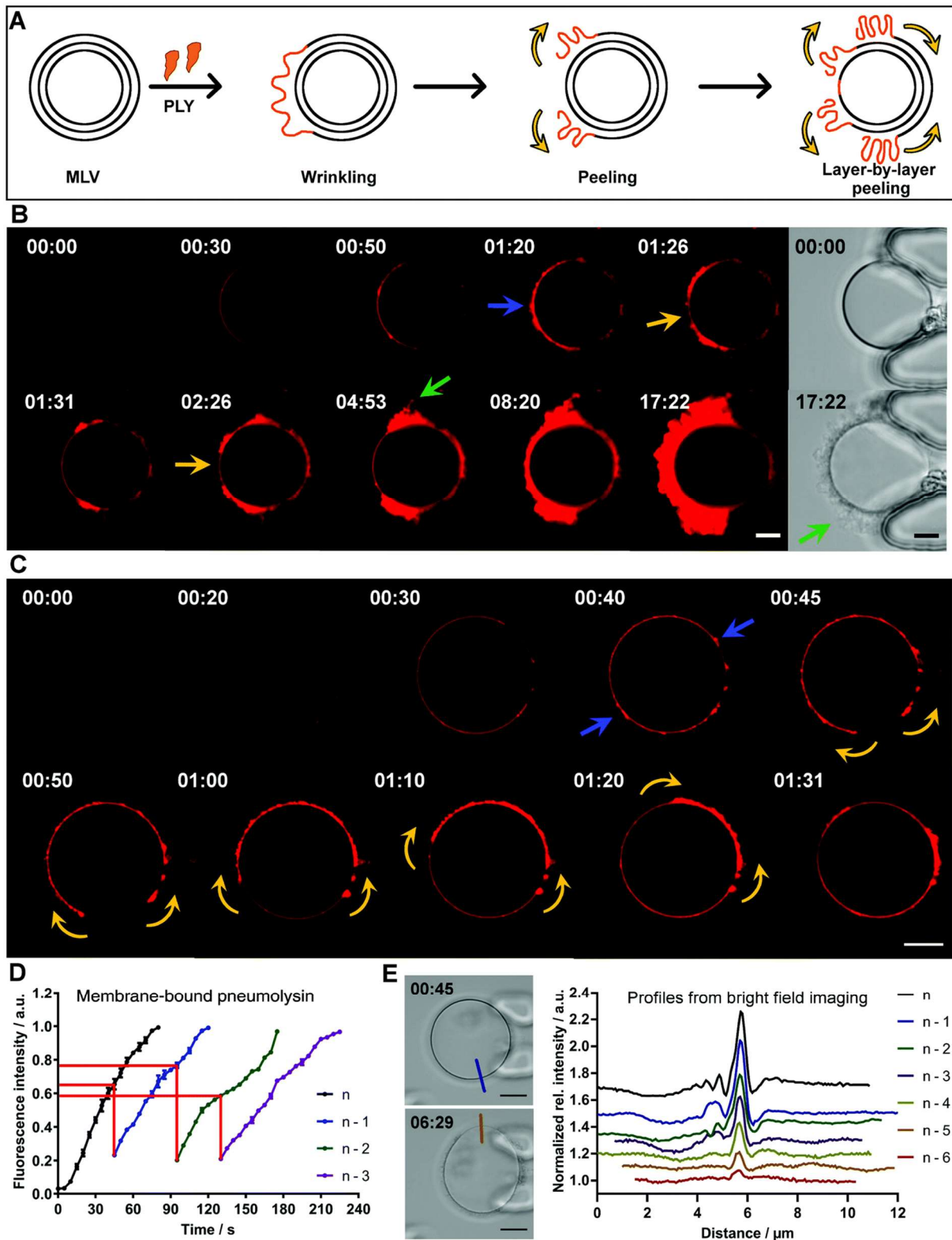


Figure 2-11: Pneumolysin (PLY) induced toxin-membrane aggregation and layer-by-layer peeling of giant vesicles (GVs). A) Schema illustrating pneumolysin-induced membrane wrinkling and layer-by-layer peeling of a multi-lamellar vesicle (MLV). B) A GV of DOPC/cholesterol (50:50) was trapped and incubated with mCherry-PLY (320 nM, red). Pneumolysin binding followed membrane wrinkling and the formation of toxin-membrane aggregates (blue arrow), few layer peelings (rupture of outer layer, yellow arrows), final large surface aggregation (image at 17:22 min), which prevented further peeling and tubule structures (green arrows). Scale bars: 5  $\mu\text{m}$ . The grayscale images are bright-field transmission images. C) A GV of DOPC/cholesterol (50:50) showing layer-by-layer peeling events during mCherry-PLY (320 nM, red) incubation. The movement of the outer membrane layer during one peeling event is indicated by the yellow arrows. The freshly exposed layer showed initial homogeneous pneumolysin binding (00:50). Scale bar: 10  $\mu\text{m}$ . D) The relative fluorescence intensity (FI) of membrane bound mCherry-PLY during initial binding to the outer layer (black), followed by the FI of underlying membranes (blue, green, purple)



after three subsequent peeling events of the GV shown in C. Red lines highlight the relative FI when a layer tears; the outer black layer ruptured at  $\approx 65\%$  FI and revealed a new layer underneath (blue). E) Two bright-field transmission images of the GV shown in C with line profiles measured perpendicular to the membrane rim. The line profiles measured from bright-field transmission images revealed six peeling events starting from the initial multilamellar membrane ( $n$ ) (stacked graph). Scale bar:  $10\ \mu\text{m}$ . Time in mm:ss. The images are representative for  $N = 8$ . Reprinted from Drücker et al. [42] with permission from Royal Society of Chemistry / Creative Commons.

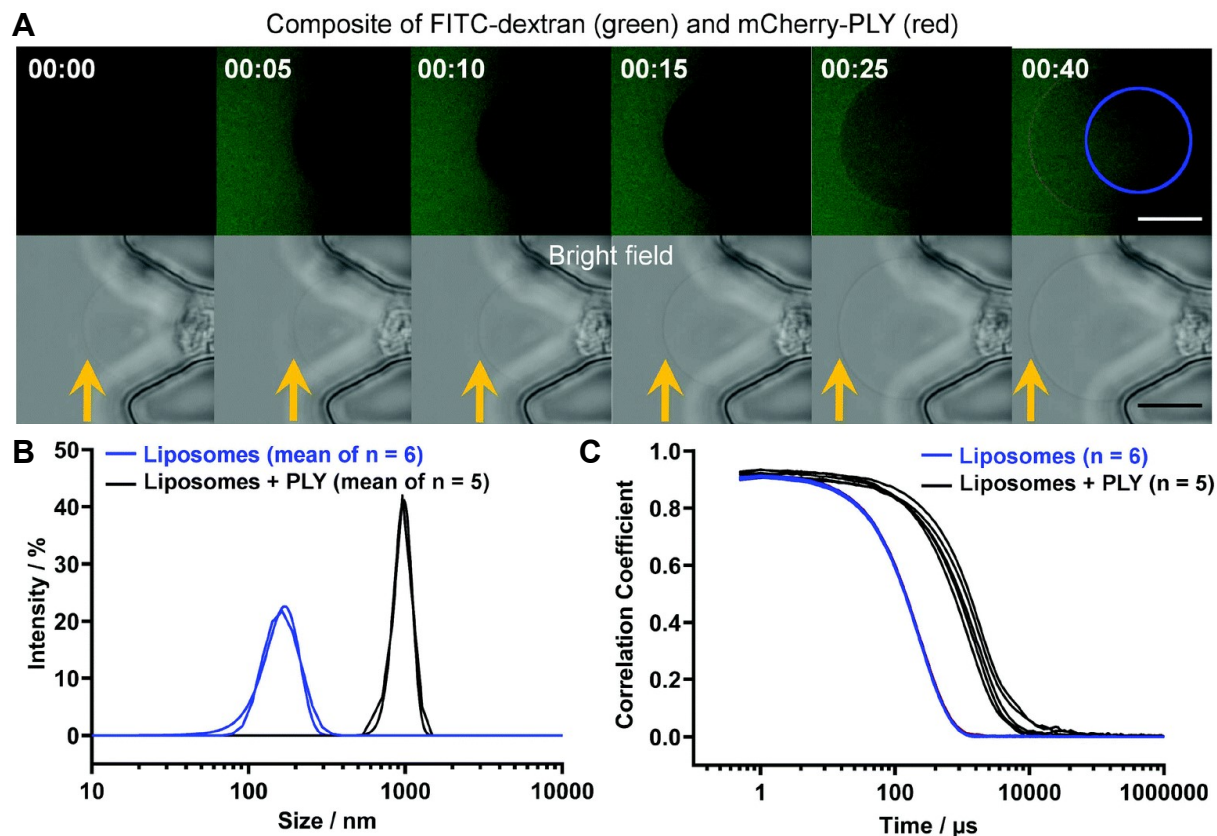


Figure 2-12: Pneumolysin (PLY) induced enlargement of vesicle membranes. A) Enlargement of a giant unilamellar vesicle (GUV) with a membrane composition of DOPC/cholesterol (50:50) and 0.05% Bodipy-PC in response to mCherry-PLY (320 nM, red) incubated in the presence of 0.5 mg/ml FITC-dextran. The blue circle refers to the original GUV size before treatment. Scale bar:  $10\ \mu\text{m}$ . B) Mean size distribution of large unilamellar vesicles (LUVs) with a membrane composition of DOPC/cholesterol (50:50) in phosphate buffered saline (blue) and the same LUVs incubated with 500 nM PLY after 5 min incubation (black), measured by dynamic light scattering (DLS). C) DLS correlation data of all the individual measurements that are summarized in B. Reprinted and adapted from Drücker et al. [42] with permission from Royal Society of Chemistry / Creative Commons.

## 2.5 Conclusion

Our microfluidic trap array has proven to be a valuable platform for drug or toxin testing and can also be used to visualize interactions of molecules with an artificial cell membrane.

The combination of the microfluidic device with FCS enabled translocation measurements of different fluorescently labelled CPPs (as well as other compounds) through the membranes of vesicles. In contrast to routine bulk methods like the parallel artificial membrane permeability assay [46], the measurement times are much shorter (a few minutes compared to several hours). Furthermore, the platform enables the visualization of membranolytic effects and allows to test for active and selective anticancer or antimicrobial peptides. In addition, toxin binding, pore formation, membrane wrinkling, and membrane surface enlargements were observed. Moreover, the lamellarity of multilamellar vesicles can be investigated due to the layer-by-layer peeling effect.

In future, our method will help to investigate new therapeutic peptides and can also be employed as a rapid testing method for cytotoxic, cell-lysing, and pore-forming molecules.

## 2.6 Acknowledgements

Financial funding from the European Research Council (ERC Consolidator Grant No. 681587, HybCell) is gratefully acknowledged. Furthermore, we would like to thank Nikolaus Naredi-Rainer for help with the fluorescence correlation spectroscopy setup and Christoph Bärtschi for constructing the pressure valve control instrument. Moreover, we appreciate the clean room facility FIRST at ETH Zurich.

## 2.7 References

1. Bachler, S., P. Drücker, A.T. Müller, C. Del Don, E.B. Babiychuk, G. Schneider, A. Draeger, and P.S. Dittrich, *Interaction of Toxins and Peptides with Lipid Membranes Studied on a Microfluidic Device*. *Biophysical Journal*, 2018. **114**(3): p. 262a.
2. Bachler, S., C.-C. Lin, and P.S. Dittrich, *Combination of a microfluidic device and fluorescence correlation spectroscopy to study peptide translocation across model membranes*. *Proceedings of the 21st International Conference on Miniaturized Systems for Chemistry and Life Sciences, MicroTAS 2017*, 2017: p. 967-968.
3. Kuhn, P., K. Eyer, T. Robinson, F.I. Schmidt, J. Mercer, and P.S. Dittrich, *A facile protocol for the immobilisation of vesicles, virus particles, bacteria, and yeast cells*. *Integrative Biology*, 2012. **4**(12): p. 1550-1555.
4. Krämer, S.D., D. Lombardi, A. Primorac, A.V. Thomae, and H. Wunderli-Allenspach, *Lipid-Bilayer Permeation of Drug-Like Compounds*. *Chemistry & Biodiversity*, 2009. **6**(11): p. 1900-1916.
5. Saparov, S.M., Y.N. Antonenko, and P. Pohl, *A new model of weak acid permeation through membranes revisited: does Overton still rule?* *Biophysical journal*, 2006. **90**(11): p. L86-L88.
6. Richard, J.P., K. Melikov, E. Vives, C. Ramos, B. Verbeure, M.J. Gait, L.V. Chernomordik, and B. Lebleu, *Cell-penetrating peptides A reevaluation of the mechanism of cellular uptake*. *Journal of Biological Chemistry*, 2003. **278**(1): p. 585-590.
7. Ciobanasu, C., J.P. Siebrasse, and U. Kubitscheck, *Cell-Penetrating HIV1 TAT Peptides Can Generate Pores in Model Membranes*. *Biophysical Journal*, 2010. **99**(1): p. 153-162.
8. Müller, A.T., G. Posselt, G. Gabernet, C. Neuhaus, S. Bachler, M. Blatter, B. Pfeiffer, J.A. Hiss, P.S. Dittrich, K.-H. Altmann, et al., *Morphing of Amphipathic Helices to Explore the Activity and Selectivity of Membranolytic Antimicrobial Peptides*. *Biochemistry*, 2020. **59**(39): p. 3772–3781.
9. Pillong, M., J.A. Hiss, P. Schneider, Y.-C. Lin, G. Posselt, B. Pfeiffer, M. Blatter, A.T. Müller, S. Bachler, C.S. Neuhaus, et al., *Rational Design of Membrane-Pore-Forming Peptides*. *Small*, 2017. **13**(40): p. 1701316.
10. Fjell, C.D., H. Jenssen, K. Hilpert, W.A. Cheung, N. Panté, R.E.W. Hancock, and A. Cherkasov, *Identification of Novel Antibacterial Peptides by Chemoinformatics and Machine Learning*. *Journal of Medicinal Chemistry*, 2009. **52**(7): p. 2006-2015.
11. Lin, Y.-C., J.A. Hiss, P. Schneider, P. Thelesklaf, Y.F. Lim, M. Pillong, F.M. Koehler, P.S. Dittrich, C. Halin, S. Wessler, and G. Schneider, *Piloting the Membranolytic Activities of Peptides with a Self-organizing Map*. *ChemBioChem*, 2014. **15**(15): p. 2225-2231.

12. Xiong, P., M. Wang, X. Zhou, T. Zhang, J. Zhang, Q. Chen, and H. Liu, *Protein design with a comprehensive statistical energy function and boosted by experimental selection for foldability*. Nature Communications, 2014. **5**(1): p. 5330.
13. Mou, Y., J.-Y. Yu, T.M. Wannier, C.-L. Guo, and S.L. Mayo, *Computational design of co-assembling protein–DNA nanowires*. Nature, 2015. **525**(7568): p. 230-233.
14. Zasloff, M., *Antimicrobial peptides of multicellular organisms*. Nature, 2002. **415**(6870): p. 389-395.
15. Fan, L., J. Sun, M. Zhou, J. Zhou, X. Lao, H. Zheng, and H. Xu, *DRAMP: a comprehensive data repository of antimicrobial peptides*. Sci Rep, 2016. **6**: p. 24482.
16. Gabernet, G., A.T. Müller, J.A. Hiss, and G. Schneider, *Membranolytic anticancer peptides*. MedChemComm, 2016. **7**(12): p. 2232-2245.
17. Kosikowska, P. and A. Lesner, *Antimicrobial peptides (AMPs) as drug candidates: a patent review (2003–2015)*. Expert Opinion on Therapeutic Patents, 2016. **26**(6): p. 689-702.
18. Gautschi, D., C.S. Neuhaus, I. Kritikos, S. Bachler, E. Darwish, P.S. Dittrich, and G. Schneider, *Activity and Selectivity Screening of Anticancer Peptides on Cancer Cells and Liposomes*. Manuscript in preparation, 2020.
19. Clark, R.A., I. Olsson, and S.J. Klebanoff, *Cytotoxicity for tumor cells of cationic proteins from human neutrophil granules*. Journal of Cell Biology, 1976. **70**(3): p. 719-723.
20. Sheu, M.J., W.W. Baldwin, and K.W. Brunson, *Cytotoxicity of rabbit macrophage peptides MCP-1 and MCP-2 for mouse tumor cells*. Antimicrobial Agents and Chemotherapy, 1985. **28**(5): p. 626.
21. Lichtenstein, A., T. Ganz, M.E. Selsted, and R.I. Lehrer, *in vitro tumor cell cytolysis mediated by peptide defensins of human and rabbit granulocytes*. Blood, 1986. **68**: p. 1407-1410.
22. Drücker, P., S. Bachler, H. Wolfmeier, R. Schoenauer, R. Köffel, V.S. Babiychuk, P.S. Dittrich, A. Draeger, and E.B. Babiychuk, *Pneumolysin-damaged cells benefit from non-homogeneous toxin binding to cholesterol-rich membrane domains*. Biochimica et Biophysica Acta (BBA) - Molecular and Cell Biology of Lipids, 2018. **1863**(8): p. 795-805.
23. Babiychuk, E.B. and A. Draeger, *Defying death: Cellular survival strategies following plasmalemmal injury by bacterial toxins*. Seminars in Cell & Developmental Biology, 2015. **45**: p. 39-47.
24. Peraro, M.D. and F.G. van der Goot, *Pore-forming toxins: ancient, but never really out of fashion*. Nature Reviews Microbiology, 2016. **14**(2): p. 77-92.
25. Lukyanova, N., B.W. Hoogenboom, and H.R. Saibil, *The membrane attack complex, perforin and cholesterol-dependent cytolysin superfamily of pore-forming proteins*. Journal of Cell Science, 2016. **129**(11): p. 2125.
26. van Pee, K., A. Neuhaus, E. D'Imprima, D.J. Mills, W. Kühlbrandt, and Ö. Yildiz, *CryoEM structures of membrane pore and prepore complex reveal cytolytic mechanism of Pneumolysin*. Elife, 2017. **6**: p. e23644.
27. Marriott, H.M., T.J. Mitchell, and D.H. Dockrell, *Pneumolysin: a double-edged sword during the host-pathogen interaction*. Current molecular medicine, 2008. **8**(6): p. 497-509.
28. Angelova, M.I., S. Soléau, P. Méléard, F. Faucon, and P. Bothorel. *Preparation of giant vesicles by external AC electric fields. Kinetics and applications*. in *Trends in Colloid and Interface Science VI*. 1992. Darmstadt: Steinkopff.
29. Robinson, T., P. Kuhn, K. Eyer, and P. Dittrich, *Microfluidic trapping of giant unilamellar vesicles to study transport through a membrane pore*. Biomicrofluidics, 2013. **7**(4): p. 044105.
30. Lin, C.-C., M. Bachmann, S. Bachler, K. Venkatesan, and P.S. Dittrich, *Tunable Membrane Potential Reconstituted in Giant Vesicles Promotes Permeation of Cationic Peptides at Nanomolar Concentrations*. ACS Applied Materials & Interfaces, 2018. **10**(49): p. 41909-41916.

31. Fjell, C.D., J.A. Hiss, R.E.W. Hancock, and G. Schneider, *Designing antimicrobial peptides: form follows function*. Nature Reviews Drug Discovery, 2012. **11**(1): p. 37-51.
32. Brogden, K.A., *Antimicrobial peptides: pore formers or metabolic inhibitors in bacteria?* Nature Reviews Microbiology, 2005. **3**(3): p. 238-250.
33. da Cunha, N.B., N.B. Cobacho, J.F.C. Viana, L.A. Lima, K.B.O. Sampaio, S.S.M. Dohms, A.C.R. Ferreira, C. de la Fuente-Núñez, F.F. Costa, O.L. Franco, and S.C. Dias, *The next generation of antimicrobial peptides (AMPs) as molecular therapeutic tools for the treatment of diseases with social and economic impacts*. Drug Discovery Today, 2017. **22**(2): p. 234-248.
34. Rios, A.C., C.G. Moutinho, F.C. Pinto, F.S. Del Fiol, A. Jozala, M.V. Chaud, M.M.D.C. Vila, J.A. Teixeira, and V.M. Balcão, *Alternatives to overcoming bacterial resistances: State-of-the-art*. Microbiological Research, 2016. **191**: p. 51-80.
35. Schweizer, F., *Cationic amphiphilic peptides with cancer-selective toxicity*. European Journal of Pharmacology, 2009. **625**(1): p. 190-194.
36. Mader, J.S. and D.W. Hoskin, *Cationic antimicrobial peptides as novel cytotoxic agents for cancer treatment*. Expert Opinion on Investigational Drugs, 2006. **15**(8): p. 933-946.
37. Gabernet, G., D. Gautschi, A.T. Müller, C.S. Neuhaus, L. Armbrecht, P.S. Dittrich, J.A. Hiss, and G. Schneider, *In silico design and optimization of selective membranolytic anticancer peptides*. Scientific Reports, 2019. **9**(1): p. 11282.
38. Tilley, S.J., E.V. Orlova, R.J.C. Gilbert, P.W. Andrew, and H.R. Saibil, *Structural Basis of Pore Formation by the Bacterial Toxin Pneumolysin*. Cell, 2005. **121**(2): p. 247-256.
39. Nöllmann, M., R. Gilbert, T. Mitchell, M. Sferrazza, and O. Byron, *The Role of Cholesterol in the Activity of Pneumolysin, a Bacterial Protein Toxin*. Biophysical Journal, 2004. **86**(5): p. 3141-3151.
40. Gilbert, R.J.C., J. Rossjohn, M.W. Parker, R.K. Tweten, P.J. Morgan, T.J. Mitchell, N. Errington, A.J. Rowe, P.W. Andrew, and O. Byron, *Self-interaction of pneumolysin, the pore-forming protein toxin of Streptococcus pneumoniae* Edited by G. Von Heijne. Journal of Molecular Biology, 1998. **284**(4): p. 1223-1237.
41. Veatch, S.L. and S.L. Keller, *Separation of Liquid Phases in Giant Vesicles of Ternary Mixtures of Phospholipids and Cholesterol*. Biophysical Journal, 2003. **85**(5): p. 3074-3083.
42. Drücker, P., I. Iacovache, S. Bachler, B. Zuber, E.B. Babiyshuk, P.S. Dittrich, and A. Draeger, *Membrane deformation and layer-by-layer peeling of giant vesicles induced by the pore-forming toxin pneumolysin*. Biomaterials Science, 2019. **7**(9): p. 3693-3705.
43. Akashi, K., H. Miyata, H. Itoh, and K. Kinoshita, Jr., *Preparation of giant liposomes in physiological conditions and their characterization under an optical microscope*. Biophys J, 1996. **71**(6): p. 3242-50.
44. Drazenovic, J., H. Wang, K. Roth, J. Zhang, S. Ahmed, Y. Chen, G. Bothun, and S.L. Wunder, *Effect of lamellarity and size on calorimetric phase transitions in single component phosphatidylcholine vesicles*. Biochim Biophys Acta, 2015. **1848**(2): p. 532-43.
45. Kauscher, U., M.C. Stuart, P. Drucker, H.J. Galla, and B.J. Ravoo, *Incorporation of amphiphilic cyclodextrins into liposomes as artificial receptor units*. Langmuir, 2013. **29**(24): p. 7377-83.
46. Faller, B., *Artificial membrane assays to assess permeability*. Current Drug Metabolism, 2008. **9**(9): p. 886-892.

## Chapter 3

# Tailored Translocation and Reaction Cascades in Nanoliter Droplet Networks

**This chapter was adapted from the following paper:**

Bachler, S., D. Haidas, M. Ort, T.A. Duncombe, and P.S. Dittrich. *Microfluidic Platform Enables Tailored Translocation and Reaction Cascades in Nanoliter Droplet Networks*. Communications Biology, 2020. Accepted.

**Author contributions:**

P.S.D. and S.B. designed the work; S.B., D.H., and M.O. developed the spotting platform and the methods; S.B. fabricated the microscopy slides, and performed and analyzed the fluorescence experiments; D.H. and T.A.D. developed the Matlab scripts; S.B., D.H., and T.A.D. performed and analyzed the MS experiments; and S.B. and P.S.D. wrote the manuscript, which all authors approved.

### 3.1 Abstract

In the field of bottom-up synthetic biology, lipid membranes are the scaffold to create minimal cells and mimic reactions and processes at or across the membrane. In this context, we employ here a versatile microfluidic platform that enables precise positioning of nanoliter droplets with user-specified lipid compositions and in a defined pattern. Adjacent droplets make contact and form a droplet interface bilayer to simulate cellular membranes. Translocation of molecules across membranes are tailored by the addition of alpha-hemolysin to selected droplets. Moreover, we developed a protocol to analyze the translocation of non-fluorescent molecules between droplets with mass spectrometry. Our method is capable of automated formation of one- and two-dimensional droplet networks, which we demonstrated by connecting droplets containing different compound and enzyme solutions to perform translocation experiments and a multistep enzymatic cascade reaction across the droplet network. Our platform opens doors for creating complex artificial systems for bottom-up synthetic biology.

## 3.2 Introduction

Liposomes formed by synthetic lipids are widely used to mimic the compartmentalization of cells and create artificial cells. Like organelles in living cells, liposomes can serve as individual chemical reactors, in which biological processes can be performed. Essential compounds are retained in large concentrations, while others diffuse or are transported across the membrane [1-5]. The formation of lipid borders played a crucial role in the origin of life [6, 7] and therefore, liposomes are versatile models of early forms of life, so-called protocells.

One of the key challenges in the creation of artificial cells is the formation of a cell-like architecture, where different biochemical compounds are retained in smaller organelles within the cell and each organelle has a specific biological function. Many pathways require multiple steps in different organelles, translocation of intermediate products between organelles, and signaling cascades to enable the cell to sense the environment or relay information between different cellular regions. In this regard, major achievements were presented recently, reporting the realization of multi-step reactions [4, 5], genetic circuits [8-10], controlled division [11], or communication pathways across membranes [12-14] in artificial cell models.

Several experimental methods were introduced to form and connect multiple compartments. A particularly versatile approach uses water-in-oil emulsions, where a phospholipid monolayer is assembled at the interface between water and oil. Upon contact of two lipid-stabilized droplets, a so-called droplet interface bilayer (DIB) is formed [15-20], allowing for the exchange of compounds from one droplet to the adjacent droplet by diffusion across the lipid bilayer or by translocation through membrane pores, e.g. alpha-hemolysin ( $\alpha$ -HL) [21-25]. Two- and three-dimensional droplet networks and the encapsulation of droplets in droplets were reported to mimic cells and tissue [14, 26, 27]. These methods were greatly improved by the use of microfluidic methods instead of manual preparation and pipetting procedures [28]. Droplet microfluidics enables the formation of monodisperse droplets with precise volumes in the order of cell volumes, i.e., a few nanoliters, as well as efficient encapsulation of compounds and smaller liposomes. Droplets can be created and guided to specific locations where they are immobilized [29-32]. These systems, however, still have several shortcomings, such as the difficulty of supplying further compounds to selected immobilized droplets and the fact that droplets are not accessible for further analytical inspection. Furthermore, most of these closed microfluidic systems are prepared with polydimethylsiloxane (PDMS). Molecules can diffuse into PDMS, resulting in swelling of PDMS when common solvents like hexadecane are used. In addition, loss of analytes or water leads to droplet shrinkage and other instabilities [4, 16, 29, 33].

In this study, we build 1D and 2D networks of biochemical reaction compartments by automated deposition of droplets in close proximity and subsequent fast formation of stable



DIBs on an *open* substrate, i.e. the substrate is not covered by a PDMS-based microfluidic system. The advantage of our method lies in controlling the initial droplet content and exact position on this substrate. Furthermore, we guide the translocation of molecules across selected droplets by the addition of the membrane pore  $\alpha$ -HL. We can therefore selectively route small hydrophilic molecules that are otherwise membrane impermeable via  $\alpha$ -HL pores. Our platform allowed for the creation of a multistep reaction, in which essential enzymes and compounds are initially separated in different compartments. The  $\alpha$ -HL pores are used to connect selected compartments with each other.

Moreover, the use of an *open* platform overcomes additional limitations of commonly used microfluidic methods for DIB formation and analysis. Typically, assays with fluorescently-tagged molecules or fluorogenic assays are required to study diffusion or reactions. Here, we show the detection of translocated molecules across DIB membranes by matrix-assisted laser desorption/ionization mass spectrometry (MALDI-MS), opening the use of the platform to a broad range of applications in the field of artificial cells, bioreactors, and pharmacological studies.

## 3.3 Methods

### 3.3.1 Fabrication of the Microarray Plates with Cavities

A 4-inch borofloat glass wafer was cleaned in an oxygen plasma for 5 min (plasma asher system 200, TePla, Germany). Immediately afterwards, SU-8 3025 negative photoresist (MicroChem, Westborough, MA, USA) was spin-coated to obtain an approximately 35  $\mu\text{m}$  high layer of photoresist (dynamic spread at 500 rpm for 10 s with 100 rpm/s and spin at 2500 rpm for 30 s with 300 rpm/s). Subsequently, after  $\sim$ 3 min at room temperature, the wafer was soft baked at 65  $^{\circ}\text{C}$  for 2 min and 95  $^{\circ}\text{C}$  for 12 min. Following this, we used a mask aligner (MA8BA8-Gen3, SÜSS MicroTec, Garching, Germany) to expose the photoresist to a UV light source through a foil mask with images of the desired cavity arrays (i-line illumination with 270  $\text{mJ}/\text{cm}^2$ ). For the post-exposure bake, we used a ramp from room temperature to 95  $^{\circ}\text{C}$  over 60 min, held at 95  $^{\circ}\text{C}$  for 5 min, and cooled down again to room temperature over 60 min. To form the cavities, we developed the wafer with mr-Dev 600 (micro resist technology GmbH, Berlin, Germany) for 6 min, followed by rinsing with 2-propanol (Technic France, Saint-Denis, France) for another 10 s, and spin-drying. We conducted a hard bake with a ramp over 4 h to 180  $^{\circ}\text{C}$ , incubated at 180  $^{\circ}\text{C}$  for 2 h, and cool down to room temperature over 4 h. Using ramps was important for the post-exposure bake and hard bake to avoid SU-8 detachment and cracks in the resist layer. Finally, the wafer was diced in two 75 mm  $\times$  25 mm microarray plates with cavities (the “droplet deposition sites”). The final microarray plates host 2520 spots (plates for networks) or 1512 spots (plates for droplet pairs) for droplet deposition. To achieve the formation of the DIBs between two droplets, adjacent cavities are positioned at a distance of 310-330  $\mu\text{m}$ .

### 3.3.2 Droplet Spotting Platform and Operation

The microarray plate was placed on a removable temperature-controlled holder with a transparent bottom (quartz microscope slide of 0.5 mm thickness, Electron Microscopy Sciences, Hatfield, PA, USA), which was mounted on a motorized XY stage (HLD117, Prior) of an inverted fluorescence microscope (Olympus IX73). The holder wall prevents oil leakage, which allowed for carrying out the experiments in an oil bath to reduce droplet evaporation [34].

For droplet formation, 1 mL syringes (309628, BD, Heidelberg, Germany) were filled with oil and aqueous solutions, mounted on syringe pumps (Nem-B101-03A, Cetoni, Korbußen, Germany), and connected to a self-made microfluidic T-junction device (material: polycarbonate) using polytetrafluoroethylene (PTFE)-tubing of 250  $\mu\text{m}$  inner diameter (PKM SA, Lyss BE, Switzerland) and polyether ether ketone (PEEK)-connectors (F-120 10-32 PEEK

Fitting and P-659 Female Luer to 10-32 Female; Ercatech AG, Bern BE, Switzerland). The T-junction was coated with 1H,1H,2H,2H-perfluorodecyltrichlorosilane (ABCR-Chemicals, Karlsruhe, Germany) carried by a nitrogen stream for ~20 min to prevent wetting of the channel walls by the aqueous phase and to ensure stable droplet generation. Droplets of several nanoliters were generated in the T-junction by injecting the aqueous phase (flow rate: 0.5  $\mu\text{L}/\text{min}$ ) into the immiscible oil phase (flow rate: 2  $\mu\text{L}/\text{min}$ ), and was monitored by a CCD camera (AD-3713TL, Dino-Lite).

The T-junction diameter is 300  $\mu\text{m}$  that is reduced to 200  $\mu\text{m}$  at the exit and further reduced to 150  $\mu\text{m}$  in the HPFA+ capillary (1933, IDEX Health & Science SA, Glattbrugg ZH, Switzerland), which is used after the T-junction to transport the droplets to the microarray plate. During droplet transit, the phospholipids in the oil aligned along the water/oil-interface and formed a monolayer [17, 35].

The end of the capillary was mounted on a motorized Z stage (M-403.2PD, Physik Instrumente, Karlsruhe, Germany) and positioned just above the microarray plate. A custom-made optical droplet detector positioned shortly before the end of the capillary [36] was used to synchronize droplet, capillary and microarray movement to selectively deposit single droplets per position. The software YouScope (R2018, v2.1.0) controlled all components of the microscope and the capillary for this automated workflow, where we spotted at frequencies of 0.2-0.4 Hz [37].

Before spotting of the droplets, the plate holder was filled with ~4 mL of a 1:1 (v/v) hexadecane/squalane mixture (without phospholipids,  $T = 37\text{ }^\circ\text{C}$ ) and 50  $\mu\text{L}$  water in all four edges to reduce droplet shrinkage. For the experiments over 68 h, twice 100  $\mu\text{L}$  water was added to the plate holder in similar manner after the first and second day. The generated droplets were detected in the capillary holder with an optical droplet detection system consisting of a red light-emitting diode (LED Fiber Optics 660 nm Superbrite Red, IF-E97, Industrial Fiber Optics, Tempe, AZ, USA), a polymeric plastic fiber-optic cable (198412, Conrad Electronic SE, Hirschau, Germany) and a phototransistor (IF-D92, Industrial Fiber Optics). The light from the LED was coupled into the optical fiber and the photodetector attached to the other side of the optical fiber was used to detect changes in the transmittance between the aqueous and the oil phase inside the capillary. The signals were recorded and processed by a real-time data acquisition system (AdWin Gold II, Jäger Computergesteuerte Messtechnik GmbH, Lorsch, Germany). The system allowed for smoothing of the raw data and threshold analysis to differentiate droplets from oil plugs. Signals were collected by a custom-made Matlab-based script (R2017b, MathWorks, Natick, MA, USA) integrated in the control software YouScope. When a droplet was detected, the Z stage raised the capillary 2 mm up, the microscope stage moved the center of the capillary over to the next spot, after which the Z stage lowered the capillary 2 mm downwards. Exceptionally, the up and down movement of the capillary for spotting the letters "ETH" was 0.3 mm. The movement was

performed while an oil plug was exiting the capillary, and the final spotting height was 300  $\mu\text{m}$  above the plate. Typical spotting frequency was 0.2-0.4 Hz. Droplets were spotted precisely on individual cavities with 300  $\mu\text{m}$  diameter and a depth of  $\sim 35$   $\mu\text{m}$ , which we monitored with a second CCD camera (AD-3713TL, Dino-Lite). When two droplets were spotted directly next to each other, the phospholipid monolayers at the droplet surfaces touched each other, and a droplet interface bilayer formed.

### 3.3.3 Lipid Solution Preparation

We used the lipid-out approach by adding phospholipids to the interface from the oil phase. 1,2-diphytanoyl-sn-glycero-3-phosphocholine (DPhPC, Avanti Polar Lipids, Alabaster, AL, USA) was purchased as a solution in chloroform. We transferred the appropriate amount of lipid solution into a pear-shaped flask and removed the solvent with a rotary evaporator (Büchi Labortechnik AG, Flawil, Switzerland). The remaining lipid film was dissolved in hexadecane (Reagent plus grade, Sigma-Aldrich) and squalane (Sigma-Aldrich) (1:1 (v/v)), if not stated otherwise, while being agitated by an ultrasonication bath at 50 °C for  $\sim 30$  min. The final phospholipid concentration in oil was 0.5-5 mg/mL. Before use, the oil solution with phospholipids was filtrated (0.45  $\mu\text{m}$  pore size, RC 4 Male Luer Slip Minisart filters, Huberlab, Switzerland).

### 3.3.4 Assays

All aqueous solutions were prepared in ultrahigh-purity water (Barnstead GenPure Pro, Thermo Scientific, Niederelbert, Germany), if not stated otherwise. The osmolarity of all solutions for donor and acceptor droplets were matched and verified with an Osmomat 3000 (gonotec, Berlin, Germany).

Calcium translocation experiments were carried out with 1 M calcium chloride dihydrate ( $\text{CaCl}_2$ , Sigma-Aldrich), 100 U/mL alpha-hemolysin from *Staphylococcus aureus* (Sigma-Aldrich), 20  $\mu\text{M}$  ethylenediaminetetraacetic acid (EDTA, Titriplex II, Merck, Darmstadt, Germany), and 10 mM 4-(2-hydroxyethyl)-1-piperazineethanesulfonic acid (HEPES, pH 7.4, gibco, Paisley, UK) in the donor droplet. We used 1.5 M potassium chloride (KCl, Reagent plus grade, Sigma-Aldrich), 100 U/mL  $\alpha$ -HL, 10  $\mu\text{M}$  Fluo-4 pentapotassium salt (Life Technologies, Eugene, OR, USA), 200  $\mu\text{M}$  EDTA, 10 mM HEPES in the acceptor droplets. For this experiment, we used 100% hexadecane without squalane to dissolve the lipids, but hexadecane/squalane in a 1:1 mixture as oil bath identical to all other experiments. No  $\alpha$ -HL was used for the negative control.

We spotted the letters “ETH” with droplets consisting of 10  $\mu$ M fluorescein isothiocyanate-dextran (FITC-dextran, 70 kDa, Sigma-Aldrich) in phosphate buffered saline (PBS, pH 7.4, gibco, Paisley, UK).

For the 4-fluoro-7-nitrobenzofurazan (NBD-F) translocation experiments, we used acceptor droplets with 0, 320, 640, or 960 U/mL  $\alpha$ -HL. The donor droplets consisted of 0.3 mM NBD-F (Sigma-Aldrich, Switzerland). To test if there was a difference whether the  $\alpha$ -HL pore was inserted from the donor or acceptor droplet side, we used 0.3 mM NBD-F in combination with 640 U/mL  $\alpha$ -HL in the donor, 640 U/mL  $\alpha$ -HL in the acceptor, or 320 U/mL  $\alpha$ -HL in both acceptor and donor droplet. All droplets in the experiments with NBD-F were filled with 10 mM HEPES and 5% dimethyl sulfoxide (DMSO, Sigma-Aldrich).

The riboflavin, Alexa488, and FITC-dextran translocation experiments were conducted with 10 mM HEPES with 0, 320, 640, or 960 U/mL  $\alpha$ -HL as acceptor droplets. For the donor droplets, we used 10 mM HEPES in combination with 60  $\mu$ M riboflavin (Sigma-Aldrich), Alexa Fluor 488 carboxylic acid (Alexa488, Life Technologies), or FITC-dextran.

For the label-free measurements, the following solutions were dissolved in LC-MS grade water (Fisher Scientific, Loughborough, UK). We used 20 mM HEPES in all acceptor droplets with 0 or 400 U/mL  $\alpha$ -HL. The donor droplets consisted of 10 mM HEPES and 10 mM L-arginine (BioUltra grade, Sigma-Aldrich) or 10 mM HEPES and 10 mM L-histidine (Reagent plus grade, Sigma-Aldrich), or 20 mM HEPES and 200  $\mu$ M riboflavin.

All solutions for the enzyme cascade assays were matched to  $\sim$ 300 mOsmol/kg with potassium chloride. We incubated 10 U/mL  $\beta$ -galactosidase (lactase) from *Escherichia coli* (Sigma-Aldrich) together with 50 mM lactose monohydrate (Hänseler, Herisau, Switzerland), and 60 mOsmol/kg PBS overnight. The spotted lactase droplets had a final concentration of 5 U/mL lactase, 25 mM lactose monohydrate (converted), 10 mM tris(hydroxymethyl)aminomethane (tris, pH 9, VWR Life Science), 400 U/mL  $\alpha$ -HL, and 30 mOsmol/kg PBS. The glucose oxidase (GOx) droplets consisted of 5 U/mL GOx from *Aspergillus niger* (Sigma-Aldrich), 10 mM tris, and 30 mOsmol/kg PBS. The luminol droplets consisted of 4 mM luminol (TCI, Tokyo, Japan), 10 mM tris, and 30 mOsmol/kg PBS. For the negative controls no  $\alpha$ -HL or no lactase were used.

### 3.3.5 Imaging

After droplet spotting, bright-field and fluorescence pictures were recorded using a light source (TH4-200, Olympus and Lumen 300, Prior) and a CMOS camera (Zyla 4.2, Andor) connected to the Olympus IX73 microscope. To fluorescently track luminol, a UV-excitation filter set (exciter BP H 365/12, dichroic BS DCLP 395, and emitter 397 LP H; Delta optical thin film,

Hørsholm, Denmark) was used. For FITC-Dextran, Fluo-4, NBD-F, riboflavin, and Alexa488 a blue excitation filter set (exciter HQ470/40x, dichroic 500dcxr BS, and emitter E515lpv2; Chroma Technology Corp, Bellows Falls, VT, USA) was used. A black anodized lid was placed on top of the plate holder for the fluorescence pictures to minimize environmental influences and heat exchange.

### 3.3.6 Data Evaluation and Statistical Information

The recorded fluorescence signals were evaluated using Fiji [38] and a custom Matlab script, and Prism (8.3.0, GraphPad). For the normalized fluorescence intensity values, 100% was the starting fluorescence of the individual donor droplets in the first image. We only normalized to the starting fluorescence and did not account for droplet shrinkage (except SI Figure 3-S3B). The background fluorescence was subtracted for data evaluation. For the translocation experiments analysis with NBD-F, riboflavin, Alexa488, and FITC-dextran, we selected the first 27 droplet networks. Droplets that did not touch each other in a network on the first image were excluded. We used the Grubbs' test (extreme studentized deviate method) to determine whether the most extreme value in the list was a significant outlier from the rest ( $\alpha = 0.05$ , two-tailed, Outlier calculator, QuickCalcs, GraphPad).

### 3.3.7 Droplet Separation and Extraction

For spotting experiments with subsequent MALDI-MS analysis, the droplet pairs were separated and extracted using a custom-made YouScope script. The capillary was flushed with hexadecane/squalane (1:1) and positioned 1300  $\mu\text{m}$  above the plate. The center of the capillary was placed between the two connecting droplets directly over the droplet interface bilayer. To separate two adjacent droplets, the capillary was moved in Z direction to 50  $\mu\text{m}$  above the plate. When this position was reached, the capillary moved 150-170  $\mu\text{m}$  in the desired Y direction to push one droplet into a neighboring cavity. Thereafter, the capillary was raised to the original level of 1300  $\mu\text{m}$  above the plate. We introduced several waiting steps between the different moves to prevent the droplets from sliding back together.

After separating all desired droplet pairs, we flushed the capillary with fluorinated oil (HFE-7500, 3M Novec, Hadfield, UK) and connected it to a 50  $\mu\text{L}$  glass syringe (Hamilton, Switzerland). The center of the capillary was positioned directly over the center of the droplet and lowered to 150-250  $\mu\text{m}$  above the plate to squeeze the droplet. The droplet was aspirated by slowly pulling the glass syringe. As soon as the droplet was aspirated, the capillary was raised above the oil level to minimize the hexadecane/squalane aspiration as much as possible. Afterwards, the capillary was moved over a ground steel BC MALDI target plate

(Bruker Daltonik GmbH, Bremen, Germany) and the aspirated droplet was ejected on a spot. The MALDI target plate was heated to 120 °C for 5 min to induce water/solvent evaporation.

### 3.3.8 MALDI-MS

We added 0.2  $\mu\text{L}$  of 20 mg/mL 2,5-dihydroxybenzoic acid (DHB, Sigma-Aldrich) in 70% LC-MS grade water with 0.1% trifluoroacetic acid (Acros Organics) and 30% acetonitrile (VWR) to the individual spots on a ground steel MALDI target plate. Mass spectra were acquired from 140  $m/z$  to 460  $m/z$  using a Bruker rapifleX MALDI-TOF/TOF in positive reflector mode (Bruker Daltonik GmbH). Each mass spectrum consisted of 1000 shots performed in a 10  $\mu\text{m}$  square region using a 10 kHz laser repetition frequency. Mass spectra were baseline subtracted and calibrated to DHB matrix ions with the mMass software tool [39]. For comparisons between donor and acceptor droplets, intensity values were normalized to the internal standard peak of HEPES (239.1  $m/z$ ). The detected and theoretical monoisotopic peaks are compared in Table 3-S1 for analytes L-histidine, L-arginine, HEPES, and riboflavin. All detected analyte peaks had an  $m/z$  error of less than 0.025.

### 3.3.9 Alpha-Hemolysin Structure

The  $\alpha$ -HL structure was obtained from the Protein Data Bank (rcsb.org) [40, 41] and visualized with Jmol (an open-source Java viewer for chemical structures in 3D. jmol.org).

## 3.4 Results

### 3.4.1 Generation of Droplet Interface Bilayer Networks

Aqueous droplets of ~25 nanoliters were generated in hexadecane/squalane with dissolved lipids (by a microfluidic T-junction, Figures 3-1A and 3-1B). The lipids self-assemble and form a lipid monolayer at the water oil interface during the transfer in the capillary [17, 35]. The droplets were deposited with micrometer-precision on an SU-8 coated microscopy glass slide with cavities in close proximity. A predefined pattern can be spotted on the glass slide. Contact between adjacent aqueous droplets united the lipid monolayers and created a lipid bilayer membrane, which was visible through the microscope.

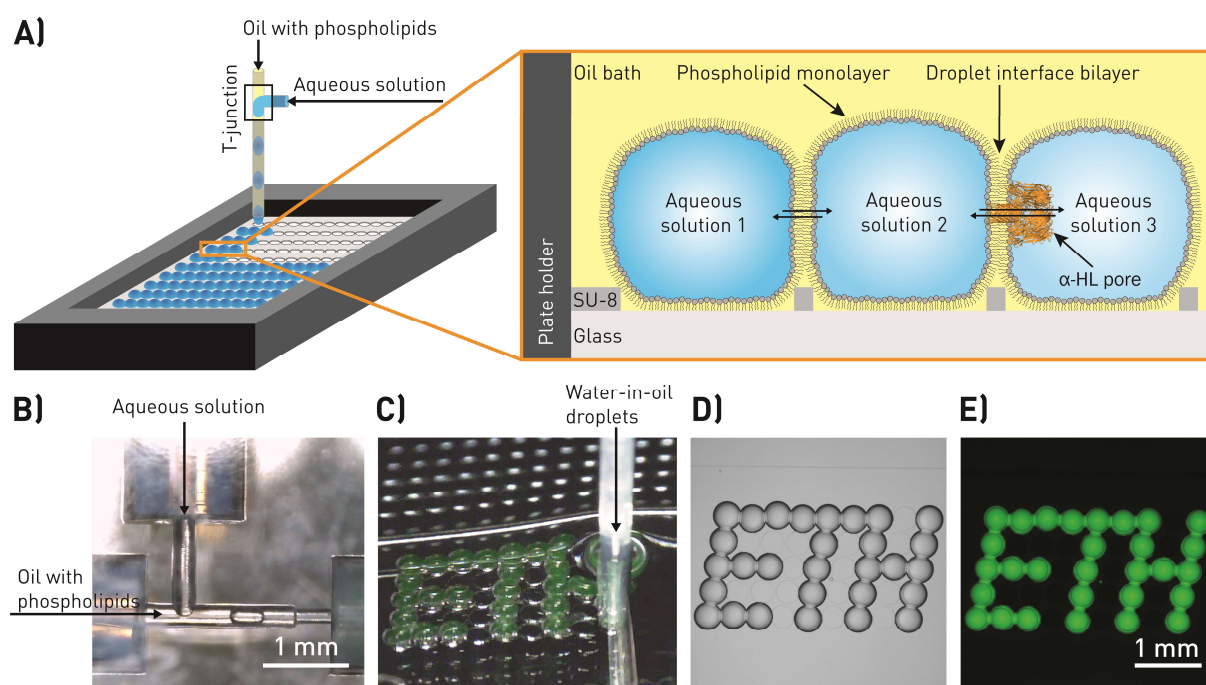


**Figure 3-1:** Concept of the microfluidic platform for artificial cell generation. **A)** Schematics of droplet spotting and formation of the droplet interface bilayer (not to scale). Left: Nanoliter droplets are formed in a microfluidic T-junction from an aqueous solution and oil with phospholipids. Thereafter, the droplets are transferred via a capillary and spotted on a glass plate with individual rows of cavities in close proximity. Phospholipids are present in the oil phase and self-assemble at the droplet interface while transitioning the capillary. Right: The spotted droplets are connected via a droplet interface bilayer. With our spotting platform, we can vary the content of the droplet next to each other and form droplet networks, here designated with aqueous solution 1-3. In addition, the pore forming toxin alpha-hemolysin ( $\alpha$ -HL) can be selectively added to allow exchange of small water-soluble molecules between droplets. The  $\alpha$ -HL structure was obtained from the Protein Data Bank ([rcsb.org](http://rcsb.org)) [41]. **B)** Photograph of the T-junction for droplet formation. **C)** Spotting of 10  $\mu$ M FITC dextran in PBS droplets. **D)** Bright-field image of the droplets spotted in Fig. 3-1C. **E)** Fluorescent image of the droplets spotted in Fig. 3-1C.

The bilayer was fully formed after approximately one minute at 37 °C. In this manner, droplets could be spotted in pairs, rows, and any other type of 2D pattern, as exemplified by the letters “ETH” in Figures 3-1C to E (and SI Video 3-S1).



It should be noted that a mixture of hexadecane and squalane was used due to the long hydrocarbon length of these molecules, which improves the formation of a thin, oil-free DIB as reported also in former studies [29, 42, 43]. Moreover, the high stability of the DIB facilitated long-term experiments for at least 68 hours.

### 3.4.2 Pores in Droplet Interface Bilayer Networks

Next, we proved the formation of unilamellar DIBs by incorporation of  $\alpha$ -HL.  $\alpha$ -HL forms a transmembrane heptameric pore with a diameter of the channel between 1.4-2.4 nm in a lipid bilayer [41, 44-47]. The pore formation facilitates the translocation of small molecules and ions such as  $\text{Ca}^{2+}$ . It is general accepted that DIB membranes that host transmembrane toxins or proteins are virtually “oil-free” membrane structures similar to vesicles [47, 48]. No translocation would be observed for multilamellar membranes since the toxin pore can only span a single lipid bilayer of physiologically relevant size. In a unilamellar lipid bilayer, on the other hand, the pore will create a passage for small molecules, which can then diffuse from one droplet into another along their concentration gradient [49]. Here, we show the reproducible formation of pores by using a row of eight droplets, each of them containing  $\alpha$ -HL. Seven (acceptor) droplets were deposited, which contained Fluo-4 that forms a fluorescent complex with  $\text{Ca}^{2+}$  (Figure 3-2). Last, a donor droplet with  $\text{Ca}^{2+}$  was placed at one end of the row. Upon diffusion of calcium through the pore, we can observe the increase of fluorescence intensity in the first droplet within 12-15 minutes and delayed in the following droplets (Figure 3-2 and SI Video 3-S2). In all droplets we found a characteristic two-phase time course. First, a rapid increase of fluorescence intensity where calcium ion influx results in the formation of the fluorescent complex was observed. Once the  $\text{Ca}^{2+}$  ions reach the next DIB and translocate into the next droplet, this efflux decreases the net influx and the fluorescence increase is slowed down. However, the same plateau height for all acceptor droplets was not reached after 22.5 hours, which is both a consequence of the slow diffusion and the influence of osmolarity in the adjacent compartments. Although we carefully adjusted osmolarity in all droplets, the donor droplet volume increased over time, while acceptor droplets are visibly smaller. We believe this is due to the binding of calcium to Fluo-4 or EDTA in the acceptor droplets, which led to small changes (reduction) of the osmolarity, thereby promoting water permeation towards the donor droplet. At the same time, we did not observe Fluo-4 (731.60 Da) translocation towards the donor droplet for 100 U/mL  $\alpha$ -HL. Calcium translocation does not occur without  $\alpha$ -HL (SI Figure 3-S1) and droplet volumes were constant in this negative control. Higher  $\alpha$ -HL concentrations of 500 U/mL (added in every droplet) resulted in droplet coalescence when also Fluo-4, EDTA, and  $\text{Ca}^{2+}$  were present. The high  $\alpha$ -HL concentration and the osmolarity changes destabilized the DIB.

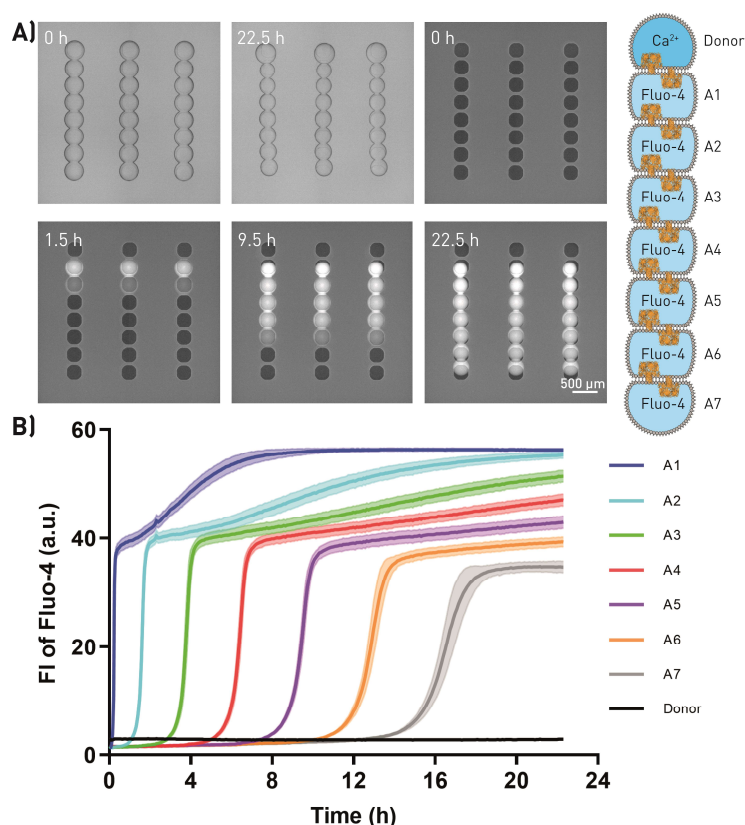


Figure 3-2: Translocation of  $\text{Ca}^{2+}$  across alpha-hemolysin ( $\alpha$ -HL) pores in a droplet network. A) Bright-field (top left and top middle) and fluorescent images of  $\text{Ca}^{2+}$  translocation across  $\alpha$ -HL pores over multiple compartments. The top droplets are filled with  $\text{Ca}^{2+}$ . The other seven acceptor droplets (A1-A7) in each row are filled with Fluo-4 pentapotassium salt, which is a membrane-impermeant calcium indicator. B) Mean fluorescence intensity (FI) over time along the droplet network. Data were collected every  $\sim 5$  min,  $N = 16$  droplet networks. The error bands represent the standard deviation.

After the successful translocation of calcium, we investigated the influence of pore direction, i.e., we supplied  $\alpha$ -HL either in the donor or in the acceptor droplet. For this experiment, we spotted two droplets. The donor droplet contained the small hydrophobic fluorescent molecule NBD-F (mass of 183.10 Da). Either the donor or the acceptor additionally contained  $\alpha$ -HL (640 U/mL), or both droplets contained  $\alpha$ -HL at a concentration of 320 U/mL. Fluorescence intensity was monitored in both droplets over time, as shown in Figure 3-3A and 3B. No difference in translocation velocity was observed for the same amount of  $\alpha$ -HL in the bilayer membrane. Increasing the  $\alpha$ -HL concentration accelerated the translocation as more pores were formed (Figure 3-3C). An equilibrium was reached with 960 U/mL  $\alpha$ -HL for NBD-F after  $\sim 12$  h. In all experiments with NBD-F, DMSO was added to the aqueous droplet to avoid leakage of NBD-F into the oil [50]. NBD-F also permeates slowly across the membrane when no  $\alpha$ -HL was present (Figure 3-S2).

Next, we tested the translocation of riboflavin with a mass of 376.37 Da (Figure 3-3D) and Alexa488 with a mass of 531.44 Da (Figure 3-3E) to demonstrate the dependence of the translocation process on molecule size and  $\alpha$ -HL concentrations. An equilibrium was reached

with 960 U/mL  $\alpha$ -HL for riboflavin after  $\sim$ 18 h and for Alexa488 after  $\sim$ 48 h, as defined by the donor and acceptor droplets having equal fluorescence intensities.

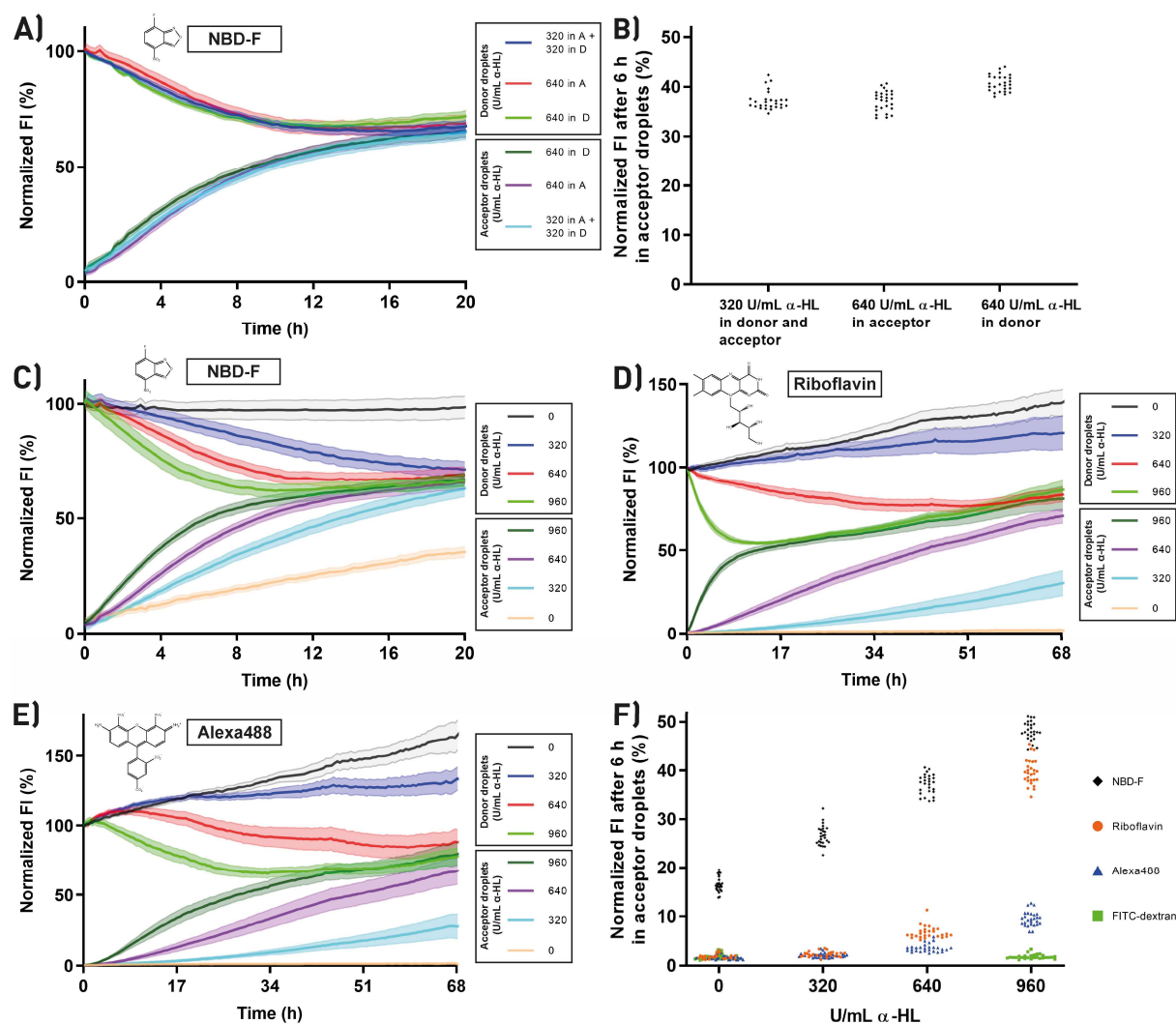


Figure 3-3: Translocation of NBD-F, riboflavin, and Alexa488 across alpha-hemolysin ( $\alpha$ -HL) pores. A) Mean fluorescence intensity (FI) over time of 300  $\mu$ M NBD-F translocation across  $\alpha$ -HL pores from donor (D) to acceptor (A) droplets. Comparison of 640 U/mL  $\alpha$ -HL in acceptor, 640 U/mL  $\alpha$ -HL in donor, or 320 U/mL  $\alpha$ -HL in acceptor and donor droplets. Data were collected every  $\sim$ 15 min,  $N = 27$  droplet networks for every curve. B) Mean FI of NBD-F after 6 hours in the acceptor droplets. C-E) Mean FI over time for translocation of the fluorophores NBD-F (300  $\mu$ M, C), riboflavin (60  $\mu$ M, D) and Alexa488 (60  $\mu$ M, E) at different concentrations of  $\alpha$ -HL. Here, the numbers in the labels refer to the  $\alpha$ -HL in the acceptor droplets, no  $\alpha$ -HL was added to the donor droplets.  $N = 27$  droplet networks for every curve. F) Mean FI of 300  $\mu$ M NBD-F, 60  $\mu$ M riboflavin, 60  $\mu$ M Alexa488, and 60  $\mu$ M FITC-dextran (0 and 960 U/ml  $\alpha$ -HL) after 6 hours in the acceptor droplets. The continuous increase in the normalized FI in the experiments can be attributed to slow droplet shrinkage over time. We only normalized to the starting fluorescence of the individual donor droplets and did not account for droplet shrinkage in the data normalization process. The error bands represent the standard deviation in all figures.

The continuous increase in fluorescence intensity in these experiments can be attributed to slow, but continuous droplet shrinkage, and therefore an increase in local fluorophore concentration over time. We observed very slow droplet shrinkage over time in all experiments, which was only clearly visible for experiments over 2-3 days. For example, for the

Alexa488-filled droplets in Figure 3-3E, the diameter decreased down to ~70 % of the original diameter within 68 hours (SI Figure 3-S3A).

For a large molecule like FITC-dextran (~70 kDa), no translocation across  $\alpha$ -HL pores (960 U/mL) was observed within 68 h (Figure 3-S4). Since we did not observe translocation of FITC-dextran through the pore with the diameter of 1.4-2.4 nm, we would also not expect translocation of other large molecules like proteins across  $\alpha$ -HL pores in our system. Figure 3-3F compares the fluorescence intensity of NBD-F, riboflavin, Alexa488, and FITC-dextran after 6 hours in the acceptor droplets. In addition, we calculated the translocation rates (SI Table 3-S2), which confirmed the fastest rate for NBD-F at the highest  $\alpha$ -HL concentration ( $180.9 \times 10^{-3}/h$ ), compared to the rates for riboflavin ( $137.0 \times 10^{-3}/h$ ) and Alexa488 ( $38.3 \times 10^{-3}/h$ ).

### 3.4.3 Label-Free Molecule Detection in Droplet Interface Bilayer Networks

Monitoring of processes at and across DIBs is frequently conducted by means of fluorescence methods, using fluorescently-labeled compounds or by the implementation of fluorogenic assays. With the aim of overcoming this limitation, we developed a protocol to interface our platform with MALDI-MS for label-free detection of translocation across the DIB (Figure 3-4A). Droplets were spotted, incubated to allow translocation, separated, and extracted for final measurements by MALDI-MS. Central in this process is the step to separate droplets, which we successfully realized by placing the capillary between the two connected droplets. This initiated the movement of the droplet to the next hydrophilic cavity (Figure 3-4B), from where it could be extracted by the capillary and transferred to the MALDI plate. After the addition of the matrix, we could analyze the content of the dried droplet. Riboflavin and HEPES were detected by MALDI-MS in the acceptor droplet when  $\alpha$ -HL was present (Figure 3-4C). In the acceptor droplet without  $\alpha$ -HL, only HEPES was detected. Therefore, the riboflavin translocation across the  $\alpha$ -HL pore was confirmed with MALDI-MS in addition to fluorescence microscopy (Figure 3-3D). This MALDI-MS readout approach opens the possibility to probe the translocation of non-fluorescent compounds. In the supplementary information, we included the results for the label-free translocation of L-arginine (SI Figure 3-S5) and L-histidine (SI Figure 3-S6) across  $\alpha$ -HL pores.

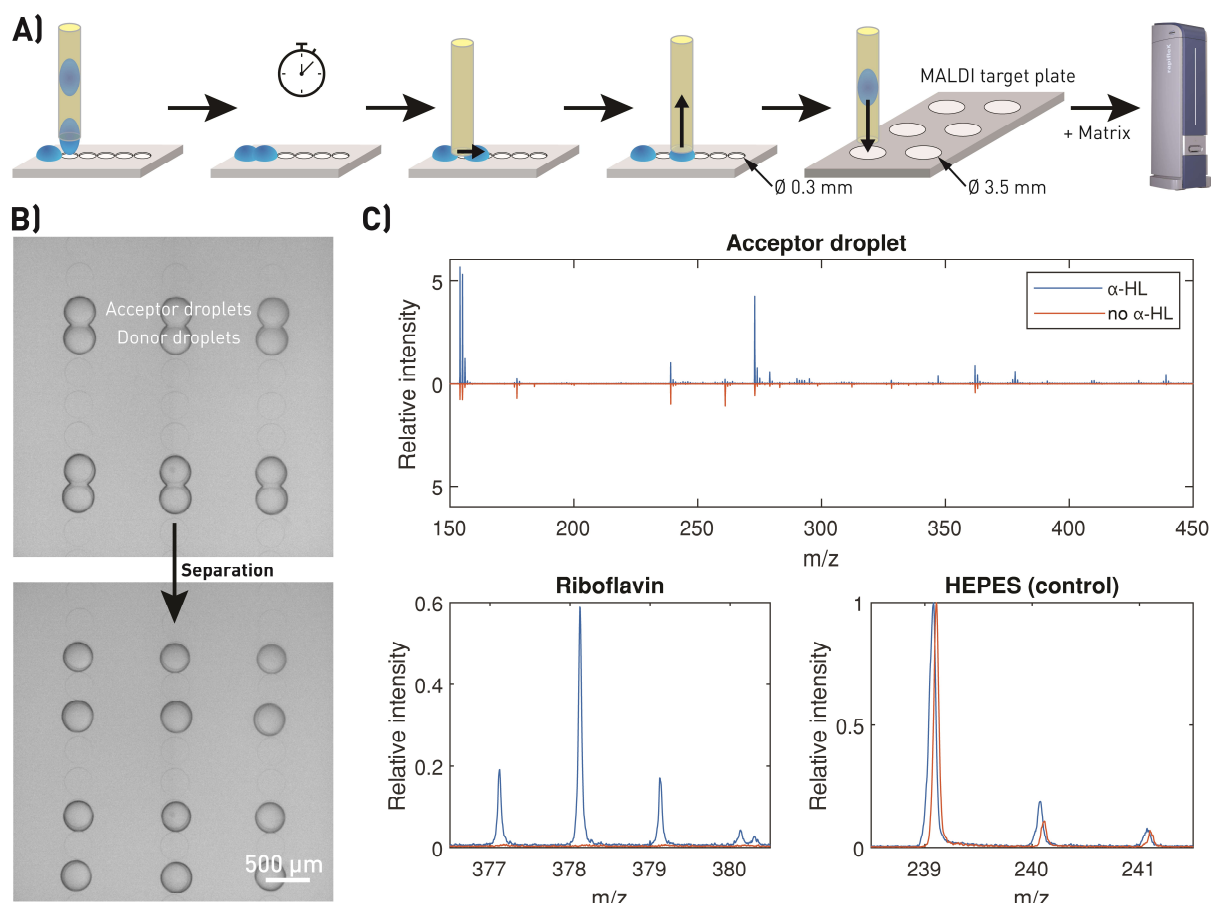


**Figure 3-4:** Label-free detection of translocation across alpha-hemolysin ( $\alpha$ -HL) pores with mass spectrometry. A) Scheme of droplet separation and extraction for MALDI-MS analysis (not to scale). From left to right: Droplet spotting; Incubation step for allowing translocation; Droplet separation; Droplet aspiration; Placing the droplet on a stainless-steel MALDI target plate; MALDI-MS analysis after matrix (DHB) deposition. B) Droplets connected by a droplet interface bilayer (top) and droplet pairs after separation (bottom). C) MALDI-MS analysis of acceptor droplets, where the donor droplet contained riboflavin (377.1 m/z) and the acceptor droplet contained  $\alpha$ -HL (blue) or not (orange, here flipped for better visualization). Data are shown for  $N = 1$  droplet network. In addition, we pooled  $N = 5$  droplet networks and received a similar result (data not shown). The isotopic pattern for riboflavin [53] and HEPES, again with (blue) and without (orange) addition of  $\alpha$ -HL. Each spectrum is normalized to the intensity of the internal control HEPES (239.1 m/z).

### 3.4.4 Cascade Reaction in Droplet Networks

Finally, we demonstrate with our droplet networks a compartmentalized enzymatic cascade reaction, where each droplet of the network contains different compounds and enzymes (Figure 3-5A). The final conversion of luminol to the fluorescent product 3-aminophthalic acid occurred in the central droplet. Luminol was stored in an adjacent droplet, from where it permeated across the DIB. The reaction requires hydrogen peroxide, which was formed during the conversion of glucose to gluconolactone by glucose oxidase. Glucose translocated via  $\alpha$ -HL from the adjacent droplet, where it was formed from lactose in the presence of  $\beta$ -galactosidase (lactase).

Once all droplets were spotted and the DIBs were formed, the reactions proceeded and the fluorescent product became detectable. The product immediately translocates via the  $\alpha$ -HL pore into the adjacent droplet, therefore we observed a rapid increase of fluorescence intensity

in these two droplets (Figure 3-5B, 3-5C, and SI Video 3-S3). The fluorescence intensity increased slowly in the original droplet with luminol due to the passive permeation of the product. Without  $\alpha$ -HL or lactase the fluorescence increase was not observed (SI Figures 3-S7 and 3-S8) confirming that all steps of the reaction cascade are required to obtain the fluorescent product.

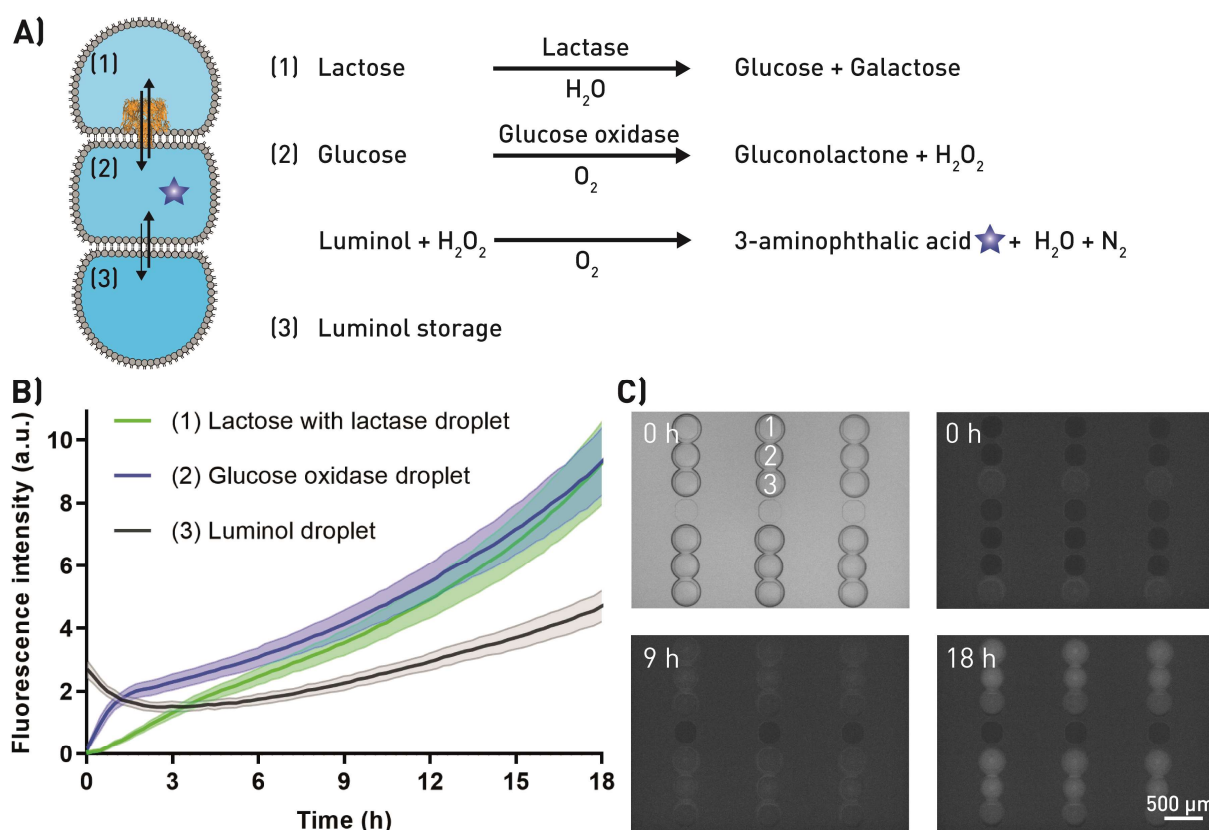


Figure 3-5: Compartmentalized enzymatic cascade reaction. A) Sketch of the three-step reaction (not to scale). Lactase hydrolyses lactose to glucose and galactose (1). Small molecules i.e. glucose translocate across alpha-hemolysin ( $\alpha$ -HL) pores to the next droplet (2), where glucose oxidase catalyzes the oxidation of glucose to hydrogen peroxide and gluconolactone. Luminol permeates from an adjacent droplet (3) into the other ones. Upon contact with hydrogen peroxide, luminol forms the highly fluorescent molecule 3-aminophthalic acid. B) Mean fluorescence intensity of the reaction in Fig. 3-5A/C in dependency of the time. Data were collected every  $\sim 15$  min,  $N = 30$  droplet networks. The lactose/lactase droplet (1) was added to the glucose oxidase droplet (2)  $\sim 80$  min before the luminol droplet (3). The imaging starting point was directly after spotting of the luminol droplet. The error bands represent the standard deviation. C) Bright-field (top left) and fluorescent images of the reaction in Fig. 3-5A/B. Lactose and lactase with  $\alpha$ -HL in the top droplet (1). Glucose oxidase in the middle droplet (2). Luminol in the bottom droplet (3).

### 3.5 Discussion

We present a platform of tailored 1D or 2D networks of nanoliter droplet microreactors interconnected by DIBs as an analytical model for studying multi-compartmental artificial cells. Arrayed droplets function as discretized reactors containing select reagents. Deliberate selection of membrane composition and functional transport units at the droplet-droplet interface enables the control of chemical communication throughout the droplet network. Monitored by real-time fluorescence microscopy and endpoint MALDI-MS, our interconnected droplet networks offers a powerful tool for researchers studying interactions of molecules with lipid membranes such as permeation and pore formation. DIBs are stable over days, and the droplets shrink very slowly within days. This is a strong improvement for long-term studies compared to DIBs created in PDMS devices, where droplets must be stabilized by coating of the PDMS walls or the addition of on-chip water reservoirs to prevent diffusion of the aqueous droplet content into the PDMS [4, 51, 52].

The current size of the droplets can be reduced to sizes of mammalian cells (15-20  $\mu\text{m}$ ) by creating droplets with other methods than the used T-junction. Also the spotting plate is easily scalable to provide smaller droplet deposition sites (theoretically down the resolution of photolithography, i.e.  $\sim 1\text{-}2\ \mu\text{m}$ ), or to increase the number of deposited droplet pairs and networks up to several hundred thousand. In principle, we can spot arbitrary arrays of networks; however, the number of droplets with different content is limited in the current system as we have to change the supplied fluids in the syringes manually.

In our study, we insert the membrane pore  $\alpha\text{-HL}$  to enable the transfer of small water-soluble molecules between two adjacent droplets. By adding  $\alpha\text{-HL}$  to specific droplets we can selectively route small hydrophilic molecules across lipid membranes while translocation is restricted without  $\alpha\text{-HL}$ .

Our complex droplet networks are directly generated with precision spotting on an *open* substrate. In addition to the ease of addressing individual droplets with spotting, the open array allows us to interface the platform with other analytical techniques such as mass spectrometry. This greatly increases the possibilities for detection of molecules in DIBs compared to fluorescence microscopy and closed microfluidic systems. Further, we are able to stop translocation and disrupt the DIBs by separating droplets, a feature that is not possible with more common techniques for studying DIBs. This could be exploited to stop supplies to the adjacent droplet e.g. for an enzymatic reaction.

We demonstrated the versatility of our platform by the creation of a cascade reaction, in which reactants and enzymes are initially separated in different compartments. We used  $\alpha\text{-HL}$  pores selectively to tailor the multi-step reaction for allowing passage of glucose and no pores were

## Chapter 3

inserted in the other membrane to create a barrier for molecules, which are impermeable or very slowly permeating.

The presented droplet networks simulate chemical communication across a long network of researcher-designed microreactors and membranes. This is well suited for conducting multistep reactions, in which each droplet contains different essential compounds or enzymes. Moreover, we demonstrate that the content analysis of droplets can be achieved by mass spectrometry, allowing for the multiplexed analysis of unknown and/or unlabeled compounds. We believe this opens the door for experiments with DIBs, where fluorescence labelling is not possible or not preferred. In the future, the platform can be employed for other membrane studies, e.g., it facilitates transporter or permeation studies as required for drug discovery and drug testing with asymmetric membranes. Our platform could mimic a simple cell / organelle model such as a mitochondria membrane in a cell, or artificial cell clusters or tissue.



## 3.6 Acknowledgements

Funding from the European Research Council (ERC Consolidator Grant No. 681587, HybCell) and Swiss National Science Foundation (NCCR Molecular Systems Engineering) is gratefully acknowledged. We highly appreciate contributions from Christoph Bärtschi, Christian Marro, Paul Argast, and Peter Buchmann (mechanical workshop, ETH Zurich) for the fabrication of the spotting device parts. Furthermore, we would like to thank Alexander Stettler, Albert Martel, and Peter Rimpf (clean room facility, ETH Zurich) for support in the cleanroom processes, Chao-Chen Lin for help with the optical setup, and Stefanie D. Krämer for providing the fitting functions. Finally, we thank Darius Rackus for proofreading.

## 3.7 References

1. Luisi, P.L. and P. Stano, *Minimal cell mimicry*. Nature Chemistry, 2011. **3**(10): p. 755-756.
2. Buddingh', B.C. and J.C.M. van Hest, *Artificial Cells: Synthetic Compartments with Life-like Functionality and Adaptivity*. Accounts of Chemical Research, 2017. **50**(4): p. 769-777.
3. Noireaux, V. and A. Libchaber, *A vesicle bioreactor as a step toward an artificial cell assembly*. Proceedings of the National Academy of Sciences of the United States of America, 2004. **101**(51): p. 17669-17674.
4. Nuti, N., P.E. Verboket, and P.S. Dittrich, *Multivesicular droplets: a cell model system to study compartmentalised biochemical reactions*. Lab on a Chip, 2017. **17**(18): p. 3112-3119.
5. Elani, Y., R.V. Law, and O. Ces, *Vesicle-based artificial cells as chemical microreactors with spatially segregated reaction pathways*. Nature Communications, 2014. **5**: p. 5305.
6. Szostak, J.W., D.P. Bartel, and P.L. Luisi, *Synthesizing life*. Nature, 2001. **409**: p. 387-390.
7. Walde, P., *Building artificial cells and protocell models: experimental approaches with lipid vesicles*. Bioessays, 2010. **32**(4): p. 296-303.
8. Adamala, K.P., D.A. Martin-Alarcon, K.R. Guthrie-Honea, and E.S. Boyden, *Engineering genetic circuit interactions within and between synthetic minimal cells*. Nature Chemistry, 2016. **9**: p. 431-439.
9. Dupin, A. and F.C. Simmel, *Signalling and differentiation in emulsion-based multi-compartmentalized in vitro gene circuits*. Nature Chemistry, 2019. **11**(1): p. 32-39.
10. Peng, R., L. Xu, H. Wang, Y. Lyu, D. Wang, C. Bi, C. Cui, C. Fan, Q. Liu, X. Zhang, and W. Tan, *DNA-based artificial molecular signaling system that mimics basic elements of reception and response*. Nature Communications, 2020. **11**(1): p. 978.
11. Steinkühler, J., R.L. Knorr, Z. Zhao, T. Bhatia, S.M. Bartelt, S. Wegner, R. Dimova, and R. Lipowsky, *Controlled division of cell-sized vesicles by low densities of membrane-bound proteins*. Nature Communications, 2020. **11**(1): p. 905.
12. Gardner, P.M., K. Winzer, and B.G. Davis, *Sugar synthesis in a protocellular model leads to a cell signalling response in bacteria*. Nature Chemistry, 2009. **1**: p. 377-383.
13. Villar, G., A.J. Heron, and H. Bayley, *Formation of droplet networks that function in aqueous environments*. Nature Nanotechnology, 2011. **6**: p. 803-808.
14. Booth, M.J., V.R. Schild, A.D. Graham, S.N. Olof, and H. Bayley, *Light-activated communication in synthetic tissues*. Science Advances, 2016. **2**(4): p. e1600056.

15. Challita, E.J., J.S. Najem, R. Monroe, D.J. Leo, and E.C. Freeman, *Encapsulating Networks of Droplet Interface Bilayers in a Thermoreversible Organogel*. Scientific Reports, 2018. **8**(1): p. 6494.
16. Malmstadt, N., M.A. Nash, R.F. Purnell, and J.J. Schmidt, *Automated Formation of Lipid-Bilayer Membranes in a Microfluidic Device*. Nano Letters, 2006. **6**(9): p. 1961-1965.
17. Leptihn, S., O.K. Castell, B. Cronin, E.-H. Lee, L.C.M. Gross, D.P. Marshall, J.R. Thompson, M. Holden, and M.I. Wallace, *Constructing droplet interface bilayers from the contact of aqueous droplets in oil*. Nature Protocols, 2013. **8**: p. 1048-1057.
18. Holden, M.A., D. Needham, and H. Bayley, *Functional Bionetworks from Nanoliter Water Droplets*. Journal of the American Chemical Society, 2007. **129**(27): p. 8650-8655.
19. Fischer, A., M.A. Holden, B.L. Pentelute, and R.J. Collier, *Ultrasensitive detection of protein translocated through toxin pores in droplet-interface bilayers*. Proceedings of the National Academy of Sciences of the United States of America, 2011. **108**(40): p. 16577-16581.
20. Dixit, S.S., H. Kim, A. Vasilyev, A. Eid, and G.W. Faris, *Light-Driven Formation and Rupture of Droplet Bilayers*. Langmuir, 2010. **26**(9): p. 6193-6200.
21. Hwang, W.L., M.A. Holden, S. White, and H. Bayley, *Electrical Behavior of Droplet Interface Bilayer Networks: Experimental Analysis and Modeling*. Journal of the American Chemical Society, 2007. **129**(38): p. 11854-11864.
22. Maglia, G., A.J. Heron, W.L. Hwang, M.A. Holden, E. Mikhailova, Q. Li, S. Cheley, and H. Bayley, *Droplet networks with incorporated protein diodes show collective properties*. Nature Nanotechnology, 2009. **4**: p. 437-440.
23. Elfaramawy, M.A., S. Fujii, A. Uyeda, T. Osaki, S. Takeuchi, Y. Kato, H. Watanabe, and T. Matsuura, *Quantitative analysis of cell-free synthesized membrane proteins at the stabilized droplet interface bilayer*. Chemical Communications, 2018. **54**(86): p. 12226-12229.
24. Funakoshi, K., H. Suzuki, and S. Takeuchi, *Lipid bilayer formation by contacting monolayers in a microfluidic device for membrane protein analysis*. Analytical Chemistry, 2006. **78**(24): p. 8169-8174.
25. Baxani, D.K., A.J. Morgan, W.D. Jamieson, C.J. Allender, D.A. Barrow, and O.K. Castell, *Bilayer Networks within a Hydrogel Shell: A Robust Chassis for Artificial Cells and a Platform for Membrane Studies*. Angewandte Chemie International Edition, 2016. **55**(46): p. 14240-14245.
26. Villar, G., A.D. Graham, and H. Bayley, *A Tissue-Like Printed Material*. Science, 2013. **340**(6128): p. 48-52.
27. Wauer, T., H. Gerlach, S. Mantri, J. Hill, H. Bayley, and K.T. Sapa, *Construction and Manipulation of Functional Three-Dimensional Droplet Networks*. ACS Nano, 2014. **8**(1): p. 771-779.
28. Deng, N.-N., M. Yelleswarapu, L. Zheng, and W.T.S. Huck, *Microfluidic Assembly of Monodisperse Vesosomes as Artificial Cell Models*. Journal of the American Chemical Society, 2017. **139**(2): p. 587-590.
29. Schlicht, B. and M. Zagnoni, *Droplet-interface-bilayer assays in microfluidic passive networks*. Scientific Reports, 2015. **5**: p. 9951-9951.
30. Taylor, G., M.-A. Nguyen, S. Koner, E. Freeman, C.P. Collier, and S.A. Sarles, *Electrophysiological interrogation of asymmetric droplet interface bilayers reveals surface-bound alamethicin induces lipid flip-flop*. Biochimica et Biophysica Acta (BBA) - Biomembranes, 2019. **1861**(1): p. 335-343.
31. Czekalska, M.A., T.S. Kaminski, K. Makuch, and P. Garstecki, *Passive and parallel microfluidic formation of droplet interface bilayers (DIBs) for measurement of leakage of small molecules through artificial phospholipid membranes*. Sensors and Actuators B: Chemical, 2019. **286**: p. 258-265.
32. Nisisako, T., S.A. Portonovo, and J.J. Schmidt, *Microfluidic passive permeability assay using nanoliter droplet interface lipid bilayers*. Analyst, 2013. **138**(22): p. 6793-6800.

33. Dangla, R., F. Gallaire, and C.N. Baroud, *Microchannel deformations due to solvent-induced PDMS swelling*. Lab on a Chip, 2010. **10**(21): p. 2972-2978.
34. Haidas, D., S. Bachler, M. Köhler, L.M. Blank, R. Zenobi, and P.S. Dittrich, *Microfluidic Platform for Multimodal Analysis of Enzyme Secretion in Nanoliter Droplet Arrays*. Analytical Chemistry, 2019. **91**(3): p. 2066-2073.
35. Venkatesan, G.A., J. Lee, A.B. Farimani, M. Heiranian, C.P. Collier, N.R. Aluru, and S.A. Sarles, *Adsorption Kinetics Dictate Monolayer Self-Assembly for Both Lipid-In and Lipid-Out Approaches to Droplet Interface Bilayer Formation*. Langmuir, 2015. **31**(47): p. 12883-12893.
36. Küster, S.K., S.R. Fagerer, P.E. Verboket, K. Eyer, K. Jefimovs, R. Zenobi, and P.S. Dittrich, *Interfacing Droplet Microfluidics with Matrix-Assisted Laser Desorption/Ionization Mass Spectrometry: Label-Free Content Analysis of Single Droplets*. Analytical Chemistry, 2013. **85**(3): p. 1285-1289.
37. Lang, M., F. Rudolf, and J. Stelling, *Use of YouScope to Implement Systematic Microscopy Protocols*. Current Protocols in Molecular Biology, 2012. **98**(1): p. 14.21.1-14.21.23.
38. Schindelin, J., I. Arganda-Carreras, E. Frise, V. Kaynig, M. Longair, T. Pietzsch, S. Preibisch, C. Rueden, S. Saalfeld, B. Schmid, et al., *Fiji: an open-source platform for biological-image analysis*. Nature Methods, 2012. **9**: p. 676-682.
39. Strohmalm, M., M. Hassman, B. Košata, and M. Kodíček, *mMass data miner: an open source alternative for mass spectrometric data analysis*. Rapid Communications in Mass Spectrometry, 2008. **22**(6): p. 905-908.
40. Berman, H.M., J. Westbrook, Z. Feng, G. Gilliland, T.N. Bhat, H. Weissig, I.N. Shindyalov, and P.E. Bourne, *The Protein Data Bank*. Nucleic Acids Research, 2000. **28**(1): p. 235-242.
41. Song, L., M.R. Hobaugh, C. Shustak, S. Cheley, H. Bayley, and J.E. Gouaux, *Structure of staphylococcal alpha-hemolysin, a heptameric transmembrane pore*. Science, 1996. **274**(5294): p. 1859-66.
42. Gross, L.C., A.J. Heron, S.C. Baca, and M.I. Wallace, *Determining membrane capacitance by dynamic control of droplet interface bilayer area*. Langmuir, 2011. **27**(23): p. 14335-42.
43. McGlone, M., A. Armetta, T. Osaki, S. Takeuchi, and S. Lee, *Characterization of monoolein bilayer thickness using specific membrane capacitance*. Proceedings of The 21st International Conference on Miniaturized Systems for Chemistry and Life Sciences, MicroTAS 2017, 2017: p. 985-986.
44. Schuster, B., D. Pum, O. Braha, H. Bayley, and U.B. Sleytr, *Self-assembled  $\alpha$ -hemolysin pores in an S-layer-supported lipid bilayer*. Biochimica et Biophysica Acta (BBA) - Biomembranes, 1998. **1370**(2): p. 280-288.
45. Gouaux, J.E., O. Braha, M.R. Hobaugh, L. Song, S. Cheley, C. Shustak, and H. Bayley, *Subunit stoichiometry of staphylococcal alpha-hemolysin in crystals and on membranes: a heptameric transmembrane pore*. Proceedings of the National Academy of Sciences, 1994. **91**(26): p. 12828.
46. Gouaux, E.,  *$\alpha$ -Hemolysin from Staphylococcus aureus: An Archetype of  $\beta$ -Barrel, Channel-Forming Toxins*. Journal of Structural Biology, 1998. **121**(2): p. 110-122.
47. Deshpande, S., Y. Caspi, A.E.C. Meijering, and C. Dekker, *Octanol-assisted liposome assembly on chip*. Nature Communications, 2016. **7**: p. 10447.
48. Trantidou, T., M.S. Friddin, A. Salehi-Reyhani, O. Ces, and Y. Elani, *Droplet microfluidics for the construction of compartmentalised model membranes*. Lab on a Chip, 2018. **18**(17): p. 2488-2509.
49. Göpfrich, K., B. Haller, O. Staufer, Y. Dreher, U. Mersdorf, I. Platzman, and J.P. Spatz, *One-Pot Assembly of Complex Giant Unilamellar Vesicle-Based Synthetic Cells*. ACS Synthetic Biology, 2019. **8**(5): p. 937-947.
50. Lee, Y. and S.Q. Choi, *Quantitative analysis for lipophilic drug transport through a model lipid membrane with membrane retention*. European Journal of Pharmaceutical Sciences, 2019. **134**: p. 176-184.

## Chapter 3

51. Akhtar, M., S. van den Driesche, A. Bödecker, and M.J. Vellekoop, *Long-term storage of droplets on a chip by Parylene AF4 coating of channels*. Sensors and Actuators B: Chemical, 2018. **255**: p. 3576-3584.
52. Shim, J.U., G. Cristobal, D.R. Link, T. Thorsen, Y. Jia, K. Piattelli, and S. Fraden, *Control and measurement of the phase behavior of aqueous solutions using microfluidics*. Journal of the American Chemical Society, 2007. **129**(28): p. 8825-35.
53. Zhang, S., L. Ding, S. Li, X. Kong, and Y. Huang, *Use of graphene as a matrix to minimize reduction in the process of matrix-assisted laser desorption/ionization*. Rapid Communications in Mass Spectrometry, 2013. **27**(11): p. 1278-1282.

## 3.8 Supplementary Information

### 3.8.1 Pores in Droplet Interface Bilayer Networks (Negative) Controls

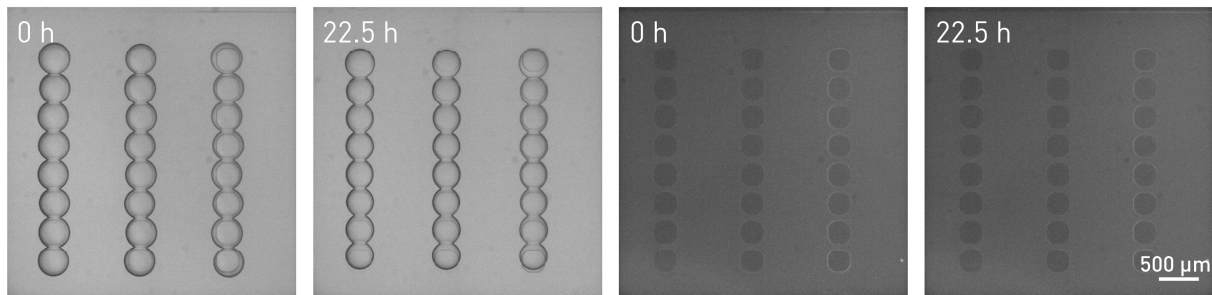


Figure 3-S1: Negative control for the  $\text{Ca}^{2+}$  translocation and Fluo-4 experiment without  $\alpha\text{-HL}$ . We did not detect  $\text{Ca}^{2+}$  translocation across the droplet networks when no  $\alpha\text{-HL}$  was present ( $N = 45$  droplet networks).

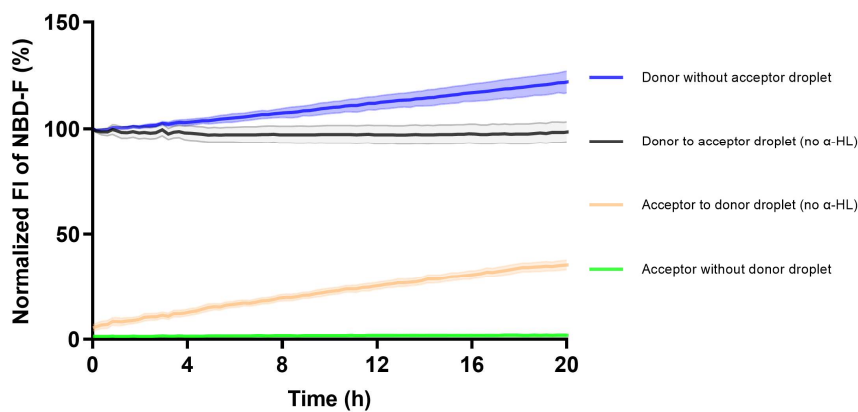


Figure 3-S2: Mean fluorescence intensity (FI) over time of NBD-F diffusion across the membrane (black and yellow curves) in comparison to acceptor without donor droplets (green curve) and donor without acceptor droplets (blue curve). Data were collected every  $\sim 15$  min,  $N = 27$  droplet networks for every curve. The increase in FI occurred (blue curve), because the droplets shrank over time to a small extent and the concentration of the local fluorophore increased. NBD-F slowly permeated across the membrane also when no  $\alpha\text{-HL}$  was present. No NBD-F passage over oil with 5% DMSO was observed as can be seen by the flat FI curve for the acceptor not connected to donor droplets (green curve) in the same oil bath as by the experiment with several donor droplets in a distance of a few millimeters. The error bands represent the standard deviation.

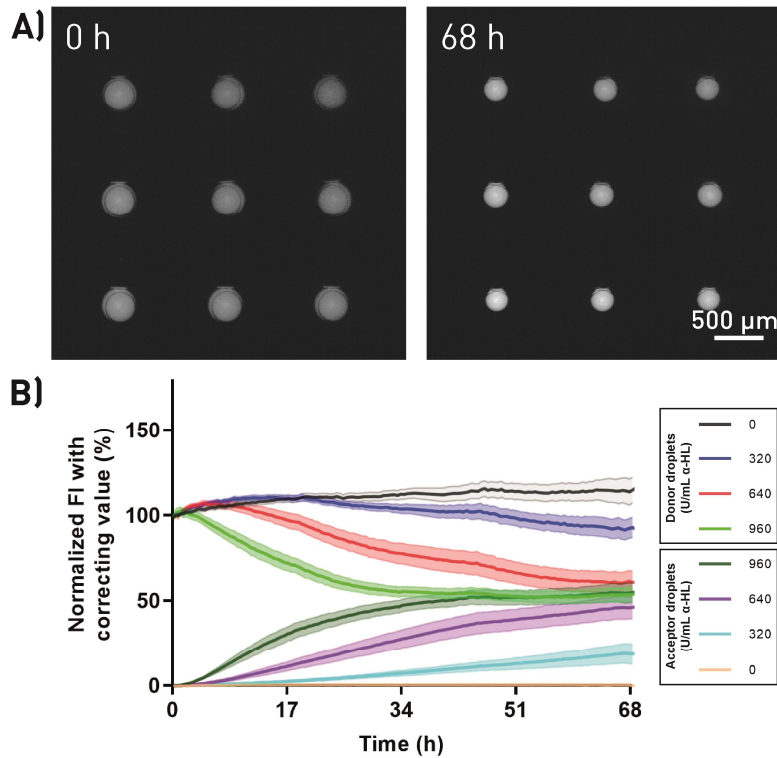


Figure 3-S3: A) Shrinkage of Alexa488 donor droplets connected to acceptor droplets without alpha-hemolysin ( $\alpha$ -HL) over 68 h. The diameter decreased down to  $\sim 70\%$  of the original diameter within 68 hours. B) Corrected graph of the translocation of Alexa488 across  $\alpha$ -HL pores, when the shrinkage is considered. The mean fluorescence intensity (FI) of every data point in Figure 3-3E was corrected with the following equation:  $FI_{corrected} = FI \times (-0.0044 \times t + 1)$ . Data were collected every  $\sim 30$  min,  $N = 27$  droplet networks for every curve,  $\alpha$ -HL was only present in the acceptor droplets. The error bands represent the standard deviation.

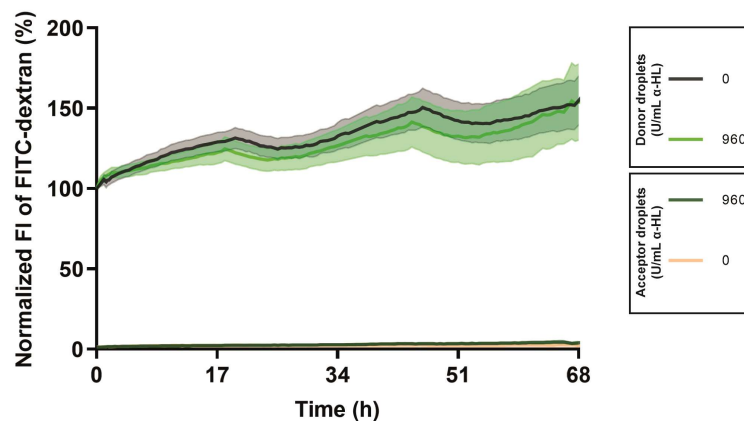


Figure 3-S4: Mean fluorescence intensity (FI) over time of  $60 \mu\text{M}$  FITC-dextran translocation across  $\alpha$ -HL pores. Data were collected every  $\sim 30$  min,  $N = 27$  droplet networks for every curve,  $\alpha$ -HL was only present in the acceptor droplets. Both drops in FI correspond to the time points when  $100 \mu\text{L}$  water was added to the plate holder to reduce droplet shrinkage. Most likely, a very small amount of FITC-dextran partitions into the oil and forms an equilibrium. When water is added without FITC-dextran, the equilibrium is adjusted (the effect of  $100 \mu\text{L}$  is greater than that of the  $25 \text{ nL}$  droplets on the equilibrium). The continuous increase in the normalized FI in the experiment can be attributed to slow droplet shrinkage over time. We only normalized to the starting fluorescence of the individual donor droplets and did not account for droplet shrinkage in the data normalization process.

### 3.8.2 Label-Free Molecule Detection in Droplet Interface Bilayer Networks with L-Arginine and L-Histidine

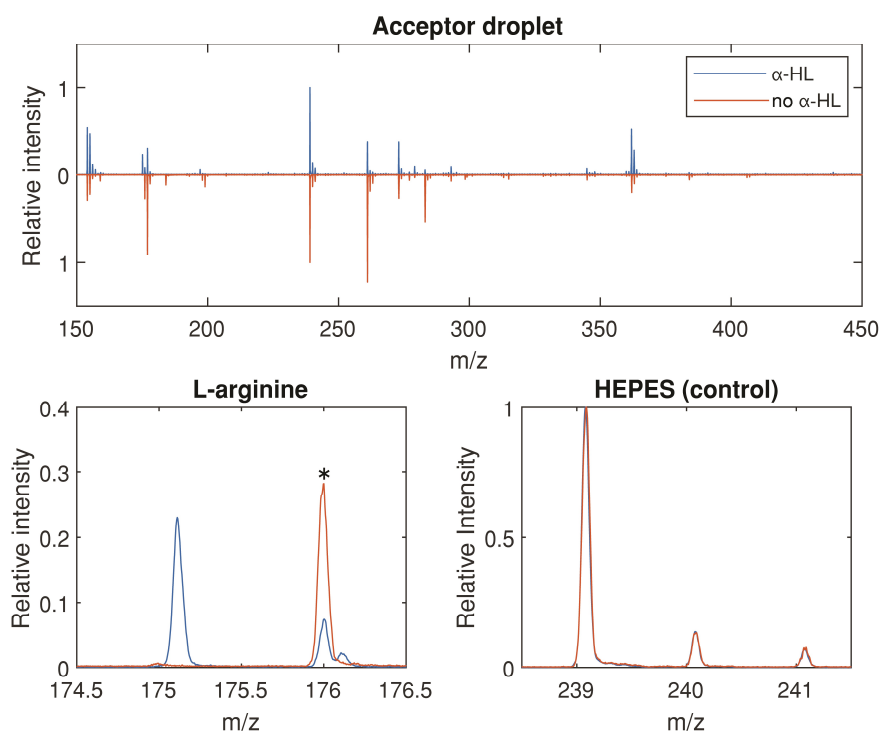


Figure 3-S5: MALDI-MS analysis of acceptor droplets. The alpha-hemolysin ( $\alpha$ -HL) dependence of membrane translocation is observed by MALDI-MS analysis for L-arginine (175.1 m/z). The acceptor droplet that contained  $\alpha$ -HL (top graph) and did not (bottom flipped graph) is displayed for each condition. Data are shown for  $N = 1$  droplet network. In addition, we pooled  $N = 7$  droplet networks and received a similar result (data not shown). The isotopic pattern is for each analyte of interest and HEPES - as a positive control - is zoomed in on. Background peaks on the zoomed in images are denoted with a \*. The matrix used was DHB. Each spectra is normalized to the intensity of the internal control HEPES (239.1 m/z).

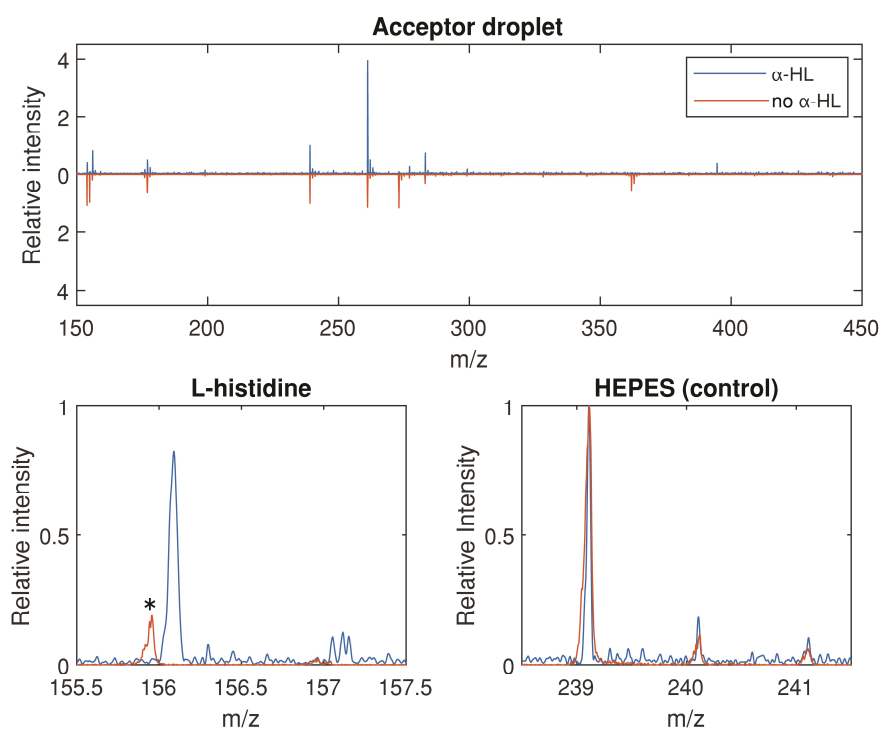


Figure 3-S6: MALDI-MS analysis of acceptor droplets. The alpha-hemolysin ( $\alpha$ -HL) dependence of membrane translocation is observed by MALDI-MS analysis for L-histidine (156.1 m/z). The acceptor droplet that contained  $\alpha$ -HL (top graph) and did not (bottom flipped graph) is displayed for each condition. Data are shown for  $N = 7$  pooled

## Chapter 3

droplet networks. The isotopic pattern is for each analyte of interest and HEPES - as a positive control - is zoomed in on. Background peaks on the zoomed in images are denoted with a \*. The matrix used was DHB. Each spectra is normalized to the intensity of the internal control HEPES (239.1 m/z).

### 3.8.3 Label-Free Molecule Detection: Detected and Theoretical Monoisotopic Peaks

Table 3-S1: Theoretical and observed monoisotopic H<sup>+</sup> m/z.

Analyte	Detected m/z	Theoretical monoisotopic H <sup>+</sup> m/z	Error in m/z
L-histidine	156.0868	156.0768	0.0101
L-arginine	175.1151	175.1190	-0.0039
HEPES	239.1104	239.1060	0.0044
Riboflavin	377.1206	377.1456	-0.0249

### 3.8.4 Cascade Reaction in Droplet Networks Negative Controls

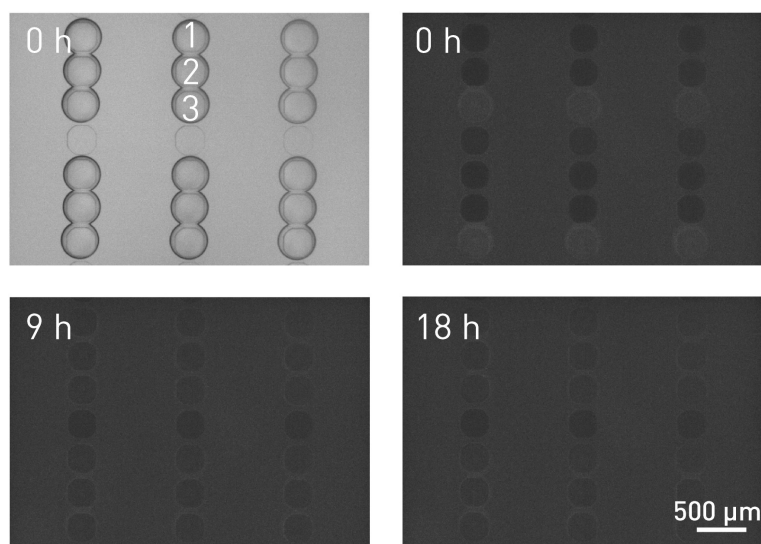


Figure 3-S7: Compartmentalized enzymatic cascade reaction negative control. No alpha-hemolysin was present. The lactose/lactase droplet (1) was added to the glucose oxidase droplet (2) ~180 min before the luminol droplet (3). The imaging starting point was directly after spotting of the luminol droplet. Three droplets in a network: Lactose and lactase in the top droplet (1). Glucose oxidase in the middle droplet (2). Luminol in the bottom droplet (3). We could not detect the formation of 3-aminophthalic acid (N = 42 droplet networks).



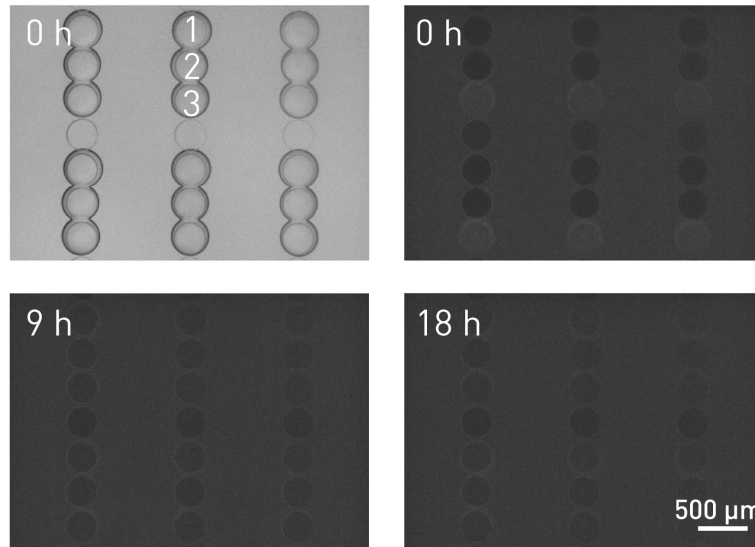


Figure 3-S8: Compartmentalized enzymatic cascade reaction negative control. No lactase was present. The lactose droplet (1) was added to the glucose oxidase droplet (2) ~120 min before the luminol droplet (3). The imaging starting point was directly after spotting of the luminol droplet. Three droplets in a network: Lactose with alpha-hemolysin ( $\alpha$ -HL) in the top droplet (1). Glucose oxidase in the middle droplet (2). Luminol in the bottom droplet (3). We could not detect the formation of 3-aminophthalic acid ( $N = 42$  droplet networks).

### 3.8.5 Rate Constants of Fluorophore Translocation across Alpha-Hemolysin Pores

In our fluorophore translocation studies (Figure 3-3), we were able to image the translocation process over a long time period. To extract more quantitative data, we calculated the rate constants ( $k$ ). The rate constants describe the fraction of translocated fluorophores that are transferred over the alpha-hemolysin pore per time. For this, we first normalized the data to 100% of the starting fluorescence intensity of the individual donor plus acceptor droplets in the first image. In a second step, we additionally normalized every data point to 100% (fluorescence intensity of the donor plus acceptor droplets equals 100%). In third step, we removed the first 3 h to account for the lag in pore formation. Equation 1 and 2 allow for extracting kinetic rate constants by plotting the mass of translocated fluorophores in the acceptor ( $M_a$ ) and donor droplet ( $M_d$ ) over time ( $t$ ) [1]. This exchange is reversible, so it is dependent on the rate constants  $k_{da}$  (donor to acceptor) and  $k_{ad}$  (acceptor to donor). The time ( $t$ ) is corrected by  $c$  to take into account both a delay in measurement start and a potential lag phase in the translocation process due to pore formation. Equations 1 and 2 were fitted to the data with OriginPro (2019, 9.6, OriginLab Corporation). The iteration algorithm was Levenberg Marquardt. Data from every droplet pair was individually fitted and evaluated. Table 3-S2 shows the calculated rate constants and correction values.

$$M_a(t) = \left( -\frac{k_{ad}}{k_{da}+k_{ad}} \times e^{-(k_{da}+k_{ad}) \times (t+c)} + \frac{k_{ad}}{k_{da}+k_{ad}} \right) \times 100\% \quad (1)$$

$$M_d(t) = \left( \frac{k_{da}}{k_{da}+k_{ad}} \times e^{-(k_{da}+k_{ad}) \times (t+c)} + \frac{k_{ad}}{k_{da}+k_{ad}} \right) \times 100\% \quad (2)$$

## Chapter 3

Table 3-S2: Rate constants ( $k$ ) and correction values ( $c$ ) for the translocation of NBD-F, riboflavin, and Alexa488 across alpha-hemolysin ( $\alpha$ -HL) pores. For every condition, the individual data of  $N = 27$  connecting donor/acceptor droplet pairs was fitted with OriginPro. The rate constants  $k_{da}$  (donor to acceptor) and  $k_{ad}$  (acceptor to donor) describe the amount of fluorophore that is transferred over the  $\alpha$ -HL pore. All values are noted as mean with the standard deviation (SD).

Fluorophore	alpha-hemolysin (U/ml)		$k_{da} \times 10^{-3}$ (1/h)		$k_{ad} \times 10^{-3}$ (1/h)		c (h)	
	Donor	Acceptor	Mean	SD	Mean	SD	Mean	SD
NBD-F	0	320	62.9	8.0	62.9	8.0	-1.0	0.2
NBD-F	320	320	103.7	11.5	103.7	11.5	-0.7	0.4
NBD-F	640	0	97.7	10.7	97.7	10.7	0.2	0.4
NBD-F	0	640	110.0	9.0	110.0	9.0	-1.2	0.3
NBD-F	0	960	180.9	32.6	180.9	32.6	-0.9	0.5
Riboflavin	0	320	3.7	1.2	3.7	1.2	-3.2	1.8
Riboflavin	0	640	19.5	3.2	19.5	3.2	-2.8	0.5
Riboflavin	0	960	137.0	30.7	137.0	30.7	-0.2	0.5
Alexa488	0	320	3.1	0.9	3.1	0.9	-3.4	4.1
Alexa488	0	640	14.8	4.6	14.8	4.6	-5.6	0.8
Alexa488	0	960	38.3	6.1	38.3	6.1	-3.6	0.4

### 3.8.6 Videos

The videos can be found in the electronic supplementary information after the paper is published.

Video 3-S1: Spotting “ETH”

Video 3-S2: Translocation  $\text{Ca}^{2+}$  across droplet network

Video 3-S3: Three-step reaction (Lactose/Lactase with  $\alpha$ -HL, Glucose Oxidase, Luminol)

### 3.8.7 Supplementary Reference

1. Krämer, S.D., *Quantitative aspects of drug permeation across in vitro and in vivo barriers*. European Journal of Pharmaceutical Sciences, 2016. **87**: p. 30-46.

## Chapter 4

# Permeation Studies across Symmetric and Asymmetric Membranes in Microdroplet Arrays

**This chapter was adapted from the following paper:**

Bachler, S., M. Ort, S.D. Krämer, and P.S. Dittrich. *Permeation Studies across Symmetric and Asymmetric Membranes in Microdroplet Arrays*. Submitted, 2020.

**Author contributions:**

P.S.D. designed the work; S.B. and M.O. developed the permeability testing platform and the methods; S.B. fabricated the microscopy slides, and performed & analyzed the fluorescence and mass spectrometry experiments; S.D.K. developed the kinetic model for data analysis; S.B. and P.S.D. wrote the manuscript, which all authors approved.

## 4.1 Abstract

We investigated the permeation of molecules across lipid membranes on an open microfluidic platform. An array of droplet pairs was created by spotting aqueous droplets, dispersed in a lipid-oil solution, onto a plate with cavities surrounded by a hydrophobic substrate. Droplets in two adjacent cavities come in contact and form an artificial lipid bilayer, called a droplet interface bilayer (DIB). The method allows for monitoring permeation of fluorescently tagged compounds from a donor droplet to an acceptor droplet. A mathematical model was applied to describe the kinetics and determine the permeation coefficient. We also demonstrate that permeation kinetics can be followed over a series of droplets, all connected via DIBs. Moreover, by changing the lipid-oil composition after spotting donor droplets, we were able to create asymmetric membranes which we used to mimic the asymmetry of the cellular plasma membrane. Finally, we developed a protocol to separate and extract the droplets for label-free analysis of permeating compounds by liquid chromatography-mass spectrometry. Our versatile platform has the potential to become a new tool for the screening of drug membrane permeability in the future.

## 4.2 Introduction

Most pharmaceutical small-molecule drugs are primarily administered orally, and mainly absorbed in the small intestine [1]. As the trans-cellular route is the most relevant for the absorption of these drugs, assays for predicting membrane permeability play an important role during the drug discovery and development process [2-5]. A commonly used cell-free *in vitro* permeability testing technique is the parallel artificial membrane permeability assay (PAMPA) [3, 4, 6, 7]. In this method, two-layered multi-well plates are used to measure permeation through barriers formed between the top and bottom wells. PAMPA is suitable for predicting purely lipoidal permeation; this is not possible in cell-based assays, in which carrier-mediated and lipoidal permeation coexist [2-4, 6, 7]. In PAMPA, the barriers formed between the donor and acceptor wells consist of porous filters with a typical thickness of ~10-100  $\mu\text{m}$  soaked in a mixture of lipid and hydrocarbon oil or pure hydrocarbon oil [3, 4, 7]. Hence, the barriers in PAMPA are much thicker than a lipid bilayer (~5 nm), and their structure is dissimilar to actual biological membranes. Furthermore, diffusion through such a thick barrier, measured by concentration changes in the acceptor and donor wells with volumes of several hundred microliters, leads to assay times in the range of 2-18 hours which can limit the throughput [4, 7]. A common alternative are *in vitro* cell-based permeation assays, using Caco-2 and Madin-Darby canine kidney (MDCK) cellular monolayers [2, 4]. However, cellular monolayers are not always well suited for a systematic and mechanistic investigation of drug absorption and require laborious cell culture.

Recently, microfluidic methods have been introduced to capture cell mimicking vesicles for permeation studies [8-11] as well as to create on-chip artificial cell membranes [12, 13]. A significant advantage of microfluidic devices compared to traditional laboratory methods is the small size and, associated with this, the small sample volumes [14, 15]. In this regard, droplet-based microfluidics is particularly intriguing as it enables the generation of nano- to picoliter-sized aqueous droplets continuously and at high frequency. The aqueous phase is injected into a carrier fluid that is not miscible with water; often surfactants are used for stabilization [16]. When lipids are added to the oil phase, they form a monolayer at the droplet-oil interface. Two adjacent droplets that contact each other form the so-called droplet interface bilayer (DIB) [4, 12, 13, 17]. The DIBs allow translocation of membrane permeable compounds from one donor droplet to the acceptor droplets by passive diffusion. Such droplet systems are therefore interesting approaches for permeation studies, however, require fluorescently labelled compounds [18], or fluorogenic assays to visualize permeation of weakly basic or acidic compounds [8]. Fluorescence spectroscopy is sufficiently sensitive and adaptable to the small volumes, but as the label – often a hydrophobic fluorophore – may influence the permeability [10, 19], label-free detection would be favorable [20, 21]. In this

context, open platforms with so-called static droplet arrays were introduced for miniaturizing biological and chemical processes and reactions, and proved particularly versatile for implementing analytical methods beyond optical microscopy, such as mass spectrometry [22-24], but were not used for permeability assays so far.

Here, we introduce a microfluidic method that combines the advantages of miniaturization and enables monitoring of labelled compounds as well as analysis of permeation of non-fluorescent small molecules by liquid chromatography-mass spectrometry (LC-MS). Our open platform facilitates automated and precise positioning of droplet pairs to create DIBs. Permeation of compounds occur along the concentration gradient from a donor droplet to an acceptor droplet that initially contains no drug. We precisely describe this process by a mathematical model and derive the permeability constants for fluorescent compounds. We also demonstrate the possibility to generate asymmetric lipid bilayers, thereby reflecting cell membranes in a more realistic model [25]. Finally, we apply this new established method for label-free detection of a model permeant.

## 4.3 Experimental Section

### 4.3.1 Assay Preparation

The lipid-out approach was used to add phospholipids to the water/oil-interface, i.e. lipids were dissolved in the oil phase. We purchased 1,2-dioleoyl-sn-glycero-3-phosphocholine (DOPC) and 1,2-dioleoyl-sn-glycero-3-phospho-L-serine (DOPS) as solutions in chloroform from Avanti Polar Lipids (Alabaster, AL, USA). We placed the required lipids in pear-shaped flasks and removed the chloroform with a rotary evaporator (Büchi Labortechnik AG, Flawil, Switzerland) forming a film. The lipid film was dissolved in a 1:1 (v/v) mix of hexadecane (reagent plus grade, Sigma-Aldrich) and squalane (Sigma-Aldrich) in an ultrasonication bath at 50 °C for ~30 min. The final phospholipid concentration in oil was 0.625 mM for donor droplets and 1.25 mM for acceptor droplets. We used either 100% DOPC or 30% DOPC and 70% DOPS mixtures (mole percentage). We filtrated the phospholipids-oil solution before use (0.45 µm pore size, RC 4 Male Luer Slip Minisart filters, Huberlab, Switzerland).

All aqueous solutions were prepared in LC-MS grade water (Fisher Scientific, Loughborough, UK). We used as buffers 20 mM 2-morpholinoethanesulfonic acid (MES, pH 6.0, Alfa Aesar), 20 mM phosphate buffer (pH 7.0, Acros Organics), 50 mM 4-(2-hydroxyethyl)-1-piperazineethanesulfonic acid (HEPES, pH 7.4, gibco, Paisley, UK), or 20 mM tris(hydroxymethyl)aminomethane (Tris, pH 8.0, VWR). The following fluorophores were dissolved in buffer: 50 µM rhodamine 6G (laser grade, Acros Organics), 50 µM fluorescein (Honeywell Fluka, Seelze, Germany), ~50 µM PEG4-NBD, and 50 µM calcein (Sigma-Aldrich). PEG4-NBD was synthesized from succinimidyl 6-(N-(7-nitrobenz-2-oxa-1,3-diazol-4-yl)amino) hexanoate (NBD NHS-ester, Molecular Probes Life Technologies, Eugene, OR, USA) and amine-terminated poly(ethylene glycol)-4 alcohol (Amino-PEG4-OH, Quanta Biodesign, Plain City, OH, USA) [26]. A 1:1 molar ratio of the NBD NHS-ester and Amino-PEG4-OH was reacted in a 10:1 (v/v) solution of chloroform (Sigma-Aldrich) and triethylamine (Brenntag Schweizerhall, Basel, Switzerland). The reaction was held at 45 °C for two hours, followed by 22 °C for twelve hours. Afterwards, the reaction products were separated with a preparative liquid chromatography system (Prep 150 LC system, Waters). The mass of the product PEG4-NBD was confirmed with an LC-MS system (Ultimate 3000 MSQ, Dionex).

### 4.3.2 Fabrication of the Microarray Plates

We used a previously developed protocol for fabricating microarray plates with cavities [24]. In brief, a 4-inch borofloat glass wafer was cleaned by oxygen plasma and subsequently spin-coated with SU-8 3025 (MicroChem, Westborough, MA, USA) to obtain an approximately 35 µm high layer of photoresist. The wafer was soft baked at 65 °C for 2 min and 95 °C for

12 min. Afterwards, we exposed the photoresist to a UV light source through a foil mask (i-line illumination with 270 mJ/cm<sup>2</sup>). We conducted a ramp from room temperature to 95 °C over 60 min, held at 95 °C for 5 min, and cooled down again to room temperature over 60 min for the post-exposure bake. The wafer was developed for 6 min with mr-Dev 600 (micro resist technology GmbH, Berlin, Germany), followed by rinsing with 2-propanol (Technic France, Saint-Denis, France) for another 10 s, and spin-drying. A hard bake with a ramp over 4 h to 180 °C, held at 180 °C for 2 h, and cool down to room temperature over 4 h was used. As final step, the wafer was diced in two 75 mm × 25 mm microarray plates, each contained more than 1500 cavities. The individual cavities had a diameter of 300 μm. The distance between two neighboring cavities was 310 μm.

### 4.3.3 Device Operation

We placed the microarray plate in a removable temperature-controlled holder ( $T = 37\text{ °C}$ ) with a transparent bottom, which was mounted on a motorized XY stage (HLD117, Prior) of an inverted fluorescence microscope (Olympus IX73). We carried out the experiments in an oil bath to reduce droplet evaporation. The plate holder was filled with ~4 mL of 1:1 (v/v) hexadecane:squalane without phospholipids and 50 μL water in all four edges to reduce droplet shrinkage. We used a self-made microfluidic T-junction device made of polycarbonate (PC) to generate droplets of ~25 nL by continuously injecting the aqueous phase (flow rate: 0.5 μL/min) into the immiscible oil phase (flow rate: 2 μL/min). The droplets were transported through a capillary onto the microarray plate. In this time, the phospholipids in the oil aligned along the water/oil-interface and formed a monolayer [27, 28]. We mounted the end of the capillary on a motorized Z stage (M-403.2PD, Physik Instrumente, Karlsruhe, Germany). The generated droplets were detected in the capillary holder with a custom-made optical droplet detection system [22]. This was utilized to selectively deposit a single droplet per predefined position by synchronizing droplet generation and capillary and microarray movement. All components of the microscope and the capillary were controlled by the software YouScope for automated microscopy (R2018, v2.1.0) [29].

### 4.3.4 Image Acquisition and Analysis

Fluorescence and bright-field pictures were recorded using a light source (Lumen 300, Prior and TH4-200, Olympus) and a CMOS camera (Zyla 4.2, Andor) connected to the Olympus IX73 microscope. To track fluorescein, calcein, and PEG4-NBD, a blue excitation filter set (exciter HQ470/40x, dichroic 500dcxr BS, and emitter E515lpv2; Chroma Technology Corp, Bellows Falls, VT, USA) was used. For rhodamine 6G, a green excitation filter set (exciter 525/50m, dichroic Q565lp, and emitter 588 LP; Chroma Technology Corp) was used. To



minimize environmental influences and heat exchange, a black anodized lid was placed on top of the plate holder. The bright-field images were used to determine the diameter of the DIB.

The recorded fluorescence signals were evaluated using Fiji [30] and OriginPro (2019, 9.6, OriginLab Corporation). First, we subtracted the background fluorescence for data evaluation. For the normalized fluorescence intensity values, 100% was the starting fluorescence intensity of the individual donor plus acceptor droplets in the first image. For the permeability calculations, we additionally normalized every data point to 100% (fluorescence intensity of the donor plus acceptor droplets equals 100%). Donor and acceptor droplets spotted on adjacent cavities, which did not touch each other and therefore, did not form a DIB were excluded.

#### **4.3.5 Combination of the Droplet Spotter with LC-MS**

For subsequent LC-MS analysis, we used a recently developed protocol to split the droplet pairs [24]. The capillary used before for spotting of droplets was flushed with hexadecane/squalane (1:1) and placed between two connecting droplets to separate the droplet pairs. To extract individual droplets, the capillary was flushed with fluorinated oil (HFE-7500, 3M Novec, Hadfield, UK) and connected to a 50  $\mu$ L glass syringe (Hamilton, Switzerland). The center of the capillary was lowered to a height where it slightly squeezed the droplet. Subsequently, by slowly pulling the glass syringe, the droplet was aspirated. Afterwards, the capillary was moved over a small tube (TreffLab Degersheim, Switzerland) and the aspirated droplet was ejected. Following this, the tube was centrifuged (3300 rounds per minutes, MiniSpin, Eppendorf) to assure that the droplet moved to the bottom. The tube was then heated to 60 °C for 30 min to induce water/solvent evaporation. After this step, the samples were re-dissolved in LC-MS grade water/acetonitrile (2:1) (HiPerSolv Chromanorm, VWR).

The sample was analyzed in a 1260 II Infinity LC Quaternary system coupled to a single quadrupole atmospheric pressure ionization-electrospray (API-ES) G6130B mass spectrometer (Agilent). It was controlled through the Agilent OpenLAB CSD ChemStation (C.01.08). To separate the analytes, we used a reversed-phase 100 mm Poroshell 120 SB-C8 column (Agilent), the solvents acetonitrile, LC-MS grade water, and isopropanol (hypergrade for LC-MS, Merck, Germany) together with 5 mM ammonium formate (AF, Agilent) buffer. All analytes were detected with selected ion monitoring (SIM) in positive mode. The signal was obtained by integration of the peak area in the SIM MS spectra.

### 4.3.6 Permeability Calculations

In our fluorophore permeation studies, we were able to image the permeation process over a long time period. Equations 1 and 2 allow for extracting kinetic rate constants by plotting the mass of model permeant in the acceptor ( $M_a$ ) and donor droplet ( $M_d$ ) over time ( $t$ ). The rate constants  $k$  describe the fraction of model permeant that is transferred over the barrier per time (mass transfer rate constants). As the permeation is equilibrative, the observed kinetics, *i.e.*, change in fluorescence over time, dependent on both  $k_{da}$  (donor to acceptor) and  $k_{ad}$  (acceptor to donor). As long as the fluorescence intensity is proportional to the concentration of the fluorophore, the intensity can be directly plotted and analyzed [31].

$$M_a(t) = \left( -\frac{k_{ad}}{k_{da}+k_{ad}} \times e^{-(k_{da}+k_{ad}) \times t} + \frac{k_{ad}}{k_{da}+k_{ad}} \right) \times 100\% \quad (1)$$

$$M_d(t) = \left( \frac{k_{da}}{k_{da}+k_{ad}} \times e^{-(k_{da}+k_{ad}) \times t} + \frac{k_{ad}}{k_{da}+k_{ad}} \right) \times 100\% \quad (2)$$

Equations 1 and 2 were fitted to the data with OriginPro. The iteration algorithm was Levenberg Marquardt. Data from every droplet pair was individually fitted and evaluated. In the graphs, we show the fit for the mean values. The rate constant for the transport from donor to acceptor compartment ( $k_{da}$ ) can be converted into the apparent permeability coefficient ( $P_{app}$ ) [31]. We used Equation 3 for the calculation of  $P_{app}$  from the fitted  $k_{da}$  ( $P_{app,fit}$ ) under assumption that volumes of the two compartments were equal ( $V_d$ ). We further approximated that the area of the droplet interface bilayer is circular [32] and we calculated the area ( $A$ ) for the individual droplet pairs via the measured droplet interface bilayer diameter from the bright-field images (as indicated in the Table 4-S1).

$$P_{app,fit} = \frac{k_{da} \times V_d}{A} \quad (3)$$

To determine the  $P_{app}$  from MS measurements with fewer time points, we used Equation 4.  $M_d(0)$  is the sample mass in the donor droplet at the start.  $\Delta M_a$  represents the sample mass permeated into the acceptor droplet after a given time ( $\Delta t$ ). We differentiated between sink- and non-sink conditions [31, 33]. Under sink conditions, the transfer of substances back from the acceptor to the donor compartment can be neglected. We assumed approximately constant  $\Delta M_a/\Delta t$  as long as less than 10% of the initial donor content permeated into the acceptor compartment.

$$P_{app,sink} = \frac{V_d}{A \times M_d(0)} \times \frac{\Delta M_a}{\Delta t} \quad (4)$$

### 4.3.7 Permeation Kinetics with Droplets in Series

For several acceptor droplets in series, the numerical solutions of a differential equation system according to Equations 5 to 7 were fitted to the normalized fluorescence data of donor and acceptor droplets. The solutions of the differential equation system and the fitting were performed with the Matlab (version 2018a, Mathworks) functions ode15s, fmincon (minimizing the sum of squared residues) and MultiStart.

$$\frac{dW(1)}{dt} = -k * W(1) + k * W(2) \quad (5)$$

$$\frac{dW(2)}{dt} = +k * W(1) - k * W(2) - (N > 2) * k * W(2) + (N > 2) * k * W(2 + (N > 2)) \quad (6)$$

$$\text{if } N > 2; \text{ for } n = 3:N; dW(n) = +k * W(n - 1) - k * W(n) - (n < N) * k * W(n) + (n < N) * k * W(n + (n < N)) \quad (7)$$

$W(n)$  is the fluorescence in the water phase of droplet  $n$ ,  $k$  is the mass transfer rate constant (the fit parameter), and  $N$  the total number of donor and acceptor droplets. The expression  $(N > 2)$  equals 1 if  $N > 2$  and 0 if  $N \leq 2$  and  $(n < N)$  equals 1 if  $n < N$  and 0 if  $n \geq N$ .

## 4.4 Results and Discussion

### 4.4.1 Spotting Platform for DIB Formation

We developed a microfluidic platform with the aim to understand key parameters of membrane permeation of molecules (Figure 4-1). Aqueous droplets were created in a simple microfluidic T-junction and afterwards positioned on hydrophilic cavities on the surface of a plate. First, the donor droplets were deposited, containing the permeating compound, and in the second spotting procedure the acceptor droplets were added to the cavities in close proximity of the donor droplets (SI Video 4-S1 in the supporting information). Droplets hosted by neighboring cavities contacted each other. As the droplet-oil interfaces consisted of a self-assembled phospholipid monolayer, the contact between this aqueous droplet and another droplet united the lipid monolayers, creating the DIB of roughly 5 nm thickness [4, 34]. The droplets were covered by oil to prevent evaporation. The oil bath had a volume of ~4 ml and did not contain phospholipids. Therefore, we expected that the few remaining phospholipids, which did not assemble to the monolayer of the aqueous droplets after droplet formation, were quickly diluted in the large volume of the oil bath. These diluted phospholipids were assumed to assemble on the surface of the four 50  $\mu$ L water reservoirs at the edges of the plate holder. One 50  $\mu$ L water reservoir had more than a 150 times larger area compared to the ~25 nL droplet. The ~25 nL droplets were already saturated with phospholipids when spotted on the plate, whereas the 50  $\mu$ L water reservoirs did not contain any phospholipids at the water/oil interface in the beginning of the experiment.

After formation of a DIB within less than one minute, we monitored the permeation process. Previously, we proved the formation of unilamellar DIBs by forming alpha-hemolysin pores with our method [24]. DIB membranes that could incorporate transmembrane proteins or toxins behaved like “oil-free” membrane structures, such as vesicles [24, 35]. Even when a tiny amount of oil was still present in the membrane, it should not affect our measurement since the membrane of a biological cell also contains cholesterol precursors.

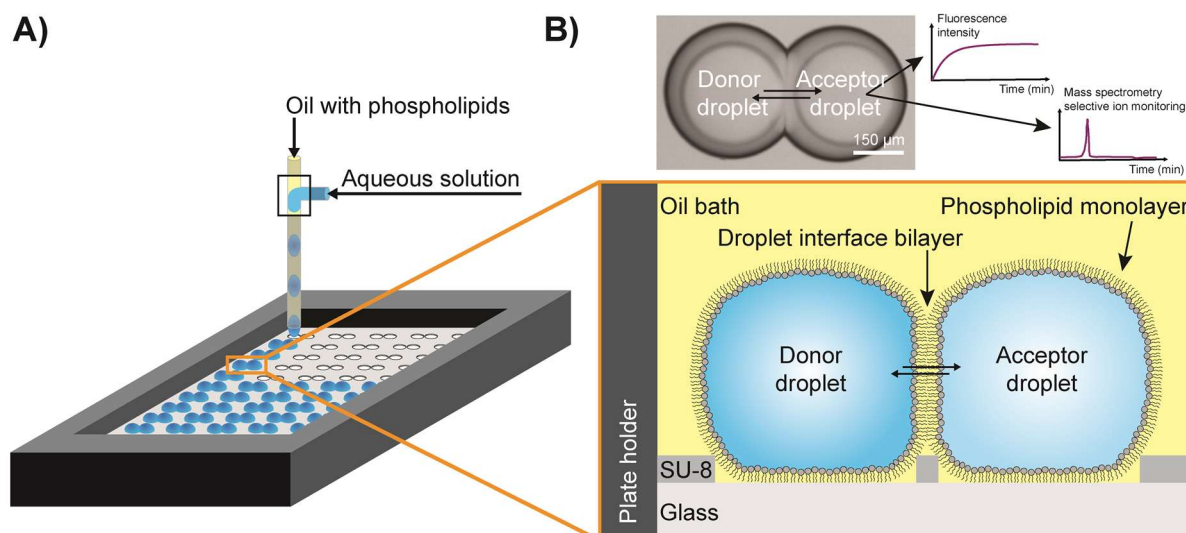


Figure 4-1: Creation of droplet interface bilayers (DIBs) for permeation studies. A) Creation and positioning of droplets on an open platform. Nanoliter droplets are formed at a microfluidic T-junction from an aqueous solution containing the model permeant and oil with phospholipids. The droplets are deposited on a glass plate into cavities, which are built in a layer of the photoresist SU-8. The enlarged schematics depicts the side view. Donor droplets with model permeants are spotted next to the acceptor droplets. The DIB forms in between these droplet pairs and facilitates passive permeation of compounds from donor to acceptor droplet and vice versa. B) Micrograph showing a droplet pair with the DIB. The small circles inside the droplets are shadows of the cavities. We measure either the fluorescence intensity in the donor and acceptor droplets, or take mass spectra of the droplet contents.

#### 4.4.2 Fluorophore Permeation Analysis with Symmetric Membranes

We optimized and evaluated the method with fluorescent dyes (rhodamine 6G, fluorescein, PEG4-NBD, and calcein), and performed kinetic measurements to assess the respective  $P_{app,fit}$ . We chose a pH of 6 in these experiments as approximation to the pH of the small intestine where most drugs are absorbed [36], and set the physiological temperature of 37 °C. Figure 4-2A, 4-2B, and 4-S1 show the permeation of rhodamine 6G from donor to acceptor droplets until an equilibrium is reached. Likewise, PEG4-NBD and fluorescein permeated across the DIB (Figure 4-S2 and 4-S3), while no permeation was observed for calcein (Figure 4-S4). This observation is in good agreement with the very low permeability coefficients ( $10^{-10}$  to  $10^{-11}$  cm/s) reported for calcein permeation across liposome membranes [37].

The apparent permeability coefficients were determined using Equations 1–3 (Figure 4-2C); all fitting values are listed in SI Table 4-S1. In addition, we determined the  $P_{app,fit}$  of fluorescein at pH 6, 7, and 8 (Figure 4-2D and SI Figure 4-S3, 4-S5 and 4-S6). As expected,  $P_{app,fit}$  of fluorescein dropped significantly for higher pH values, since the phenolic  $pK_a$  of fluorescein is 6.4 and the fraction of the di-anionic form (carboxylate, phenolate) increases from pH 6 to 8, resulting in reduced permeability.

The  $P_{app,fit}$  values for fluorescein across 100% DOPC DIBs match well with findings in former studies with DIBs [4, 12], vesicles [26] or cell monolayers [38, 39]. For example, our values at pH 6, 7, and 8 were  $(193.03 \pm 17.79) \times 10^{-6}$  cm/s,  $(7.05 \pm 0.42) \times 10^{-6}$  cm/s, and  $(1.05 \pm 0.06)$

$\times 10^{-6}$  cm/s, respectively, similar to the permeation constants reported by Schlicht et al. ( $(2.01 \pm 1.46) \times 10^{-6}$  cm/s at pH 7.4) [12], and by Nisisako et al. ( $(60.0 \pm 22.4) \times 10^{-6}$  cm/s at pH 6.4 and  $(5.1 \pm 1.8) \times 10^{-6}$  cm/s at pH 7.5) [4]. Likewise, the determined permeability constant for PEG4-NBD and rhodamine 6G are in the same order of magnitude to previous results [26, 40].

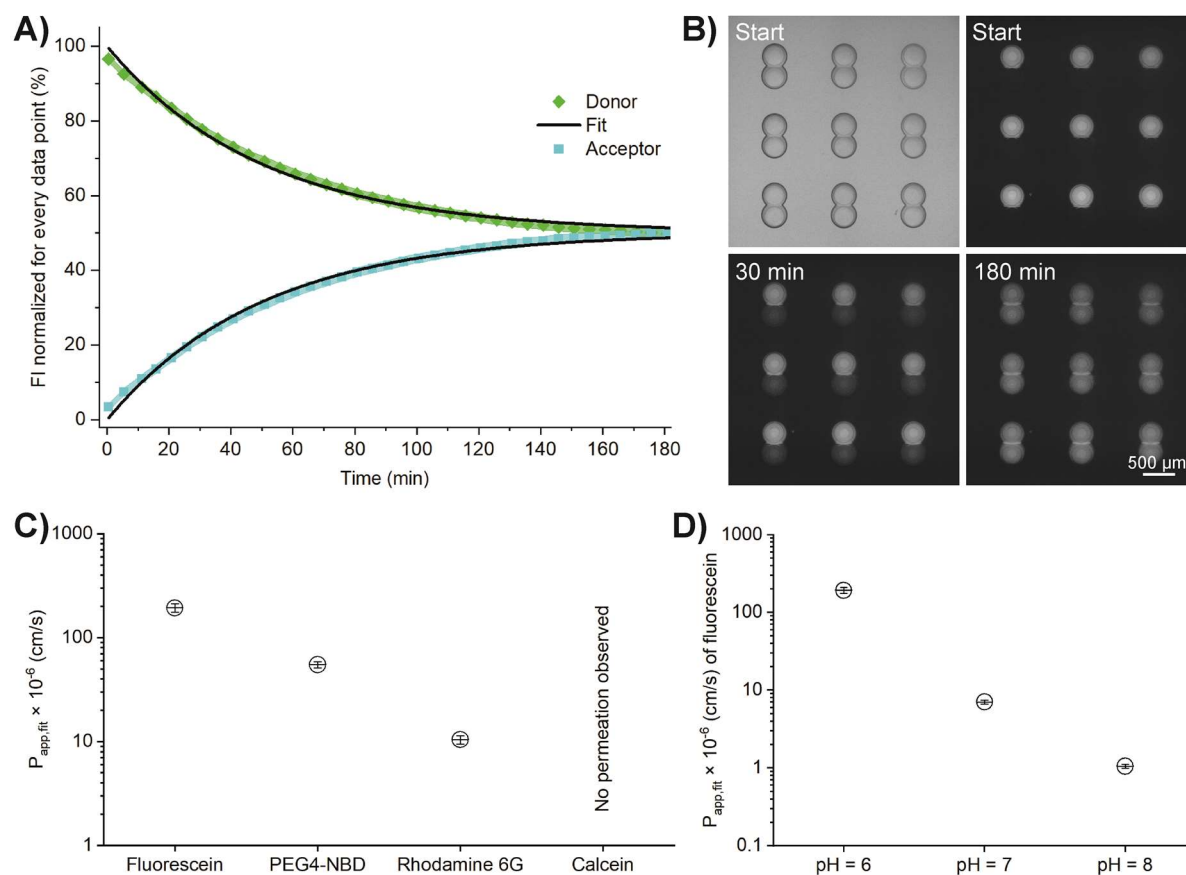


Figure 4-2: Permeation of different fluorophores across 100% DOPC droplet interface bilayer (DIB) membranes. A) Mean normalized fluorescence intensity (FI) over time of rhodamine 6G in donor and acceptor droplets at pH 6.0. The color-shaded areas represent the standard deviation of every data point ( $N=27$ ). The fit is shown for the mean values. B) Bright-field (top left) and fluorescent images of donor and acceptor droplets for the graphs shown in Fig. 4-2A. C) Apparent permeability coefficients and standard deviations of fluorescein, PEG4-NBD, rhodamine 6G, and calcein (all at pH = 6.0,  $N = 27$ ) D) Mean  $P_{app,fit}$  and standard deviations of fluorescein at different pH ( $N = 27$ ).

#### 4.4.3 Fluorophore Permeation Analysis with Asymmetric Membranes

Next, we varied the composition of the DIB. We created symmetric DIBs by spotting droplet pairs of the same type, e.g. all with a DOPC monolayer, and asymmetric DIBs by spotting donor and acceptor droplets with different lipid monolayers. We chose DOPC and, as a second monolayer, a formulation of 30% DOPC and 70% DOPS, because the negatively charged phosphatidylserine (PS) is an important constituent of the plasma membrane of cells. PS is located in the inner leaflet of healthy cells, and transferred to the outer leaflet in apoptotic cells. The asymmetry due to PS may result in an asymmetric partitioning of the permeant between the two lipid layers. We monitored the influence of this asymmetry on the permeation kinetics

of rhodamine 6G (Figure 4-2 and SI Figures 4-S1, 4-S7 to 4-S9). Depending on the membrane composition, extensive lag phases were observed in the fluorescence-time curves of both donor and acceptor droplets. Analysis with Equations 1 and 2 for the complete data set, including the lag phase, resulted in different rate constants for the four membrane compositions. Taking into account the differences in DIB diameters in Equation 3 still resulted in different  $P_{app,fit}$  values for the different membrane compositions (Figure 4-3 and SI Table 4-S1). The highest apparent rate constant and  $P_{app,fit}$  were observed for the permeation across the asymmetric lipid bilayer of 30% DOPC and 70% DOPS to 100% DOPC (SI Figure 4-S7). The lowest  $P_{app,fit}$  and apparent rate constant for rhodamine 6G were found for the opposite composition which also had the most prominent lag phase (SI Figure 4-S8). For symmetric DIBs, the values for  $P_{app,fit}$  were in between those for asymmetric DIBs (Figure 4-2A/B, SI Figures 4-S1 and 4-S9).

In theory, the permeability coefficients across asymmetric membranes should be independent of the direction of the initial concentration gradient [31]. The differences between the  $P_{app,fit}$  values of the two asymmetric bilayers in our experiments could result from interactions of cationic rhodamine 6G with the negatively charged DOPS, visible by increased fluorescence at the lipid monolayer of the droplets. This accumulation or aggregation of the fluorophore is clearly visible in SI Figures 4-S8A and 4-S9A, where the acceptor droplet's monolayer comprises 30% DOPC and 70% DOPS. These interactions may result in the observed lag phase in the fluorescence-time curves (SI Figures 4-S8 and 4-S9), reducing the apparent rate constants when fitting the complete data set with Equations 1 and 2. Further general sources of error could be leakage out of the droplet and bleaching, both reducing the observable fluorophore in the droplets over time.

It should be mentioned that the asymmetric membranes could equilibrate due to lipid flip-flop [41], resulting in equal lipid compositions on both sides of the DIB. Since the exchange of lipids is very slow in defect-free membranes ( $\sim 10^{-15} \text{ s}^{-1}$  [42]), we expect a stable asymmetric DIB for several hours and assume that lipid flip-flop has no influence on our results.

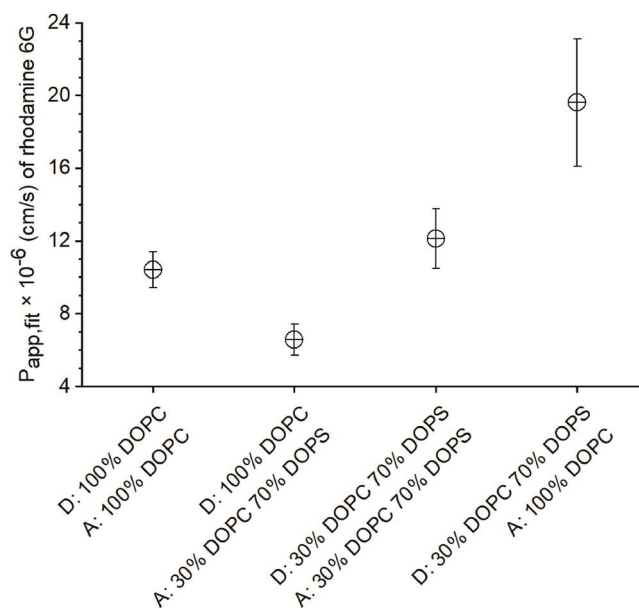


Figure 4-3:  $P_{app,fit}$  for rhodamine 6G at pH 6.0 across symmetric and asymmetric DIBs. The error bars represent the standard deviation,  $N = 27$  droplet pairs.

#### 4.4.4 Fluorophore Permeation over Multiple Compartments

Our platform allows for spotting droplet lines, instead of just pairs. With this, we can monitor how permeation and diffusion of compounds progress over several compartments. For creation of multiple droplets, connected via DIBs, we used a modified glass plate, where cavities were created in lines. Several fluorophore-free acceptor droplets were deposited in this line accordingly. The last droplet contained fluorescein, which permeates over the multiple compartments. Equilibrium was reached in all five droplets after approximately 30 min at pH 6 (Figure 4-4 and SI Figure 4-S10). We determined  $P_{app,fit}$  using Equations 5-7 and 3 to be  $(199.68 \pm 9.73) \times 10^{-6}$  cm/s, similar to the value determined with the droplet pairs, i.e.,  $(193.03 \pm 17.79) \times 10^{-6}$  cm/s. Permeation at pH 7.4 was slower as expected from the experiments with the droplet pairs and from the ionization state of fluorescein (SI Figure 4-S11).  $P_{app,fit}$  at pH 7.4 was  $(19.01 \pm 1.16) \times 10^{-6}$  cm/s, higher than determined with the droplet pairs at pH 7.0  $(7.05 \pm 0.42) \times 10^{-6}$  cm/s. We did not further investigate the discrepancy at the higher pH. The lag phase observed at pH 7.0 (SI Figure 4-S5) has a higher impact on the fit parameters in the assay with only two droplets (reducing the apparent rate constants) than with several droplets in series.



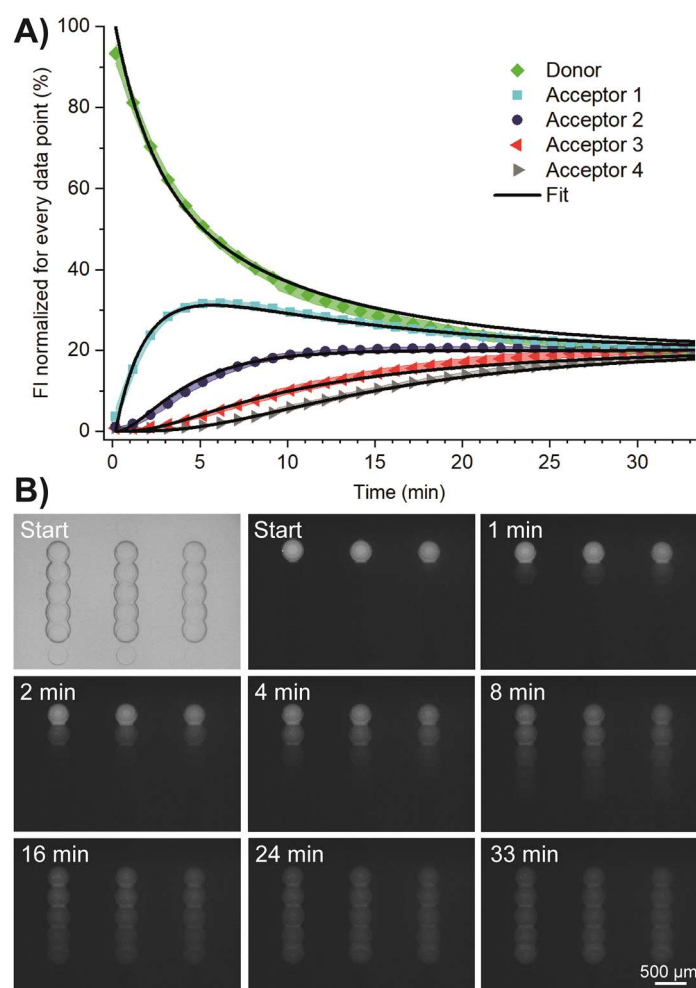


Figure 4-4: Permeation of fluorescein over multiple compartments. A) Mean fluorescence intensity (FI) and standard deviation (color-shaded areas) over time from one donor to four acceptor droplets (100 % DOPC droplet interface bilayer, pH 6.0,  $N = 12$  droplet networks). Black lines, fit according to Equations 5-7. B) Bright-field (top left) and fluorescent images of the permeation.

#### 4.4.5 Label-Free Permeation Analysis

Finally, we developed a protocol to interface our platform with LC-MS, and to measure  $P_{app}$  of non-fluorescent compounds in future. Here, we demonstrate the workflow (Figure 4-5A) and perform the MS analysis of donor and acceptor droplets for rhodamine 6G. In contrast to fluorescence microscopy, the analysis by MS was not done continuously, but at a defined time point. For MS analysis, droplet pairs were separated by placing a capillary in between the pair (SI Video 4-S2) and the individual droplets were then aspirated into the capillary (SI Video 4-S3). These droplets were then transferred into a tube, where water was exchanged by a mixture of MS-grade water-acetonitrile. We performed this procedure for different time points and determined the MS signals (integrated peak area) for both donor and acceptor droplets (Figure 4-5B). We calculated  $P_{app}$  by using Equation 3 ( $P_{app,fit} = 6.28 \pm 0.68 \times 10^{-6}$  cm/s) as well as Equation 4 ( $P_{app,sink} = 9.42 \pm 2.17 \times 10^{-6}$  cm/s using the first two data points), which assumes sink condition (neglecting back-permeation into the donor droplet).

The slightly slower value obtained when fitting all data ( $P_{app,fit}$  MS) can be presumably attributed to heat losses during sampling of the droplets (opening the lid positioned over the plate to allow separation and extraction of the droplet pairs). Since  $P_{app,sink}$  MS was calculated with the droplet pairs, which were separated first, only a minimal heat loss is expected at these data points.

The results confirm that our method facilitates the determination of the permeation coefficient by either fluorescent microscopy or mass spectrometry.

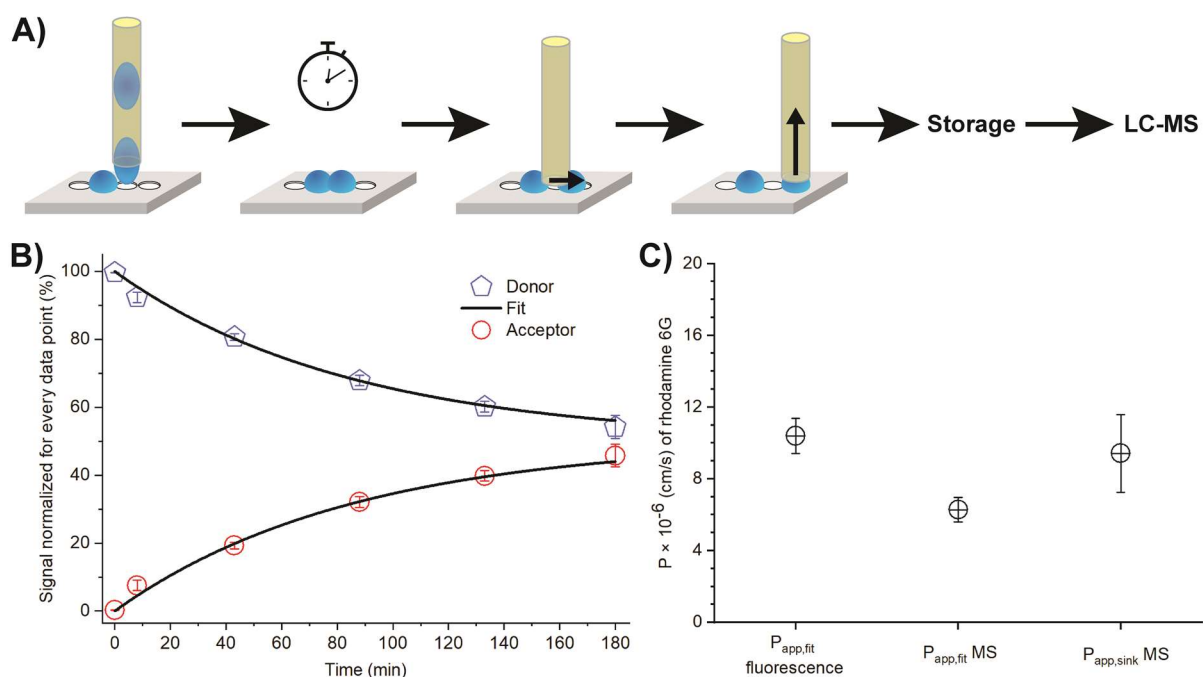


Figure 4-5: A) Scheme of droplet separation and extraction for liquid chromatography-mass spectrometry (LC-MS) analysis. From left to right: droplet spotting; incubation step for allowing permeation; droplet separation; droplet aspiration; placing the droplet in a storage place to evaporate the remaining water/solvents and, following this, a defined volume of water/acetonitrile (2:1) is added for redissolution; LC-MS analysis. B) Permeation of rhodamine 6G across droplet interface bilayer (DIB) membranes at pH 6.0 measured by MS ( $N = 4$  for every individual data point). Black lines, fit according to Equations 1 and 2 ( $P_{app,fit}$ ). C) Apparent permeability coefficients ( $N = 27$  for  $P_{app,fit}$  fluorescence;  $N = 4$  for MS measurements).

## 4.5 Conclusion

We developed a versatile microfluidic method to determine the permeability coefficients of small molecules by monitoring their permeation across artificial lipid bilayers. The lipid bilayers are formed between two adjacent nanoliter droplets that are deposited on a glass substrate. We showed on-demand droplet generation, spotting, on-site continuous investigation of fluorescent molecules with a microscope, and subsequent LC-MS analysis, opening doors for permeability studies of non-fluorescent compounds.

The method is much faster than the current state-of-the art, PAMPA, i.e. normally less than 1 hour for  $P_{app.sink}$  compared to 2-18 hours PAMPA assay time, requires approximately 8,000 times smaller compartments ( $V = 25$  nL compared to  $\sim 200$   $\mu$ L) and can be equally parallelized as PAMPA. Therefore, our method is ideally suited for rapid determination of drug permeability during the drug screening process.

Moreover, we can investigate specific aspects of the permeation process by systematic alterations of various parameters. For example, the membrane compositions can be changed and asymmetric membranes can be created, which leads to a better understanding of the permeation mechanisms. We believe that it is also possible to reconstitute membrane proteins into the DIB, which will ultimately enable studies on membrane transporters or determination of ligand-receptor binding.

## 4.6 Acknowledgements

Funding from the European Research Council (ERC Consolidator Grant No. 681587, HybCell) and the NCCR Molecular Systems Engineering (Swiss National Science Foundation) is gratefully acknowledged. We would like to thank Dominik Haidas for the Matlab data evaluation script, Marcel Grogg for help with the synthesis and analysis of PEG4-NBD, and Chao-Chen Lin for help with the optical microscope. We highly appreciate support from the team of the Department's cleanroom facility, and the workshop team for the fabrication of the spotting device parts. In addition, we thank Darius Rackus for proofreading.

## 4.7 References

1. Wilson, C.G., *The Organization of the Gut and the Oral Absorption of Drugs: Anatomical, Biological and Physiological Considerations in Oral Formulation Development*, in *Controlled Release in Oral Drug Delivery*, C.G. Wilson and P.J. Crowley, Editors. 2011, Springer US: Boston, MA. p. 27-48.
2. Sugano, K., M. Kansy, P. Artursson, A. Avdeef, S. Bendels, L. Di, G.F. Ecker, B. Faller, H. Fischer, and G. Gerebtzoff, *Coexistence of passive and carrier-mediated processes in drug transport*. *Nature reviews Drug discovery*, 2010. **9**(8): p. 597-614.
3. Avdeef, A., *Absorption and drug development: solubility, permeability, and charge state*. 2012: John Wiley & Sons.
4. Nisisako, T., S.A. Portonovo, and J.J. Schmidt, *Microfluidic passive permeability assay using nanoliter droplet interface lipid bilayers*. *Analyst*, 2013. **138**(22): p. 6793-6800.
5. Krämer, S.D., D. Lombardi, A. Primorac, A.V. Thomae, and H. Wunderli-Allenspach, *Lipid-Bilayer Permeation of Drug-Like Compounds*. *Chemistry & Biodiversity*, 2009. **6**(11): p. 1900-1916.
6. Kansy, M., F. Senner, and K. Gubernator, *Physicochemical high throughput screening: parallel artificial membrane permeation assay in the description of passive absorption processes*. *Journal of Medicinal Chemistry*, 1998. **41**(7): p. 1007-1010.
7. Faller, B., *Artificial membrane assays to assess permeability*. *Current Drug Metabolism*, 2008. **9**(9): p. 886-892.
8. Eyer, K., F. Paech, F. Schuler, P. Kuhn, R. Kissner, S. Belli, P.S. Dittrich, and S.D. Krämer, *A liposomal fluorescence assay to study permeation kinetics of drug-like weak bases across the lipid bilayer*. *Journal of Controlled Release*, 2014. **173**(1): p. 102-109.
9. Robinson, T., P. Kuhn, K. Eyer, and P. Dittrich, *Microfluidic trapping of giant unilamellar vesicles to study transport through a membrane pore*. *Biomicrofluidics*, 2013. **7**(4): p. 044105.
10. Lin, C.-C., M. Bachmann, S. Bachler, K. Venkatesan, and P.S. Dittrich, *Tunable Membrane Potential Reconstituted in Giant Vesicles Promotes Permeation of Cationic Peptides at Nanomolar Concentrations*. *ACS Applied Materials & Interfaces*, 2018. **10**(49): p. 41909-41916.
11. Bachler, S., C.-C. Lin, and P.S. Dittrich, *Combination of a microfluidic device and fluorescence correlation spectroscopy to study peptide translocation across model membranes*. *Proceedings of the 21st International Conference on Miniaturized Systems for Chemistry and Life Sciences, MicroTAS 2017*, 2017: p. 967-968.
12. Schlicht, B. and M. Zagnoni, *Droplet-interface-bilayer assays in microfluidic passive networks*. *Scientific Reports*, 2015. **5**: p. 9951-9951.

13. Funakoshi, K., H. Suzuki, and S. Takeuchi, *Lipid bilayer formation by contacting monolayers in a microfluidic device for membrane protein analysis*. Analytical Chemistry, 2006. **78**(24): p. 8169-8174.
14. Figeys, D. and D. Pinto, *Lab-on-a-chip: a revolution in biological and medical sciences*. Analytical Chemistry, 2000. **72**(9): p. 330A-335A.
15. Whitesides, G.M., *The origins and the future of microfluidics*. Nature, 2006. **442**(7101): p. 368-373.
16. Thorsen, T., R.W. Roberts, F.H. Arnold, and S.R. Quake, *Dynamic Pattern Formation in a Vesicle-Generating Microfluidic Device*. Physical Review Letters, 2001. **86**(18): p. 4163-4166.
17. Malmstadt, N., M.A. Nash, R.F. Purnell, and J.J. Schmidt, *Automated Formation of Lipid-Bilayer Membranes in a Microfluidic Device*. Nano Letters, 2006. **6**(9): p. 1961-1965.
18. Korner, J.L., E.B. Stephenson, and K.S. Elvira, *A bespoke microfluidic pharmacokinetic compartment model for drug absorption using artificial cell membranes*. Lab on a Chip, 2020. **20**(11): p. 1898-1906.
19. Kitchens, K.M., R.B. Kolhatkar, P.W. Swaan, N.D. Eddington, and H. Ghandehari, *Transport of Poly(Amidoamine) Dendrimers across Caco-2 Cell Monolayers: Influence of Size, Charge and Fluorescent Labeling*. Pharmaceutical Research, 2006. **23**(12): p. 2818-2826.
20. Lee, Y. and S.Q. Choi, *Quantitative analysis for lipophilic drug transport through a model lipid membrane with membrane retention*. European Journal of Pharmaceutical Sciences, 2019. **134**: p. 176-184.
21. Booth, M.J., V. Restrepo Schild, F.G. Downs, and H. Bayley, *Functional aqueous droplet networks*. Molecular BioSystems, 2017. **13**(9): p. 1658-1691.
22. Küster, S.K., S.R. Fagerer, P.E. Verboket, K. Eyer, K. Jefimovs, R. Zenobi, and P.S. Dittrich, *Interfacing Droplet Microfluidics with Matrix-Assisted Laser Desorption/Ionization Mass Spectrometry: Label-Free Content Analysis of Single Droplets*. Analytical Chemistry, 2013. **85**(3): p. 1285-1289.
23. Haidas, D., S. Bachler, M. Köhler, L.M. Blank, R. Zenobi, and P.S. Dittrich, *Microfluidic Platform for Multimodal Analysis of Enzyme Secretion in Nanoliter Droplet Arrays*. Analytical Chemistry, 2019. **91**(3): p. 2066-2073.
24. Bachler, S., D. Haidas, M. Ort, T.A. Duncombe, and P.S. Dittrich, *Microfluidic platform enables tailored translocation and reaction cascades in nanoliter droplet networks*. Communications Biology, 2020.
25. Doktorova, M., *On the Long and Winding Road to a Perfect Membrane Model*. Biophysical Journal, 2020. **118**(2): p. 273-275.
26. Li, S., P. Hu, and N. Malmstadt, *Confocal imaging to quantify passive transport across biomimetic lipid membranes*. Analytical Chemistry, 2010. **82**(18): p. 7766-7771.
27. Leptihn, S., O.K. Castell, B. Cronin, E.-H. Lee, L.C.M. Gross, D.P. Marshall, J.R. Thompson, M. Holden, and M.I. Wallace, *Constructing droplet interface bilayers from the contact of aqueous droplets in oil*. Nature Protocols, 2013. **8**: p. 1048-1057.
28. Venkatesan, G.A., J. Lee, A.B. Farimani, M. Heiranian, C.P. Collier, N.R. Aluru, and S.A. Sarles, *Adsorption Kinetics Dictate Monolayer Self-Assembly for Both Lipid-In and Lipid-Out Approaches to Droplet Interface Bilayer Formation*. Langmuir, 2015. **31**(47): p. 12883-12893.
29. Lang, M., F. Rudolf, and J. Stelling, *Use of YouScope to Implement Systematic Microscopy Protocols*. Current Protocols in Molecular Biology, 2012. **98**(1): p. 14.21.1-14.21.23.
30. Schindelin, J., I. Arganda-Carreras, E. Frise, V. Kaynig, M. Longair, T. Pietzsch, S. Preibisch, C. Rueden, S. Saalfeld, B. Schmid, et al., *Fiji: an open-source platform for biological-image analysis*. Nature Methods, 2012. **9**: p. 676-682.
31. Krämer, S.D., *Quantitative aspects of drug permeation across in vitro and in vivo barriers*. European Journal of Pharmaceutical Sciences, 2016. **87**: p. 30-46.
32. Dixit, S.S., A. Pincus, B. Guo, and G.W. Faris, *Droplet shape analysis and permeability studies in droplet lipid bilayers*. Langmuir, 2012. **28**(19): p. 7442-7451.

33. Hubatsch, I., E.G.E. Ragnarsson, and P. Artursson, *Determination of drug permeability and prediction of drug absorption in Caco-2 monolayers*. Nature Protocols, 2007. **2**(9): p. 2111-2119.
34. Bayley, H., B. Cronin, A. Heron, M.A. Holden, W.L. Hwang, R. Syeda, J. Thompson, and M. Wallace, *Droplet interface bilayers*. Molecular BioSystems, 2008. **4**(12): p. 1191-1208.
35. Trantidou, T., M.S. Friddin, A. Salehi-Reyhani, O. Ces, and Y. Elani, *Droplet microfluidics for the construction of compartmentalised model membranes*. Lab on a Chip, 2018. **18**(17): p. 2488-2509.
36. Hermann, K.F., C.S. Neuhaus, V. Micallef, B. Wagner, M. Hatibovic, H.E. Aschmann, F. Paech, R. Alvarez-Sanchez, S.D. Krämer, and S. Belli, *Kinetics of lipid bilayer permeation of a series of ionisable drugs and their correlation with human transporter-independent intestinal permeability*. European Journal of Pharmaceutical Sciences, 2017. **104**: p. 150-161.
37. Shimanouchi, T., H. Ishii, N. Yoshimoto, H. Umakoshi, and R. Kuboi, *Calcein permeation across phosphatidylcholine bilayer membrane: Effects of membrane fluidity, liposome size, and immobilization*. Colloids and Surfaces B: Biointerfaces, 2009. **73**(1): p. 156-160.
38. Simon, M.J., W.H. Kang, S. Gao, S. Banta, and B.M. Iii, *TAT Is Not Capable of Transcellular Delivery Across an Intact Endothelial Monolayer In Vitro*. Annals of Biomedical Engineering, 2011. **39**(1): p. 394-401.
39. Berginc, K., S. Žakelj, L. Levstik, D. Uršič, and A. Kristl, *Fluorescein transport properties across artificial lipid membranes, Caco-2 cell monolayers and rat jejunum*. European Journal of Pharmaceutics and Biopharmaceutics, 2007. **66**(2): p. 281-285.
40. Cruysberg, L.P.J., R.M.M.A. Nuijts, D.H. Geroski, L.H. Koole, F. Hendrikse, and H.F. Edelhauser, *In Vitro Human Scleral Permeability of Fluorescein, Dexamethasone-Fluorescein, Methotrexate-Fluorescein and Rhodamine 6G and the Use of a Coated Coil as a New Drug Delivery System*. Journal of Ocular Pharmacology and Therapeutics, 2002. **18**(6): p. 559-569.
41. Taylor, G., M.-A. Nguyen, S. Koner, E. Freeman, C.P. Collier, and S.A. Sarles, *Electrophysiological interrogation of asymmetric droplet interface bilayers reveals surface-bound alamethicin induces lipid flip-flop*. Biochimica et Biophysica Acta (BBA) - Biomembranes, 2019. **1861**(1): p. 335-343.
42. Contreras, F.X., L. Sánchez-Magraner, A. Alonso, and F.M. Goñi, *Transbilayer (flip-flop) lipid motion and lipid scrambling in membranes*. FEBS Letters, 2010. **584**(9): p. 1779-1786.

## 4.8 Supplementary Information

### 4.8.1 Fluorophore Permeation Fitting and Calculation Values

Table 4-S1: Summary of the fitting results with Equations 1 and 2, and calculation of the apparent permeability coefficient according Equation 3 for all fluorescence experiments.

Fluorophore	pH	Membrane composition		$k_{da} \times 10^{-6}$ (1/s)		$k_{ad} \times 10^{-6}$ (1/s)		~DIB diameter ( $\mu\text{m}$ )		$P_{app,fit} \times 10^{-6}$ (cm/s)	
		Donor	Acceptor	Mean	SD	Mean	SD	Mean	SD	Mean	SD
Fluorescein	6	100% DOPC	100% DOPC	4046.0	315.7	4046.0	315.7	259	4.7	193.03	17.79
Fluorescein	7	100% DOPC	100% DOPC	145.0	9.8	145.0	9.8	256	6.7	7.05	0.42
Fluorescein	8	100% DOPC	100% DOPC	20.3	1.2	20.3	1.2	248	3.2	1.05	0.06
PEG4-NBD	6	100% DOPC	100% DOPC	818.1	66.3	818.1	66.3	218	3.7	54.88	3.80
Rhodamine 6G	6	100% DOPC	100% DOPC	166.8	14.1	166.8	14.1	226	5.0	10.42	0.98
Rhodamine 6G	6	100% DOPC	30% DOPC 70% DOPS	99.8	13.2	99.8	13.2	220	3.7	6.56	0.85
Rhodamine 6G	6	30% DOPC 70% DOPS	30% DOPC 70% DOPS	112.8	15.1	112.8	15.1	173	16.1	12.12	1.66
Rhodamine 6G	6	30% DOPC 70% DOPS	100% DOPC	251.9	38.3	251.9	38.3	204	26.5	19.60	3.50

### 4.8.2 Graphs and Microscopy Images for the Permeation of Fluorophores across Symmetric and Asymmetric DIBs

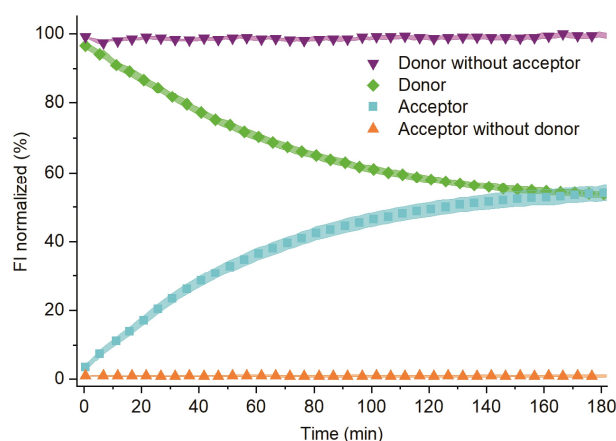


Figure 4-S1: Permeation of rhodamine 6G across 100% DOPC droplet interface bilayer membranes at pH 6.0. Mean fluorescence intensity (FI) over time from the donor and acceptor droplets. The fluorescence intensity values were normalized to 100% for the starting fluorescence of the individual donor plus acceptor droplets in the first image (data before further normalization at each time point). The color-shaded areas represents the standard deviation of every data point.  $N = 27$  connecting donor/acceptor droplet pairs.  $N = 9$  for the donor without acceptor and  $N = 9$  for acceptor without donor droplets. Further normalized data and fluorescence images are shown in Fig. 4-2A and 4-2B.

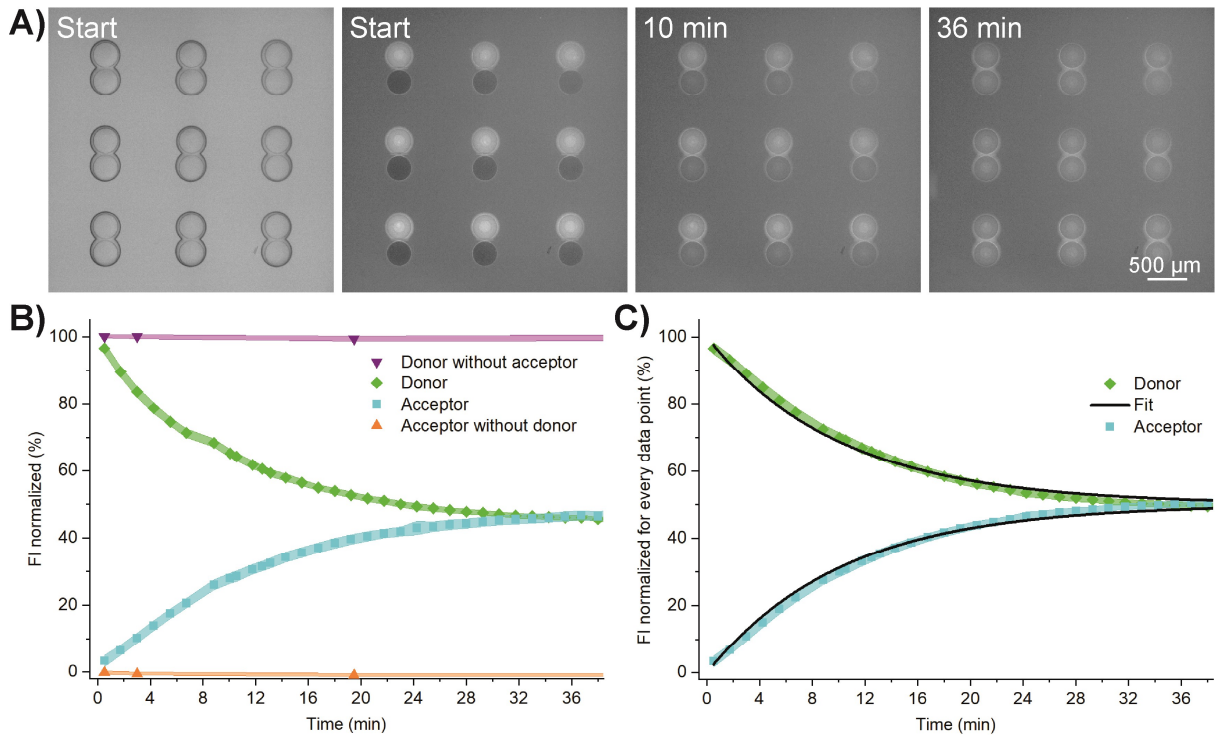


Figure 4-S2: Permeation of PEG4-NBD across 100% DOPC DIBs at pH 6.0. A) Bright-field (top left) and fluorescent images of PEG4-NBD permeation from donor into acceptor droplets. B) Mean fluorescence intensity (FI) and standard deviations for droplet pairs and controls ( $N = 27$  for droplet pairs and  $N = 9$  for controls). C) In addition to the normalization to the starting fluorescence (Fig. 4-S2B), every data point was normalized to the FI of the donor and acceptor droplets (equals 100% at the given time).

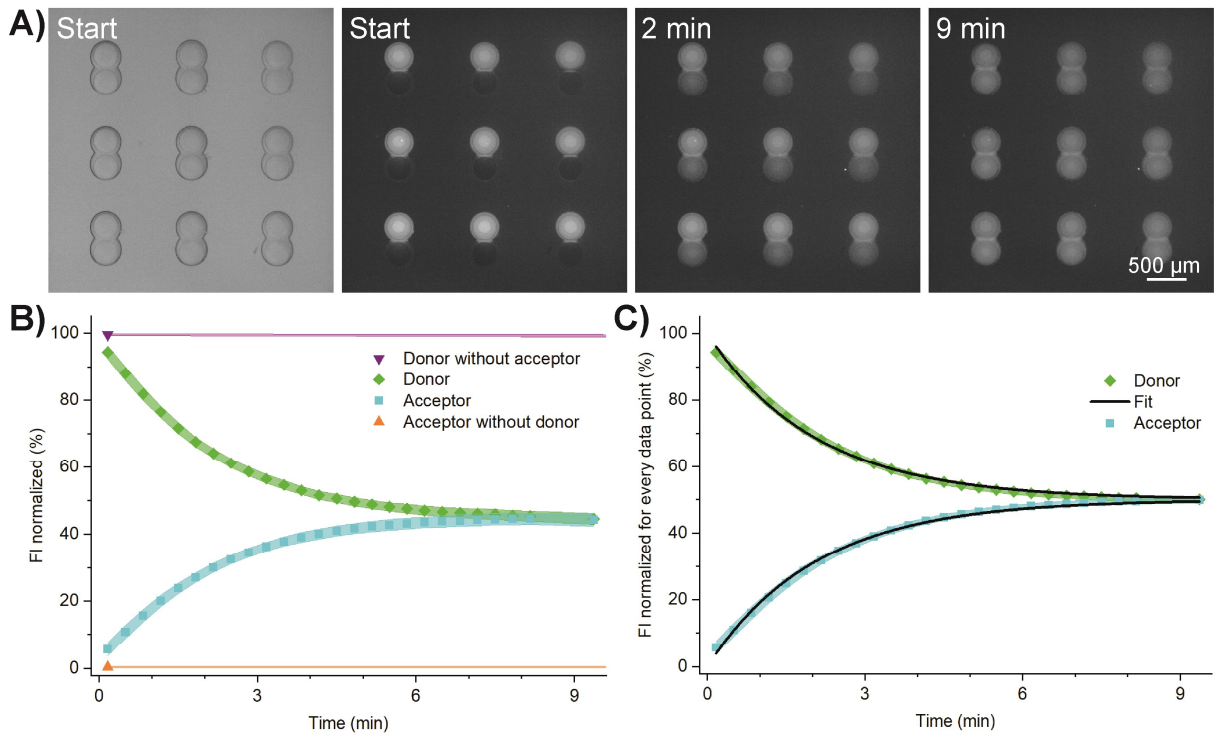


Figure 4-S3: Permeation of fluorescein across 100% DOPC DIBs at pH 6.0. A) Bright-field (top left) and fluorescent images of fluorescein permeation from donor into acceptor droplets. B) Mean fluorescence intensity (FI) and standard deviation over time for droplet pairs and control droplets without DIB ( $N = 27$  for droplet pairs and  $N = 9$  for controls). C) In addition to the normalization to the starting fluorescence (Fig. 4-S3B), every data point was normalized to the FI of the donor and acceptor droplets (equals 100% at the given time).



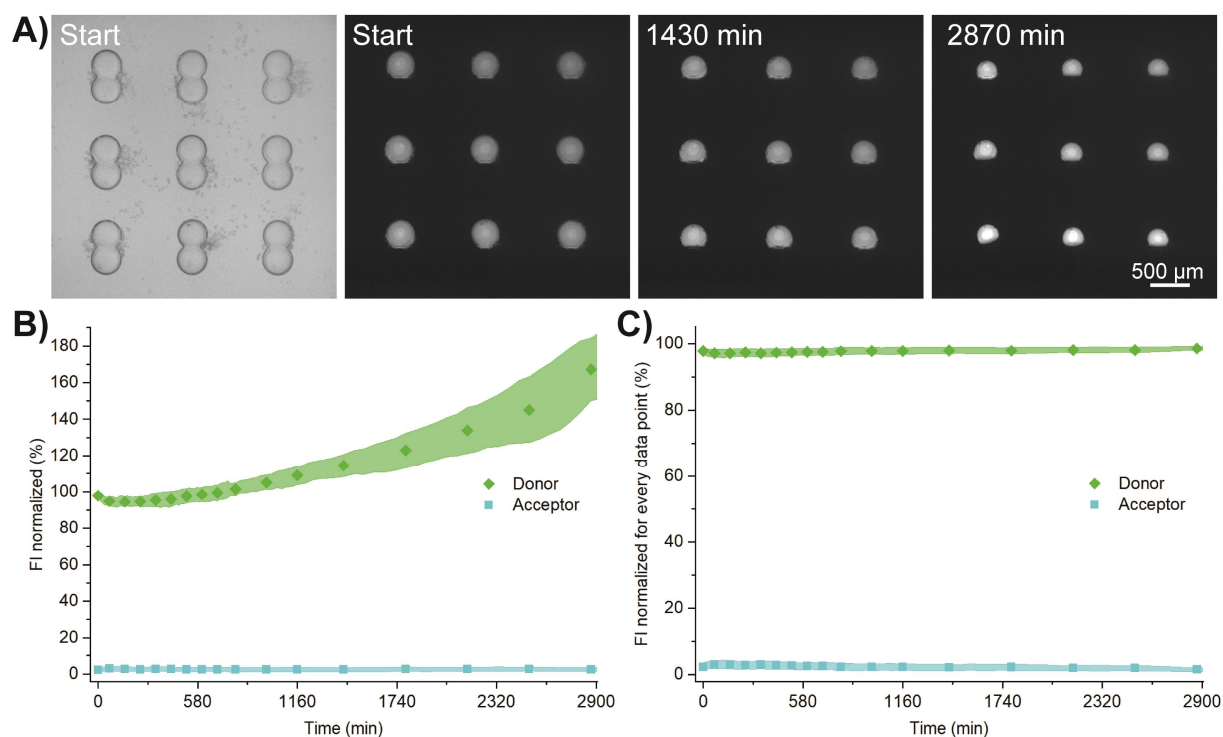


Figure 4-S4: Calcein did not permeate across 100% DOPC DIBs at pH 6.0. A) Bright-field (top left) and fluorescent images of droplet pairs, where the donor droplet is filled with calcein. B) Mean fluorescence intensity (FI) and standard deviation over time of calcein in donor and acceptor droplets. Note the observation time of 2900 minutes (~2 days), where no calcein was observable in the acceptor droplet. The increase of FI in the donor droplet is due to droplet shrinkage, i.e. water dissipates into the oil phase ( $N = 27$  droplet pairs). C) In addition to the normalization to the starting fluorescence (Fig. 4-S4B), every data point was normalized to the FI of the donor and acceptor droplets (equals 100% at the given time). Fitting was not possible in this experiment.

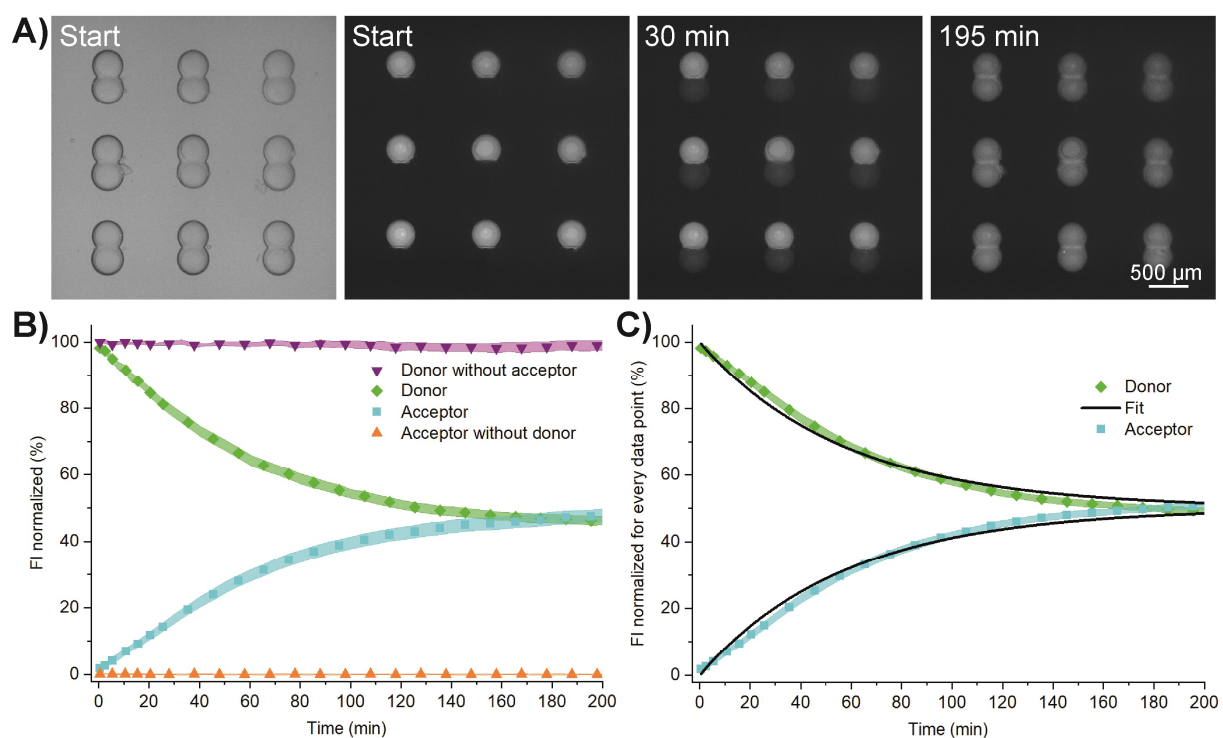


Figure 4-S5: Permeation of fluorescein across 100% DOPC DIBs at pH 7.0. A) Bright-field (top left) and fluorescent images of fluorescein permeation from donor into an acceptor droplets. B) Mean fluorescence intensity (FI) and standard deviations over time for connected droplet pairs and isolated droplets (controls) ( $N = 27$  for droplet pairs

## Chapter 4

$N = 9$  for controls). C) In addition to the normalization to the starting fluorescence (Fig. 4-S5B), every data point was normalized to the FI of the donor and acceptor droplets (equals 100% at the given time).

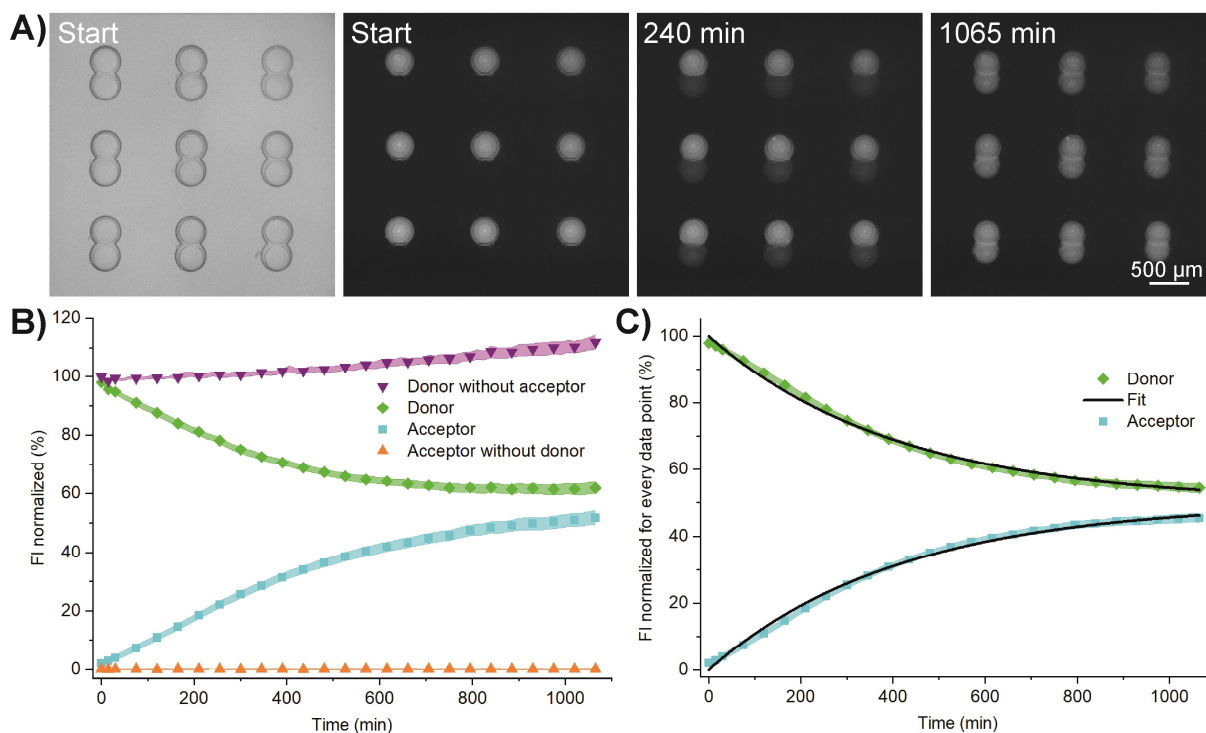


Figure 4-S6: Permeation of fluorescein as in figure 4-S5, except here at  $pH = 8.0$ . Note the slow permeation in figure 4-6B. Here, the increase in FI over time is observed due to slow droplet shrinkage.

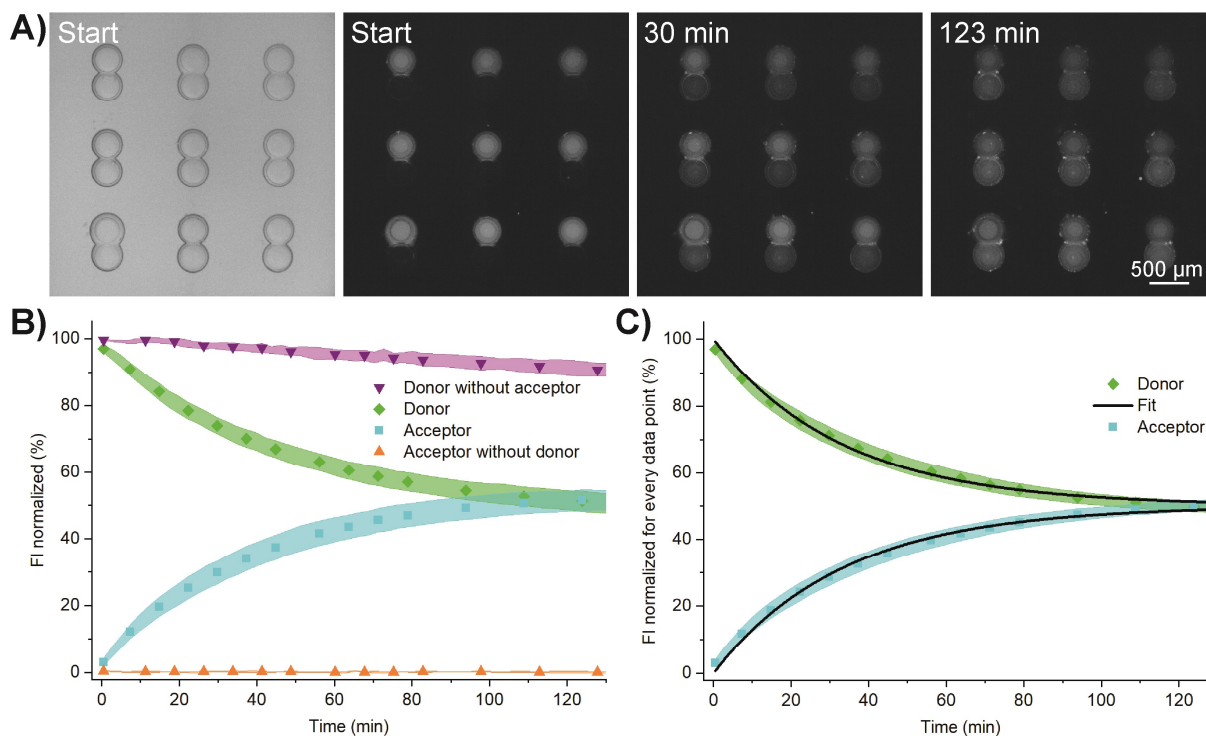


Figure 4-S7: Permeation of rhodamine 6G across asymmetric DIBs at  $pH 6.0$ , here lipid monolayer of donor droplet: 30% DOPC 70% DOPS; and lipid monolayer of acceptor droplet: 100% DOPC. A) Bright-field (top left) and fluorescent images of rhodamine 6G permeation from donor into acceptor droplets. B) Mean fluorescence intensity (FI) and standard deviations over time of rhodamine 6G in connected droplets and controls of isolated donor and

acceptor droplets, respectively ( $N = 27$  for droplet pairs and  $N = 9$  for controls). C) Same data as in S7B, but every data point was normalized to the FI of the donor and acceptor droplets (equals 100% at the given time).

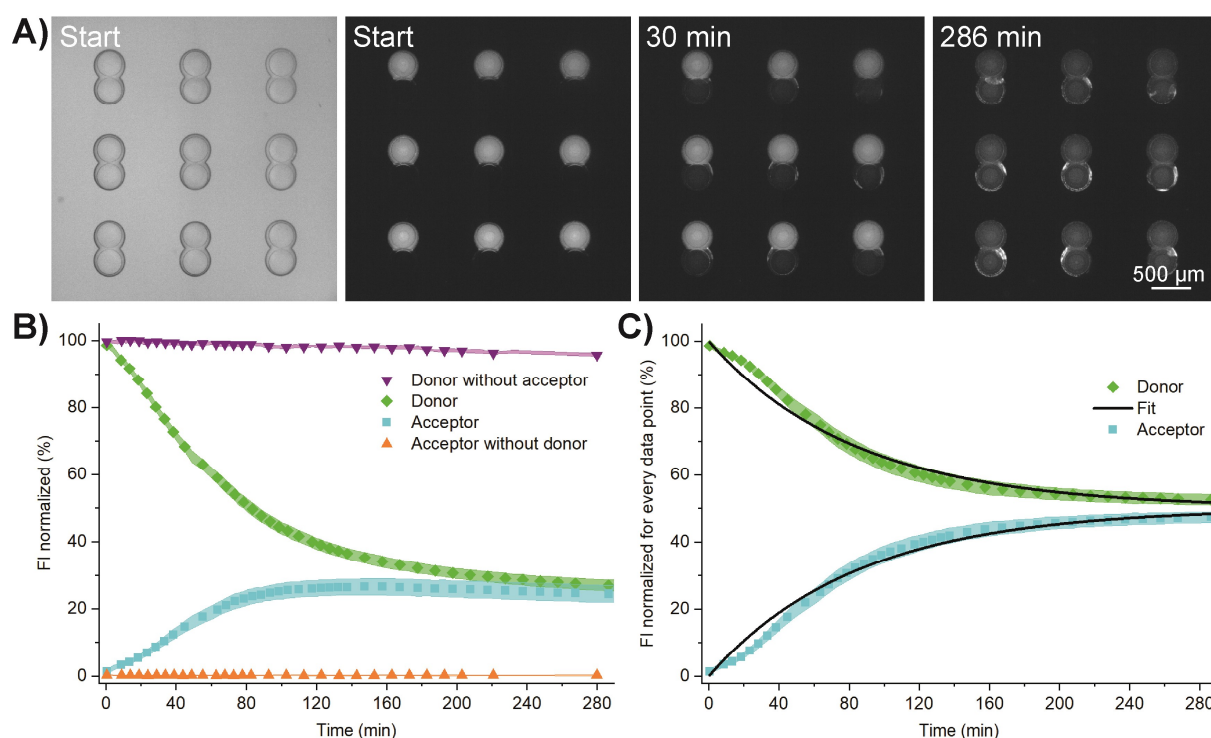


Figure 4-S8: Same as before. The lipid monolayer of donor droplets consists of 100% DOPC and lipid monolayer of acceptor droplets of 30% DOPC 70% DOPS.

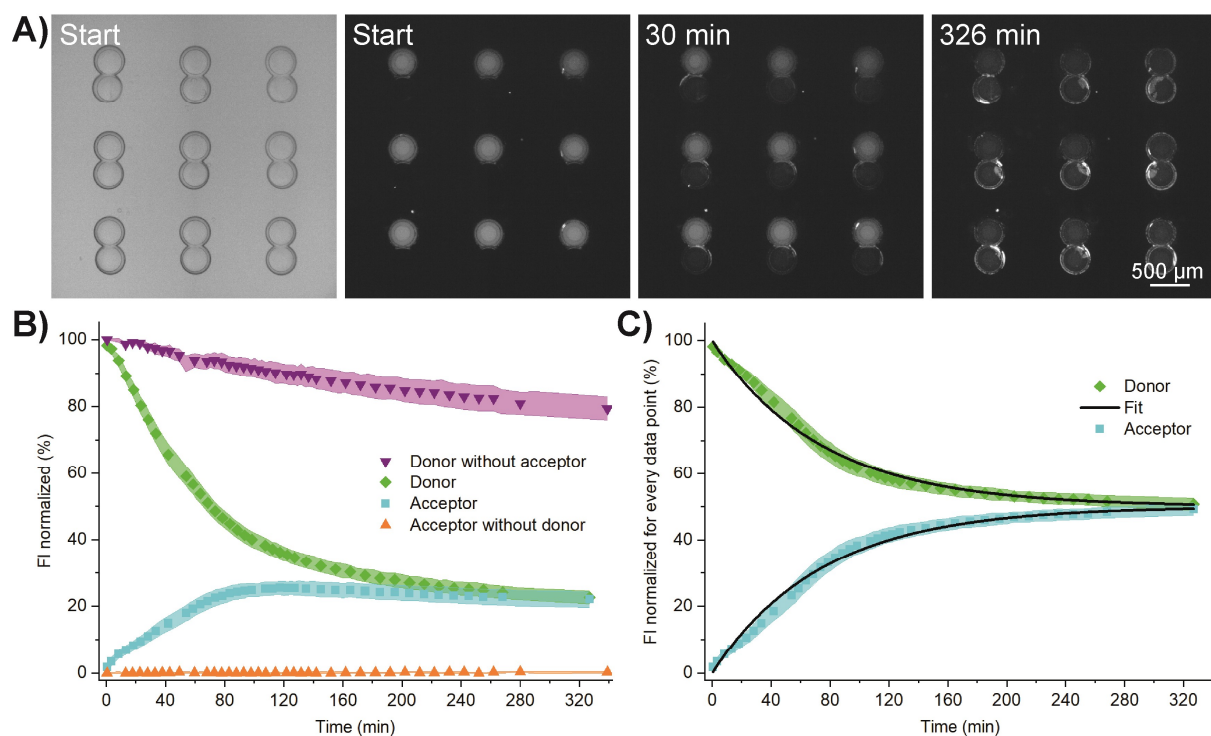


Figure 4-S9: Permeation of rhodamine 6G across a symmetric DIB at pH 6.0 composed of 30% DOPC 70% DOPS. A) Bright-field (top left) and fluorescent images of rhodamine 6G permeation from donor into acceptor droplets. B) Mean fluorescence intensity (FI) and standard deviations over time for droplet pairs and individual, non-connected droplets filled with rhodamine 6G ("donor without acceptor") or buffer only ("acceptor without donor")

( $N = 27$  for droplet pairs and  $N = 9$  for controls). C) Same data as in S9B, but every data point was normalized to the FI of the donor and acceptor droplets (equals 100% at the given time).

### 4.8.3 Graphs and Microscopy Images for the Permeation across Multiple Compartments

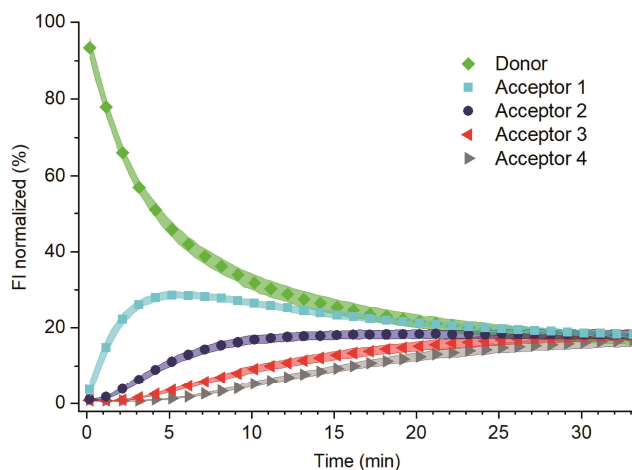


Figure 4-S10: Permeation of fluorescein across 100 % DOPC DIBs over multiple compartments (all at pH 6.0), which are arranged in a line. Mean fluorescence intensity (FI) and standard deviations over time for fluorescein from one donor to four acceptor droplets ( $N = 12$  droplet networks). Further normalized data and fluorescence images are shown in Fig. 4-4.

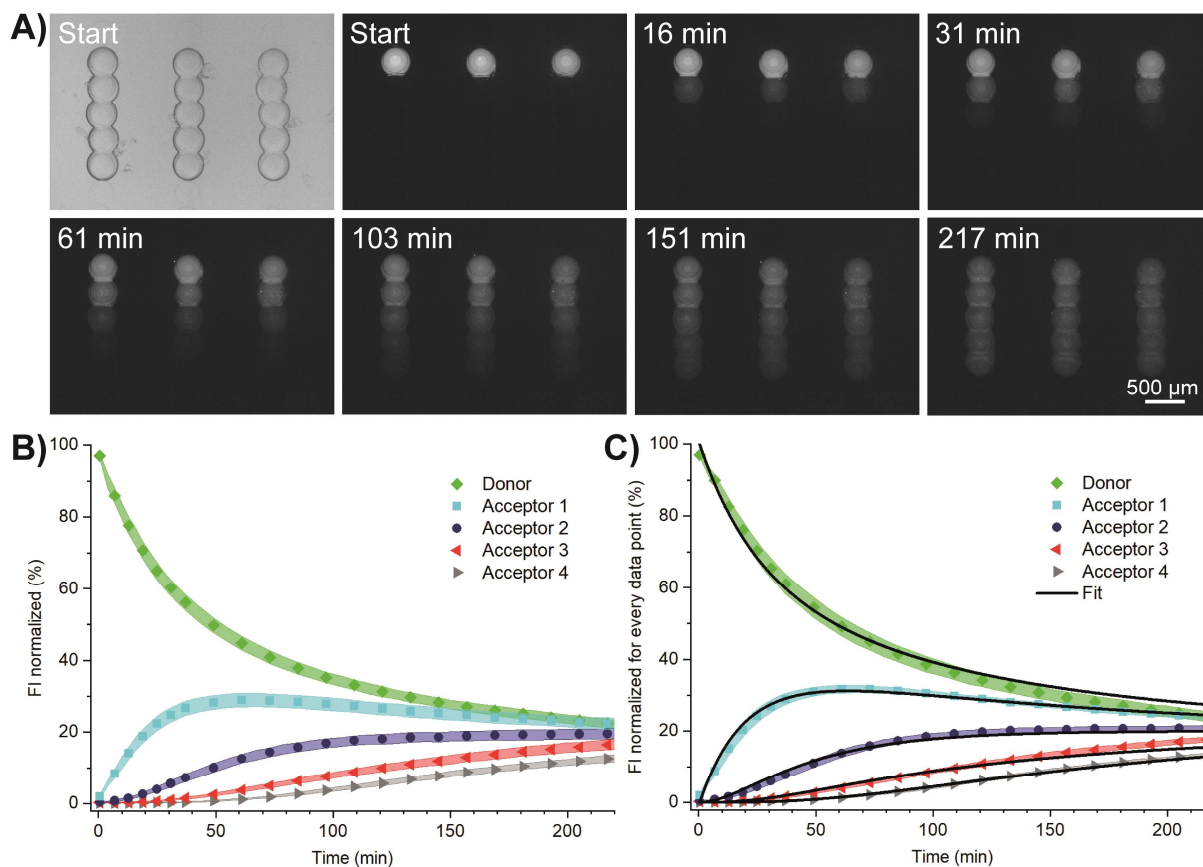


Figure 4-S11: Permeation of fluorescein over multiple compartments at pH 7.4. A) Bright-field (top left) and fluorescent images of fluorescein permeation from one donor droplet into four acceptor droplets. B) Mean fluorescence intensity (FI) and standard deviations over time ( $N = 12$  droplet networks). C) Same data as in

*Figure 4-S11B, but every data point was normalized to the FI of the donor and acceptor droplets (equals 100% at the given time). Black lines, fit according to Equations 5-7 in the main manuscript.*

#### **4.8.4 Videos**

The videos can be found in the electronic supplementary information after the paper is published.

Video 4-S1: Droplet spotting

Video 4-S2: Droplet separation

Video 4-S3: Droplet aspiration

## **Chapter 5**

# **Conclusion and Outlook**

## 5.1 General Conclusion

In this thesis, we presented microfluidic devices for studying and manipulating artificial cell membranes and compartments. These model systems are realized using vesicles or droplet interface bilayers (DIBs). They can be applied to a wide range of applications from bioanalytics, to biomimetics, to pharmacological permeation studies. Microfluidic methods provide precise control at the microscale. We use this to our advantage to form monodisperse artificial cell compartments, with a thickness and composition similar to that of cellular lipid membranes. By utilizing microfluidics during experiments, we could control the experimental conditions more precisely than is possible in bulk assays.

Our improved microfluidic hydrodynamic trap array for vesicles (or cells) constitutes a valuable platform for model drug or toxin testing. The design of the microfluidic chip was adapted from a previous design [1] to implement multiple traps in each chamber to increase the probability of giant lipid vesicle loading. The platform was able to visualize interactions of peptides and toxins with artificial cell membranes. Fluorescence correlation spectroscopy was applied to observe translocation down to the low nanomolar concentrations, which further reduces saturation phenomena and material consumption. Moreover, we visualized membranolytic effects and tested active and selective anticancer or antimicrobial peptides. It was possible to mimic the membrane of a cancer cell or bacteria to study the membrane-rupture process and confirm the selectivity of certain peptides. To illustrate the rupturing effect, we used relatively high peptide concentrations of 100  $\mu\text{M}$ . Our approach may be used to find minimal effective concentrations and thus compare the potency of membranolytic peptides. Furthermore, we observed pneumolysin binding to vesicle membrane and pore formation. We provided a better understanding of the pore-forming process and with further experiments evidence for the existence of plasmalemmal domains that are able to attract pneumolysin at high local concentrations. During the investigation of protein-membrane interactions of pneumolysin on individual multilamellar giant vesicles, we observed membrane wrinkling, membrane surface enlargements, and in some experiments an unexpected layer-by-layer peeling effect. The number of lamellae of giant vesicles was revealed with transmission wide-field microscopy without being restricted by photobleaching as in other studies [2]. While powerful for many applications, the hydrodynamic trap platform has a several major limitations, including vesicle polydispersity and encapsulation of substances. To address this, we developed a novel microfluidic platform for immobilizing and forming of artificial cell membranes and compartments.

The presented platform forming DIBs allowed the formation of tailored 1D or 2D artificial cell networks with a spotting device. The transparent T-junction offered the possibility to monitor the droplet generation more precisely compared to previously developed spotting platforms [3].

Many other studies use closed systems and PDMS to generate DIBs with some shortcomings [4-6]. Our open system circumvents these limitations and enables manipulation and extraction of the droplets. Fluorescence-based readouts are often the method of choice in droplet-based microfluidic platforms for analytical applications when a fluorescent label for the particular experiment is available. Unfortunately, for many applications no such fluorescent probe is available. Mass spectrometry offers an alternative readout that is able to detect (simultaneous and multiple) analytes without a fluorescent label. Due to the open microarray, we were able to perform label-free droplet content analysis. This greatly increases the possibilities for detection of molecules compared to closed microfluidic systems that are overwhelmingly reliant on fluorescence microscopy.

We demonstrated the versatility of our platform by the creation of a cascade reaction, in which reactants and enzymes are initially separated in different compartments. Further, we investigated specific aspects of the permeation process, which allowed for systematic testing of various parameters. Measured permeability coefficients using our system for fluorescein were in the range of other studies with DIBs and Caco-2 cellular monolayers [6, 7]. The membrane compositions were easily altered, and symmetric and asymmetric membranes were formed to investigate different experimental conditions.

The microfluidic platforms presented in this thesis are highly suitable for fundamental studies on membrane transport processes. We demonstrated the generation and use of DIB arrays with a high degree of flexibility and parallelization that has not been reported to this extent before. Furthermore, the platform enables a superior throughput in comparison to conventional pipetting techniques. The interconnected droplet networks offer a powerful tool for studying translocation and reaction cascades across compartments, or generally, any interactions of molecules with lipid membranes such as permeation and pore formation.



## 5.2 Outlook

In general, the presented platforms could become relevant for drug screening in the future. On the one hand, to predict the absorption in the gut. On the other hand, when the medicine has to cross specific cell membranes, e.g. when the target is in the cell. Our assays would allow ranking and classifying different drugs according to the BCS, which could support decisions in drug development. Besides, to assess off-target side effects it could be relevant if a substance reaches the target via permeating across different cell membranes or not. A drug could be tailored specifically for certain membrane types. Moreover, microfluidics only consumes low sample amounts for the experiments and this is especially relevant in the field of medicinal chemistry, where newly synthesized drug candidates sometimes are only available in limited amounts. Therefore, the reduction of sample size could present a significant advantage.

The hydrodynamic trap method could help to investigate new therapeutic peptides and be employed as a rapid testing method for cytotoxic, cell-lysing, and pore-forming molecules. Vesicle focusing structures on the chip could further increase the vesicle loading of the traps in the individual chambers.

The microfluidic DIB platform can be employed for several membrane studies, e.g., it facilitates transporter or permeation studies as required for drug discovery and drug testing with symmetric and asymmetric membranes. The observations could help to increase the understanding of the permeation process itself. Our platform could mimic a simple cell / organelle model such as a mitochondria membrane in a cell, or artificial cell clusters or tissue. The platform may prove useful for other studies such as artificial cellular networks and transporter studies or molecule-receptor binding with cell-derived membranes [8]. For example, cell-derived vesicles containing the membrane P-glycoprotein could be fused with DIBs. In addition, we were able to stop translocation and disrupt the DIBs by separating droplets. This could be exploited to stop supplies to the adjacent droplet e.g. for an enzymatic reaction.

Surface electrodes could be added to allow the use of parallel electrophysiology [9]. To achieve longer lasting experiments, DIBs could be encapsulate in a thermoreversible organogel [10]. Smaller droplet size can be achieved with other microfluidic T-junctions, which would allow for the possibility of more spotted droplets per plate as well as more different experimental conditions. Replacing the T-junction and parts of the spotting capillary with a PDMS [11] (or another material) or 3D printed chip could serve this purpose and would enable the execution of additional steps in this chip. For example, it would be possible to integrate fast mixing of different solutions and to spot on-demand specific droplets by adding microfluidic valves for quickly switching solutions.

Complex three-dimensional droplet network on a plate or in a chamber could be generated with our platform. As an inspiration Figure 5-1 shows aqueous droplets assembled as a three-dimensional network in a hanging oil drop at the spotting capillary. The platform could be used to generate a tissue-like material printed as a 3D aqueous droplet network [12], where the droplet are precisely positioned.



*Figure 5-1: Photograph of the spotting capillary with a three-dimensional droplet network in a hanging drop. The aqueous phase consisted of 50  $\mu$ M rhodamine 6G in 20 mM MES and the oil phase consisted of 0.625 mM DOPC in 1:1 hexadecane/squalane.*

The content analysis of droplets by mass spectrometry would allow for the multiplexed analysis of other unknown and/or unlabeled compounds. We used LC-MS as a quantitative method in contrast to MALDI-MS, which we only used to detect if a substance is present or not. However, MALDI-MS could also become useful for quantitative applications with an internal standard [13]. Furthermore, we believe our platform opens the door for experiments with DIBs in the field of synthetic biology, where fluorescence labelling is not possible.

To increase the analytical throughput of the platform, an automated interface could be added. An auto-sampler could allow for faster droplet solution changes and on-demand spotting. Further, the interface between the spotting device and the MALDI-MS or LC-MS should be improved. Robots for liquid handling could be combined with our platform. Moreover, the sensitivity of detecting the content of a single droplet could be improved with other MS devices. Another possibility to achieve higher throughput would be the use of surface-facilitated droplet array generation [14] for acceptor droplets (with the same content) and then spotting donor droplets on top of the generated array.

The developed platform is not limited to fluorescence and mass spectrometry readouts, its open design could be integrated with additional bioanalytical methods. For example, UV-vis spectroscopy, surface plasmon resonance, confocal Raman microscopy, and focal molography [15] could potentially be used to analyze reactions and biopharmaceutically relevant permeation kinetics of molecules without fluorescent labels. Furthermore, it is possible to detect potential oil residues in DIBs with Raman scattering spectroscopy [16].

Overall, the developed platforms form a powerful foundation for studying lipid bilayers. Going forward, their high accessibility for modifications and improvements in readouts and throughput makes it highly adaptable for a large range of analytical applications.

## 5.3 References

1. Robinson, T., P. Kuhn, K. Eyer, and P. Dittrich, *Microfluidic trapping of giant unilamellar vesicles to study transport through a membrane pore*. *Biomicrofluidics*, 2013. **7**(4): p. 044105.
2. Akashi, K., H. Miyata, H. Itoh, and K. Kinoshita, Jr., *Preparation of giant liposomes in physiological conditions and their characterization under an optical microscope*. *Biophys J*, 1996. **71**(6): p. 3242-50.
3. Küster, S.K., S.R. Fagerer, P.E. Verboket, K. Eyer, K. Jefimovs, R. Zenobi, and P.S. Dittrich, *Interfacing Droplet Microfluidics with Matrix-Assisted Laser Desorption/Ionization Mass Spectrometry: Label-Free Content Analysis of Single Droplets*. *Analytical Chemistry*, 2013. **85**(3): p. 1285-1289.
4. Nuti, N., P.E. Verboket, and P.S. Dittrich, *Multivesicular droplets: a cell model system to study compartmentalised biochemical reactions*. *Lab on a Chip*, 2017. **17**(18): p. 3112-3119.
5. Dangla, R., F. Gallaire, and C.N. Baroud, *Microchannel deformations due to solvent-induced PDMS swelling*. *Lab on a Chip*, 2010. **10**(21): p. 2972-2978.
6. Schlicht, B. and M. Zagnoni, *Droplet-interface-bilayer assays in microfluidic passive networks*. *Scientific Reports*, 2015. **5**: p. 9951-9951.
7. Berginc, K., S. Žakelj, L. Levstik, D. Uršič, and A. Kristl, *Fluorescein transport properties across artificial lipid membranes, Caco-2 cell monolayers and rat jejunum*. *European Journal of Pharmaceutics and Biopharmaceutics*, 2007. **66**(2): p. 281-285.
8. Eyer, K., M. Herger, S.D. Krämer, and P.S. Dittrich, *Cell-Free Microfluidic Determination of P-glycoprotein Interactions with Substrates and Inhibitors*. *Pharmaceutical Research*, 2014. **31**(12): p. 3415-3425.
9. Nguyen, M.-A., B. Srijanto, C.P. Collier, S.T. Retterer, and S.A. Sarles, *Hydrodynamic trapping for rapid assembly and in situ electrical characterization of droplet interface bilayer arrays*. *Lab on a Chip*, 2016. **16**(18): p. 3576-3588.
10. Challita, E.J., J.S. Najem, R. Monroe, D.J. Leo, and E.C. Freeman, *Encapsulating Networks of Droplet Interface Bilayers in a Thermoreversible Organogel*. *Scientific Reports*, 2018. **8**(1): p. 6494.
11. Chang-Yen, D.A., D.G. Myszka, and B.K. Gale, *A novel PDMS microfluidic spotter for fabrication of protein chips and microarrays*. *Journal of microelectromechanical systems*, 2006. **15**(5): p. 1145-1151.
12. Villar, G., A.D. Graham, and H. Bayley, *A Tissue-Like Printed Material*. *Science*, 2013. **340**(6128): p. 48-52.
13. Duncan, M.W., H. Roder, and S.W. Hunsucker, *Quantitative matrix-assisted laser desorption/ionization mass spectrometry*. *Briefings in Functional Genomics*, 2008. **7**(5): p. 355-370.
14. Sakakihara, S., S. Araki, R. Iino, and H. Noji, *A single-molecule enzymatic assay in a directly accessible femtoliter droplet array*. *Lab on a Chip*, 2010. **10**(24): p. 3355-3362.
15. Fattering, C., *Focal Molography: Coherent Microscopic Detection of Biomolecular Interaction*. *Physical Review X*, 2014. **4**(3): p. 031024-031024.
16. Kirchner, S.R., A. Ohlinger, T. Pfeiffer, A.S. Urban, F.D. Stefani, A. Deak, A.A. Lutich, and J. Feldmann, *Membrane composition of jetted lipid vesicles: a Raman spectroscopy study*. *Journal of Biophotonics*, 2012. **5**(1): p. 40-46.

# Acknowledgements

I would like to especially thank Prof. Petra S. Dittrich for the supervision of this dissertation and the opportunity to work in her research group at ETH Zurich. Further, I would like to express my gratitude and appreciation to Prof. Dr. Stefanie D. Krämer as committee member and for her help regarding the permeability studies, Prof. Dr. Martin Kuentz as committee member, and Prof. Dr. Kobi Benenson as chair of the doctoral defense committee.

Many people helped me with their experience or in another way for the projects discussed in this thesis. I would like to thank the mechanical workshop team (ETH Zurich) Christoph Bärtschi, Christian Marro, Paul Argast, and Peter Buchmann for the fabrication of mechanical devices. Moreover, I appreciate Alexander Stettler, Peter Rimpf, Albert Martel, and Tomislav Rebac for help with the clean room processes in the clean room facility in Basel (ETH Zurich). I am thankful to all the people working at the clean room facility FIRST in Zurich, HCI shop, biophysics facility at Biozentrum Basel, and everyone from the D-BSSE services in Basel (IT, shop, infrastructure, administration, and single-cell facility).

I particularly acknowledge Dr. Dominik Haidas for working together with me to develop the spotting platform, for helpful discussions, and for programming scripts. Very special thanks goes to the former master students Céline Del Don and Marion Ort for conducting experiments (under my supervision) and helpful discussions. Furthermore, I want to thank Dr. Chao-Chen Lin and Dr. Nikolaus Naredi-Rainer for help with fluorescence correlation spectroscopy and optical setups. I am also very grateful to my collaboration partners: Dr. Patrick Drücker, Dr. Todd A. Duncombe, Dr. Alex T. Müller, Dr. Claudia S. Neuhaus, Damian Gautschi, Prof. Dr. Annette Draeger, Dr. Eduard B. Babiychuk, Prof. Dr. Gisbert Schneider, Dr. Jan A. Hiss, Dr. Volker Gatterdam, Andreas Frutiger, Prof. Dr. Janos Vörös, Dr. Christof Fattinger, Dr. Marcel Grogg, Dr. Angéline Kernalléguen, Dr. Robert Steinhoff, Dr. Joanna Hajduk, Prof. Dr. Renato Zenobi, and Prof. Dr. Peter J. Walde.

Many thanks to all other current and former bioanalytics laboratory members: Dr. Lucas Armbrecht, Yannick Schmid, André Kling, Dr. Mario Saucedo Espinosa, Dr. Darius Rackus, Dr. Felix Kurth, Dr. Bernhard Sebastian, Dr. Mario Lenz, Dr. Pascal Verboket, Dr. Simone Stratz, Ariane Stucki, Andrea Marti, Nicola Nuti, Elisabeth Hirth, Jonas Nikoloff, Dr. Petra Jusková, Simon Berlanda, Maximilian Breitfeld, Claudius Dietsche, and Bianca Mikulasek.

Finally yet importantly, I want to thank all my friends and my family for the tremendous amount of support. I am especially grateful to my parents, Milena, and my brother.

# Abbreviations

$\alpha$ -HL	Alpha-hemolysin
ACP	Anticancer peptide
ADME	Absorption, distribution, metabolism, and excretion
ADP	Adenosine diphosphate
AF	Ammonium formate
AMP	Antimicrobial peptide
API-ES	Atmospheric pressure ionization-electrospray
ATP	Adenosine triphosphate
BCS	Biopharmaceutical classification system
BDDCS	Biopharmaceutical drug disposition classification system
BSA	Bovine serum albumin
Chol	Cholesterol
CPP	Cell-penetrating peptide
DCS	Developability classification system
DHB	2,5-dihydroxybenzoic acid
DIB	Droplet interface bilayer
DiD	1,1'-dioctadecyl-3,3,3',3'-tetramethylindodicarbocyanine perchlorate
Dil	1,1'-dioctadecyl-3,3,3',3'-tetramethylindocarbocyanine perchlorate
DLS	Dynamic light scattering
DMSO	Dimethyl sulfoxide
DNA	Deoxyribonucleic acid
DOPC	1,2-dioleoyl-sn-glycero-3-phosphocholine
DOPE	1,2-dioleoyl-sn-glycero-3-phosphoethanolamine
DOPS	1,2-dioleoyl-sn-glycero-3-phospho-L-serine
DPhPC	1,2-diphytanoyl-sn-glycero-3-phosphocholine
EDTA	Ethylenediaminetetraacetic acid

FCS	Fluorescence correlation spectroscopy
FI	Fluorescence intensity
FITC	Fluorescein isothiocyanate
FL	Fluorescein
GOx	Glucose oxidase
GUV	Giant unilamellar vesicle
GV	Giant vesicle
HEPES	4-(2-hydroxyethyl)-1-piperazineethanesulfonic acid
HIV	Human immunodeficiency virus
HRP	Horseradish peroxidase
ITO	Indium tin oxide
LC-MS	Liquid chromatography-mass spectrometry
LOC	Lab-on-chip
LUV	Large unilamellar vesicle
MALDI-MS	Matrix-assisted laser desorption/ionization mass spectrometry
MDCK	Madin-Darby canine kidney
MES	2-morpholinoethanesulfonic acid
MLV	Multi-lamellar vesicle
MS	Mass spectrometry
NBD	Nitrobenzofurazan
NBD-F	4-fluoro-7-nitrobenzofurazan
NHS	1-hydroxy-2,5-pyrrolidindion
PAMPA	Parallel artificial membrane permeability assay
$P_{app}$	Apparent permeability
PBS	Phosphate buffered saline
PC	Phosphatidylcholine
PDMS	Polydimethylsiloxane
PEEK	Polyether ether ketone
PEG	Poly(ethylene glycol)

## Abbreviations

PLY	Pneumolysin
PS	Phosphatidyl-L-serine
PSA	Polar surface area
PTFE	Polytetrafluoroethylene
PVA	Poly(vinyl alcohol)
SD	Standard deviation
SIM	Selected ion monitoring
SUV	Small unilamellar vesicle
TAT	Trans-acting activator of transcription
TIRF	Total internal reflection fluorescence
Tris	Tris(hydroxymethyl)aminomethane
UV-vis	Ultraviolet-visible
μTAS	Miniaturized total analysis systems



# Curriculum Vitae

**Name:** Simon Bachler  
**Date of birth:** 11<sup>th</sup> January 1989  
**Nationality:** Swiss  
**E-Mail:** simon.bachler@bsse.ethz.ch

## Education

05/2015 – 06/2020 Doctoral Student, ETH Zurich  
09/2012 – 12/2014 Master of Science in Pharmaceutical Sciences, University of Basel  
09/2009 – 09/2012 Bachelor of Science in Life Science Technologies with Major in Pharmaceutical Technology, University of Applied Sciences and Arts Northwestern Switzerland (FHNW)  
08/2004 – 07/2008 Technical Professional Certification, Allgemeine Gewerbeschule Basel

## Work Experience

05/2015 – 07/2020 Scientific Assistant, ETH Zurich  
08/2008 – 07/2009 Technical Designer (Konstrukteur), Novartis  
08/2004 – 07/2008 Apprenticeship as a Technical Designer, Novartis

## Awards

Best Poster Award at the Membrane Lipids Symposium in Berlin, 2019  
Roche Life Science Award, 2012

## Supervision

M. Ort, Master Thesis: Evaluation of a novel drug permeability screening platform combining microfluidics and liquid chromatography-mass spectrometry, 06/2017 – 05/2018.  
C. Del Don, Master Thesis: Investigation of permeation through model membranes in single vesicle traps by fluorescence correlation spectroscopy, 03/2017 – 08/2017.

## Conference and Symposium Contributions

**Bachler, S.**, D. Haidas, M. Ort, and P.S. Dittrich. *Droplet interface bilayer membranes for reaction cascades and permeation studies*, Membrane Lipids Symposium, 09.05. – 10.05.2019, Berlin (Germany), poster presentation.

Hümmer, D., **S. Bachler**, M. Köhler, S. Schulte, L. Blank, R. Zenobi, and P.S. Dittrich. *Multimodal analysis of phytase-producing yeast in nanoliter droplet arrays*, MicroTAS, 12.11. – 15.11.2018, Kaohsiung (Taiwan), oral presentation.

**Bachler, S.**, M. Ort, D. Hümmer, A. Stettler, and P.S. Dittrich. *Novel Drug Permeability Screening Platform Combining Microfluidics with LC-MS*, Swiss Industrial Chemistry Symposium, 19.10.2018, Basel (Switzerland), poster presentation.

**Bachler, S.**, P. Drücker, A.T. Müller, C. Del Don, E.B. Babiychuk, G. Schneider, A. Draeger, and P.S. Dittrich. *Interaction of Peptides and Toxins with Lipid Membranes Studied on a Microfluidic Device*, Material and Process (MaP) Graduate Symposium, 26.06.2018, Zurich (Switzerland), poster presentation.

Ort, M., **S. Bachler**, D. Hümmer, A. Stettler, S.D. Krämer, and P.S. Dittrich. *Novel Drug Permeability Screening Platform combining Microfluidics and LC-MS*, CHanalysis 2018, 12.04. – 13.04.2018, Beatenberg (Switzerland), oral presentation.

**Bachler, S.**, P. Drücker, A.T. Müller, C. Del Don, E.B. Babiychuk, G. Schneider, A. Draeger, and P.S. Dittrich. *Interaction of toxins and peptides with lipid membranes studied on a microfluidic device*. Annual Meeting of the Biophysical Society, 17.02. – 21.02.2018, San Francisco (California, USA), poster presentation.

**Bachler, S.**, C.-C. Lin, and P.S. Dittrich. *Combination of a microfluidic device and fluorescence correlation spectroscopy to study peptide translocation across model membranes*. MicroTAS, 2.10. – 26.10.2017, Savannah (Georgia, USA), poster presentation.

**Bachler, S.**, P. Drücker, A.T. Müller, C. Del Don, E.B. Babiychuk, G. Schneider, A. Draeger, and P.S. Dittrich. *Interaction of Peptides and Proteins with Lipid Membranes Studied on a Microfluidic Device*. 22.08.2017, Swiss Pharma Science Day, Bern (Switzerland), poster presentation.

**Bachler, S.**, N. Naredi-Rainer, and P.S. Dittrich. *Fluorescence Correlation Spectroscopy to Probe for Membrane Permeation and Membrane Partitioning of Peptides*. ANAKON, 03.04. – 06.04.2017, Tübingen (Germany), poster presentation.

**Bachler, S.**, N. Naredi-Rainer, and P.S. Dittrich. *Investigation of Permeation through Model Membranes in Single Vesicle Traps by Fluorescence Correlation Spectroscopy*. 18.11. – 19.11.2016, CHanalysis, Beatenberg (Switzerland), poster presentation.

**Bachler, S.**, N. Naredi-Rainer, and P.S. Dittrich. *Investigation of Permeation through Model Membranes in Single Vesicle Traps by Fluorescence Correlation Spectroscopy*. Swiss Pharma Science Day, 31.08.2016, Bern (Switzerland), poster presentation.

**Bachler, S.**, C.-C. Lin, N. Naredi-Rainer, and P.S. Dittrich. *Membrane permeation studies with FCS*. HCI Joint Minisymposium, 16.06.2016, Zurich (Switzerland), oral presentation.

**Bachler, S.**, C.-C. Lin, N. Naredi-Rainer, and P.S. Dittrich. *Investigation of Permeation through Model Membranes in Single Vesicle Traps by Fluorescence Correlation Spectroscopy*. Material and Process (MaP) Graduate Symposium, 09.06.2016, Zurich (Switzerland), poster presentation.

## List of Publications

### Full Papers

**Bachler, S.**, M. Ort, S.D. Krämer, and P.S. Dittrich. *Permeation Studies across Symmetric and Asymmetric Membranes in Microdroplet Arrays*. Submitted, 2020.

**Bachler, S.**, D. Haidas, M. Ort, T.A. Duncombe, and P.S. Dittrich. *Microfluidic Platform Enables Tailored Translocation and Reaction Cascades in Nanoliter Droplet Networks*. *Communications Biology*, 2020. Accepted.

Gautschi, D., C.S. Neuhaus, I. Kritikos, **S. Bachler**, E. Darwish, P.S. Dittrich, and G. Schneider. *Activity and Selectivity Screening of Anticancer Peptides on Cancer Cells and Liposomes*. Manuscript in preparation, 2020.

Müller, A.T., G. Posselt, G. Gabernet, C. Neuhaus, **S. Bachler**, M. Blatter, B. Pfeiffer, J.A. Hiss, P.S. Dittrich, K.-H. Altmann, S. Wessler, G. Schneider. *Morphing of Amphipathic Helices to Explore the Activity and Selectivity of Membranolytic Antimicrobial Peptides*. *Biochemistry*, 2020. **59**(39): p. 3772-3781.

Haidas, D., **S. Bachler**, M. Köhler, L.M. Blank, R. Zenobi, and P.S. Dittrich. *Microfluidic Platform for Multimodal Analysis of Enzyme Secretion in Nanoliter Droplet Arrays*. *Analytical Chemistry*, 2019. **91**(3): p. 2066-2073.

Drücker, P., I. Iacovache, **S. Bachler**, B. Zuber, E.B. Babychuk, P.S. Dittrich, and A. Draeger. *Membrane deformation and layer-by-layer peeling of giant vesicles induced by the pore-forming toxin pneumolysin*. *Biomaterials Science*, 2019. **7**(9): p. 3693-3705.

Lin, C.-C., M. Bachmann, **S. Bachler**, K. Venkatesan, and P.S. Dittrich. *Tunable Membrane Potential Reconstituted in Giant Vesicles Promotes Permeation of Cationic Peptides at Nanomolar Concentrations*. *ACS Applied Materials & Interfaces*, 2018. **10**(49): p. 41909-41916.

Drücker, P., **S. Bachler**, H. Wolfmeier, R. Schoenauer, R. Köffel, V.S. Babychuk, P.S. Dittrich, A. Draeger, and E.B. Babychuk. *Pneumolysin-damaged cells benefit from non-homogeneous toxin binding to cholesterol-rich membrane domains*. *Biochimica et Biophysica Acta (BBA) - Molecular and Cell Biology of Lipids*, 2018. **1863**(8): p. 795-805.

Kernalléguen, A., R. Steinhoff, **S. Bachler**, P.S. Dittrich, F. Saint-Marcoux, S. El Bakhi, F. Vorspan, G. Léonetti, D. Lafitte, A.-L. Pélissier-Alicot, R. Zenobi. *High-Throughput Monitoring of Cocaine and Its Metabolites in Hair Using Microarrays for Mass Spectrometry and Matrix-Assisted Laser Desorption/Ionization-Tandem Mass Spectrometry*. *Analytical Chemistry*, 2018. **90**(3): p. 2302-2309.

Pillong, M., J.A. Hiss, P. Schneider, Y.-C. Lin, G. Posselt, B. Pfeiffer, M. Blatter, A.T. Müller, **S. Bachler**, C.S. Neuhaus, P.S. Dittrich, K.-H. Altmann, S. Wessler, G. Schneider. *Rational Design of Membrane-Pore-Forming Peptides*. Small, 2017. **13**(40): p. 1701316.

#### **Published Conference Contributions**

**Bachler, S.**, P. Drücker, A.T. Müller, C. Del Don, E.B. Babiychuk, G. Schneider, A. Draeger, and P.S. Dittrich. *Interaction of Toxins and Peptides with Lipid Membranes Studied on a Microfluidic Device*. Biophysical Journal, 2018. **114**(3): p. 262a.

#### **Proceeding Papers**

Hümmer, D., **S. Bachler**, M. Köhler, S. Schulte, L. Blank, R. Zenobi, and P.S. Dittrich. *Multimodal analysis of phytase-producing yeast in nanoliter droplet arrays*. Proceedings of the 22nd International Conference on Miniaturized Systems for Chemistry and Life Sciences, MicroTAS, 2018. p. 315-317.

**Bachler, S.**, C.-C. Lin, and P.S. Dittrich. *Combination of a microfluidic device and fluorescence correlation spectroscopy to study peptide translocation across model membranes*. Proceedings of the 21st International Conference on Miniaturized Systems for Chemistry and Life Sciences, MicroTAS, 2017: p. 967-968.